Models of coupled smooth muscle and endothelial cells

Mohsin Ahmed Shaikh

A thesis presented for the degree of
Doctor of Philosophy in Bioengineering at the
University of Canterbury,
Christchurch, New Zealand.
December 19th, 2011

Acknowledgements

I would like to thank my supervisor Prof Tim David for giving me this wonderful opportunity of working on this project. I would have not gotten this far without his excellent guidance, feedback and support. It was a great pleasure working with him.

Many thanks to Prof David J N Wall, my associate supervisor, who has been very helpful and has guided me thoroughly over the past three and half years.

I would like to acknowledge the patience and support my wife, Dr. Hajrah Moshin, has shown. Her composure gave me room to recollect myself during turbulent phases.

How can I forget my son, Muhammad Ahmed, who has been a breeze of fresh air for me all the way.

I would also thank my parents who have been there for me every step of the way in this endeavour and in the past.

Most of all, I thank Allah Almighty. It is He who gave me the opportunity, the health, the strength and the intellect to prusue the problem, and has made everything possible.

Contents

List of Figures

List of Tables

Abstract

Impaired mass transfer characteristics of blood borne vasoactive species such as ATP in regions such as an arterial bifurcation have been hypothesized as a prospective mechanism in the aetiology of atherosclerotic lesions. Arterial endothelial (EC) and smooth muscle cells (SMC) respond differentially to altered local hemodynamics and produce coordinated macro-scale responses via intercellular communication. Using a computationally designed arterial segment comprising large populations of mathematically modelled coupled ECs & SMCs, we investigate their response to spatial gradients of blood borne agonist concentrations and the effect of micro-scale driven perturbation on the macro-scale. Altering homocellular (between same cell type) and heterocellular (between different cell types) intercellular coupling we simulated four cases of normal and pathological arterial segments experiencing an identical gradient in the concentration of the agonist. Results show that the heterocellular calcium (Ca^{2+}) coupling between ECs and SMCs is important in eliciting a rapid response when the vessel segment is stimulated by the agonist gradient. In the absence of heterocellular coupling, homocellular Ca^{2+} coupling between smooth muscle cells is necessary for propagation of Ca^{2+} waves from downstream to upstream cells axially. Desynchronized intracellular Ca^{2+} oscillations in coupled smooth muscle cells are mandatory for this propagation. Upon decoupling the heterocellular membrane potential, the arterial segment looses the inhibitory effect of endothelial cells on the Ca^{2+} dynamics of underlying smooth muscle cells. The full system comprising hundreds of thousands of coupled nonlinear ordinary differential equations simulated on the massively parallel Blue Gene architecture. The use of massively parallel computational architectures shows the capability of this approach to address macro-scale phenomena driven by elementary micro-scale components of the system.

Chapter 1

Introduction

The scientific method has been predicated on the thesis that by "breaking down" complex phenomena into its component parts we may be able to further understand the natural beauty of our world both surrounding us and inside us. Both animals and plants are formed from a collection of cells which in some cases numbers into the billions. Each cell within three dimensional space connects to many providing a unit capable of complex interactions. We are now at the stage where through the use of supercomputing technologies we are able to "rebuild" those parts into a viable whole and thus compare with phenomena normally seen with the naked eye.

One such example of this "connectedness" is the human vasculature. Vascular tissue comprises of billions of specialized cells. These cells are tightly packed in structures that form hollow tubes of various diameters. These tube, categorized as arteries or veins depending on whether they take blood to or away from the heart, are the primary source of transport of matter *in vivo*, from one organ to another. Endothelial cells and smooth muscle cells are the two constituent units of the vascular wall, that are of interest in this thesis. These cells form networks which give rise to vascular tissue and react to the signals originating locally, upstream (away from the direction of blood flow) and downstream (in the direction of blood flow). The channel through which this information flows between the connected cells are known as gap junctions. Through these channels, vascular cells interact with each other to produce coordinated response by the vascular tissue in response

to the blood borne signal/stimuli.

Atherosclerosis is a disease of blood vessels, primarily of arteries, in which the plaques (or obstructions) are formed and occlude the blood flow. It is a progressive disease and at mature stages, can cause *ischemia*, improper blood supply, to downstream tissue. Acute case of ischemia can cause an *infarct*, or area of necrosis where permanent damage occurs due to cells death due to severe *hypoxia* or lack of oxygen. The coincidence of the atherosclerotic plaques and *disturbed* blood flow has been indicative of an underlying relationship between the local hemodynamics and pathogenesis of the disease for decades now (Caro et al., 1969). Reliable proof of this correlation in mouse models have been shown by only recently (Cheng et al., 2006). These experiments, however, are not able to fully elucidate the mechanistic basis of this correlation. A strong hypothesis has prevailed for a long time regarding involvement of impaired mass transport in the areas of low wall shear stress and subsequent formation of atherosclerotic plaques (Caro et al., 1969). The cells (ECs and SMCs) have been found to respond the hemodynamic signals (e.g. wall shear stress) and blood borne agonists (e.g. ATP), in isolation or in as network, connected via gap junctions. A detailed literature review in Chapter 2 addresses the multiple facets of the disturbed flow regions, the associated mass transport impairment and the gap junction expressions in these region.

Computational models of ECs and SMCs have proven to be a reliable source of information on the intracellular dynamics and interaction of molecules and cell organelles. Often such information cannot be acquired in *in vitro* conditions. There are several limitations associated with *in vitro* studies that are beyond the scope of this thesis. These studies, on the other hand, have contributed enormously to the building of the computational models. It is possible to connect these mathematical models, representing an EC and SMC, into large scale multicellular models in a geometry that conforms to the anatomical structure of an artery. This multicellular model then can be used to simulate onto them, physiologically relevant environments such as hemodynamics that are characteristic of an arterial bifurcation, to elucidate the mechanisms resulting in terms of the cellular dynamics of the underlying cells. This can help understand the mechanism(s) that correlates impairment in mass transport to the pathogenesis of atherosclerosis. These are thus the aims

of this study.

In the Chapter 2, a literature review will be presented that covers the anatomy of an artery, the flow conditions and their impact within the region of an arterial bifurcation and the a review of coupled models. Chapter 3 to 6 progressively build on the methodology. Chapter 7 implements the spatially varying mass transfer profile on a computationally designed arterial section. Chapter 6 and 7 present the discussion and conclusions on the observed phenomena.

Chapter 2

Literature Review

2.1 Vascular Anatomy

The human vasculature is a continuous conduit supplying blood in approximately all tissues (exceptions include cornea in the eye is not vascularized). Depending on what an artery or vein is feeding, the radius of the artery, and to a significant extent its structure varies with its anatomical location and function. A main artery such as aorta which feeds downstream branches has radius of the order of a centimetre, where as a tertiary arteriole feeding surrounding tissue is has a radius of merely few micrometers. Thus this variation of radii across the vasculature makes it a multiscale architecture. A blood vessel is categorized as an artery or a vein depending on whether it is transporting blood into an organ or taking the blood away from it. Surely, there are structural differences between the anatomy of an artery and a vein. From here on, the discussion will be focused on an artery, as the transport is vein and its anatomy is beyond the scope of this thesis.

2.1.1 Layers of Arteries

Figure 2.1 show typical anatomy of an artery. The inner most layer, *tunica intima* (tunica=layer), is made up of endothelial cells (ECs) which lye parallel to the longitudinal axis of the arterial lumen and are the primary and direct interface between blood flow and the arterial wall. The middle layer, *tunica media*, is composed of of smooth muscle cells (SMCs). This layer is much thicker than

tunica intima. Smooth muscle cells are circumferentially assembled and are excitable (contract and relax). The outer layer,*tunica externa* also known as *tunica advetitia*is mainly composed of fibrous connective tissue, collagen. This layer is innervated (supplied with nerve endings) and is the main interface between the artery and peripheral nervous system. Adventitia is also vascularized with small arteries, called *vasa vasorum*, feeding the cells of the inner layers that are not in direct contact with the blood. *Internal elastic membrane or lamena* (IEL) or *basement membrane* as shown in the figure, is a perforated curtain between intima and tunica.

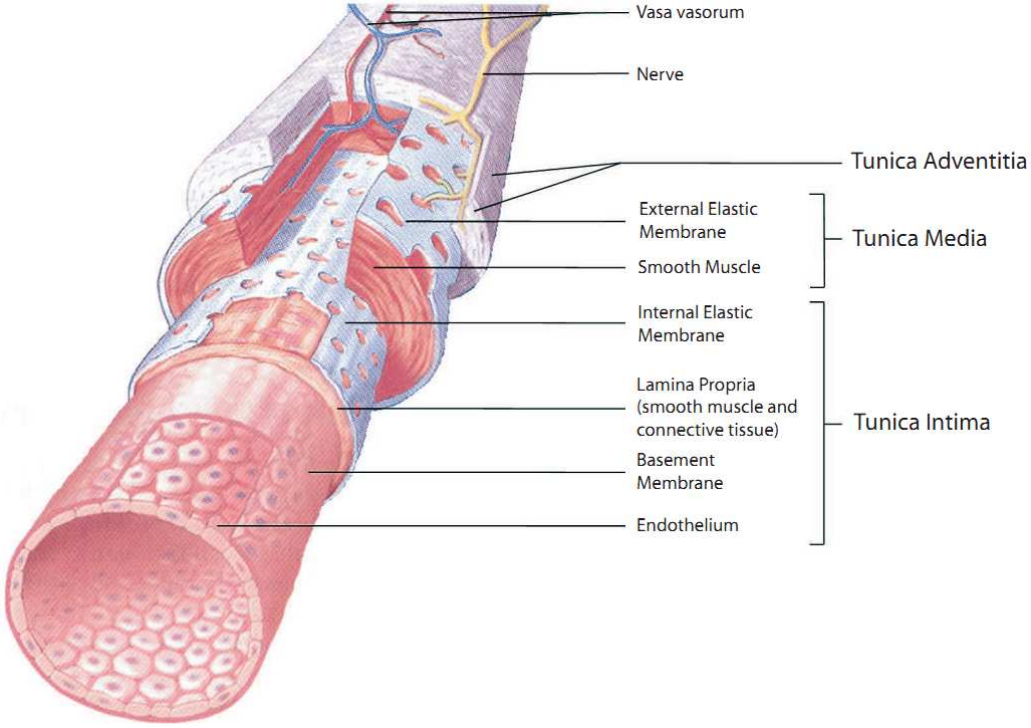

Figure 2.1: Figure shows anatomy of an artery, its layers and there positioning. (adapted from Seeley et al. (2006).

2.1.2 Anatomical Characterization of Arteries

Arteries are characterized on the basis of the thickness of tunica media and tunica media. The aorta and its branches (e.g. subclavian, common carotid (beginning

portion), pulmonary, etc) are elastic. This is to help respond the variations in blood pressure that arise within a cardiac cycle. Histologically (when studied under a microscope after staining a tissue section with colored stains), intima of the large/elastic arteries is thick. Intimal border is delineated by internal elastic lamena which is does not appear so prominent in the case of elastic arteries. Figure 2.2a shows a high power microscope image of the aortic tissue. The tunica media is most prominent and thickest of all the layers. Upon examining the cross-section of an elastic artery, one can see multiple layers of SMCs, sitting one on another. This is proportion of intimal/medial thickness is a characteristic of an elastic artery.

Muscular arteries, also termed as distributive arteries are branches of the main arteries that supply blood to organs. As shown in Figure 2.2b, tunica media is thinner compared to its thickness in elastic arteries. The IEL is distinguishable and intima is thinner than in elastic arteries. Medial layer is mainly composed of SMCs. Examples of the muscular arteries are the coronary arteries, internal and external carotid, femoral, radial, and pial artery, to name a few.

As we go down the scale, the medial layer becomes thinner and the layers of SMCs become significantly less (around 8-10 layers circumferentially). Distinguishing intima becomes increasingly difficult and the IEL remains visible. These serve as feed artery downstream to which the radius decreases further and this network is collectively characterized as the resistance arteries. The main goal of this scale of arteries is to maintain perfusion of the downstream tissue, therefore, keeping it sufficiently oxygenated as required. Tunica media is further reduced in thick, down to approximately 2 layer of SMCs, and these vessels are characterized as arterioles. Figure 2.2c & d shows examples of small arteries and arterioles. Arterioles feed the downstream capillary network.

2.2 Localization of atherosclerotic lesions

Atherosclerosis is predominantly a disease of large or proximal arteries however it also occur in small or distal vessels. The definition or specification of small arteries varies with arterial beds where the lesions form(Aboyans et al., 2007). Three arterial beds are of main concern due to their link to morbidity and mortality:

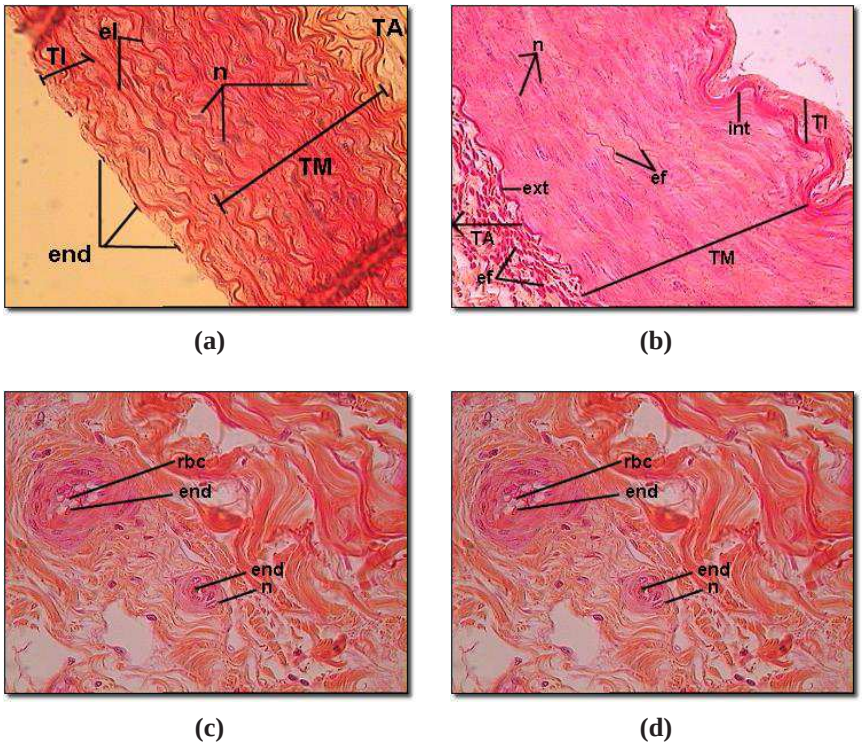

Figure 2.2: Figure shows histological images of sections of arterial tissue of different scales. (a to d) show images of an elastic, muscular, small artery and arteriole respectively. The abbreviations used in (a) are *el* = elastic lamellae, *end* = endothelial cell nuclei, *n* = smooth muscle cell nuclei, *TA* = tunica adventitia, *TI*=tunica intima and *TM*= tunica media.(b) *ef* = elastic fibre, *ext*= external elastic membrane, *int*= internal elastic membrane, *n*= nuclei of smooth muscle cells, *TA*= tunica adventitia, *TI*= tunica intima, *TM* = tunica media. (c) *end* = endothelial cell nucleus, *n* = smooth muscle nucleus, *rbc* = red blood cells. (d) *end* = endothelial cell nucleus, *n* = smooth muscle nucleus, *rbc* = red blood cells. This information was adapted from http://www.courseweb.uottawa.ca/medicine-histology

- the cerebrovascular arterial bed, including internal carotid artery
- the coronary bed
- and network of arteries supplying to peripheries such as toes and fingers etc.

The localization of atherosclerotic plaque formation is not limited to these vascular beds however and involves large arteries bifurcations and bends such as the aorta, ascending, descending, and aortic arch, abdominal aorta, renal and iliac bifurcation etc. Figure 2.3 shows in a mouse model, the localization map of prospective sites of formation of atherosclerotic lesions (adapted from (VanderLaan et al., 2004)).

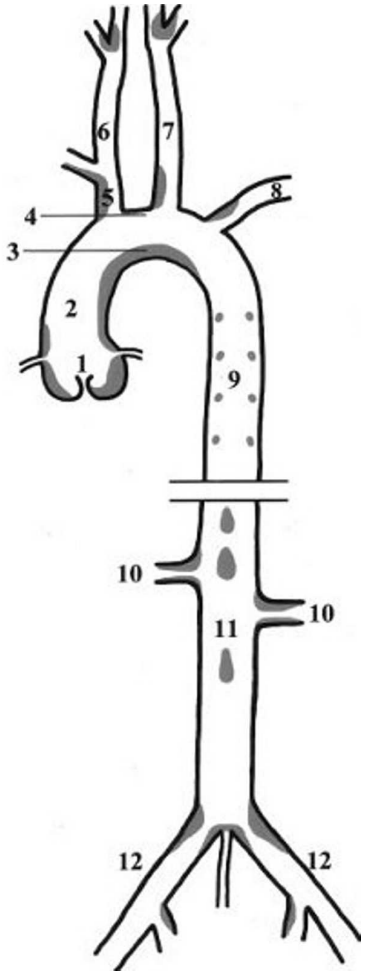

Figure 2.3: Longitudinal representation of the major arterial vasculature illustrating observed distribution of atherosclerosis (grey shading) in the vasculatures of LDL receptor-deficient mice fed a high-fat atherogenic diet. (1) Indicates aortic sinus; (2) ascending aorta; (3) lesser curvature of aortic arch; (4) greater curvature of aortic arch; (5) innominate artery; (6) right common carotid artery; (7) left common carotid artery; (8) left subclavian artery; (9)thoracic aorta; (10) renal artery; (11) abdominal aorta; and (12) iliac artery (VanderLaan et al., 2004).

Predisposing or triggering factors described by (Aboyans et al., 2007) involve:

- genetic predisposition
- age
- race
- gender (weak correlation with race)
- hypertension
- chronic high systolic and/or diastolic blood pressure
- diabetes mellitus (especially important in the lesions formation in small/distal arteries)
- smoking
- hypercholestrimia & hyperlipidemia etc.

These risk factors play a pivotal part in the progression of lesions towards plaque formation, but the aetiology of lesions has been indicated to coincide with the period as early as prenatal and infancy. Although there are some risk factors such as maternal smoking, maternal hypercholestrimia, maternal diabetes and postnatal usage of breast milk substitutes that correlate significantly with the incidence of atherosclerotic lesions at foetal and infant stage, lesions were also found to occur in some cases in spite of the lack of these risk factors(Matturri et al., 2004; Milei et al., 2008; Mukherjee, 2009).

Bifurcations, curvatures and sharp bends occur systemically in the vasculature, the focal incidence of atherosclerotic plaque in certain preferential sites and regions in human arterial system has been of research interest for quite some time now. In the case of bifurcations, fatty streaks (composed of macrophages and white blood cells and represent early atheroma) and early lesions in large arteries were established to have a significant relationship with the local hemodynamics as late as 1960's. (Caro et al., 1969) studied postmortem samples of aortic segments bifurcating/branching into the coeliac artery or the celiac trunk, superior mesenteric and renal arteries, and aortic bifurcation for evidence of lesions at branching sites, from a mixed/unselected population of cadavers. They reported a high incidence of developed lesions and fatty streaks at the outer wall of the daughter/branching arteries downstream of flow divider, except for the celiac trunk. Almost in all cases the inner wall of the daughter arteries was smooth and lacked any physical expression of lesion formation. They hypothesized that low wall shear

stress (frictional force exerted on the vessel wall due to blood flow) and altered mass transfer characteristics could contribute to formation of these lesions. The observation of unilateral involvement of daughter arteries in lesion localization at bifurcation and suggested link to limited mass transfer of solutes in these regions has been seconded by a number of subsequent studies over the time(Asakura and Karino, 1990; Comerford and David, 2008; Ethier, 2002; Kjaernes et al., 1981; Ku et al., 1985; Ma et al., 1997; Mahinpey et al., 2004; Nollert and McIntire, 1992; Tada and Tarbell, 2006).

As described in the previous chapter (Anatomy and physiology chapter yet to be written), the blood flows parallel to the long axis of the artery and there are three types of mechanical stimuli that the intimal layer experiences simultaneously. Figure 2.4 shows the directions of these mechanical forces/stimuli acting on an arterial segment (adapted from (Chien, 2007)). Wall shear stress (WSS) is the tangential component of the stress tensor acting up on the EC surface. Intramural pressure which acts perpendicular to the intimal lining varies with cardiac cycle and brings about myogenic response where underlying SMCs contract or relax thus altering the elastic stress and produces the circumferential stretch. We focus here on the tangential component of this stress tensor, the WSS, which has been found associated to the localization of early lesions.

2.3 Disturbed flow

The nature of systemic flow in non pathological vasculature is by and large laminar, except for aorta where higher flow rates caused by exercise and exertion can be observed and are capable of producing mild turbulent flow. Also, in the early systole in cardiac cycle, relatively higher flow rates could be observed which rapidly subside (not implying that the resultant flow becomes turbulent but due to high higher flow rate it nears the threshold Reynolds number (the ratio of inertial to viscous forces in fluid medium) of 2000, past which turbulence is observed. This feature has been observed only in aorta). With decrease in diameter and further branching from aorta, the Reynolds number drastically decreases and flow remains laminar throughout the vasculature for the whole cardiac cycle(Truskey et al., 2009).

Although flow is laminar in these secondary branches, the flow characteristics are very complex. Flow is pulsatile and velocity profiles are also asymmetric. The resulting wall shear stress is not only time varying but also spatially varying in these arteries. Low wall shear stress region is a area of composite phenomena rather than its literal meaning, when looking at its causative effect on atherogenesis. In addition to the magnitude variation of the WSS, there also exists a flow separation region in this area spanned by the Low WSS profile. Here the residence times of the solutes, that are carried convectively in bulk fluid, are notably different(Ma et al., 1997). Another phenomenon taking place in this region is the secondary flows or flow recirculation. By definition, secondary flows are fluid

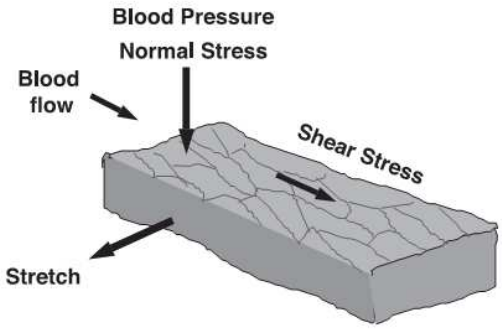

Figure 2.4: Diagram shows the generation of wall shear stress parallel (tangential to the EC surface) by blood flow and the generations of normal stress (perpendicular to the endothelial cell surface) and circumferential stretch due to the action of pressure [adapted from (Chien, 2007)].

motions which occur in a plane perpendicular to that of the distally directed blood flow and thus are secondary to the primary direction of motion(Nerem, 1992). Although tricky to measure because of their very low velocities, they do have an effect on the resultant WSS direction (or so to say WSS gradient). Another phenomenon associated to this region is impairment of the mass transfer of the metabolic entities or solutes to which the intimal wall is reactive. Thus the resulting magnitude and direction of WSS influence the concentration boundary layer of these entities and hence the response of intimal cells to this stimulus. The dynamics of this phenomenon are discussed in Section 3. The collection of these phenomena is characterized as low wall shear stress effect and the characteristic of flow is called disturbed flow.

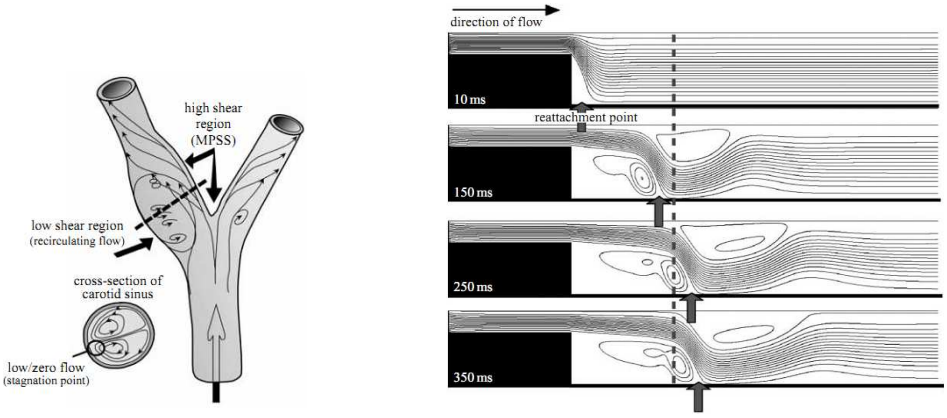

(a) Streamlines showing the velocity in different regions of common carotid (CCA) branching into internal (ICA) and external carotid arteries(ECA). Near to the apical region, high shear stress is cumulated where as disturbed flow is observed on the lateral/outer side of the bifurcation, especially in the sinus of ICA

(b) The stagnation point (marked by arrow) migrates spatially due to the sudden onset of flow. Cells under developing eddy at any location are experience temporal gradients. Cells between the step change in geometry and the dashed line experience spatial gradients due to the movement of the recirculation zone downstream.

Figure 2.5: Flow orientation in regions susceptible to atherogenesis (White and Frangos, 2007).

2.3.1 Patterns of disturbed flow at lateral wall of arterial bifurcations

Arterial blood flow is pulsatile and the absolute WSS varies with cardiac cycle continuously. In straight geometries in vasculature, blood flows unidirectionally and there is no recirculation of flow. In these regions, the time averaged WSS or mean pulsatile shear stress (MPSS) is positive (positive representing forward flow). MPSS greater than 6 dynes/cm^2 predominates throughout the arterial system(White and Frangos, 2007). Even with the laminar flow in these regions, the WSS changes with phases of cardiac cycle such as early systole, end systole, early diastole and late/end diastole. These phases govern the resultant velocity profile and hence the WSS. Thus we do witness moderate amount of time dependent WSS gradient in these regions but all in all the steady state shear stress value does not change.

The proximal and distal areas immediate to branching of the arteries and ar-

terial bends experience a different story, especially the lateral wall of the vessel. Here recirculating zones are evident as shown in Figure 2.5a. In this region flow departs from its conventional trajectory and moves away from the wall producing secondary flows, defined in the previous section. The flow eventually detaches from the wall due to adverse pressure gradient and consequent flow reversal. The point where flow reattaches itself to a location distal to the flow detachment region is known as stagnation point because of zero WSS there. The results is spatial and temporal gradients in this region. By definition, spatial gradient in WSS is the difference of shear stress between two nearby points of a cell at a time. Temporal gradient is fluctuation of WSS over a small period of time at the same location. Using a step flow apparatus in vitro (Glagov et al., 1988) showed that due the down-stroke of systole in a cardiac cycle or sudden change in flow in their case, the recirculation zone can migrate downstream thus shifting the stagnation point and returning back during diastole (see Figure 2.5b). Thus, with pulsatility, the stagnation point oscillates spatially. Due to the flow reversal, i.e. negative flow, the MPSS in this region is low. At a given location, the WSS oscillates in time because of the spatial oscillation of recirculation region and this is measured by a relative index called oscillatory shear index (OSI), and is defined by equation 1.

$$OSI = 0.5 \times \left(1 - \frac{\left| \int_0^T \tau_w dt \right|}{\int_0^T |\tau_w| \, dt} \right) \tag{2.1}$$

τ_w is the WSS at a specific location on the vessel wall and the limit 0 to T time, typically of the order of one or more cardiac cycles. Thus OSI can fluctuate between 0 to 0.5, 0.5 being highly oscillatory thus representing sever flow reversal. Magnetic resonance imaging based studies coupled with computational fluid dynamics applications have attempted to investigate the causative potential of oscillatory flow in the regions of interest. Figure 2.6 shows the mapping of OSI in carotid sinus of ICA. By looking at the figure it can be observed that the largest OSI values (represented by red in Figure 2.6b) coincides with the patches of the vessel experiencing low time averaged WSS at or around bifurcation in Figure 2.6a. This means that the intimal layer of this region will be experiencing a spatial and temporal gradient of low magnitude wall shear stress simultaneously.

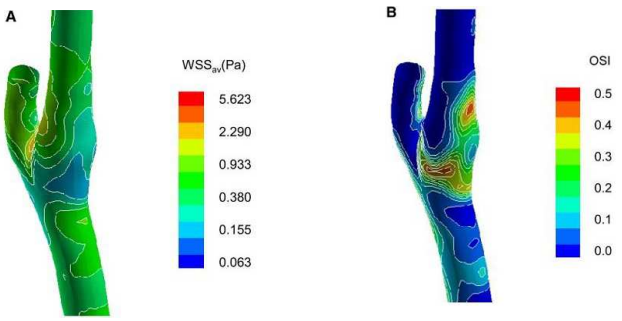

(a) Time averaged wall shear stress

(b) OSI map

Figure 2.6: Time averaged hemodynamics in a realistic model of carotid artery. Some areas under low WSS in (a) also experience oscillatory flow thus facing a synergistic spatial and temporal gradient(Augst et al., 2007).

2.3.2 Effects of disturbed flow on vascular endothelium

Cellular morphology

Vascular endothelial cells form the surface or intimal lining of the arterial lumen and is exposed to hemodynamic and or humoral stimuli brought into their vicinity by bulk flow. In addition to being reactive to various blood borne solutes, the endothelial cells also respond to alterations in WSS and it is found capable of changing the intracellular haemostasis of a vascular endothelial cell. This is not only manifest biochemically but also affect the cells morphology. A substantial number of in vitro studies have shown effect of flow on the cytoskeleton of an endothelial cell (Chiu et al., 1998; Colgan et al., 2007; DePaola et al., 1999; Jeng-Jiann et al., 2004; Malek et al., 1999; Sakamoto et al., 2010). In static or no flow conditions, where WSS is low or zero, the endothelial cells appear polygonal in shape under a microscope as opposed to when laminar flow with high WSS, where cells are elongated in the direction of flow. Under both laminar flow with low WSS and disturbed flow conditions, ECs express similar morphological behaviour as when under stagnant flow. Also, while elongated under a laminar flow with relatively moderate to high WSS, the ECs are in close contact with neighbouring ECs. Figure 2.7 illustrates the EC elongation and alignment in the direction of flow which is capable of producing moderately high WSS. This cellular adhesion

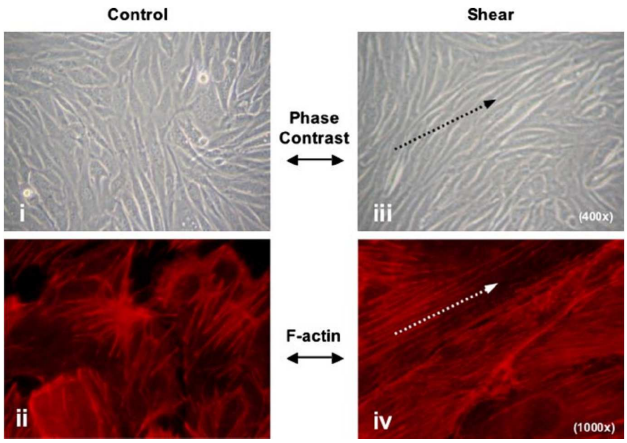

(a) Effect of steady shear stress on bovine brain microvascular endothelial cell (BBMvEC) morphology. Following shear stress (10 dyn/cm^2,24h),BBMvEC realignment was monitored by phase contrast microscopy (i and iii) and standard fluorescent microscopy (rhodamine-phalloidin staining for F-actin; ii and iv). Dotted arrows highlight alignment in direction of flow. Images are representative of 3 independent experiments (Colgan et al., 2007).

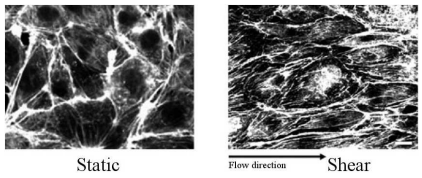

(b) Bovine aortic EC under static and flow conditions. Under no flow condition cells have random shape but under shear the shape is more homogeneous and definitive (Tzima, 2006).

Figure 2.7: Influence of fluid shear stress on EC cytoskeleton.

allows more surface area for cell - cell contact and better intercellular communication either via paracrine or gap junctional communication. Under high WSS ECs respond by activating the rearrangement of endothelial cytoskeleton. One of the possible mechanism for shear stress stimulated restructuring of microtubules is proposed by (Tzima, 2006), as shown in Figure 2.8, which involves membrane bound G protein activation followed by a complex downstream process which rearranges not only the cell's own cytoskeleton but also communicated with adjacent ECs to allow the expansion in the longitudinal direction.

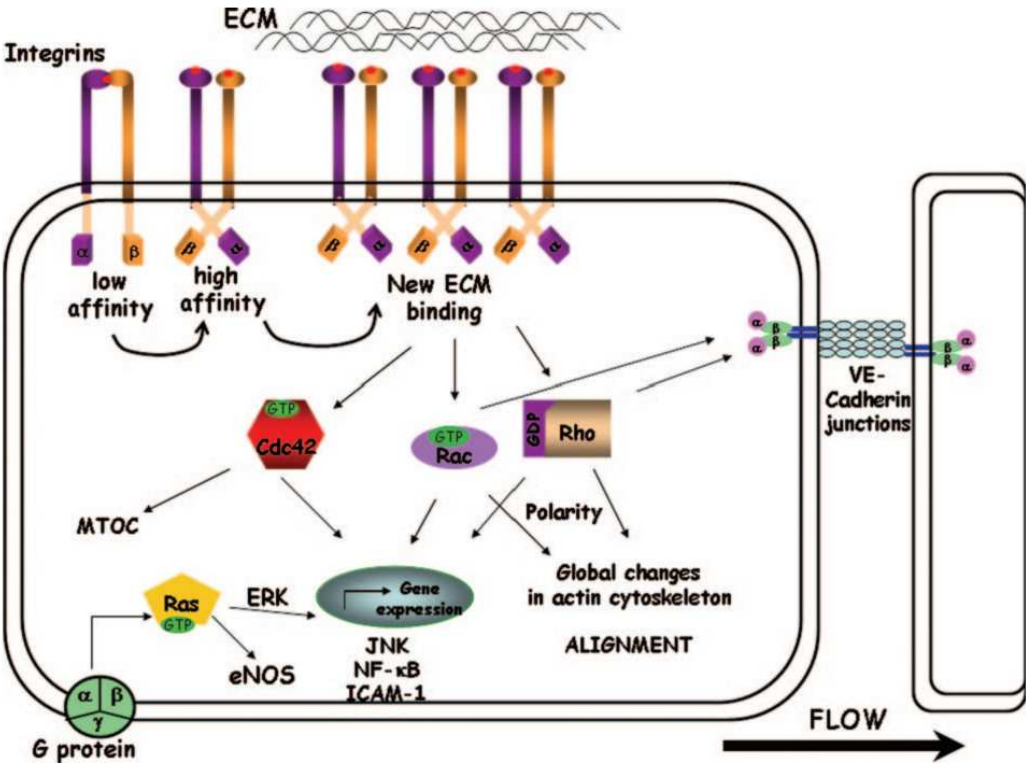

Figure 2.8: Model for mechanotransduction. Shear stress activates integrins, which bind to extracellular matrix. Ligated integrins transiently deactivate Rho, which causes disassembly of stress fibers. Ligated integrins also activate Rac at the downstream edge of the cell, which facilitates alignment of the newly formed stress fibers in the direction of flow. Polarized activation Cdc42 mediates reorganization of the microtubule organizing centre (MTOC). GTPases also control gene expression and regulate endothelial junctions. Ras GTPase is activated through G proteins and regulates gene expression under flow through extracellular signal regulating kinase (ERK) and C-Jun-N-terminal kinase (JNK) as well as endothelial nitric oxide synthase(eNOS) activation (Tzima, 2006).

Cell migration

Another important effect of WSS on morphology of EC layer is related to geometries where flow impingement can occur, for example the apex of an arterial bifurcation. In vitro studies have shown that local hemodynamics profoundly effect EC migration and proliferation rates in these regions. In the apical region of bifurcation, an impinging flow is observed. This is characterised by having a stagnation point (where WSS is zero and WSS gradient is zero) surrounded by high WSS regions on both side where WSS gradient has also reached a maximum. (Szymanski et al., 2008) created such regions using an inverted T shaped flow divider where flow would enter from the top and then go sideways when reaching the divider. The bottom of this inverted T shaped conduit (see Figure 2.9 where ECs are cultured on a cover slip).

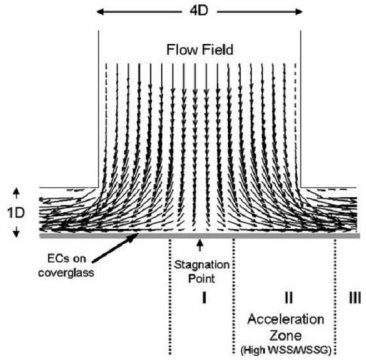

(a) 2D sketch of inverted T shape conduit used in the experiment. The velocity magnitude, direction in the impingement flow field, and the three flow zones (I, II, III) are also shown

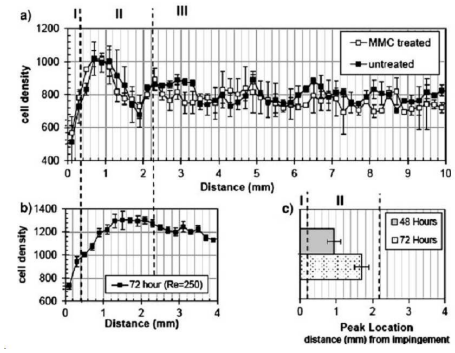

(b) (a) Cell density vs. distance for ECs treated with and without Mitomycin-C (MMC), an irreversible inhibitor of cellular proliferation after exposure to high flow (Re=250) for 48 h. (b) Representative cell density peak for untreated cells exposed to high flow (Re=250) for 72 h, showing a shift downstream compared to 48 h. (c) Peak location measured from the impingement at 48 and 72 h experiments under high flow.

Figure 2.9: Migratory behaviour of EC seen in the case of impinging flow mimicking that seen at spices of arterial bifurcations(Szymanski et al., 2008).

At the beginning of the experiment, the region where stagnation point was formed, cells presented random polygonal shape with a uniform cell density as its adjacent regions on both sides. In regions with high WSS ECs were elongated in the direction of the flow. With passage of time, the cell density decreased in

the area of low or zero WSS and increased in the surrounding high WSS region (where WSS gradient is also high) but was unaffected in the areas beyond where WSS gradient was either low or non existent. This behaviour persisted in the presence of proliferation inhibitors showing that the cell density increase in the regions of high WSS and high WSS gradient was not because of the cell growth but ECs migrated from low or no WSS regions to high WSS and this migration was promoted by existence of WSS gradient.

Cellular proliferation

Local flow patterns have also been found to affect the growth rate or rate of proliferation of ECs. Laminar flow with adequately high WSS reduces DNA synthesis and ECs are arrested in cell cycle thus they age slower and hence the turn over time of such populations is higher(Davies, 2000). In the areas of disturbed flow such as bifurcation points, ECs age faster(Cooke, 2003), thus the proliferative rate is higher that the laminar flow (high WSS) regions. Aged ECs produce less nitric oxide (NO), and generate free radicals such as superoxide anions(Tseng et al., 2010). Thus, laminar flow with high WSS acts as atheroprotective agent compared to the disturbed flow in branching point and bends, that encourages atherogenic processes.

Disturbed flow and endothelial calcium dynamics

As has been established earlier, the correlation between complex fluid flow, low and/or oscillatory WSS and atherosclerotic plaque localization firmly exists, yet less is known about the mechanistic basis of formation of the early lesions. WSS is a known stimulus for second messenger mediated signal transduction in the ECs that leads to important downstream intracellular processes and perturbs cellular haemostasis. These effects include manipulation of intracellular Ca^{2+} concentrations, activation of gene expressions specific to production of proteins that bring about definitive changes in endothelial cytoskeleton and altering vasomotor tone, in dose dependent manner, which is thought to be mediated by what is known today as *Endothelial derived relaxing factor (EDRF)*, widely accepted to be nitric oxide (NO). NO is a potent vasodilator that diffuses into the medial layer of

the artery and enforces relaxation of contracted SMCs. Endothelial Nitric Oxide Synthase (eNOS) is a enzyme that when activated initiates production of NO from an intracellular substrate L-arginine(L-Arg), in the presence of oxygen. Of multiple pathways for the activation of eNOS, bioavailability of cytosolic Ca^{2+} is one. In response to certain external stimuli such as WSS or agonist binding to specific receptors located in plasma membrane, Ca^{2+} can enter the cytosol of an EC via specific and/or non specific Ca^{2+} channels, thus increasing the intracellular Ca^{2+} concentration and providing means of eNOS activation and consequent NO production. Figure 2.10 depicts this process.

NO rapidly diffuses past basement membrane and into the SMCs in the medial layer where it activates an intracellular hemoprotein soluble guanylate cyclase (sGC) which catalyze the conversion of Guanosine triphosphate (GTP) into cyclic Guanosine MonoPhosphate(cGMP). cGMP then activates a pivotal entity called protein kinase G (PKG) which performs a number of important regulatory cell functions including the relaxation of SMCs. PKG disables the Ca^{2+} influx pathways and also desensitizes the myosin light chain kinase (MLCK), the building block in the contractile cytoskeleton of a SMC, to Ca^{2+} calmodulin(Ca^{2+}-CaM) complex. PKG has also been found to induce gene expression which enables the potassium(K^{+}) efflux via Ca^{2+} activated K^{+} channels. All these concurrent processes result in SMC relaxation. Hence, NO activation of cGMP pathway to bring about vasodilation through SMC relaxation is partially dependent on the Ca^{2+} influx into and EC in response to external stimuli such as agonist binding or WSS. Not much literature exists on the response of coupled ECs/SMCs to disturbed flow as a unit but the information on how isolated cells or homogeneous populations of ECs or SMCs react to steady and unsteady flow is available.

2.4 Mass Transport and Atherosclerosis Localization

Whole blood carries many solutes which sever as either ligands to specific receptors, or are to be excreted or to be transported to distant organs. These blood borne species vary in size, mass/molecular weight, diffusivity, electrostatic properties and several other factors that come into account in determining their mass transfer characteristics. Amongst these blood borne species are vasoactive solutes

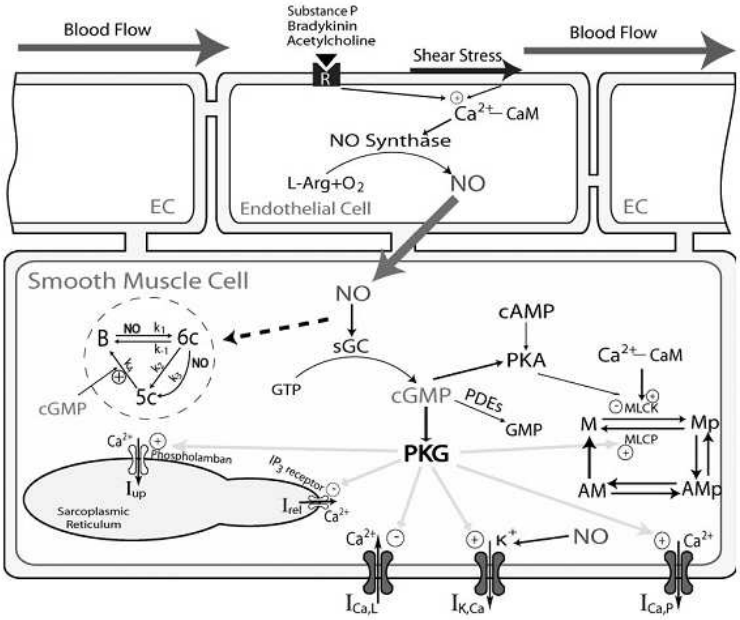

Figure 2.10: Schematic diagram of endothelium-derived smooth muscle relaxation via nitric oxide (NO)/cGMP pathway(Yang et al., 2005).

such as vasodilators (e.g. histamine, adnosine, acetylcholine, bradykinin, noradrenaline, substance P etc..) and vasoconstrictors (e.g. adenosine triphosphate and adenosine biphosphate (ATP and ADP), phenylephrine, endothelin, angiotensin II, norepinephrine etc..) which are of interest here. These solutes serve as agonists to specific receptors expressed by EC surface and upon attachment activate complex downstream processes that result in a number of agonist specific alterations such as reorganization of cellular cytoskeleton, gene expressions which initiate further downstream processes such as cell proliferation or apoptosis, activation of exocrine processes, or even release of agents that further affect the cells in periphery such as in vasomotion; to name a few. Local mass transfer characteristics of these molecules heavily rely on the hemodynamics of that region. (Caro et al., 1969) first hypothesized the correlation of impaired mass transfer in regions of disturbed flow and early atheroma. In a subsequent publication (Caro et al., 1971) they elaborated that the altered mass transfer characteristics, specifically for cholesterol in their case, were coupled to low WSS profiles. Cholesterol is excreted out of the cell into the blood stream and carried to the liver where it is metabolized. In

pathology cholesterol accumulates in the cell leading to cytotoxicity. According to the authors, WSS has a sweeping effect on the concentration of cholesterol on the wall surface hence maintaining the concentration gradient for further efflux of cholesterol from wall phase to fluid phase. In the areas of low WSS, the reduction of this sweeping effect diminishes and the concentration boundary layer of the surface cholesterol thickens, thus lowering the drive of the molecules moving from inside of the cell to the outside on the wall surface. This causes retention of cholesterol inside the cell. This hypothesis was further seconded by (Kjaernes et al., 1981). Thus in a historic perspective there exists this notion of involvement of impaired mass transfer in the regions of disturbed flow.

Later advances in computational techniques and imaging modalities have improved the mechanistic understanding of the altered mass transport coupled to the disturbed flow. Using computational fluid dynamics for a realistic geometric model of human carotid artery, (Ma et al., 1997) computed the mass transport characteristics at and around carotid bifurcation. Emphasis was given on the mass transport of small molecules such as oxygen and is suggested that it may also imply to other blood borne species with relatively low diffusivity e.g. ATP and ADP in ambient conditions. The velocity profiles of their computational fluid dynamic (CFD) study showed disturbed flow characteristics particularly on the lateral wall (outer wall) of sinus located immediately after the point of bifurcation in the internal carotid branch (ICA). This included both substantially large recirculation zones and areas of flow separation followed by reattachment of fluid distal to the flow separation region. The specie concentration in this region was reduced when compared to the rest of the locations in geometry where flow was undisturbed. Coupled with the thickening of the hydordynamic layer (a thin immobile layer of fluid that always exists at a solid/moving fluid interface) was the progressive thickening of specie concentration boundary layer (the height of the region from the wall to the centre of the axis devoid of specie). The thickened concentration boundary layer extended upstream of the bifurcation point (see Figure 2.11). Interestingly, the authors also found that the peak of the concentration boundary layer did not coincide with the minute region of flow separation where the WSS was 0, but was located slightly upstream to it where low WSS existed. This region where low WSS existed would also have nonzero WSS gradient. Downstream of

the flow reattachment the concentration boundary layer fades and becomes thin once again.

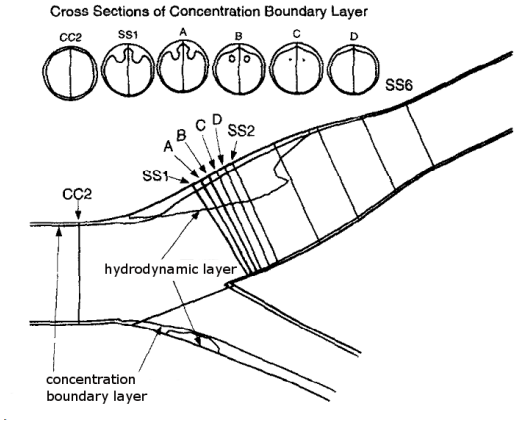

Figure 2.11: Region of flow recirculation correlates well with thickened concentration boundary layer. Cross sectional views show that the concentration boundary layer is convoluted in the sinus. However, the thickest concentration boundary layer does not coincide identically with flow separation (Ma et al., 1997).

Other subsequent studies focusing species of similar size or other important larger molecules such as low density lipoproteins (LDL) with similar diffusivities, have also been conducted with more contemporary techniques revealing more information on the mechanics of the mass transfer in regions with altered flow characteristics. Some studies have attempted to model the effects of geometry (Comerford et al., 2006) on the species mass transfer to the wall where as other have modelled the effects of flow characteristics such as pulsatality (Barakat, 2001), Reynolds number (Mahinpey et al., 2004). (David, 2003) considered the dependence of local specie mass transfer as a function of local flow derived parameters such as WSS and its spatial variability . (Kaazempur Mofrad et al., 2005) have modelled the mass transfer of small molecules such as oxygen and ATP in stenosed arteries. Thus this problem has been looked upon from various angles but all these studies focus on the hemodynamics and the resultant specie concentration on the wall. The biochemical influence of the alteration in concentration boundary layer vasoactive substances on the vessel wall has rarely been studied (Comerford and David, 2008; Comerford et al., 2008; Plank et al., 2006a,b). (Plank et al., 2006b) modelled the effects of spatial variation of WSS on Ca^{2+} dynamics of an EC by coupling a mass transport model of ATP and an EC Ca^{2+} dynamics model in 2D backward facing step geometry. This geometry simulated widening of an artery and recirculation zones and stagnation point occurs past a wedge. WSS varied as a function of axial location and ATP concentration on EC surface is de-

pendent on both the axial distance and local WSS in this study. The fact that ECs produce ATP which in turn stimulates the cell itself in autocrine and neighbouring cells in paracrine manner, is also included in the model as increasing function of WSS. Ca^{2+} influx via IP_3 dependent and independent pathways due to either ATP or WSS stimulation respectively is taken into the account. Results, as shown in Figures 2.12(a) to (c) show that the steady state ATP concentration is spatially varying in the areas where WSS gradient exists. Moreover, unlike (Ma et al., 1997), the minimum ATP concentration coincides with the stagnation point where magnitude of WSS is zero. The Ca^{2+} concentration is lowest in the recirculation zone and minimum at the stagnation point. The magnitude of maximum and minimum Ca^{2+} however is a function of the flow velocity but the spatial variation feature is retained even at higher laminar flows. (Comerford et al., 2008) used the model presented by (Plank et al., 2006b) to numerically study using CFD, the effects of arterial bifurcation geometry on the eNOS production and Ca^{2+} dynamics in a near realistic geometry. The localization of spatial gradient in ATP concentration conferred with the (Ma et al., 1997) finding and occurred at the outer wall just upstream of the bifurcation region and followed the regional WSS profile very closely.

Spatial variation of ATP concentration in arterial regions with disturbed flow is evident in steady state scenarios. The fact that the flow rate and Reynolds number fluctuates over the period of a cardiac cycle which consists of a systole phase where flow accelerates due to the emptying of contracting left ventricle of the heart and pushing the blood into the arteries. This is followed by a deceleration which relates to the closure of the aortic valve and initiation of the refilling of the left ventricle. A diastole phase follows the end of the systole which is relates to the refilling period of the left ventricle for the next systole. The flow remains relatively steady in this phase. Thus WSS varies with pusatlity at the arterial wall in straight segments. In regions of disturbed flow the time varying WSS profiles are different then in a straight segment and the very fact that the atherosclerotic lesions occur in these regions, these profiles are referred to as atheroprone or atherogenic. Thus it would be logical to ask the question whether the mass transport also shows time varying characteristics atheroprone regions. (Barakat, 2001; Comerford and David, 2008) have studied the time varying characteristics of the nucleotide con-

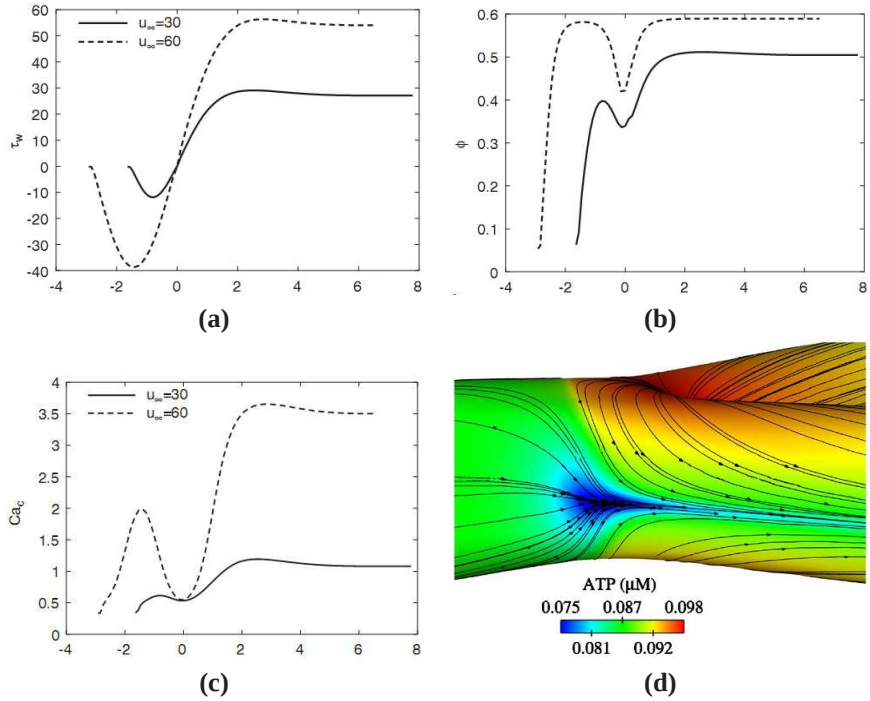

Figure 2.12: Spatial gradients in WSS and ATP concentration at arterial bifurcations. (a),(b) and (c) show stable steady value of WSS (τ_w), ATP concentration (ϕ) on EC surface and intracellular Ca^{2+} concentration (Ca_c), respectively, plotted against axial distance (x) for two different flow velocities where x=0 is the reattachment point (Plank et al., 2006b). (d) shows the ATP contours with limiting streamlines overlain,θ=75 deg and Re=500 at the outer wall (Comerford et al., 2008).

centration in regions of disturbed flow numerically.

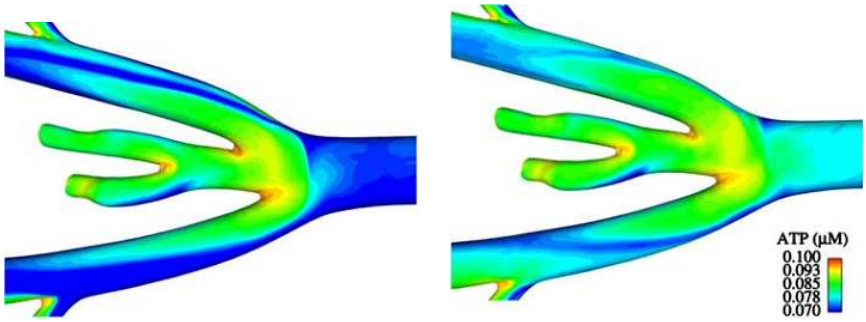

Figure 2.13: Comparison of ATP topology: (a)Steady, (b)time averaged. Although the surface concentrations are different to a certain degree there are very similar characteristics (Comerford and David, 2008).

(Comerford and David, 2008) contributed some vital information regarding the ATP mass transfer characteristics in steady and unsteady/pulsatile flow. The authors did an intensive CFD study in a realistic porcine trifurcation which was focused at investigating the effects of pulsatile flow on the concentration boundary layer of ATP in non-uniform geometry such as near the branches and gave emphasis to the outer walls of the proximal regions of parent and daughter vessels in the branching areas. Figure 2.13 shows compared the ATP concentration distribution in time invariant spatially non-uniform flow profile in (a) as opposed to the time varying case in (b). It is evident that although the level of depletion of ATP in the areas known to have reduced mass transfer is exaggerated in steady flow case compared to the time varying, the pattern or localization remains unaffected. Moreover, even in the case of pulsatile flow the ATP surface concentration did not show any noticeable transient behaviour. Figure 2.14 shows this by comparing the early and end systole flow were the velocity profile are distinctively changed but surface distribution of ATP concentration remains relatively unaltered, suggesting that the mass transfer of species such as ATP with high Peclet number i.e. low diffusivity as compared to advective transport, dose not change transiently under time varying flow. The authors attributed this limited transient behaviour of ATP concentration to the low diffusivity of ATP.

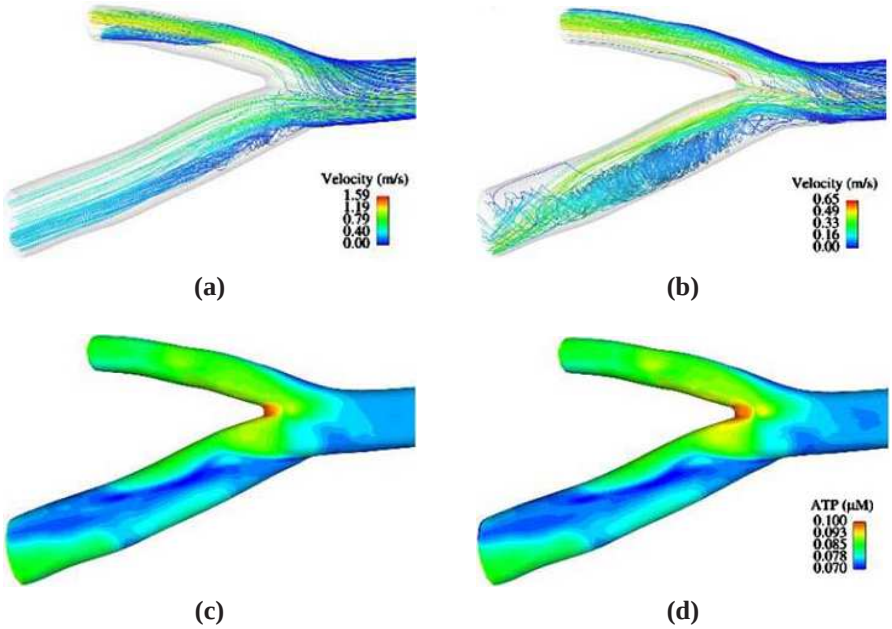

Figure 2.14: Comparison of hemodynamics and resulting ATP distribution in the iliac artery in the region of femoral branch (a)time=0.15 and (b)time=0.27. The size and strength of secondary flow is considerably greater during systolic deceleration (time=0.27), however ATP distribution does not change significantly due to the very low diffusivity (Comerford and David, 2008).

2.5 Intercellular communication and atherosclerosis

Appropriate tissue perfusion is mainly regulated by the supplying arterial diameter that controls the resistance of the feeding arterial tree and thus the flow in it (Pohl et al., 1993). Thus to alter the conductance of the arterial conduit there has to be a means of communicating the message from the tissue end to the upstream vasculature which could react by increasing the blood flow by vasodilation. Ascending or conducted dilation is a concept where by the dilation of the vessels start from arteriolar scale moving up to the secondary or muscular arteries(Wit and Wolfle, 2009). To make this coordinated dilation possible, it is necessary that the vessel segments which are made up of individual ECs and SMCs, work together as a unit and bring about the change in diameter. Intercellular communication provides that pathway to establish such a network through intercellular gap junctions.

Gap junctions are intercellular channels that directly connect the cytoplasm of adjacent cells, allowing the passage of current and small signalling molecules (molecular mass< 1,000 Da), such as Ca^{2+} and IP_3 (Figueroa and Duling, 2009). They are constituted by channels made of protein called connexin (Cx). A collection of six connexins form a connexon, or a hemichannel. Two hemichannels, contributed one from each apposing cell forms a functional gap junction. Hemichannels remain close unless docked with the complementary hemichannel in the adjacent cell.

A connexon or hemichannel can be formed of a single type of connexin, in which case it is called a homomeric channel or of a mixture of connexins forming a heteromeric channel (Haefliger et al., 2004). The constituency of hemichannels forming a gap junction directly influences the functional properties of that channel, such as ion permeability, selectivity to solutes, its open probability and its subcellular localization. It is becoming increasingly evident that the heteromeric nature of formation of hemichannels could be a means of fine tuning the selectivity of the channel(Johnstone et al., 2009). Two hemichannels on adjacent cells can interact and form a functional gap junction in either of the two manners: homotypic or heterotypic. A homotypic junction is one where all the twelve connexin subunits are identical. In heterotypic junction, each hemichannel is homomeric and of different connexin isoform (Rackauskas et al., 2007a). On cell-cell level, gap junctions

formed between identical cell types are known as homocellular junction and between different cell types it is called heterocellular junction. EC-EC homocellular contact is well documented in both marco (Ebong et al., 2006) and microvessels (Segal and Beny, 1992). SMC-SMC communication has also been demonstrated to conduct vasoconstriction through gap junctions in arterioles (Figueroa and Duling, 2008).

All the discussion that follows will consider homotypic gap junctions from here on. Intercellular transport of ions or metabolic species such as Ca^{2+}, IP_3 , cGMP, cAMP, ATP, glutamate, glutathione and monovalent ions such as Na^+,$K^+$and Cl^- which act as charge carriers form the basis of the intercellular coupling. There can be two topologies forming the network comprising of two types of cells. Cells can couple either homocellularly (EC↔EC or SMC↔SMC) or heterocellularly (EC↔SMC or SMC↔EC). (Beny, 1999) suggests that there can be four possible coupling modes which are plausible in propagating information from the point of stimulation or where the signal arises.

1. Transmission of metabolic species e.g. Ca^{2+} and IP_3 which traverses the cytoplasm of the receiving cell and passed on to the apposing cell. This mode of transmission would pass the message to very short distances at a very slow rate.
2. Intercellular exchange of second messenger e.g. Ca^{2+} and IP_3 which triggers an intercellular release of Ca^{2+} via Ca^{2+} induced Ca^{2+} release (CICR). The speed of propagation will match that of diffusion but it may carry the signal to finitely long distances.
3. Between non-excitable cells like ECs, rapid electrostatic coupling which is made possible by the close apposition of cell membranes of adjacent cells may take place. This modes cannot traverse long distance because of the exponential decay in the transmitted charge with increasing distance.
4. Electrostatic coupling between excitable cells like SMCs (because of having voltage operated Ca^{2+} channels), which is rapid and theoretically could propagate the signal for infinitely long distances.

Keeping in line with these observations of (Beny, 1999) we consider the intercellular coupling via three media, Ca^{2+}, IP_3 and electrostatic or membrane potential

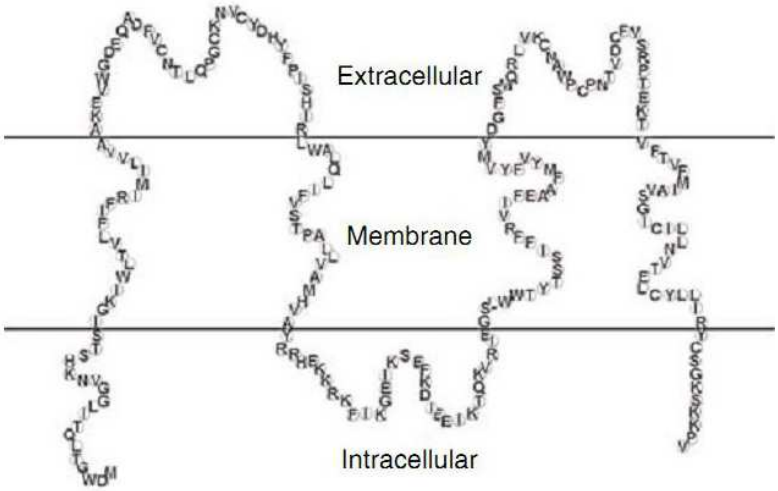

(a) Transmembrane domains, two extracellular and two intracellular loops are shown for Cx26 protein.

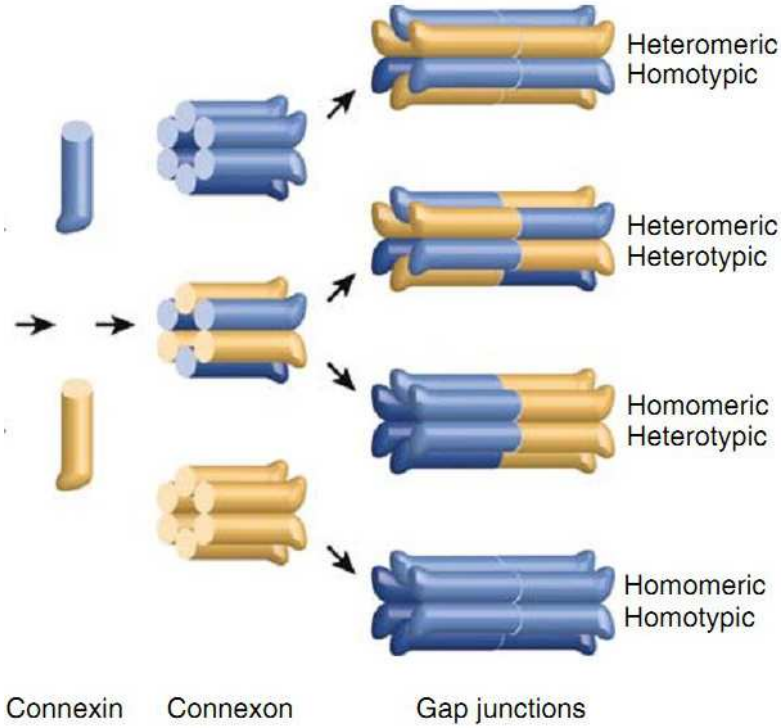

(b) A hierarchical scheme that results in a functional gap junction of one of the four types.

Figure 2.15: Schematic representation of an intercellular gap junction between two adjacent cells (adapted from (Mese et al., 2007))

homocellular and heterocellular coupling between apposing cells. Association of these coupling media to relevant connexins constituting the connexons through which these ions pass, has been made in previous section (gap junctions in Ch1).

2.5.1 Localization of vascular connexins

Three connexin isoforms, Cx37, Cx40 and Cx43 are commonly expressed in vasculature (Arensbak et al., 2001; Johnstone et al., 2009; van Kempen and Jongsma, 1999). The expression is not uniform systemically (i.e. is heterogeneous) and varies with specie, vascular bed and in stasis and pathology (Hill et al., 2001). Cx40 has been recognized as one of the most commonly expressed connexin in ECs in general and in SMCs in muscular and small arteries (van Kempen and Jongsma, 1999). Cx37 is also expressed in most if not all small arteries and arterioles (Ebong et al., 2006; Gustafsson et al., 2003; Isakson et al., 2006; Isakson and Duling, 2005; Toma et al., 2008; van Kempen and Jongsma, 1999; Yeh et al., 2003). Cx43 in ECs is more heterogeneous and site specific. .Cx43 in ECs has been reported in areas with disturbed flow (Dai et al., 2004; DePaola et al., 1999) or in tissue manifesting pathology (Kwak et al., 2002).

In SMCs the connexin expression is much more heterogeneous and sometimes absent in a few vascular beds. Cx43 expression has been widely reported in elastic and muscular arteries (aorta and carotid (Arensbak et al., 2001; Haefliger et al., 2004; Kwak et al., 2002) while there have been disparate reports about expression of Cx37 by SMCs in few species (Arensbak et al., 2001; Haefliger et al., 2004; Kwak et al., 2002; Simon and McWhorter, 2003) which can be due to intra-specie difference. Cx40 in SMCs has been rarely been reported and only at small artery to arteriolar scale (Burt et al., 2001; Kwak et al., 2002; Little et al., 1995; van Kempen and Jongsma, 1999; Zhang and Hill, 2005).

Propagation or spread of a local stimulus in the intercellular network of an artery is oriented either longitudinally (i.e. parallel to the vessel axis, upstream and downstream) or transversely (into the wall to the SMCs, which are connected to the ECs via MEJs). Homocellular coupling enables the longitudinal transmission where as the heterocellular coupling enables the transverse signalling. Both the homocellular and heterocellular gap junctions have been implicated in patho-

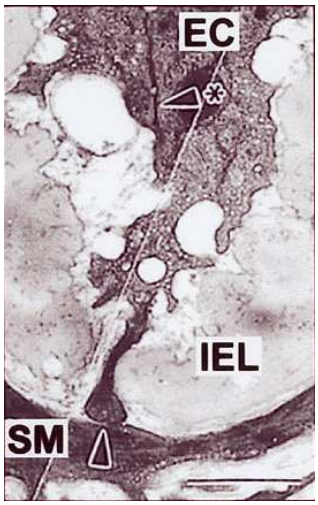

Figure 2.16: Myoendothelial gap junction. Transverse section of an artery viewed by electron microscopy showing the projection of an EC through the internal elastic lamina (IEL) to an underlying SMC (SM). Arrow heads indicate homocellular and heterocellular gap junctions (Sandow and Hill, 2000).

genesis of atherosclerosis. MEJs provide means of physical contact between ECs and SMCs. Projections of ECs protrude from the perforated internal elastic lamina to come in close apposition to the underlying SMC, as shown in Figure 2.16.

Advancement in experimental technique has enabled identification of the constituency of these gap junctions in a variety of specie specific vascular beds. Using Transwell^{TM} (Corning) insert (see Figure 2.17a), mouse ECs and SMCs were co-cultured and allowed to form the MEJs, Figure 2.17b showing the cell cell contact between EC and SMC and the relevant fluorescent membrane markers forming a MEJ in IEL. In this study (Isakson and Duling, 2005) aimed at examining the constituent connexins and gap junctional communication between ECs and SMCs via the MEJs. Both Cx40 and Cx43 were significantly expressed at the MEJ level. Cx37 was absent in this domain but was abundantly found when homocellular EC-EC or SMC-SMC populations were allowed to grow in these Transwells^{TM}. Using a charge neutral dye, biocytin(MW=357Da), intercellular communication was monitored. The authors confirmed that both Cx40 and Cx43 contributed in transfer of the dye from ECs to SMCs and eliminated the presence or role of Cx37 in MEJ domain. Figure 2.17c shows the status of transfer of biocytin from EC to SMC in the presence and absence of all gap junctional blocker 18α Glycyrrhetinic acid (18α-GA). In the same study, using connexin specific gap junction inhibitors Gap27^{40} and Gap27^{37,43} and letting a charged dye, Cy3 (MW=767Da, Z=-1), pass

through the MEJs, the authors suggested that the formed hemichannles might be heterotypic and their conductance could depend on the stoichiometry of Cx40 and Cx43. Thus this indicates a possibility that this stoichiometry may alter the extent of heterocellular coupling with varying connexin specific stimuli or in different vascular beds.

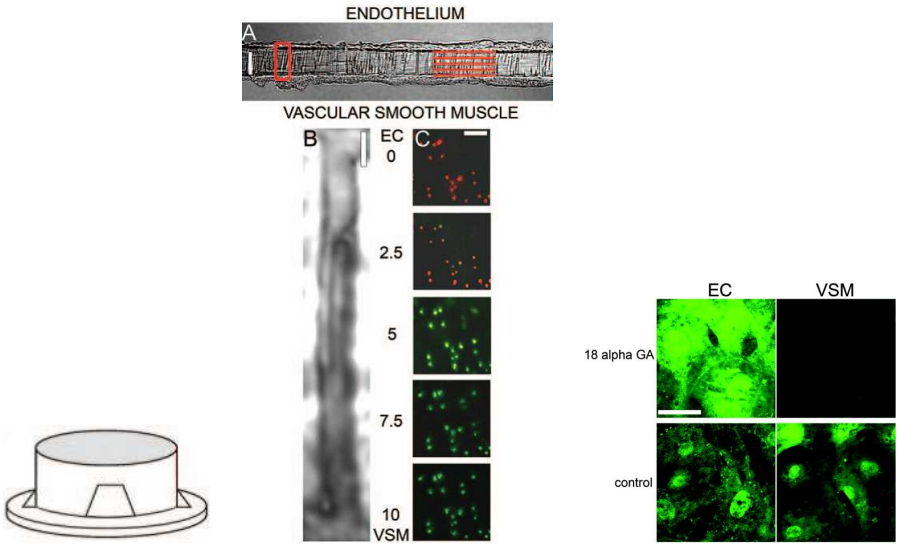

(a) A Transwell^{TM} (Corning) insert.ECs cultured on top side and SMCs at the bottom.

(b) A: formed myoendothelial region. B: physical EC and SMC projections . C: EC (red) and SMC(green) membrane marker as we go down vertically in the transwell from top to bottom.

(c) Effect of gap junction inhibitor 18α-GA on biocytin transfer from EC to SMC.

Figure 2.17: Gap junctional communication via MEJ (Isakson and Duling, 2005)

2.5.2 Effect of hemodynamics on local connexin expression

Blood flow has been shown to alter connexin expression in both ECs and SMCs. (Rummery et al., 2002) did a 12 week long study to examine endothelial connexin expression (for Cxs 37,40&43) in caudal artery of spontaneously hypertensive male rats (SHR) and compared the results with Wistar-Kyoto (WKY) type normotensive rats, using immunohistochemistry. The onset of hypertension in SHR was observed at the age of 9 weeks with significant increase in systolic blood pressure. Cx40 expression in ECs was significantly low in SHR at 3 weeks, well be-

fore the onset of hypertension. After 12 weeks their was significant decrease in the expression of all the Cxs with prominent decrease in the density of Cx40 plaque (cell-cell contacts forming gap junctions between cells). In ECs from WKY, there was no change in amount of Cx expression over this period of time, thus showing a link between flow characteristics and Cx expression. Reduction of Cx37 and Cx40 was also demonstrated in aortic ECs of hyperlipidemic mice (Yeh et al., 2003) of which Cx37 expression recovered after certain pharmaceutical intervention.

In diseased the alteration of Cx expression in normal and pathological tissue is most evident. The extent of alteration is not an abrupt jump from on constituency of Cxs to another but is more differential. (Kwak et al., 2002) studied the expression of connexin in ECs and SMCs of in three segments of an atherosclerotic plaque, non diseased, early atheroma, and advanced atheroma in aorta of LDL receptor deficient mice fed with high fat diet for 14 weeks. Figure 2.18 is a schematic representation of the differential pattern of connexin expression found in different parts of the atherosclrotic plaque. Antibodies of respective Cxs were

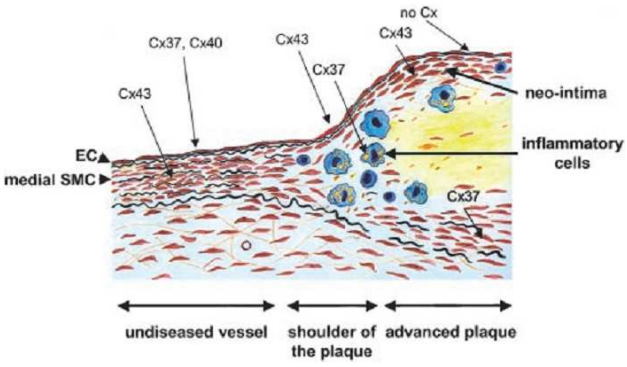

Figure 2.18: Schematic drawing of an artery containing an atherosclerotic lesion is shown. Expression patterns of the 3 connexins are indicated for the nondiseased part of the vessel, the shoulder of the plaque, and the centre of the advanced lesion.(Kwak et al., 2002)

used for immunolabeling the tissue for the analysis, thus this would label the membrane presentation of the relevant connexin in intimal, neointimal or medial layer. Cx37 and Cx40 but not Cx43 were present in nondiseased endothelium, whereas only Cx43 was found in the medial tissue. At the shoulder of the atheroma, EC layer presented Cx43 only and no expression of Cx37 and Cx40 was found. Cx37 was expressed by SMC of medial layer near this region. In mature atheroma, no connexin expression was found in endothelium however, Cx43 was present in SMCs of neointima (the newly formed intimal layer consisting of endothelial and

one or two layers of SMCs recruited from medial layer). For details of the Cx expression please see Table of (Kwak et al., 2002).

(Gabriels and Paul, 1998) studied the connexin expression in EC at arterial bifurcation. Aortic ECs of mice generally expressed Cx40 in abundance where as Cx37 was also present in most if not all the ECs from regions considered atheroresistant. At points where abdominal aorta either branched in to renal artery or bifurcated into common illiac arteries, Cx43 was strikingly upregulated. These sites are associated with disturbed flow. Figure 2.19a& (b) show Cx43 immunofluorescence at these sites. Of interest is the observation that Cx43 was expressed immediately downstream of the ostium (opening) in the branch vessel and extended further for short distance after which the expression vanished. In the case of flow divider, Cx43 was most localized at the apex and nonexistent downstream in the daughter branch. Another important finding was the coexpression of Cx40 and Cx43 upstream of the ostium but the absence of Cx37. Cx37 resumed its expressed downstream of the ostial edge where Cx43 expression subsides. This was confirmed by inducing flow disturbance in the aortic arch by surgical coarctation (deliberate narrowing of vessel by surgical ligature). These sites were originally negative for Cx43 but after the coartation, the Cx43 was signidicantly upregulated. These results strongly suggest that Cx43 is upregulated by disturbed flow.

In vitro studies examining flow mediated connexin regulation has given greater insight into the their relationship with the WSS. (DePaola et al., 1999) used a parallel plate flow chamber with backward facing step geometry to obtain flow dynamics exhibiting disturbed flow with flow separation and recirculation zones. A monolayer of bovine thoracic aortic ECs was cultured on a glass cover slip and fluid was allowed to pass over the cells. Four zones of shear stress gradients (SSGR), progressively decreasing with increasing axial distance, were also defined in this study, as shown in Figure 2.20. Along with Cx43 mRNA, protein, gap junctional coupling was also monitored by dye transfer between cells of the monolayer. Lucifer Yellow (LY) (MW=457.3Da, Z=-2) was used for intercellular dye transfer. Sustained increased in Cx43 mRNA was observed in ECS under SSGR I&II, 5 and 16 hours after exposure to fluid shear. In cells under SSGR III&IV the mRNA expression increased at 5 hours but returned to basal level at 16 hours.

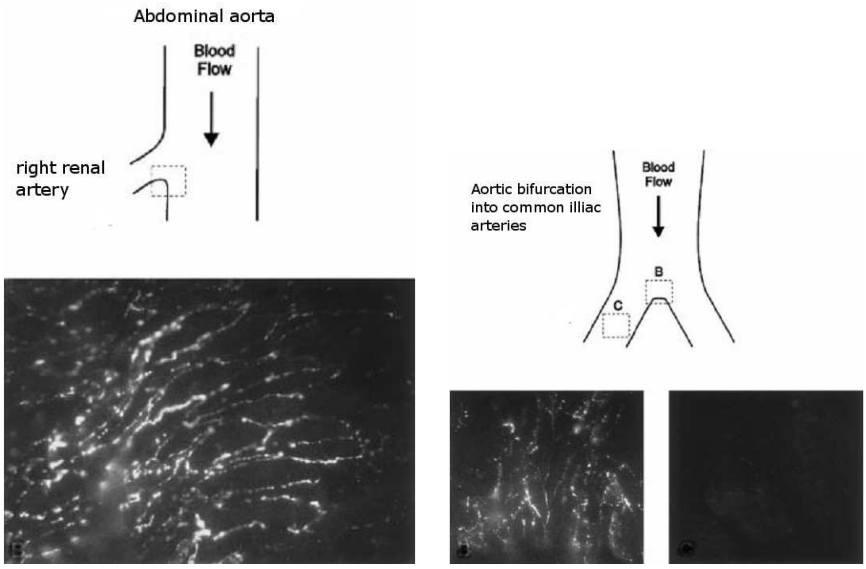

(a) Cx43 expression at the downstream edge of the ostium of the right renal artery.

(b) Localized Cx43 expression at the apex where abdominal aorta bifurcates into the right and left common illiac arteries. Staining for Cx43 was not evident on the wall of the right common iliac artery.

Figure 2.19: Cx43 upregulation by disturbed flow (Gabriels and Paul, 1998)

Under no flow condition (control in this case) there was moderate (punctate) expression of Cx43 protein on the cell membrane. At SSGR I&II, after 5 hours, the Cx43 protein density increased and localized in perinuclear region. This means most of the Cx43 was internalized and not making any cell-cell contact. This disruption in the pattern of Cx43 protein localization was also evident in SSGR III&IV after 5 hours. After 30 hours the protein expression patter in ECs under SSGR I&II was still disorganized but in cells experiencing SSGR III&IV, the punctate pattern was restored. ECs exposed to SSGR III&IV were elongated in orientation even at a moderately high WSS of magnitude 13.5 dynes/cm^2. After 5 hours ECs injected with LY either under SSGR I&II or SSGR III&IV passed the dye to less number of cells compared to control. After 30 hours, cells under SSGR III&IV passed the dye to farther neighbours compared to ECs in region with SSGR I&II. An EC although under SSGR I&II passed the dye relatively farther compared to its 5 hour reading but the communication was no as wide spread as a cell SSGR III&IV or control. Thus Cx43 expression of mRNA or protein or

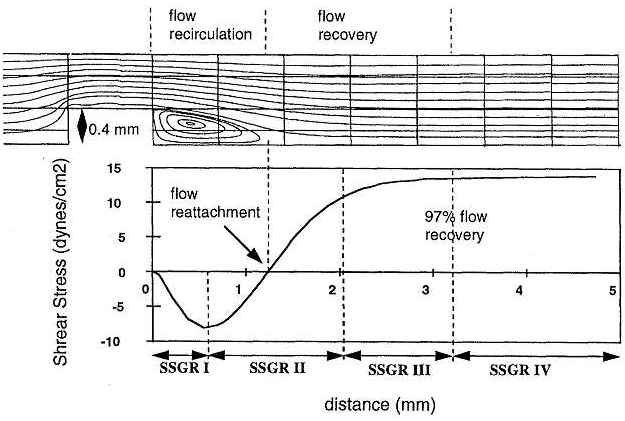

Figure 2.20: Flow streamlines in the chamber showing regions of flow separation, recirculation, reattachment, and recovery. (Lower) The corresponding shear stress distribution on the coverslip surface. The average shear stress gradients (slope of shear stress curve) in regions SSGR I to IV are 188, 182, 22, and 0 dynes/cm^2, respectively. (DePaola et al., 1999)

even gap junction formation is not only regulated by magnitude of local WSS but also the WSS gradient.

This flow mediated connexin regulation was further investigated by (Ebong et al., 2006) in similar experimental setup but with human aortic ECs. Cell monolayer was exposed to laminar flow with a moderately high WSS of 11 dynes/cm^2. The authors used synthetic connexin memtic peptides which serve as connexin specific gap junction inhibitor to study the intercellular dye transfer (LY) under flow. Under control (no flow) condition, the intercellular dye transfer was very limited but increased upon exposure to flow. This increase was time dependent and kept on increasing for 24 hours. Inhibition of Cx37 and Cx43 gap junctions did not stop the dye transfer. Blockade of Cx40 gap junctions significantly reduced the intercellular communication. Thus the study concluded that Cx40 was significant in establishing intercellular communication between ECs under steady flow condition. This again points out the differential and stimulus dependent nature of connexin expression in ECs.

From the above information, some corollaries can be driven. ECs generally express Cx40 and in large number of cases Cx37 in tissue under undisturbed flow. Cx43 expression is elevated in the ECs at sites where flow disturbance occurs such as arterial bifurcations and branch points. Reviewing the experimental results from different groups suggest that at bifurcations, the alteration in connexin expression from one isoform to another is not abrupt but a gradual decrease in

Cx40 and Cx37 and an increase in Cx43 with locations where Cx40 and Cx43 coexist, as shown by (Gabriels and Paul, 1998).For SMCs, they are coupled primarily by Cx43 and there is some evidence to support the existence of Cx40 in small arteries and arterioles. Cx37 hemichannels were shown to make homocellular gap junctions by (Isakson and Duling, 2005) in SMCs. Table 2.1 lists possible scenarios that will implemented later to investigated Ca^{2+} dynamics in cells under spatial gradients of stimuli and coupled in configurations listed in this table.

Case	Homocellular coupling		Heterocellular coupling	
	SMC	EC	SMC↔EC	EC↔SMC
1	V, Ca^{2+}, IP_3	V, Ca^{2+}	V, IP_3	V, IP_3
2	V, Ca^{2+}, IP_3	V, Ca^{2+}	V, IP_3 , Ca^{2+}	V,IP_3 ,Ca^{2+}
3	V, Ca^{2+}, IP_3	V, Ca^{2+}, IP_3	V, IP_3 ,Ca^{2+}	V, IP_3 , Ca^{2+}
4	V, Ca^{2+}, IP_3	IP_3	IP_3	IP_3

Table 2.1: The various coupling modes establishing intercellular communications between cells in stasis and pathology. (V=membrane potential coupling (via Cx37), Ca^{2+}=Ca^{2+} coupling (via Cx40), IP_3 =IP_3 coupling (via Cx43))

2.6 Models of vascular ECs and SMCs

Calcium is central in major cell signalling cascades and plays a pivotal role in regulation of vascular tone and blood flow. In excitable cells such as SMCs, intracellular Ca^{2+} concentration can oscillate upon either humoral, nervous or electrogenic stimulation and result in many direct and indirect consequences. This free unbound cytosolic Ca^{2+} can bind to another endogenous molecule calmodulin (CaM) and modulate cytoskeletal contractililty by activating the myosin light chain kinase (MLCK) which enables the sliding of myosin head. Other intracellular utilizations of this nascent Ca^{2+} can be but are not limited to, eNOS activation to make NO in ECs, binding to regulatory proteins to initiate a cascade leading to exocytosis, binding gated ion channels to allow fluxes of specific ions in and out of the cell, to name a few. A cellular oscillator is a requirement of the occurrence of vasomotion, and it is modelled as a series of events forming a feedback loop,

where inertia in one or more steps in the loop ensures oscillation (Aalkjaer and Nilsson, 2005).There are three essential components of a cellular oscillator:

1. a cytosolic oscillator to increase intracellular Ca^{2+}
2. a system for removal of Ca^{2+}, and
3. a system of transduction of extracellular stimuli

2.6.1 Cytosolic Oscillator

In SMCs of A7r5 (a cell line of rat thoracic aorta) (Blatter and Wier, 1992) showed the Ca^{2+} wave, which moved in the direction of longitudinal axis was a consequence of oscillations in intracellular Ca^{2+} concentration. Blockade of sarco/endoplasmic reticulum Ca^{2+} ATPase (SERCA) pump in an SMC inhibited this Ca^{2+} wave pointing out a pivotal role of SR Ca^{2+} release in Ca^{2+} oscillations (Iino et al., 1994). Ca^{2+} wave is when Ca^{2+} upon release from ER/SR traverses to other compartments in the cytoplasm and propagates in the form of a spiral wave. These finding suggest that the primary origin of Ca^{2+} resides in intracellular domain. In rabbit portal vein voltage operated Ca^{2+} channels (VOCC), Na-Ca^{2+} exchanger (NCX) and a current through non-selective ion channels is involved in inducing an oscillatory increase in intracellular Ca^{2+} concentration (Lee et al., 2001).

Of vital importance is the influence of agonist mediated IP_3 receptor activation, an ER/SR membrane bound receptor, followed by release of ER/SR luminal Ca^{2+} in rat portal vein myocyte (Boittin et al., 1999). This increase in intracellular Ca^{2+} is dose dependent and exhibited frequency and amplitude modulation (Berridge, 2007). Blockade of IP_3R completely inhibited the oscillations in Ca^{2+} concentration (Boittin et al., 1999). Following the activation of receptors, spread of this Ca^{2+} release from intracellular stores is not by simple diffusion but involves a regenerative release of $Ca^{2+}$by a process called Ca^{2+} induced Ca^{2+} release (CICR). Ryanodine receptors, also ER/SR membrane bound receptors, contributes in the release of Ca^{2+} via CICR from ER/SR upon activation and blockade of these receptors also significantly inhibit the Ca^{2+} wave in an SMC (Iino et al., 1994). In some instances the emphasis on inclusion of ryanodine as essential

mediator in inducing CICR has been relaxed and is suggested that adequate IP_3 availability alone is sufficient to produce intracellular Ca^{2+} oscillations (Aalkjaer and Nilsson, 2005).

In SMCs from some small calibre vessels, the ER/SR Ca^{2+} release in conjunction with Ca^{2+} removal mechanisms is sufficient to induced intracellular Ca^{2+} oscillations but in relatively larger bore arteries such as mesenteric artery where agonist activation predominantly induces vasomotion, VOCCs are required. These L-Type voltage gated Ca^{2+} channels open on depolarization of plasma membrane and allow influx of extracellular Ca^{2+} into the cytosolic space (Nelson et al., 1990). For VOCCs to open, the membrane depolarization can be an external stimulus originating from electrical coupling between two adjacent SMCs or the intracellular rise in Ca^{2+} concentration following CICR can trigger the opening of these channels. It has been demonstrated by a number of studies that membrane depolarization precedes a large Ca^{2+} transient in SMCs (Haddock and Hill, 2005). The increase in cytosolic Ca^{2+} concentration makes intracellular side more positive compared to the extracellular side of the plasma membrane thus depolarizing (or making more positive) and reduce the electrostatic gradient across the plasma membrane. This allows the opening of VOCCs and extracellular Ca^{2+} rushes into the cell. The open channel probability of VOCCs in excitable cells is high, i.e. maximum number of channels existing in the plasma membrane will open simultaneously thus allowing a large influx of Ca^{2+}. Thus this is a fast channel and the response time after depolarization is quick.

2.6.2 Removal of cytosolic calcium

Excessive retention of Ca^{2+} in the cytosol is toxic to the cell therefore, all the additional Ca^{2+} released as consequences of different signalling pathways, must go somewhere or be utilized to regain basal Ca^{2+} concentration and membrane potential. Ca^{2+} is constantly removed from the cytosol by three main active and passive pathways: (i) Na^+/Ca^{2+} exchanger, (ii) extrusion via plasmalemmal Ca^{2+}ATPase, and (iii) and the refilling of intracellular stores of Ca^{2+} in SR through a sarcoplasmic/endoplasmic Ca^{2+}ATPase pump, also called the SERCA pump. Ca^{2+} can also be removed via gap junctions. High Ca^{2+} concentration is a driving force for dif-

fusion of Ca^{2+} and other monovalent ions and some neutral molecules (molecular weight <1000 Da) through to a neighbouring cell connect via intercellular gap junction.

2.6.3 Signal Transduction

The influence of the extracellular environment must be transduced into an "intracellular friendly" form via signalling pathways. This is crucial to be able to responds to the external stimuli. For this, plasma membrane contains membrane bound receptors which can either induce conformational changed in some ion channels and activates them, or it can induce a cascade of reactions which result in the production of a *second messenger molecule* such as IP_3 in the cytosol. Figure 2.21 shows one such membrane bound apparatus that has been identified in increasing intracellular IP_3 concentration in a number of cell types, upon binding of the receptor to its specific agonist. Agonist such as ATP, binds to the purinergic (P2Y) receptors expressed on the EC surface, activating the G protein coupled receptor complex (GPCR) which then activates the membrane bound phospholipase C(PLC). PLC activation allows phosphorylation of phosphatidylinositol 4,5-bisphosphate (PIP_2) generating IP_3 that is then released in the intracellular space.

Multicellular models constructed from single vascular cell models have been used in previous studies, investigating various function consequences in networks of coupled cells. The scale of these models, however, has been limited to that of microvasculature and its physiology. Some examples of such studies have been cited in the following literature review.

Jacobsen et al. (2007) investigated the role of cyclic guanosine monophosphate (cGMP) in arterial vasomotion. Vasomotion is the cyclic variation of the arterial diameter induced by Ca^{2+} oscillations in the SMCs. The significance of this cyclic alteration of arterial radius plays a vital role in altering the peripheral vascular resistance and thus plays an important part in control of arterial blood pressures. Single cell model of SMC was employed here to construct a coupled network of SMCs. In addition to the standard Ca^{2+} influx and efflux pathways, their SMC model included Ca^{2+} buffering in both SR domain and cytosolic domain. In addition to that, a cGMP sensitive Ca^{2+} activated chloride channel was also included.

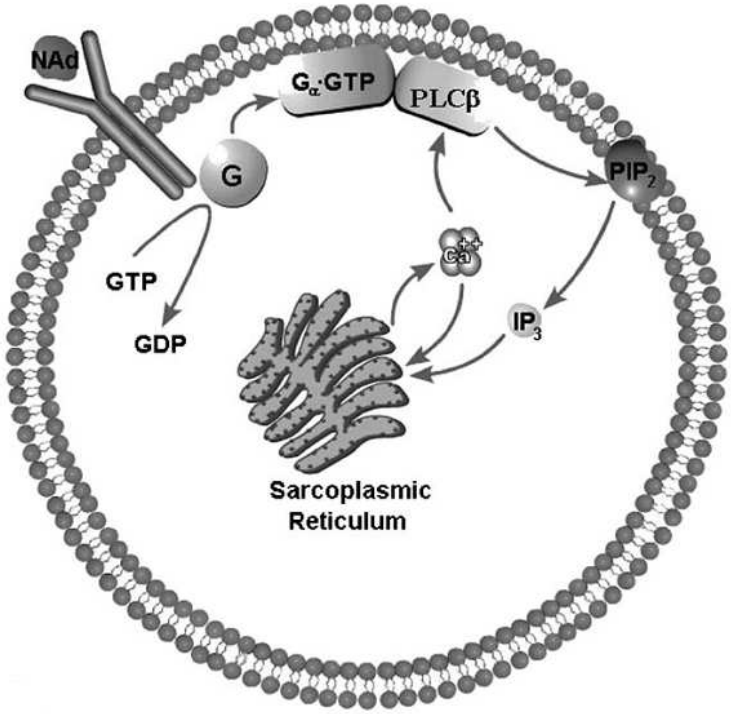

Figure 2.21: Simplified schematic diagram of the steps leading from receptor activation to Ca^{2+} release from the SR. Transmitter noradrenaline (NAd) binds to the receptor which then interactswith the G-protein (G), leading to the replacement of GDP with GTP and the subsequent dissociation of the G-protein into subunits. The subunit G_αGTP binds to a site on PLCβ and this activated unit initiates an interaction with membrane-bound PIP_2; catalysed by Ca^{2+}; leading to the hydrolysis of PIP_2 and the production of IP_3 : This diffuses into the cytosol where it opens IP_3 -sensitive channels in the SR, allowing the release of Ca^{2+} into the cytosol. (adapted from Bennett et al. (2005)).

From the perspective of the computational layout, the number of intercellular gap junctions coupling the SMCs was a function of the surface area overlapping between two SMCs, hence resulting in an asymmetric coupling strength for each SMC with its nearest neighbours. Figure 2.22. The gap junctional transfer of ions was modelled as a function of both the potential difference and concentration difference between two coupled SMCs.

This study tested the effects of cGMP on Ca^{2+} dynamics of coupled SMCs simulating a microvascular arteriole. Their results showed a permissive role of cGMP in establishing the intercellular synchronization of the Ca^{2+} oscillations. It was suggested that cGMP activates cGMP sensitive Ca^{2+} activated chloride channels which causes tight synchronization between SR Ca^{2+} release, the membrane potential depolarization, and the influx of extracellular Ca^{2+}.

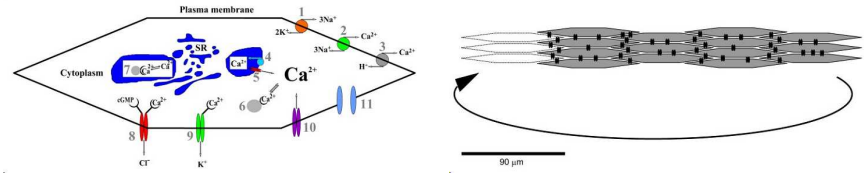

(a) **(b)**

Figure 2.22: Cell and vessel model. (a) the compartments considered in the model are the plasma membrane, the cytoplasm, and the sarcoplasmic reticulum (SR). The picture shows the components related to each of these compartments: Na^+/K^+-ATPase (1), Na^+/Ca^{2+}exchanger (2), plasma membrane Ca^{2+}-ATPase (3), sarco(endo)plasmic reticulum Ca^{2+}-ATPase (4), SR calcium release channel (5), cytoplasmic calcium buffer (6), SR calcium buffer (7), cGMP sensitive calcium dependent chloride channel (8), calcium activated potassium channels (9), voltage operated Ca^{2+} channel (L-type calcium channel; 10), and gap junction (11). (b) Vessel model. Example of a single layered cell plate used in the simulations is shown. The plate forms a tube by making end-to-end contact. Each spindle-shaped cell couples to neighbouring cells through gap junctions (black double-barrel structures) (figure and caption adapted from (Jacobsen et al., 2007))

Coupled cell models comprising computationally coupled single EC and SMC models have been used to study the physiological basis of vasoreactivity in small arteries and arterioles. (Diep et al., 2005) coupled ECs/SMCs where each cell was modelled as a capacitor coupled to a nonlinear resistor and the intercellular gap junction was modelled by an ohmic resistor, as shown in the Figure 2.23.

Using this multicellular structure simulating a resistance artery, they investigated the spread of the electrical signal following a local agonist stimulation, initiating either in the endothelium or the SMC layer. Their results revealed that membrane potential changes did not spread equivalently to all unstimulated cells but depended heavily on the orientation and the strength of coupling. Membrane potential responses originating in endothelium conducted more efficiently (i.e. to farther distances) than the SMC layer initiated signal. In a subsequent study by Tran and Welsh (2009), using the same multicellular infrastructure modelling a skeletal muscle feed artery, a dominant mechanism was proposed for the poor conduction of membrane potential change initiating in SMC layer. The authors attributed this to the loss of charge due to intercellular electrical coupling between SMCs for which the local agonist stimulation could not elicit a global membrane potential change. Furthermore, the spread of focal phenylephrine (a potent vasoconstrictor) stimulation which resulted in a global vasoconstriction, was proposed to be membrane potential independent. The dominant mechanism in the spread of this vasoconstrictive response was suggested to be the SR Ca^{2+} mobilization and the activation of IP_3 receptors on the SR in SMCs.

Similarly, Kapela et al. (2010), coupled very detailed models of ECs and SMCs to construct a multicellular unit of rat mesenteric arteriole coupled by non-selective gap junctional transfer. The study was aimed at the conducted vasoreactivity and the role of myoendothelial junctions. With respect to the membrane potential dependence of the spread of the signal, their results were in agreement with Diep et al. (2005) and endothelium dependent spread was more efficient in the case when myoendothelial coupling was strong. In the case of weak myoendothelial coupling, the SMCs showed poor conductivity but the unstimulated cells became sensitive to any further extracellular current. They also suggested that the conduction amongst ECs was favoured by IP_3 coupling rather than the intercellular Ca^{2+} diffusion between ECs.

Coupled EC/SMC models have also been used by Koenigsberger et al. (2005) to study the role of endothelium in arterial vasomotion. Single ECs and SMCs modelled by ODEs were used to construct multicellular model of an arteriole coupled via heterocellular and homocellular coupling. These models are further elaborated in Chapter 3 and 5 where the computational infrastructure has been

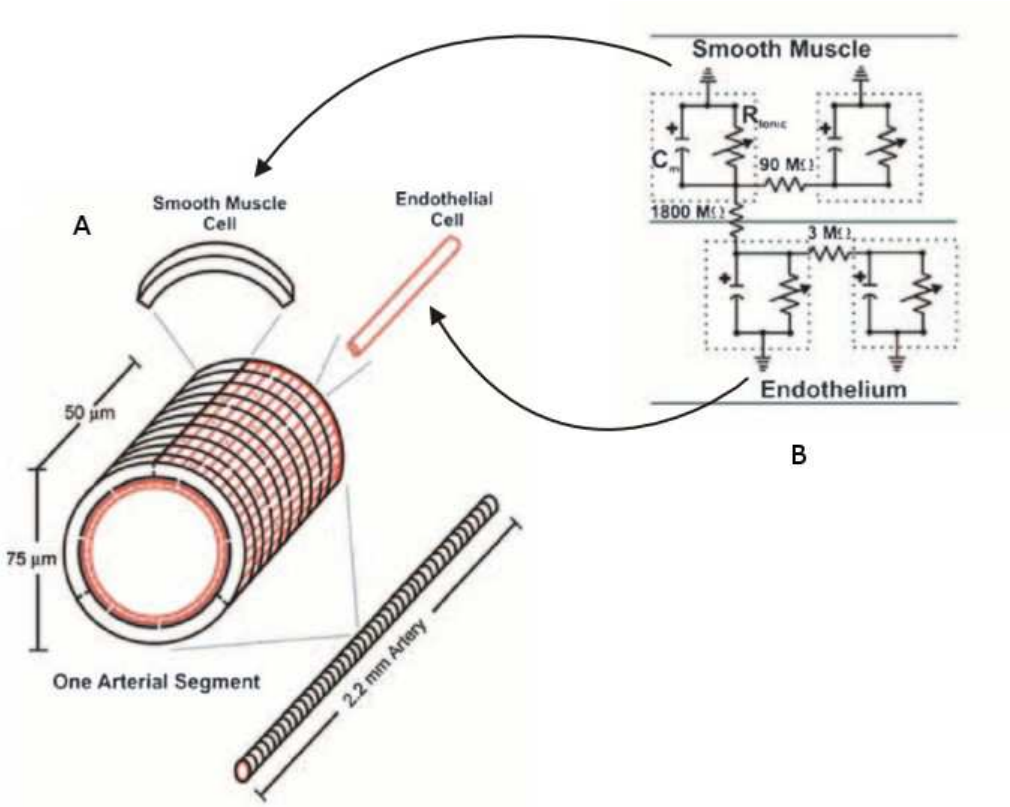

Figure 2.23: (A) the virtual artery was 2.2 mm long and comprised of one layer of endothelium (red) and one layer of smooth muscle (black). Each arterial segment (n = 44) consisted of 48 endothelial cells and 30 smooth muscle cells. Cells were treated as discrete elementswith defined physical dimensions, gap junctional coupling and ionic conductance. Neighbouring smooth muscle cells were electrically coupled to one another as were neighbouring endothelial cells. Every smooth muscle cell was randomly coupled to two endothelial cells (red dot denotes myoendothelial contact site). (B) equivalent circuit representation of the virtual artery. Each cell was modelled as a capacitor coupled in parallel with a non-linear resistor representing ionic conductance of the plasma membrane; gap junctions were represent by ohmic resistors. (Diep et al., 2005)

discussed. Koenigsberger et al. (2005) found that the presence of endothelium modulated the oscillatory behaviour of underlying SMCs. The effects of endothelium derived factors were tested and the endothelial hyperpolarization was found to be a significant factor in this modulatory effect of endothelium on the SMC layer and abolished vasomotion.

In a subsequent study, Koenigsberger et al. (2006) used the same computational infrastructure (coupled circumferentially to form a tube, as shown in the Figure 2.24) to test the role of pressure in modulating the vasomotion in arterioles. In this study the SMC single cell model was extended to have radius as a variable. This was done by coupling Hai and Murphy (1988) myosin light chain kinase (MLCK) to the Ca^{2+} dynamics of a SMC. This addition implemented to make a compliant arterial model. The results of study showed that pressure increased cytosolic Ca^{2+} concentration in the SMCs. This increase was capable of inducing vasomotion in an artery with steady state radius or it can abolish vasomotion in the case where arterial radius oscillated.

All the models of coupled vascular cells discussed above, and others not included in this review, address the scale of 1^{st} order arteriole or small arteries, in the case of Koenigsberger et al. (2006). The present study is intended to employ the mathematical model coupled cells to investigate cellular dynamics in atherosclerosis. Atherosclerosis is prevalent in muscular arteries and the diameter of muscular arteries is in the order of millimetres compared to the diameter of an arteriole which is of the order of few hundred μm. Amongst other objective, this project aims at providing a computational framework which is capable of simulating physiologically relevant scale in the case of atherosclerosis. The chapters following this literature review is an effort to achieve the aim in a scalable manner.

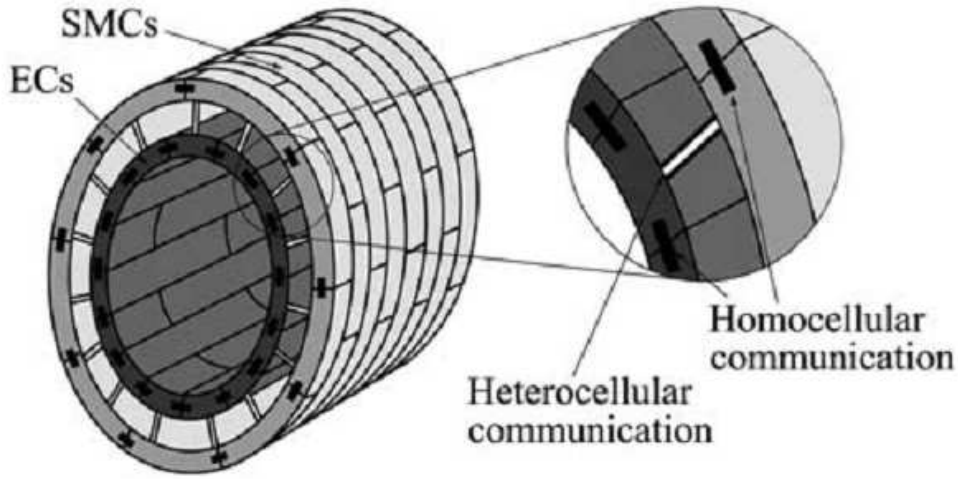

Figure 2.24: A cylindrical grid of SMCs (outer layer) superposed on a cylindrical grid of ECs (inner layer) simulates an arterial section. ECs are arranged parallel and SMCs perpendicular to the vessel axis. Cell geometry is approximated by a rectangle. The width of an EC is taken as twice that of an SMC, and the length of an EC 1.3 times that of an SMC (Sandow and Hill, 2000). With a size of a single SMC of 5 mm and a mean vessel diameter in the order of 150 mm, nine SMCs are necessary to surround the arterial lumen. Each cell is connected with its nearest neighbours on the same layer (homocellular connection) and with the cells on the other layer directly superposed on it (heterocellular connection) (Koenigsberger et al., 2006).

Chapter 3

Computational Method:
Single Cell Models

To simulate a physiologically valid arterial segment, appropriate mathematical models of contributing entities are required. These models are then put together in a computational layout representing the desired geometry and are solved using a robust numerical solver and integrated over a given range of an independent variable(s). This chapter presents the mathematical model of EC and SMC used to study the coupled vascular cell populations, the numerical method and numerical solver of choice and lays out the programming infrastructure which is used to layout appropriate geometric aspects in order to simulate a straight arterial segment.

3.1 Background

In a cell, the transport of charged species ,*ions*, through the plasma membrane are often at the very core of the complex cellular processes. The plasma membrane, a phospholipid bilayer, is an interface for the cell with the extracellular space. Chemical species, e.g. molecules and ions, charged or neutral, move into and out of the cell through the plasma membrane, though gates called *channels*. Numerous groups of these channels have been characterized until now and many are to be investigated. One thing is clear is that the properties of these channels vary, thus their function significance and their roles in intracellular and intercellular processes also vary according to the properties they exhibit. These properties include

conductance, permselectivity, facilitation of active or passive transport, size exclusion to allow selective molecules, voltage gating and receptor mediated gating, etc. Despite such complex nature of its existence, the cells electrical behaviour can be modelled, in its simplified form, as a *RC* circuit, as shown in Figure 3.1. This can help investigate the conductance of the plasma membrane to various ionic charges with time and hence look at their current voltage relationship.

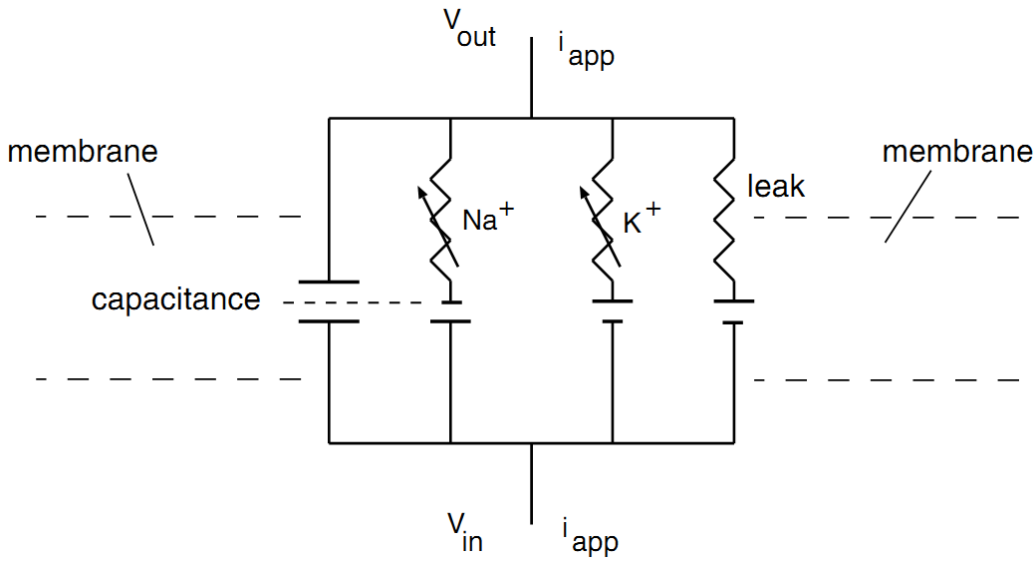

Figure 3.1: The equivalent electrical circuit for an electrically active membrane. The capacitance is due to the phospholipid bilayer separating the ions on the inside and the outside of the cell. The three ionic currents, one for Na^+, one for K^+, and one for a nonspecifc leak, are indicated by resistances. The conductances of the Na^+ and K^+ currents are voltage dependent, as indicated by the variable resistances. The driving force for the ions is indicated by the symbol for the electromotive force, which is given in the model by the difference between the membrane potential $V = V_{in} - V_{out}$ and the reversal potential (Fall et al., 2002). I_{app} is a current that can be experimentally applied using patch clamp technique to study the current/voltage characteristics of an ion channel.

The model utilizes the cell phospholipid bilayer as a *capacitance*, accumulating ionic charge, *ionic permeabilities* are modelled as variable resistors and the *electrochemical driving forces*, modelled as batteries. Often we are interested in the dynamics of how the concentrations of ions, moving in and out of the cell, reach their steady states. This information gives insight of the interaction of the

membrane bound *ion channel* through which it is transported and the transported species. For instance, for K^+, the current flow through a single K^+ ion can be written, using Ohm's law, as

$$I_K = -g_K(V - V_K) \tag{3.1}$$

where g_K is the conductance of K^+ channel and V_K is what is called the *reversal potential* or *Nernst potential* of K^+. In the real world, there are more than one ions passing through an ion channel, with varying conductances. Thus total ionic current through an ion channel can be approximated as a sum of all the currents or ionic fluxes through the channel, such that,

$$I_{ion} = \sum -g_i(V - V_i) \tag{3.2}$$

Employing Kirchoff's law, equation 3.2 can be translated into an *ordinary differential equation* or ODE. Since the membrane is modelled as a capacitor, the capacitative current through it can be given by

$$I_{cap} = C\frac{dV}{dt} \tag{3.3}$$

But Kirchoff's current law states that sum of all the currents in the circuit be zero, so

$$I_{cap} = I_{ion} + I_{app} \tag{3.4}$$

where I_{app} is a current that can be experimentally applied using patch clamp technique to study the current/voltage characteristics of an ion channel. Therefore,

$$C\frac{dV}{dt} = -\sum g_i(V - V_i) + I_{app} \tag{3.5}$$

In order to solve the equation 3.5, which is an ODE in time, the dependence of g_i on V must be known, formally called *voltage dependent gating* property of an ion channel. To model the activation and inactivation of an ion channel (i.e. whether if it is in conductance or non-conductance mode), let us suppose that an ion channel can assume either of the two states, *open* (denoted by O or activation

) or *close* (denoted by C or inactivation). The transition between these two states is reversible hence,

$$C \underset{k^-}{\overset{k^+}{\rightleftharpoons}} O \tag{3.6}$$

where k^+ and k^- are the reaction rates or the rate of transition from closed state to open state and vice versa. Let the rate of transition $O \rightarrow C$ be given by

$$j_+ = k^+[C]$$

, where $[C]$ denotes concentration of channel molecules in closed state. Similarly, the transition $C \rightarrow O$ can be given by

$$j_- = k^-[O]$$

, where the rates of transition, k, have units of s^{-1}. Let $[O] = f_O$ and $[C] = f_C$ be the fractions of channels open or closed respectively, such that $f_o + f_c = 1$, then j_- and j_+, the fluxes of transition between states, can be written as

$$j_- = k^- f_O \tag{3.7}$$

$$j_+ = k^+(1 - f_O) \tag{3.8}$$

In terms of these fluxes, the rate of change of *open channle fraction* or f_O can be written as,

$$\begin{aligned} \frac{df_O}{dt} &= j_+ - j_- \\ &= -k^- f_O + k^+(1 - f_O) \\ &= -(k^- + k^+)(f_O - \frac{k^+}{k^- + k^+}) \end{aligned} \tag{3.9}$$

Let $\frac{1}{k^- + k^+} = \tau$ and $f_\infty = \frac{k^+}{k^- + k^+}$, then equation 3.9 becomes,

$$\frac{df_O}{dt} = -\frac{f_O - f_\infty}{\tau} \tag{3.10}$$

Ion channels composed of proteins with charged amino acids side chains reside on both the intracellular and the extracellular sides of the plasma membrane. The potential difference across the membrane potential, caused by the charge different of the side chains, can influence the rates of opening and closing of the ion channels. Arrhenius expression for the rate constant says that the membrane potential V contributes to the energy barrier for the transitions (Fall et al., 2002):

$$k^+ \propto exp(\frac{-\Delta V^+}{RT}) \tag{3.11}$$

$$k^- \propto exp(\frac{-\Delta V^-}{RT}) \tag{3.12}$$

For the expression in equation 3.9, the rate constants will have the form,

$$k^+ = k_o^+ exp(-\alpha V) \tag{3.13}$$

$$k^- = k_o^- exp(-\beta V) \tag{3.14}$$

where constant k_o^+ and k_o^- do not depend on V. Substituting these new forms of k^+ and k^- in equation 3.9, after rearraging, gives,

$$f_\infty = \frac{1}{1+(k_o^-/k_o^+ exp((\alpha-\beta)V))} \tag{3.15}$$

and

$$\tau = \frac{1}{k_o^+ exp(-\alpha V)} \cdot \frac{1}{1+(k_o^-/k_o^+ exp((\alpha-\beta)V)} \tag{3.16}$$

Let

$$S_o = \frac{1}{\beta-\alpha} \tag{3.17}$$

and

$$V_o = \frac{ln(k_o^-/k_o^+)}{\beta-\alpha} \tag{3.18}$$

then, by substituting these definitions in equations 3.15 and 3.16, we get,

$$f_\infty = \frac{1}{1+exp(-(V-V_o)/S_o)} \tag{3.19}$$

and

$$\tau = \frac{exp(\alpha V)}{k_o^+} \cdot \frac{1}{1+exp(-(V-V_o)/S_o)} \tag{3.20}$$

At membrane potential V, f_∞ is the fraction of channels open at the equilibrium. τ is the characteristic time (in s^{-1}) that f_O takes to reach this equilibrium.

Depending on the sign of S_o, the ion channel opens or closes upon depolarization of membrane potential. "+" sign of S_o implies the activation of the channel on depolarization where as "-"S_o characterizes inactivation of the channel on depolarizing membrane potential. Figure 3.2a show examples of the open channel fraction at equilibrium of an activation and inactivation gating with depolarizing membrane potential. Figure 3.2b shows how the dependence of characteristic time constant τ on membrane potential V. The peak of τ is determined by the value of V_o where as the spread of the curve is determined by the value of S_o. In the case

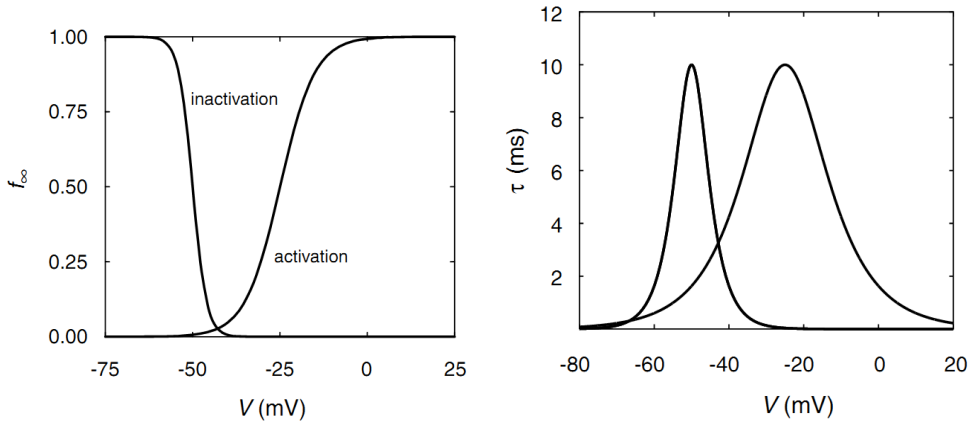

Figure 3.2: (a) Equilibrium open fractions (f_∞) for an inactivation gate ($V_o = -50$mV) and ($S_o = -2$mV) and activation gate ($V_o = -50$mV) and ($S_o = 5$mV) as a function of voltage. (b) The characteristic relaxation times τ for the activation and inactivation gates in (a) as a function of voltage, which are peaked around the values of V_o and have a width determined by S_o (Fall et al., 2002).

where $\alpha = -\beta$,

$$\tau = \frac{\phi}{cosh((V-V_o)/2S_o)} \tag{3.21}$$

where

$$\phi = \frac{1}{2\sqrt{k_o^- k_o^+}}$$

The expressions for f_∞ and τ can be written in terms of hyperbolic expressions,

$$f_\infty = \frac{1}{2}(1 + tanh(\frac{V - V_o}{2S_o})) \tag{3.22}$$

and

$$\tau = \frac{exp(V(\frac{\alpha+\beta}{2}))}{2\sqrt{k_o^- k_o^+}cosh((V - V_o)/2S_o)} \tag{3.23}$$

The above expressions model the dynamics of voltage dependent ion channels. In the mathematical models discussed in the following section, the voltage dependent ion channels are modelled by equations 3.22 and 3.23.

3.2 Mathematical model

(Koenigsberger et al., 2005) published a mathematical model for coupled ECs and SMCs as a system of first order nonlinear differential equations (ODEs). This is a sufficiently detailed model covering all essentials set out in Section 2.6. Essentially for a mesenteric artery EC and SMC, it efficiently accounts for the essential mechanisms of IP_3 induced cytosolic Ca^{2+} release and the cascade of events following it, in both cell types. The set of ODEs describing SMC cell dynamics in the Koenigsberger model compare well with the experimental results published by Lamboley et al. (2003), where rat mesentric arteries were stimulated with phenylephrine (PE), a potent vasoconstrictor. The set of ODEs describing the EC Ca^{2+} dynamics in Koenigsberger et al. (2005) model comes from Goldbeter et al. (1990) & Schuster et al. (2003) and the cytosolic Ca^{2+} response upon stimulation by Bradykinin (a vasoconstrictor) fits well to the experimental results by Frieden et al. (1999).

There are three major component models that work together to form a functional coupled cell model; a single EC and SMC model, coupled by equations modelling gap junctional coupling of homocellular and heterocellular nature between the cells. Each component is discussed here separately.

3.2.1 Single cell SMC model

A single SMC is modelled by a set of 5 ODEs in time. The state variables considered for a SMC are:

1. Free/unbound cytosolic Ca^{2+} concentration (c)
2. SR Ca^{2+} concentration (s)
3. plasma membrane potential (v)
4. open state probability of Ca^{2+} activated potassium channels (ω)
5. cytosolic IP_3 concentration (I)

All concentrations are in micromoles (μM), membrane voltage in millivolts (mV) and open channel probability is dimensionless. Values and definitions of the rate constants are listed in Table A.1.

A linear combination of individual transmembrane ionic fluxes and transporting in and out of the SR constitute a time dependent expression for each state variable. At any time t, these a balance of these ionic fluxes dictates the instantaneous value of unbound c in μM. These ionic currents or fluxes can be grouped together according to the location of their their respective channels which they pass through. IP_3 induced Ca^{2+} release, CICR, SR uptake by SERCA pump and Ca^{2+} leak from SR are associated to SR membrane bound channels. Influx of Ca^{2+} via VOCCs, Ca^{2+} activated potassium channels, Na/Ca exchanger and all other monovalent ionic current mentioned here pass through channels which reside in plasma membrane.

IP_3 induced Ca^{2+} release, denoted by J_{IP_3} is a function of IP_3 concentration available in the cytosol as a consequence of its agonist dependent formation and degradation/metabolism by IP_3 kinase A. Equation 3.24 gives the dependence of the proportion of maximal rate of IP_3 induced Ca^{2+} release from intercellular stores on the cytosolic IP_3 concentration and J_{IP_3}can be modelled by Hill equations as

$$J_{IP_3} = F \frac{I^2}{K_r^2 + I^2} \tag{3.24}$$

Adequate increase in Ca^{2+} in the cytosol following the its release from SR initiates Ca^{2+} induced Ca^{2+} release (CICR), modelled by equation 3.25. J_{CICR} is a function of both the Ca^{2+} in cytosol and in SR. Because SMC is an excitable cell, the rate constant C for this Ca^{2+} flux is kept substantial as compared to the EC thus small variations in concentration of either cytosolic or SR Ca^{2+} will result in an amplified response. With high affinity binding capacity of Ca^{2+} on the inside and low affinity binding on the cytosolic side of the SR membrane, J_{CICR} can be expressed as a product of two Hill equations

$$J_{\mathrm{CICR}} = C\frac{s^2}{s_{\mathrm{c}}^2 + s^2}\frac{c^4}{c_{\mathrm{c}}^4 + c^4} \tag{3.25}$$

Removal of cytosolic Ca^{2+} is done by three pathways (Ca^{2+}ATPase, SERCA pump and Na/Ca exchanger) and together with the cytosolic oscillator, it forms the basis of oscillatory mechanism of cytosolic Ca^{2+} concentration. $J_{SR\ uptake}$ models the replenishment of SR luminal Ca^{2+} by pumping in the cytosolic Ca^{2+} back into SR via SERCA pump. This is a Ca^{2+} ATPase that resides in the SR membrane and equation 3.26 models this refill. $J_{SR\ uptake}$ has been shown to have a sigmoidal dependence on cytosolic Ca^{2+} concentration with a Hill coefficient of 2 (Fall et al., 2002), thus

$$J_{\mathrm{SRuptake}} = B\frac{c^2}{c_{\mathrm{b}}^2 + c^2} \tag{3.26}$$

Again, in order to maintain oscillatory behaviour of the SMC, the authors have kept the Ca^{2+} uptake rate in SR, relatively high than what is set an EC. The cytosol is never devoid of free Ca^{2+} and there is a basal concentration that is maintained. J_{Leak} models Ca^{2+} leak as a linear function of the SR luminal Ca^{2+} s, as follows

$$J_{\mathrm{Leak}} = Ls \tag{3.27}$$

Here, L is the maximal rate of leak from SR.

Although a number of plasma membrane bound ion channels contribute different proportions of extracellular Ca^{2+} into the cytosol, most significant channels are included in this model. In equation 3.28 J_{VOCC} models the influx of extracellular Ca^{2+} through voltage gated Ca^{2+} channels and is a function of the SMC

membrane potential v. Notice the negative sign in equation 3.35 preceding J_{VOCC}. Relative to the Ca^{2+} Nernst potential (v_{Ca_1}), the more positive or depolarized the membrane potential, the more the channel allows Ca^{2+} to pass through into the cytosol from extracellular space. Closure of these channels is controlled either by hyperpolarization induced by K_{Ca} channels (described in equation 3.31) or inactivation of VOCC (when denominator in equation 3.28 becomes large), thus diminishing the flux through these channels. J_{VOCC} channels can therefore be modelled by

$$J_{\mathrm{VOCC}} = G_{\mathrm{Ca}} \frac{v - v_{\mathrm{Ca}_1}}{1 + e^{-[(v - v_{\mathrm{Ca}_2})/R_{\mathrm{Ca}}]}} \tag{3.28}$$

In addition to SERCA pump, few plasma membrane channels also take part in removal of cytosolic Ca^{2+}. $J_{Na/Ca}$, in equation 3.29 models the plasma membrane Na/Ca exchanger. The influx of Na^{+} versus the efflux of Ca^{2+} via this channel is driven by both the cytosolic Ca^{2+} concentration and the plasma membrane potential. Therefore, at higher c, Ca^{2+} will be pushed out of the cell but at the same time the rate of this efflux will also be limited by the extent of depolarization of membrane potential v and with more negative v increasing the rate of efflux, such that

$$J_{\mathrm{Na/Ca}} = G_{\mathrm{Na/Ca}} \frac{c}{c + c_{\mathrm{Na/Ca}}} (v - v_{\mathrm{Na/Ca}}) \tag{3.29}$$

Plasma membrane bound Ca^{2+}ATPase pushes out the cytosolic Ca^{2+} unidirectionally to extracellular space. In equation 3.30 the rate of efflux of Ca^{2+} is a function of v and c. J_{Eff} models the Ca^{2+} efflux through Ca-ATPase as

$$J_{\mathrm{Eff}} = Dc \left(1 + \frac{v - v_{\mathrm{d}}}{R_{\mathrm{d}}}\right) \tag{3.30}$$

Influx of Ca^{2+} into the cytosol either from intracellular stores or extracellular space, depolarizes the membrane potential. Because of this newly created imbalance of the charges inside the cell relative to the outside, their exists a gradient driven force or potential to neutralize the charge imbalance. In response, K^{+}ions move out of the K^{+}specific channels which, upon activation by Ca^{2+} ions, open and let K^{+}pass through to extracellular space. This repolarizes the membrane potential close to its resting state to regain electrostatic equilibrium. These channels,

known as Ca^{2+} activated K^+ channels or K_{Ca}, thus rectify the membrane depolarization caused by the Ca^{2+} signalling in response to an exogenous stimulus. Since this compensatory response kicks in with a delay i.e. after when cytosolic Ca^{2+} has increased to a certain level, they are also called delayed rectifiers. Equation 3.31 models the efflux of K^+ ions from the K_{Ca}channels under the membrane potential gradient where as the activation of open state of these channels, ,modelled by $K_{activation}$ in equation 3.32, is a function of both the c and v, therefore

$$J_K = G_K \omega (v - v_K) \tag{3.31}$$

and

$$K_{activation} = \frac{(c + c_\omega)^2}{(c + c_\omega)^2 + \beta e^{-[(v - v_{Ca_3})/R_K]}} \tag{3.32}$$

Other ionic currents include trafficking of monovalent ions such as K^+, Na^+ and Cl^-. Membrane bound Na/K pump pushes out $K^+$and brings in Na^+ from extracellular space, where as chloride channels are influenced by v as follows:

$$J_{Cl} = G_{Cl}(v - v_{Cl}) \tag{3.33}$$

and

$$J_{Na/K} = F_{Na/K} \tag{3.34}$$

Cytosolic Ca^{2+} concentration can now be stated as a sum of all the contributing ionic currents either adding to or removing the free unbound Ca^{2+} from cytosol. The ODE for c in time can be written as

$$\frac{dc}{dt} = J_{IP_3} - J_{SRuptake} + J_{CICR} - J_{Eff} + J_{Leak} - J_{VOCC} + J_{Na/Ca} \tag{3.35}$$

Similarly, with respect to the inside of the SR, Ca^{2+} dynamics in SR will be a sum of currents leaving the SR domain and currents refilling it. Therefore s can be written as

$$\frac{ds}{dt} = J_{SRuptake} - J_{CICR} - J_{Leak} \tag{3.36}$$

An ODE for the membrane oscillator of a SMC can also be formulated from the constitutive ionic currents from membrane bound channels, either entering or leav-

ing the cell, with intracellular side as reference and the measured side being extracellular, time dependent v can be written as

$$\frac{dv}{dt} = \gamma(-J_{\mathrm{Na/K}} - J_{\mathrm{Cl}} - 2J_{\mathrm{VOCC}} - J_{\mathrm{Na/Ca}} - J_{\mathrm{K}}) \tag{3.37}$$

The open channel probability of K_{Ca}channels, the main indigenous source of hyperpolarization in a SMC, with respect to time can be written in the form of an ODE as

$$\frac{d\omega}{dt} = \lambda\,(K_{\mathrm{activation}} - \omega) \tag{3.38}$$

And finally, cytosolic IP_3 concentration, not bound to receptors on SR, can be expressed as a balance of its agonist dependent formation and IP_3 kinase dependent metabolism or degradation. The dependence of formation of IP_3 on the activation of membrane bound PLC by agonist is considered as a parameter, $J_{PLC_{agonist}}$, where rate of the dynamics of the conversion from agonist stimulation to formation are deemed much faster than the time scale at which agonist concentration changes on the extracellular side. Also, the degradation of IP_3 has also been modelled as a linear function of instantaneous IP_3 concentration. Together, these two can form the intracellular IP_3 dynamics as

$$\frac{dI}{dt} = J_{\mathrm{PLC_{agonist}}} - J_{\mathrm{degrad}} \tag{3.39}$$

where $J_{degrade}$ related to the cytosolic IP_3 concentration as

$$J_{\mathrm{degrad}} = kI \tag{3.40}$$

where k is the rate constant for IP_3 metabolism. Later we eliminate the $J_{PLC_{agonist}}$ term from equation 3.39 when simulating the effects of spatial variation on coupled cells. (Koenigsberger et al., 2005) used this term to simulate the sympathetic nervous stimulation applied to the SMC layer in the coupled cells case to account for the action of agonists such as acetylcholine. Following this stimulation, the authors demonstrated the effects of endothelial derived hyperpolarization factor (EDHF) on the Ca^{2+} oscillation in SMCs. Here, since the effects of blood borne vasoconstrictor, ATP, is examined, its more logical to eliminate the parameter that

can locally stimulate a SMC.

3.2.2 Single cell EC model

Principally, an EC model will have the a similar constituency as a SMC model but with a few differences to make it a relatively non-excitable cell, as it physiologically is. Ca^{2+} and membrane potential dynamics can not sustain oscillations but do show transient behaviour. Koenigsberger et al. (2005) also included a moderately comprehensive model for a single EC. It IP_3 and SR dynamics resemble that of the SMC model described above. Ca^{2+} dynamics, with a few inclusions such as, Ca^{2+} influx through nonselective ion channels and a constant Ca^{2+} influx from channels which contribute a very small proportion of Ca^{2+} compared to the other ions passing through them, and exclusions such as elimination of VOCCs, differs from the SMC model. The authors have employed the membrane potential model published by Schuster et al. (2003) which was used to examine electrophysiology of an porcine coronary EC upon stimulation of a potent vasodilator, Bradykinin. An important feature contributed by the membrane potential model of Schuster et al. (2003) is the hyperpolarization of membrane potential which plays a vital role in endothelial dependent relaxation, as an alternative to NO pathway. Parameters or rate constant, defined in Table A.2, are set so that the EC cannot sustain oscillation.

A single EC is modelled by a set of 4 ODEs in time. The state variables considered for an EC are:

1. Free/unbound cytosolic Ca^{2+} concentration ($\widetilde{c}$)
2. SR Ca^{2+} concentration ($\widetilde{s}$)
3. plasma membrane potential ($\widetilde{v}$)
4. cytosolic IP_3 concentration ($\widetilde{I}$)

The Ca^{2+} dynamics of an EC, similar to that of a SMC, can be defined as a sum of constitutive ionic currents evaluated instantaneously, such that:

$$\frac{d\widetilde{c}}{dt} = \widetilde{J}_{IP_3} - \widetilde{J}_{ERuptake} + \widetilde{J}_{CICR} - \widetilde{J}_{Eff} + \widetilde{J}_{Leak} + \widetilde{J}_{cation} + \widetilde{J}_0 \tag{3.41}$$

where, similar to the SMC model, $\widetilde{J}_{IP_3}$ is modelled as Hill equation in $\widetilde{I}$ in equation 3.42, $\widetilde{J}_{CICR}$ is modelled as a product of two Hill equations in $\widetilde{s}$ and $\widetilde{c}$ respectively in equation 3.43 , with different cooperativities or Hill's coefficients, and $\widetilde{J}_{Eff}$ and $\widetilde{J}_{Leak}$ are modelled as linear functions of $\widetilde{c}$ and $\widetilde{s}$ respectively in equations 3.44 and 3.45.

$$\widetilde{J}_{IP_3} = F\frac{\widetilde{I}^2}{\widetilde{K}_r^2 + \widetilde{I}^2} \tag{3.42}$$

$$\widetilde{J}_{CICR} = \widetilde{C}\frac{\widetilde{s}^2}{\widetilde{s}_r^2 + \widetilde{s}^2}\frac{\widetilde{c}^4}{\widetilde{c}_{\widetilde{c}}^4 + \widetilde{c}^4} \tag{3.43}$$

$$\widetilde{J}_{Eff} = \widetilde{D}\widetilde{c} \tag{3.44}$$

$$\widetilde{J}_{Leak} = \widetilde{L}\widetilde{s} \tag{3.45}$$

Refilling of cytosolic Ca^{2+} in ER by SERCA pump is defined in as function of $\widetilde{c}$ with a Hill's coefficient of 2 (because it has two Ca^{2+} binding sites at the cytoplasmic face), as in SMC model, but the term $\widetilde{B}$ is set so as to suppress any oscillatory response, and can be written as

$$\widetilde{J}_{ERuptake} = \widetilde{B}\frac{\widetilde{c}^2}{\widetilde{c}_b^2 + \widetilde{c}^2} \tag{3.46}$$

$\widetilde{J}_{cation}$ is the Ca^{2+} influx from nonselective cation channels. With the relative permeability P_{Na}:P_K:P_{Ca} (1:1:0.7) the Ca^{2+} influx through these channels is constituted by extracellular $Ca^{2+}$and is essentially sensitive to log[$\widetilde{c}$], as modelled by equation 3.47. Originally modelled by (Schuster et al., 2003) and adapted by (Koenigsberger et al., 2005), the hyperbolic tangent was used to fit the data for the porcine coronary EC, whose open channel probability follows a sigmoidal curve. The opening of the channel is highly sensitive to intracellular Ca^{2+} and is relatively independent of the membrane potential except for the influence caused by the electrostatic gradient on hyperpolarization. The hyperpolarization of the membrane potential encourages the opening of the channel and the Ca^{2+} influx through these nonselective ion channels. Other than this effect, the membrane potential and Ca^{2+} influx through these channels is uncoupled. $\widetilde{J}_{cation}$ therefore can

be modelled as

$$\widetilde{J}_{\text{cation}} = \widetilde{G}_{\text{cat}}\,(E_{\text{Ca}} - \widetilde{v})\,\frac{1}{2}\left(1 + \tanh\left(\frac{\log_{10}\widetilde{c} - \widetilde{m}_{3_{\text{cat}}}}{\widetilde{m}_{4_{\text{cat}}}}\right)\right) \tag{3.47}$$

Intracellular Ca^{2+} dynamics in this EC model is a balance of three major ionic currents, $\widetilde{J}_{\text{ER uptake}}$, $\widetilde{J}_{\text{cation}}$ and $\widetilde{J}_{\text{Eff}}$. The influence of extracellular Ca^{2+} on the cytosolic Ca^{2+} concentration $\widetilde{c}$ is largely depicted by the availability of $\widetilde{J}_{\text{cation}}$ as this is the only source of influx of extracellular Ca^{2+} contribution in this model. Keeping this in view, the $\widetilde{J}_{\text{Eff}}$ must be greater than both $\widetilde{J}_{\text{ER uptake}}$ and $\widetilde{J}_{\text{cation}}$combined at all times to ensure that Ca^{2+} entering the cell from outside, under any stimulus, dose not retain intracellularly. Thus $\widetilde{c}$ could reach a peak value as a transient increase when stimulated, which then decreases to a basal level after the removal of the stimulus.

With respect to the interior of the ER, Ca^{2+} dynamics consist of a summation of CICR and a constant Ca^{2+} leak currents leaving the ER domain whereas refilling by SERCA pump is the only means to restore luminal Ca^{2+} load inside ER. Thus ER Ca^{2+} dynamics represented by $\widetilde{s}$ can be written as

$$\frac{d\widetilde{s}}{dt} = \widetilde{J}_{\text{ERuptake}} - \widetilde{J}_{\text{CICR}} - \widetilde{J}_{\text{Leak}} \tag{3.48}$$

Membrane potential dynamics in this model come from (Schuster et al., 2003). In their study on porcine coronary EC, they found that the on agonist stimulation, the reversal/Nernst potential (the equilibrium potential where net current across the membrane becomes zero) was very close to that of K^+ and was predominantly contributed by K^+ transmembrane flux, other ionic species contributing a negligible share to it which they called *residual* current. This residual current comprised of an inward Na^+ orK^+ current and an outward Cl^- current and is modelled by

$$\widetilde{I}_{\text{Residual}} = \widetilde{G}_R\,(\widetilde{v} - \widetilde{v}_{rest}) \tag{3.49}$$

Upon agonist stimulation, the outward hyperpolarizing K^+ current was contributed by two distinct Ca^{2+} activated K^+ channels (K_{Ca}),a large conductance BK_{Ca} channel, activated by cytosolic Ca^{2+} and membrane potential, modelled

by

$$\widetilde{I}_{\mathrm{BK_{Ca}}} = \frac{0.4}{2}\left(1+\tanh\left(\frac{(\log_{10}\widetilde{c}-z)(\widetilde{v}-y)-x}{\widetilde{m}_{3\mathrm{b}}(\widetilde{v}+x(\log_{10}\widetilde{c}-z)-y)^2+\widetilde{m}_{4\mathrm{b}}}\right)\right) \tag{3.50}$$

and a small conductance SK_{Ca} channel which was sensitive to intracellular Ca^{2+} only, and modelled by

$$\widetilde{I}_{\mathrm{SK_{Ca}}} = \frac{0.6}{2}\left(1+\tanh\left(\frac{(\log_{10}\widetilde{c}-\widetilde{m}_{3\mathrm{s}})}{\widetilde{m}_{4\mathrm{s}}}\right)\right) \tag{3.51}$$

Thus the total current outward K^+ current through K_{Ca} channels is a sum of the currents from these two K_{Ca} channels is different conductances and therefore can be written, along with a membrane potential activation function, as

$$\widetilde{I}_{\mathrm{K}} = \widetilde{G}_{\mathrm{tot}}(\widetilde{v}-\widetilde{v}_{\mathrm{K}})\left(\widetilde{I}_{\mathrm{BK_{Ca}}}+\widetilde{I}_{\mathrm{SK_{Ca}}}\right) \tag{3.52}$$

Since voltage across the plasma membrane, which acts like a capacitor, is

$$\frac{dV}{dt} = \frac{I_c}{C}$$

therefore by summing all the transmembrane fluxes the membrane potential dynamics can be written as

$$\frac{d\widetilde{v}}{dt} = -\frac{1}{C_{\mathrm{m}}}\left(\widetilde{I}_{\mathrm{K}}+\widetilde{I}_{\mathrm{Residual}}\right) \tag{3.53}$$

The intracellular IP_3 dynamics are similar to that modelled for a single SMC in section 3.2.1. Agonist induced IP_3 formation is modelled by a free parameter $\widetilde{J}_{\mathrm{PLC_{agonist}}}$whereas intracellular IP_3 degradation is modelled by $\widetilde{J}_{\mathrm{degrad}}$ and $\widetilde{I}$ therefore can be written as

$$\frac{d\widetilde{I}}{dt} = \widetilde{J}_{\mathrm{PLC_{agonist}}} - \widetilde{J}_{\mathrm{degrad}} \tag{3.54}$$

In the case of an EC, the term $\widetilde{J}_{\mathrm{PLC_{agonist}}}$ is retained and is varied spatially in the later chapters to simulate the variation of agonist concentration and the consequent PLC induced intracellular IP_3 generation.

3.3 Numerical method

In several cases, analytical solution to a set of ordinary differential equations dose not exist. For these cases, numerical approximations to the exact solutions are used. Each ODE of the the two sets representing a SMC and an EC respectively, is of the form,

$$y' = f(t, y(t)), \qquad y(t_0) = y_0 \tag{3.55}$$

where t is time between $a \leq t \leq b$ and rate of change of y is not only dependent on time but also on itself. From (Koenigsberger et al., 2005) it is known that the cell models have oscillatory response to a particular range of the stimulus or input parameter. This is a result of some constituent fast and slow processes and the time varying dominance of a slow or fast process at different times, making the set of ODEs stiff in nature. Thus in an oscillatory state, it is expected that the rise time will be contributed by certain very fast processes followed by their saturation, and consequent dominance of fast and then slow processes accounting for the refractory period before the next oscillation arrives. In addition to that, the dependence of each variable on other state variables, established by the negative or positive feedback mechanisms obtained from underlying physiology, also make the ODEs nonlinear due to difference in time scales. Examples of it can be the interaction of SR Ca^{2+} with intracellular Ca^{2+}, intracellular Ca^{2+} with the membrane potential and the delayed rectification by K_{Ca} in response to depolarized membrane potential. Together these equations present a computationally expensive problem because of variable cost of computation within a time interval and the computation expense dictated by the speed of the dominant processes.

In practice, higher order Runge Kutta (RK) methods are used to solve such problems because of their superior convergence and stability features. 4^{th} order explicit RK method is a common choice. Other higher order explicit methods can also be used and some implicit methods will also produce results with stability and accuracy. Using other methods adds to the computational cost. To solve an ODE such as equation 3.55, an explicit p^{th} order RK uses the present value of the y at time step t to approximate $y(t+\Delta t)$ at the next time step $(t+\Delta t)$, Δt being a

small increment in time such that

$$y_{(n+1)} = y_{(n)} + \sum_{i=1}^{s} b_i k_i \tag{3.56}$$

where

$k_1 = h * f(t_n, y_n)$

$k_2 = h * f(t_n + c_2 h, y_n + a_{21} k_1)$

.

.

$k_s = h * f(t_n + c_s h, y_n + a_{s1} k_1 + ... + a_{s,s-1} k_{s-1})$

Here n is the n^{th} iteration, h is a constant time step size, s is the number of stages, $a, b\&c$ are the coefficient corresponding as given in the Butcher tableau (a method for writing the coefficients for a given method) of the method being used. An implicit method uses the value of y both at the present time step t and the next time step $(t + \Delta t)$ to approximate $y(t + \Delta t)$, such that the following equation is satisfied

$$G \cdot (y_{(n)} + y_{(n+1)}) = 0 \tag{3.57}$$

From the above condition it is noticeable that there is an extra step involved in approximating the solution $y(t + \Delta t)$. This extra step ensures stability while dealing with stiff ODEs of the sort

$$y' = |l|y + f(t) \tag{3.58}$$

where l is large, therefore the derivative is heavily dependent on y. Thus implicit methods do ensure solution of such an equation in proposed time interval but at the expense of additional computational cost of an added step. Also, these methods are algorithmically complex to write as computer programs. On the other hand, when dealing with equations like 3.58, an explicit method takes small time steps to ensure a stable solution which is well within the defined error bounds. These methods however are relatively easier to code.

Explicit methods can be made faster by use of extra stages, while maintaining the order of the method, i.e. its characteristic accuracy to produce a reliable approximation in comparison to its exact solution (if it exists). Embedded methods are constructed to estimate the local truncation error of each RK step taken. The local truncation error is the error caused by one iteration while computing an approximation to the exact solution of $y(t)$. To achieve this estimate in an embedded method, an extended Butcher tableau is constructed by halving of two methods one with order p and another with order $p-1$. The $(p-1)$ order step is given by

$$y_{(n+1)} = y_{(n)} + \sum_{i=1}^{s} b_i^* k_i \tag{3.59}$$

and k is identical for both the p^{th} and $(p-1)^{th}$ order methods (* relates to the lower order method). The local truncation error for such a scheme is the difference of the approximations from both the methods

$$\varepsilon_{n+1} = y_{n+1} - y_{n+1}^* = h \sum_{i=1}^{s} (b_i - b_i^*) k_i \tag{3.60}$$

which is $O(h^p)$ (i.e. ε scales as h^p). Given the error tolerance, a new step size h_{new} can be calculated using the estimated ε_{n+1}. This makes the step size calculation adaptive to the complexity of the latest approximation thus known as adaptive step size control. The idea is that the solver should carefully select many small steps where solution exhibits stiffness, as we go forward in time, and may take large steps when the solution behaves relatively smooth. Based on the performance of the solver and the nature of the problem, the improvement in efficiency can be tens to hundred folds (Press et al., 1992). Given the information on ε the attempt would be to keep it in desired bound for accuracy of the solution. For an embedded RK5(4), if h_1 is the step taken by the solver to produce an error, ε_1, then the step size h_0 that would have produced an error ε_0 can be calculated by

$$h_0 = h_1 \left| \frac{\varepsilon_0}{\varepsilon_1} \right|^{1/p} \tag{3.61}$$

Here ε_0 represents desired accuracy, also termed as *tolerance* or *tol*. Thus if

$\varepsilon_1 > \varepsilon_0$, the equation tells how much to decrease h_0 and if $\varepsilon_1 < \varepsilon_0$, it tells how much can the next step be safely increased. Generally, in cases where embedded methods are solvers of choice, the solution $y(t)$ is a vector representing the variables in a system of ODEs, as in our case. The magnitudes of these representative members of this vector may be several orders different from one another. In this case, desired accuracy, ε_0, may differ. To include this feature of defining accuracy control of individual elements of the solution vector, *absolute tolerance* is defined.

C implementation of 4^{th} order Runge Kutta (RK4) was tested on single cell models for an EC and SMC respectively. The algorithm was able to solve the systems of ODEs with a fixed step size of $1e^{-2}$. For the coupled systems of ODEs, a the maximum step size of $1e^{-4}$ was required and this was irrespective of the simulated number of cells.

To solve the coupled system of ODEs, a embedded RK pair BS(4,5), derived by Bogacki and Shampine (1996), was also tested. RKSUITE, described in detail in Section 3.4 is a software written in C++ that implements BS(4,5). This is a 7 stage method with an accuracy of fifth order and is acclaimed to be more efficient than the popular Erwin Fehlberg 's (RKF(4,5)) and J R Dormand and P J Prince's (DP5(4)) pairs. Generally, when a RK code is implemented, the user defined instances of independent variable (time in our case) may not exactly be met because of the adaptive step size selection which estimates next step size dictated by the local truncation error of the last successful step. In order to get the solution at user specified points, interpolation is usually used, the cost of is problem dependent. An interesting feature of BS(4,5) is the lack of dependence of local error of the interpolant on the problem. The local truncation error of the interpolant is a function of local error of the last step (or end of the step). Mathematical intricacies proving the superiority of this method over RKF(4,5) and DP5(4) can be reviewed in (Bogacki and Shampine, 1996). RKSUITE, in addition to BS(4,5) pair also implements BS(2,3) and BS(7,8). BS(2,3), also implemented as *ode23* in MATLAB, is popular for computation of mildly stiff problems. BS(7,8) is an efficient higher order method which is used when high accuracy is required of BS(4,5), thus making it a computationally expensive choice. BS(7,8) in that case is more efficient.

3.4 Numerical Algorithm: RKSUITE

RKSUITE is a robust numerical solver written by (Brankin et al., 1991) to solve initial value problems for a first order system of ODEs of the form 3.55. Both Fortran and C++ versions are available and the later is used in this study. y is a vector of N solution components for a system of ODEs and t is the independent variable, time in the present case, for which interval is user defined. RKSUITE has two integration codes to choose from UT and CT. Depending on the nature of the problem and/or algorithmic approach to solve it, one of the two options can be used. UT stands for 'Usual task' and is employed when solution at sequence of specific points is required, whereas CT, acronym for 'Complicated task', is for integrating for a solution between t_{start} and t_{end}. Another way of using CT is to reset the t_{end} repeatedly to obtain relatively short time intervals to ensure solution of mildly stiff problems.

RKSUITE implements 3 RK methods, namely BS(2,3), BS(4,5) and BS(7,8). Depending on how tight the global error tolerance is required, one method is superior than the other in terms of its efficiency. In the case of solving the ODEs presented in section 3.2, the BS(4,5) was found most efficient. It was able to solve the coupled systems of ODEs 10 times faster than solving the same set of equations with a 4^{th} *order Runge Kutta (RK4)*. RKSUITE is an object oriented algorithm where an instance of class RKSUITE must first be invoked. Call to founding function, namely *setup*, is mandatory before any other function is called. Some compulsory initialization parameters of *setup* include:

- neq: Integer number of equations or state variables
- tstart: lower bound of time interval (double precision)
- ystart: an array of initial values of each state variable (double precision)
- tend: lower bound of time interval (double precision)
- tol: relative error tolerance (double precision)
- thres: an array of threshold applied on the value of $y(L)$ where $L = 1...neq$ at every time step, below which $y(L)$ is insignificant (double precision).

- method: An integer number representing the RK pair to be used for integration. 1 for BS(2,3) pair, 2 for BS(4,5) pair and 3 for BS(7,8).
- task: selection for executing either using UT or CT code
- errass: a parameter of type boolean, which if set *true* will enable estimation of global error for each solution component $y(L)$ where $L = 1...neq$.
- hstart: initial step size to be taken (double precision). If set to 0.0, the code will automatically select an appropriate first step size which is the choice in the present study case when using using CT. While using UT in parallel code where equal step size is taken at each iteration, the first step size is nonzero.
- message: a parameter of type boolean, which if set *true* will enable printing the error message on stdout.

tol is the desired relative accuracy in the solution and must be set >0.01. The smaller tol is, the more correct significant figures we get, thus more computation is usually required. Error tolerance is applied on the solution value by test the condition $tol * max(size(L), thres(L))$, where $size(L)$ is the average magnitude of $y(L)$ over one time step. If $thres(L)$ is smaller than the present value of $size(L)$, the value of tol is considered so that the solution is correct to those many significant figures (e.g. if $tol = 10^{-4}$, then the code will make the effect to minimize the error to 4^{th} significant figure). In the case when $size(L)$ is smaller than $thres(L)$, than the tolerance will be matched to $tol * thres(L)$. This is very helpful when the solution components are varying at different orders of magnitudes. In the present study, $tol = 10^{-4}$ to 10^{-6} should be sufficient to include any significant change of magnitude in any state variable. $thres(L)$ has also been set to 1 which helps retain a uniform criteria of tolerance as the fluctuation in the values in all the solution components is relatively of the same order of magnitude. Moreover, as nominated in the RKSUITE manual (Brankin et al., 1991) as relative tolerance test, this is a recommended criteria that should be implemented.

The accuracy criteria discussed in the above paragraph enables selection of appropriate step size as the solution proceeds in time. As the CT task is opted

to solve the system of ODEs under consideration, this adaptive step size selection helps proceed in the solution in time, swiftly. In the later section where we discuss the parallelization of the code, UT is the task of choice because of its suitability on the parallel platform and will be discussed their. *ystart* is a double precision array of the same size as *y* holding the initial values for each solution component in *y*. Initial values of each state variable greatly influence the time evolution of the solution towards its steady state or bistable/oscillatory response. The steady state or oscillatory behaviour remains unaffected by changing the initial values. Since the steady state or oscillatory behaviour is the major focus of the study, we assume solution components have initial values as if they were at physiological equilibrium. We present the effect of initial values on the solution in each cell both in single cell models and in coupled cells later in Chapters 4 and 5.

Once the *setup* has been called and parameters are set, the solver can be called recursively. In the serial algorithm programming our system of ODEs CT is used to integrate. The function CT has following mandatory arguments:

- ComputeDerivatives(t,y,dxdt): This is a function to evaluate all the derivatives. In our case, call to this function by CT will invoke evaluation of the right hand side of equations like 3.35 or 3.41 etc. *t* is the current time after taking the step. Depending on the accuracy set in the *setup*, the expense of computation is judged by the calls made by CT to this function. Inside the body of the function ComputeDerivatives, call to another function, namely fluxes, is made which holds expressions for all the individual currents mentioned in the single SMC or EC model. *y* updated at previous step is passed as argument to this function which then evaluates all the currents and returns their updated values to ComputeDerivatives. These updated currents are then used to update a derivative vector *dxdt* (where the size of this array is same as *y*) and returned back to CT.

- tnow: Current time (double precision)

- y: Solution vector where the updated values of the solution components are returned .

- yp: A vector to hold the solution vector *y* from previous time step (double

precision array).

- cflag: This is an integer in which error (from 1 to 6) is returned. This can be monitored and decisions can be made according to the incurring error.

To ensure stable and accurate solution CT is called repeated over a short time interval. The span of this interval is between *tnow* and *tend*. At the completion of first iteration, *tend*, which was set in *setup*, is incremented and CT is called again between *tnow* and *tend*, until t_{final} is reached. After completion of each iteration, the updated *y* can be written in files to record the results. Within the time interval defined by the user, CT may take numerous small steps according to the stiffness of the problem. If the solution is consistently smooth over first few small step, CT inherently calls UT to do the integration over a large time step. This mixing of CT and UT increases efficiency in compute time when dealing with stiff problems.

Importantly, *fluxes(A,y)* is a function called by *ComputeDerivatives(t,y,dxdt)* to evaluated individual ionic currents, as stated in sections 3.2.1 & 3.2.2, each time ComputeDerivatives is called by CT. Results of these evaluations are stored in a double precision array *A* of length equal to the total number equations expressing the ionic currents. *y* in the input vector to this function, which hold the values of solution components from latest step. Upon return to the calling function, ComputeDerivatives, the components of the array *A* are used to evaluated the rate of change of each state variable which is a sum of corresponding ionic currents (as given in respective equation of c,$\widetilde{c}$...). This rate of change at time *t* is stored in array *dxdt[]*, whose length is equal to the number of solution components or *neq*. Flowchart 3.3 gives a schematic of the C code implementing RKSUITE to solve either SMC or EC single cell model mathematically expressed in previous sections.

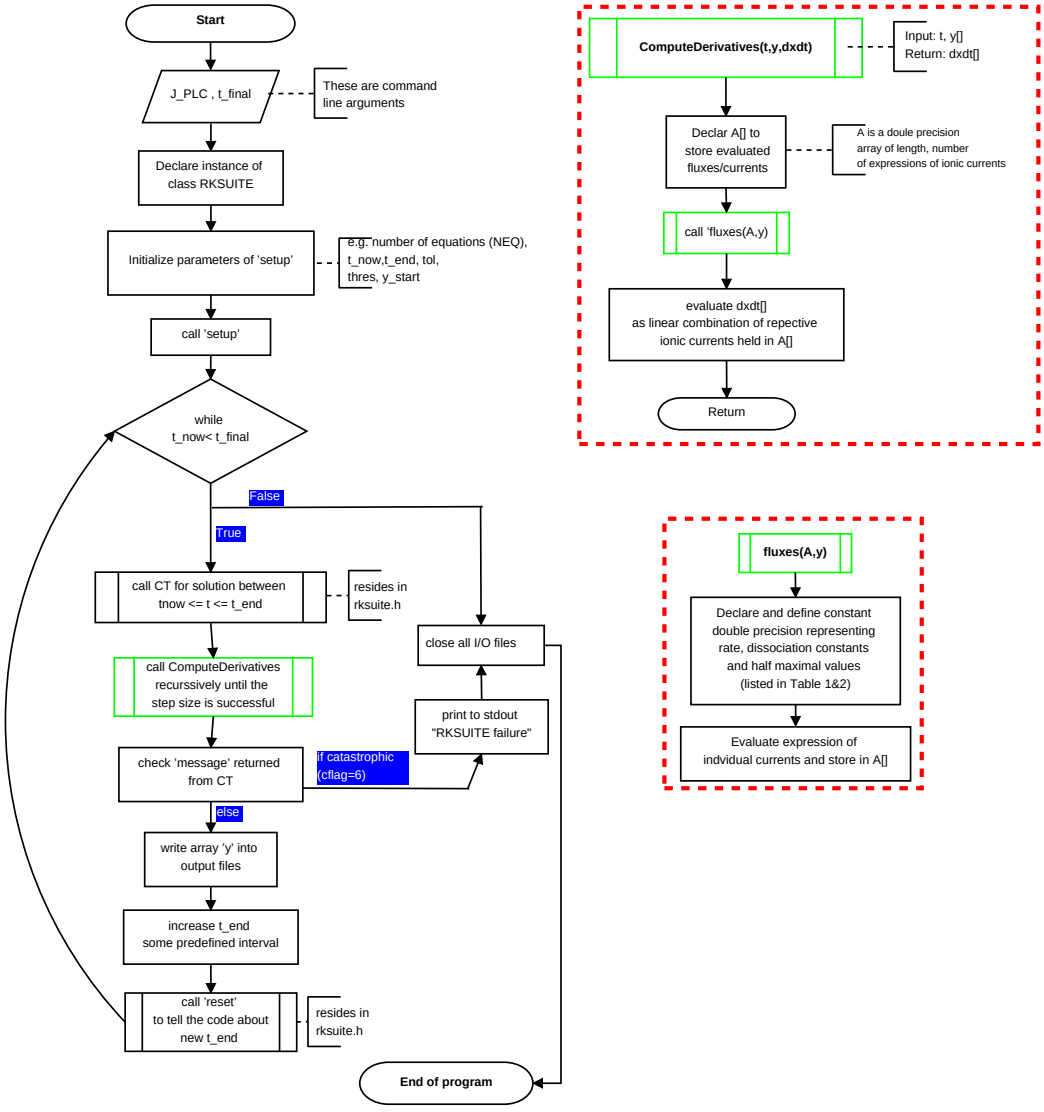

Figure 3.3: Execution of C code for solving system of ODEs with RKSUITE for either a single SMC or EC.

Chapter 4

Cellular Dynamics of Single Cell Models

In previous chapters the physiological processes and the mathematical model expressing the Ca^{2+} dynamics of a single vascular SMC and EC were discussed. These physiological processes are interconnected through negative and positive feedback mechanisms and give rise to complex, agonist concentration dependent responses. The time evolution of cytosolic Ca^{2+} concentration becomes significant when considered to have a direct influence on downstream processes where cytosolic Ca^{2+} concentration regulated cell processes, e.g. cytoskeletal reorientation, growth, apoptosis and development. The present focus on c and $\widetilde{c}$ in a single vascular SMC and EC is to elaborate the cellular dynamics of an uncoupled cell under agonist stimulation. Single cell dynamics are particularly responsible for morphological reorientation of an EC and regulation of contractililty of SMC which signifies the importance of understanding the Ca^{2+} dynamics in the two cell types in uncoupled environment. This chapter, therefore, is intended to translate the cellular dynamics approximated by the models to the responsible physiologically cellular processes in each cell type.

4.1 The Basis of Ca^{2+} Oscillations in an Uncoupled Vascular SMC

Vasoactive substances such as blood borne species, neurotransmitters and biomechanical stimuli such as fluid shear stress and circumferential stretch, can induce Ca^{2+} transients in cytosol of vascular cells, both ECs and SMCs. This cytosolic Ca^{2+} increase, especially in response to vasoacticve agonists such as acetylcholine and ATP etc.., is via IP_3 dependent pathway in both types of cells. Purinoreceptors (P_2Y) on SMC cell membrane bind to specific agonists on their extracellular side which stimulates the G protein complex and consequent activation of membrane phospholipid PLC_β. The activation of PLC_β catalyses the hydrolysis of PIP_2, another membrane bond phospholipid PIP_2 resulting in the formation of IP_3 . This is a fast process compared to the time scales over which either the downstream intracellular processes operate (Meyer and Stryer, 1988) or the transport of agonist on the extracellular side takes place. It is therefore modelled as a lumped parameter which when increases, simulates the increase in the agonist stimulation on extracellular side and consequent IP_3 production on cytosolic side. The increasing intracellular IP_3 concentration is regulated by the activity of IP_3 kinase (IP3K), which phosphrylates it to IP_4 which dose not bind efficiently to IP_3R on the SR membrane. Figure 4.1 is a schematic of the intracellular events following the new presence of IP_3 upon agonist stimulation.

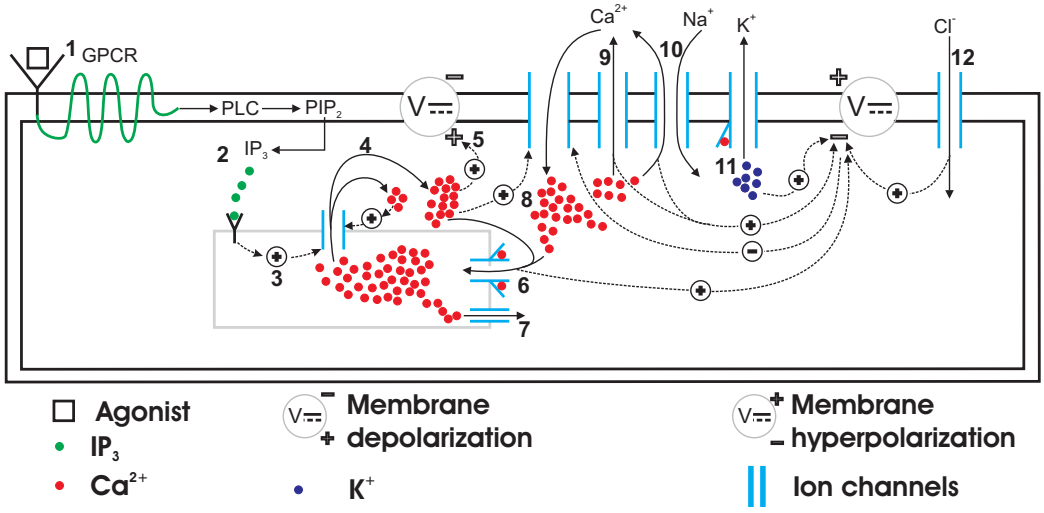

Figure 4.1: Schematic of a single SMC showing cellular dynamical processes. (1)Agonist binds to the purinoreceptors (P_2Y) on the SMC cell membrane activating the G protein complex, which then activates membrane bound Phospholipase C (PLC). PLC activation catalyses the hydrolysis of PIP_2 to form (2) IP_3 that is then release in the cytosol. This nascent IP_3 binds to the SR membrane bound IP_3 receptor (IP_3R). (3)IP_3 bound to IP_3R enables release of Ca^{2+} ions from the SR into the cytosol. (4) The Ca^{2+} release from intracellular store sensitizes the IP_3R further which releases more Ca^{2+} referred to as CICR, thus making a Ca^{2+} rich domain in the cytosol of the SMC. The excess of intracellular Ca^{2+} depolarizes the membrane potential. (5)The IP_3 induced and CICR Ca^{2+} depolarizes the membrane potential.(6) SR has low affinity Ca^{2+} binding sites on the cytosolic side of a channel which passively (fuelled by ATP) pumps Ca^{2+} back inside the SR, by SERCA. Cytosolic Ca^{2+} encourages the replenishment of the intracellular stores via this pathway. (7) Ca^{2+} leaks from SR consistently under concentration gradient between cytosolic and SR luminal Ca^{2+} and keep the Ca^{2+} in equilibrium during non-stimulated state of the cell. (8)The membrane depolarization result in the influx of Ca^{2+} from VOCCs which will close upon repolarization in the following steps. (9) CaATPase pushes out cytosolic Ca^{2+} to extracellular space. (10)Ca^{2+}, in addition to other pathways, is pushed out into extracellular space via Na/Ca exchanger. (11) Binding of Ca^{2+} ions to K_{Ca} opens BK_{Ca} channels in SMC causing K^+ efflux and membrane repolarization. (12) Influx of Cl^- ions add to the repolarization.

For investigation of the response of a dynamical system represented by set of ODEs, to the change in a parameter value (e.g. $J_{PLC_{agonist}}$ in this case), a bifurcation diagram is a common representation. The solution may reach to an *equilibrium point* or *fixed point* as the independent variable (*time* in our case) progress, or it may enter a *periodic orbit* (a solution that repeated itself in time). A *Hopf bifurcation* is said to have occurred when solution of a dynamical system departs from an equilibrium solution to a stable periodic orbit, or vice versa, with a smooth variation in the parameter value. Such behaviour is a common place while dealing with nonlinear dynamical system.

Examining the response of the model of SMC with changing $J_{PLC_{agonist}}$, two Hopf bifurcations occur. For a change of $0.065 \leq J_{PLC_{agonist}} \leq 0.19$ μM/s, the SMC model is simulated for a time interval of $0 \leq t \leq 1000$ seconds. Figure 4.2a plots the peak maximum and minimum of c between time interval $0 \leq t \leq 1000$ seconds against $J_{PLC_{agonist}}$. In Figure 4.2a, the solution reaches to an equilibrium before the $J_{PLC_{agonist}}$ is increased to 0.075μM/s. Here, the first Hopf bifurcation occurs and the solution starts to oscillate with respect to time. These oscillation are sustained, i.e. they do not dampen as time increase. This oscillatory behaviour of the cytosolic Ca^{2+} concentration persists until $J_{PLC_{agonist}}$=0.160μM/s, where the second Hopf bifurcation occurs and the solution changes its response from oscillatory to assuming a steady state equilibrium, with respect to time. This gives rise to three domains of the solution, with respect to the parameter $J_{PLC_{agonist}}$. In domains 1 and 3 the solution attains equilibria, and the domain 2 is oscillatory. Time course of cytosolic Ca^{2+} concentration is depicted in Figure 4.2b at a $J_{PLC_{agonist}}$ value from each domain.

The three domains occurring in the bifurcation diagram are comparable to Koenigsberger's model results(see Figure 2 (Koenigsberger et al., 2005)) for an uncoupled SMC. The results of Koenigsberger's model have been validated with the experiments conducted by Lamboley et al. (2003), where the plot identifies three distinct domains of responses corresponding to low, moderate and high agonist concentration.

The negative and positive feedback mechanisms working in individual processes shown in Figure 4.1 and the difference in their time scales because of their differential cooperativities (i.e. the number of ions required to be attached to cer-

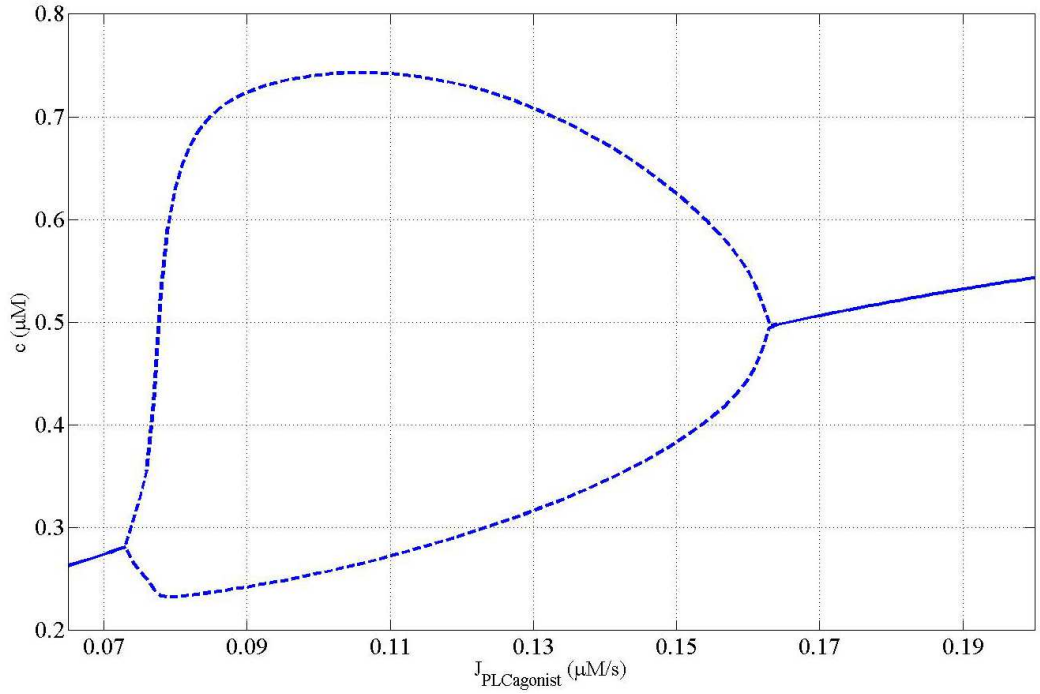

(a) Bifurcation diagram showing the response of the solution of system of ODE represent an uncoupled SMC. The responses can be divided into three disticnt domains with respect to the parameter values $J_{PLC_{agonist}}$. Two Hopf bifurcations occur at $J_{PLC_{agonist}}$=0.075μM/s and $J_{PLC_{agonist}}$=0.160μM/s respectively, and is named domain 2 (demarcated by dashed lines). In domains 1 and 3 (solid lines), the cytosolic Ca^{2+} concentration of a SMC attains an equilibrium with distinct steady state values.

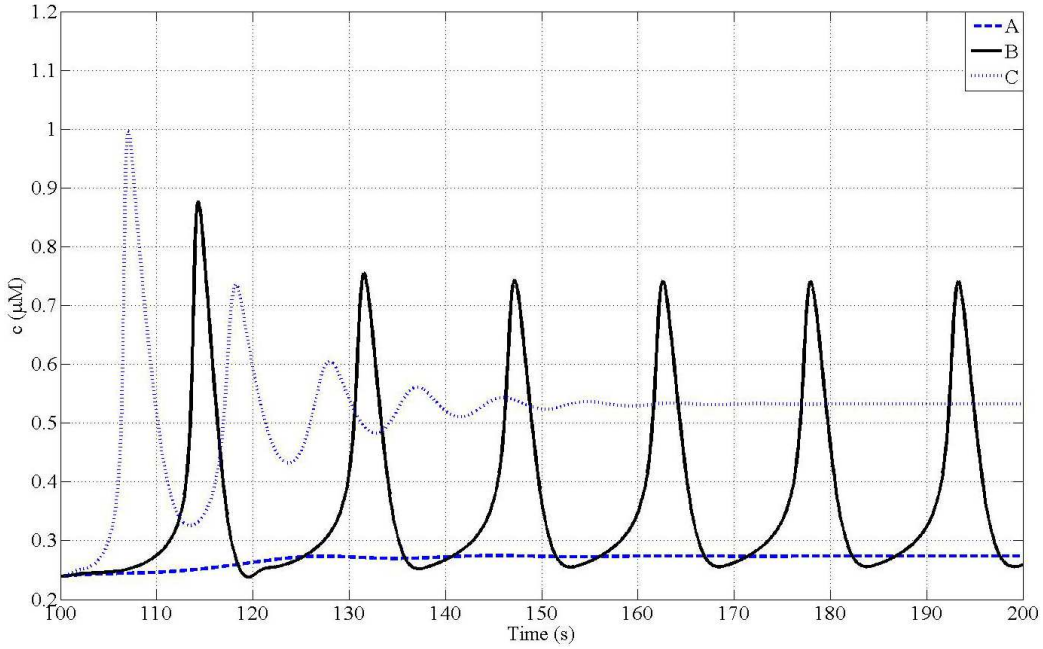

(b) Time evolution of cytosolic Ca^{2+} concentration in a SMC stimulated with (A)0.07μM/s, (B)0.1μM/s and (C)0.19μM/s, from solution domains 1,2 and 3 respectively.

Figure 4.2: Cytosolic Ca^{2+} concentration in SMC versus $J_{PLC_{agonist}}$.

tain ion gated channels to increase the open channel probability) gives rise to the three domains witnessed in Figure 4.2a. Thus to understand the basis of oscillations, it is important to review how the individual currents respond to a certain level of stimulation. Nascent IP_3 , upon binding to the IP_3R activate the release of luminal Ca^{2+} from SR, J_{IP_3}. The rate of this Ca^{2+} release follows the rate at which cytosolic IP_3 concentration is maintained. Cytosolic IP_3 is regulated by the its generation and its metabolism by IP3K, as expressed in equation 3.39. Figure 4.3a shows the proportional increase in J_{IP_3} as cytosolic IP_3 increases. The difference in the slopes of the two curves comes from the fact that a certain number of IP_3 molecules is required to bind to the IP_3R to activate the channel. This model considers two IP_3 molecules as the requirement for release of Ca^{2+} from SR where as other models (Kapela et al., 2008; Meyer and Stryer, 1988) model this current with three ip molecules. This newly added cytosolic Ca^{2+} further sensitized the IP_3R to cytosolic IP_3 which results in an enhanced release of SR Ca^{2+} denoted as J_{CICR} in equation 3.25 (also shown in Figure 4.3a), although other models include Ca^{2+} dependence to express the IP_3R sensitization via cytosolic Ca^{2+} concentration (Kapela et al., 2008). Notice that the J_{CICR} increases rapidly soon as J_{IP_3} reaches a steady state value corresponding to the cytosolic IP_3 availability. After J_{CICR} reaches a peak, the decreasing slope can be attributed to the refilling of the intracellular stores via SERCA pump, its rate denoted by $J_{SR\ uptake}$ in equation 3.26. Figure 4.3b shows the time evolution of $J_{SR\ uptake}$ in conjunction with the dynamics of the luminal or SR $Ca^{2+}$where loss of s coincides with the increase in J_{CICR}. A Ca^{2+} leak current operates at all times from SR into the cytosol and is dependent on cytosolic Ca^{2+} concentration (also shown in Figure 4.3b). This is important to maintain the equilibrium Ca^{2+} concentrations both in the cytosol and SR in the absence of any extracellular stimulation.

The increase in cytosolic Ca^{2+} depolarizes the membrane potential (v) which otherwise was at a resting potential (approximately -40mV) governed by an equilibrium of ionic concentrations inside and outside the cell. This depolarization enables the opening of plasma membrane bound voltage operated Ca^{2+} channels (VOCC), denoted by J_{VOCC}, through which extracellular Ca^{2+} moves into the SMC cytosol and further depolarizes the membrane potential. Figure 4.3c shows the time evolution of J_{VOCC} and v. Notice that the depolarization in membrane

potential, i.e extracellular side is more negative than intracellular side, makes J_{VOCC} more negative. Since the term J_{VOCC} in the ODE for cytosolic Ca^{2+} dynamics, equations 3.35and 3.37, is preceded by a negative sign, this implies that the more negative the extracellular side relative to the cytosolic side, more the open state probability of VOCCs, therefore higher the influx of Ca^{2+}through them. Conversely, the repolarization of membrane potential towards its resting voltage reduces J_{VOCC}. This becomes significant when considering the forced hyperpolarization (i.e. exacerbated negativity of extracellular side) of the membrane potential in the EC-SMC heterocellular electrical coupling scenario.

In order to bring the cytosolic Ca^{2+} concentration to its basal state, Ca^{2+} efflux currents continuously remove Ca^{2+} from cytosol to the extracellular space. Plasma membrane bound CaATPase, denoted as J_{Eff} actively transport Ca^{2+} from cytosol to extracellular space where as Na^+/Ca^{2+}antiporter, denoted as $J_{Na/Ca}$ brings in two Na^+ ions and removes three Ca^{2+} ions in exchange from cytosol. Both these currents are shown in Figure 4.3d. Equations 3.30 and 3.29, modelling J_{Eff} and $J_{Na/Ca}$ are dependent on both c and v, therefore the maximum efflux occurs when cytosolic Ca^{2+} is maximum and membrane potential is depolarized.

Increased cytosolic Ca^{2+} concentration and the membrane depolarization coupled to it has an effect on the cytosolic K^+ concentration. Plasma membrane bound, large conductance Ca^{2+} activated K^+ channels (K_{Ca}) are responsible for efflux of K^+ from cytosol to extracellular space. This efflux of K^+ ions with single positive charge has a significant effect on the membrane potential. As the name suggests, two Ca^{2+} ions attach to the cytosolic side of this channel and equation 3.32 models the activation of this channel. Figure 4.3e shows the time course of the K^+ current through this channel along with its open state probability ω. Efflux of K^+ ions from this channel tends to repolarize the membrane to its resting potential and in doing so, the Ca^{2+} influx through VOCCs also decrease. Simultaneously, Ca^{2+} efflux through CaATPase also increase and the consequence is the decrease in cytosolic Ca^{2+} concentration, as shown in Figure 4.3f. Correlating the time courses of the above processes provides a better understanding of their influence on the cytosolic Ca^{2+} concentration of the SMC.

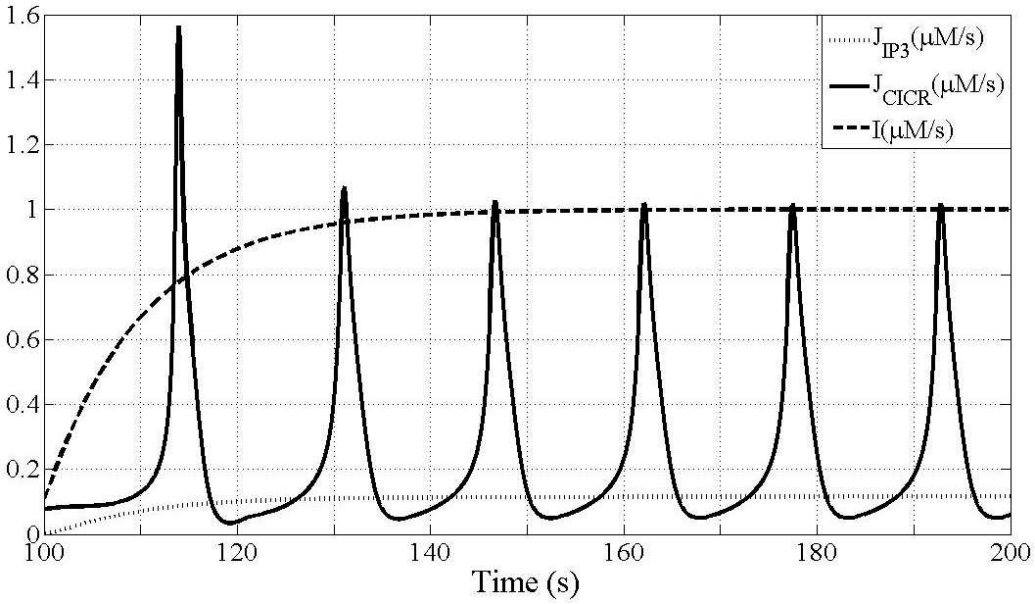

(a) Time evolution of cytosolic IP_3 ,J_{IP_3} and J_{CICR}. As J_{IP_3} reaches its steady state value correspondingly set by cytosolic IP_3 , J_{CICR}rapidly increases.

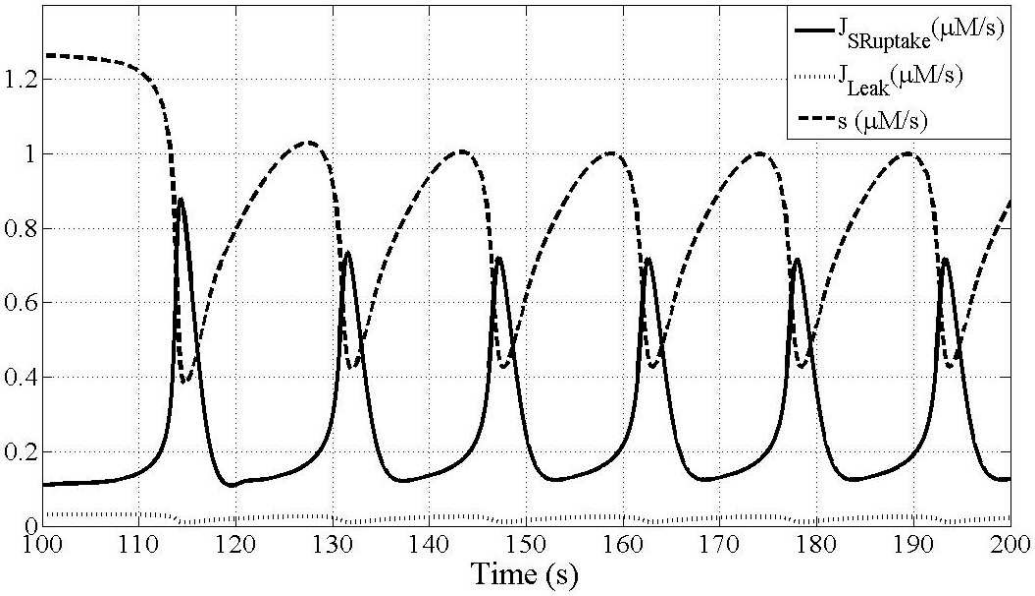

(b) Time evolution of $J_{SR\ uptake}$,J_{Leak} and SR Ca^{2+}. Notice that J_{CICR} in (a) leads $J_{SR\ uptake}$. Also, the decrease in SR Ca^{2+} (*s*) coincides with simultaneous increase in J_{CICR}. Since J_{Leak} depends on *s*, it therefore follows that curve.

Figure 4.3

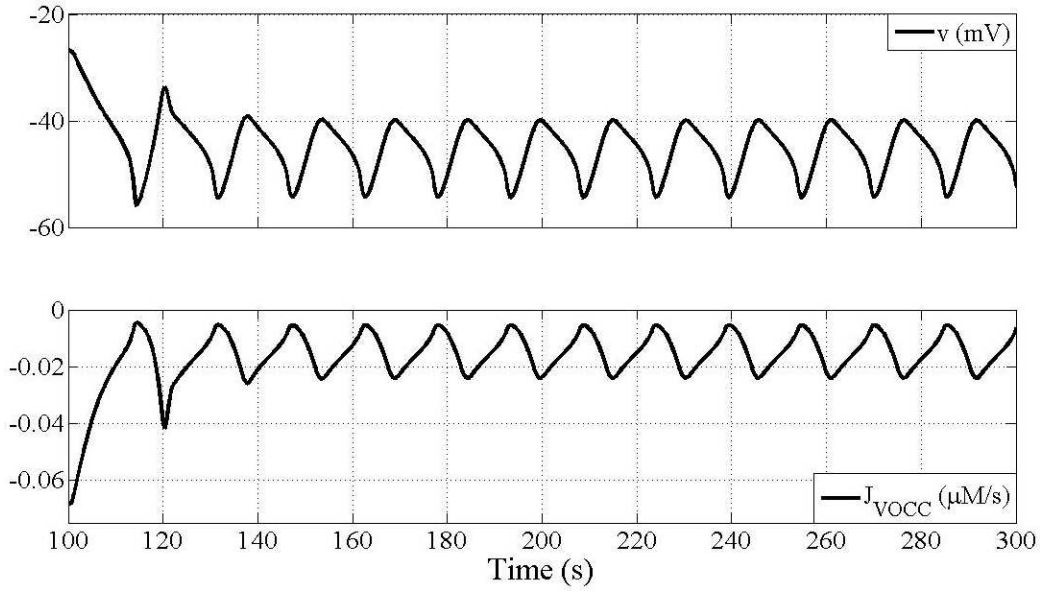

(c) Time evolution of v and J_{VOCC}.

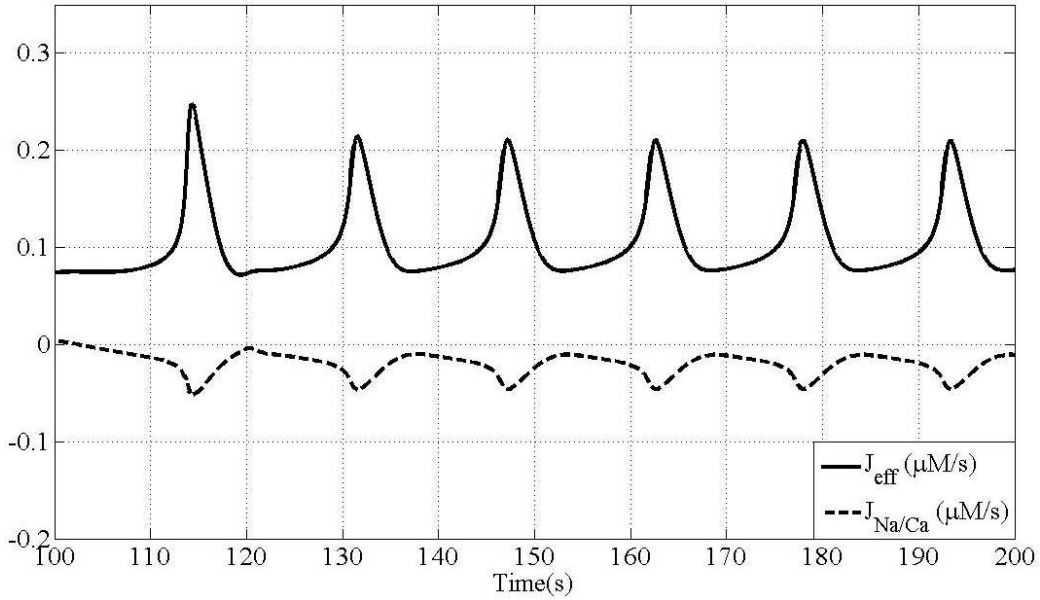

(d) Time evolution of J_{Eff} and $J_{Na/Ca}$. Both currents are c and v dependent and in addition to $J_{SR\ uptake}$ from (b), they are the main pathways of efflux of cytosolic Ca^{2+} to bring it back to basal concentration.

Figure 4.3

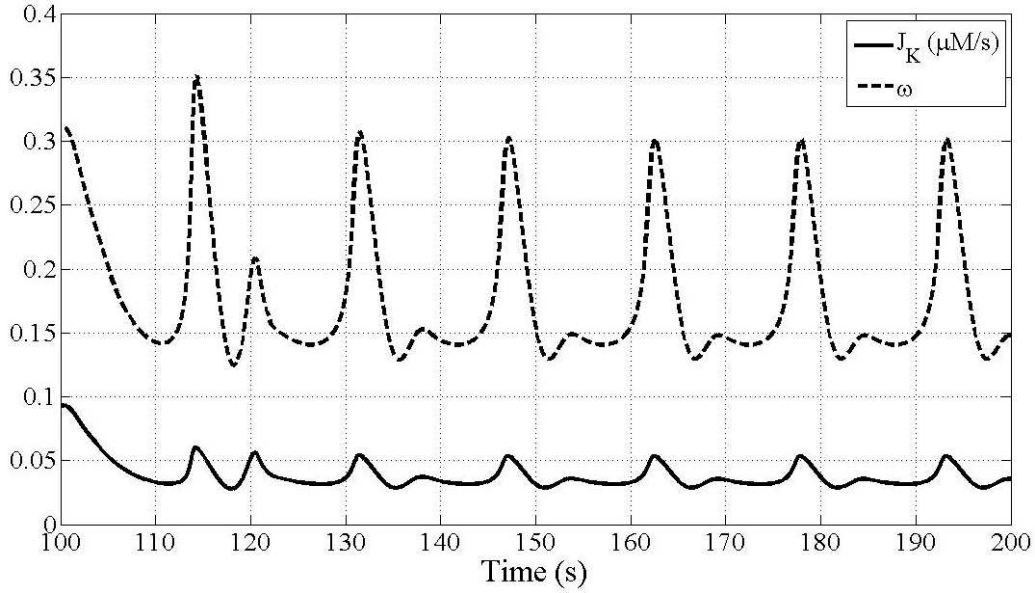

(e) Time course of K_{Ca} open state probability (ω) and K^+ efflux from K_{Ca}, J_K. Notice that the channel opening and K^+ efflux follows the rate of increase of cytosolic Ca^{2+} in fig:osicllationF.

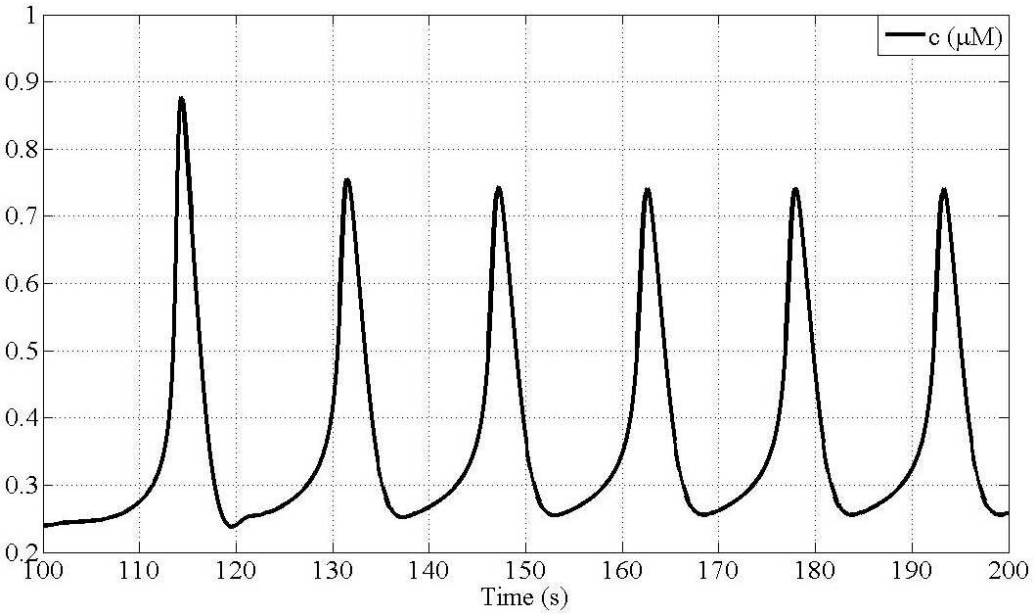

(f) Time evolution of cytosolic Ca^{2+} concentration.

Figure 4.3: Intracellular dynamics of the Ca^{2+},membrane potential and IP_3 in a SMC stimulated by $J_{PLC_{agonist}}$=0.1μM/s.

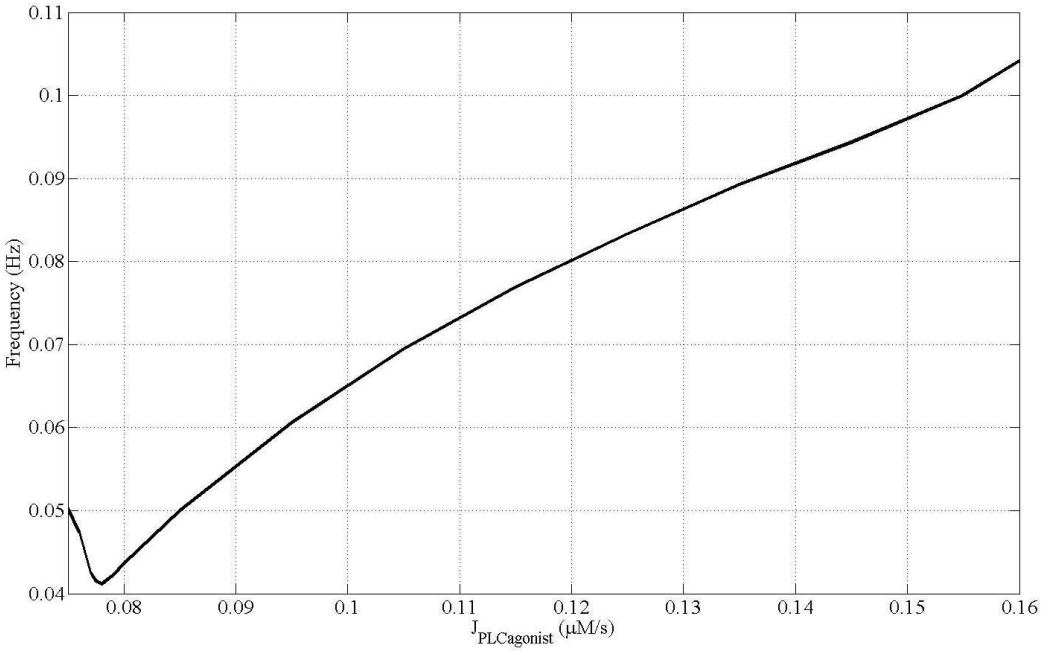

Figure 4.4: Number of Ca^{2+} oscillations in cytoslic Ca^{2+} concentration at equilibrium as a function of increasing $J_{PLC_{agonist}}$ with range corresponding to the oscillatory domain of Figure 4.2a. Number of oscillations per minute, or frequency, increases with increasing $J_{PLC_{agonist}}$.

4.2 Agonist Effects On SMC Ca^{2+} Oscillations

The bifurcation diagram in Figure 4.2a highlights the steady state responses as three domains those are elicited by the different ranges of $J_{PLC_{agonist}}$. The cytosolic Ca^{2+} concentration in domain 2 oscillates upon stimulation by $J_{PLC_{agonist}}$ between the range 0.075μM/s, where the first Hopf bifurcation occurs, and 0.160μM/s, where the second Hopf bifurcation is seen. For domains 1 and 3, the cytosolic Ca^{2+} concentration attains a steady state equilibrium. The oscillations produced in the cytosolic Ca^{2+} concentration are sustained and do not wane with time. The frequency and amplitude of the Ca^{2+} oscillations seen in domain 2, are inversely related. The amplitude of the Ca^{2+}oscillations, as shown in the Figure 4.2a, increases with enhanced sensitivity to $J_{PLC_{agonist}}$ but as the parameter values increase further, the amplitude decrease. The frequency of the Ca^{2+} oscillations, which is the inverse of the period of an oscillation, increases with the increasing $J_{PLC_{agonist}}$,

as shown in Figure 4.4. A depiction of the relationship of amplitude and frequency of the oscillations is presented in Figure 4.5. Upon occurrence of the first Hopf bifurcation, where domain 2 starts from, the increase in the amplitude of the oscillations is steep. The frequency decreases initially, with increasing amplitude, and then increases gradually, until $J_{PLC_{agonist}}$=0.105μM/s, where the Ca^{2+} concentration oscillates with an amplitude of 0.74μM. Progressive increase in $J_{PLC_{agonist}}$ from that point on results in consistent decrease in amplitude of the Ca^{2+} oscillations and an increase in their frequency. At $J_{PLC_{agonist}}$=0.160μM/s the second Hopf bifurcation occurs and the steady state response of the system changes from an oscillatory to equilibrium behaviour.

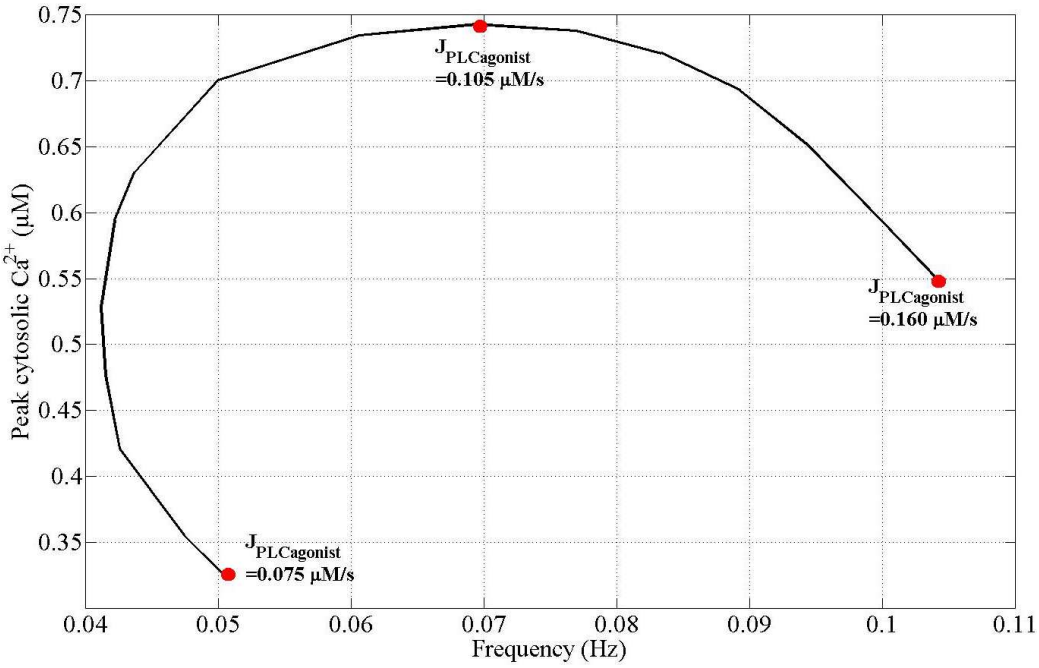

Figure 4.5: Amplitude and frequency relationship of the sustained Ca^{2+} oscillation (calculated when the system has attained equilibrium) of a SMC stimulated by a range of $J_{PLC_{agonist}}$, ($0.075 \leq J_{PLC_{agonist}} \leq 0.160\mu M/s$). The red markers represent the start and end of Hopf bifurcation seen in Figure 4.2a. The arrowheads indicate the direction the curve takes with increasing $J_{PLC_{agonist}}$. Amplitude first increase, then decreases, as frequency of oscillations increase with increasing $J_{PLC_{agonist}}$, until oscillation ultimately cease. The maximum number of oscillation with largest amplitude is observed at stimulation by $J_{PLC_{agonist}}$=$0.105\mu M/s$ (highlighted by blue marker).

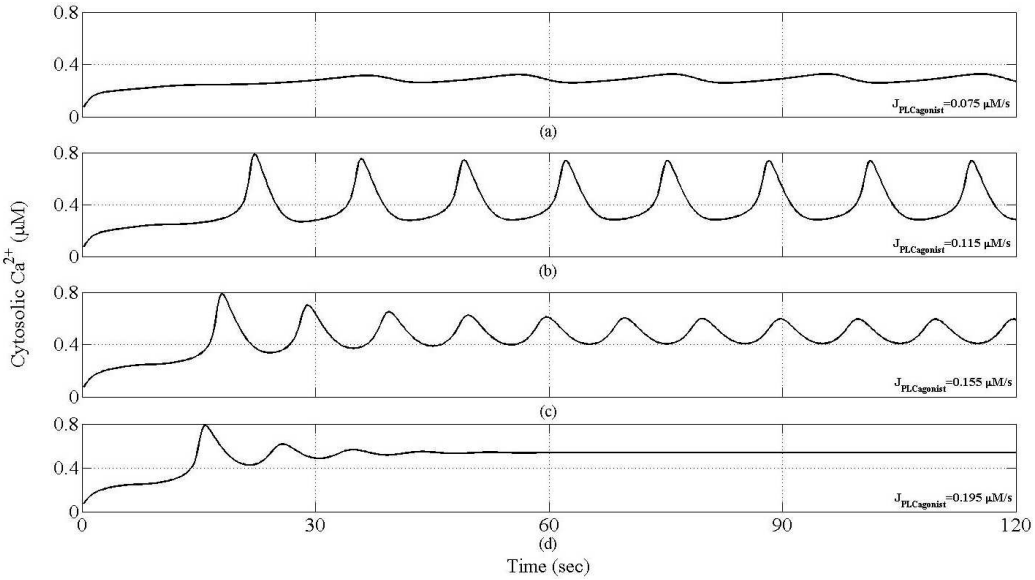

Figure 4.6: Figures (a to d) show the effect of increasing agonist on the waveform of the cytosolic Ca^{2+} oscillations in a SMC. Oscillations in (a to c) are sustained oscillations where as those in (d) damp to a steady state value with time.

A cell is said to be *excitable* if an induced membrane depolarization, which perturbs the plasma membrane from its resting potential, results in generation of an *action potential*. The cell tends to regain the resting membrane potential and in that effort allows passage of ions into or out of the cell to pull the polarity of the cell membrane back to its resting state, a process known as *repolarization*, there by producing *repolarization currents*. In the case of the agonist stimulating a SMC, it perturbs the established equilibrium of the membrane potential by initiating a depolarization phase via IP_3 induced Ca^{2+} release from intracellular stores and following downstream cascade. Several cellular processes, described in Figure 4.1 at part in this effort. The oscillations in Ca^{2+} concentration is a result of the attempt by the system to regain that equilibrium. The transition of the system from steady state equilibrium response to an oscillatory domain is due to the difference in time scales of the fast membrane potential kinetics and the relatively slow ion channel kinetics. This is responsible for the influx and efflux of Ca^{2+} into and from the cytosol. The major contributor to the membrane depolarization is the opening of voltage operated Ca^{2+} channels which exhibit fast kinetics, i.e. they open and let extracellular Ca^{2+} in the cytosol upon slight depolarization caused

by IP_3 induced Ca^{2+} release from SR. The major participant to the membrane repolarization, the K_{Ca} channels, are strongly dependent on cytosolic Ca^{2+} concentration, i.e. each BK_{Ca} channel requires binding of two Ca^{2+} ions to open and allow K^+ efflux, thus are known as delayed rectifiers. Th dependence of K_{Ca} on Ca^{2+} ions makes the membrane repolarization a slower process compared to the membrane depolarization.

Increasing $J_{PLC_{agonist}}$ increases the IP_3 induced Ca^{2+} release from SR, and also increases the subsequent J_{CICR}. The elevated availability of Ca^{2+} ions in the SMC cytosol increases the probability of opening of K_{Ca}(represented by state variable ω), thus enabling a relatively fast repolarization response. Increasing $J_{PLC_{agonist}}$ values further results in reaching an equilibrium state where the cytosolic Ca^{2+} availability has increased so much that the repolarization is simultaneous, thus eliminating the time difference between the two processes, hence no Ca^{2+} oscillation.

4.3 Ca^{2+} Dynamics of an Uncoupled Vascular EC

Unlike a vascular SMC, an EC is not an excitable cell. Following induced membrane depolarization or agonist stimulation, cytosolic Ca^{2+} concentration increases transiently but does not oscillate. A reason, for this inability of cytosolic Ca^{2+} to oscillate, could be the absence of high conductance VOCCs (such as L type channels) in the endothelial plasma membrane(Nilius and Droogmans, 2001).

Both P_2X and P_2Y receptors are expressed on the luminal side of the endothelial surface. P_2X allows influx of extracellular Ca^{2+} into the EC cytosol upon simultaneous activation by shear stress and ATP binding. P_2Y, however, is a G protein coupled receptor and is stimulated by a range of agonists including ATP. The agonist induced IP_3 generation following the agonist binding to the P_2Y receptor, causes IP_3 induced Ca^{2+} release from intracellular stores. This Ca^{2+} release and the subsequent Ca^{2+} induced Ca^{2+} release results in membrane depolarization and opening of a nonselective cation channel. An influx of monovalent and divalent cations from these channels (with the relative permeability P_{Na}:P_K:P_{Ca} (1:1:0.7)), allows further depolarization. In the presence of excess cytosolic Ca^{2+}, the Ca^{2+} activated K^+ channels (K_{Ca}) open and pump out K^+ to the extracellular space. Based

on their conductances, two types of vascular endothelial K_{Ca} have been characterized. $B_{K_{Ca}}$ or large conductance K_{Ca} have higher K^+ conductance (160-240 pS) than $S_{K_{Ca}}$, the small conductance K_{Ca} (10-40pS) (Ledoux et al., 2006; Nilius and Droogmans, 2001). Efflux of K^+ repolarizes the membrane potential which further becomes negative, upon loss of cytosolic Ca^{2+} via refilling of intracellular stores and efflux of Ca^{2+} via plasma membrane bound Ca^{2+} ATPase and Na/Ca exchanger. This excessively negative membrane potential is termed as hyperpolarization. Figure 4.7 provides a schematic of the cellular processes involved and their permissive or inhibitory effects on other intracellular or membrane bound processes.

Using the model described in Section 3.2.2 for an uncoupled EC the time course of the processes in Figure 4.7 can be analysed, following agonist stimulation, modelled by $\widetilde{J}_{PLC_{agonist}}$. Four state variable, cytosolic Ca^{2+}, ER Ca^{2+} , membrane potential and cytosolic IP_3 , are considered in the case of an EC. Figure 4.8 compares the cellular dynamics of an EC, stimulated with $\widetilde{J}_{PLC_{agonist}}$=0.1$\mu$M/s, at which the cytosolic Ca^{2+} concentration of a single SMC would oscillate. In the case of an EC, the cytosolic Ca^{2+} transiently increases following the IP_3 binding to IP_3R, followed by the CICR. This produces two rates of increase in cytosolic Ca^{2+} curve (as seen between 0 to 10 seconds and 10 and 40 seconds in Figure 4.8), first corresponding to the IP_3 induced Ca^{2+} release (J_{IP_3} in Figure 4.8 and the second corresponding to $\widetilde{J}_{CICR}$). With the increase in cytosolic Ca^{2+}, the K^+ efflux also increases, thereby hyperpolarizing the membrane potential to $\approx$-67.0 mV, which is more negative than the value attained by a SMC stimulated with the same agonist level. The hyperpolarized plasma membrane causes encourages replenishment of the ER luminal Ca^{2+} and extracellular Ca^{2+} influx through nonselective cation channels. Since the rate constants for $\widetilde{J}_{ER\ uptake}$ and $\widetilde{J}_{CICR}$are lowered for EC (in Table A.2) as compared those used for SMC (in Table A.1), the resulting time scales for the two expressions are so long that neither the membrane potential nor the cytosolic Ca^{2+} concentration, oscillates.

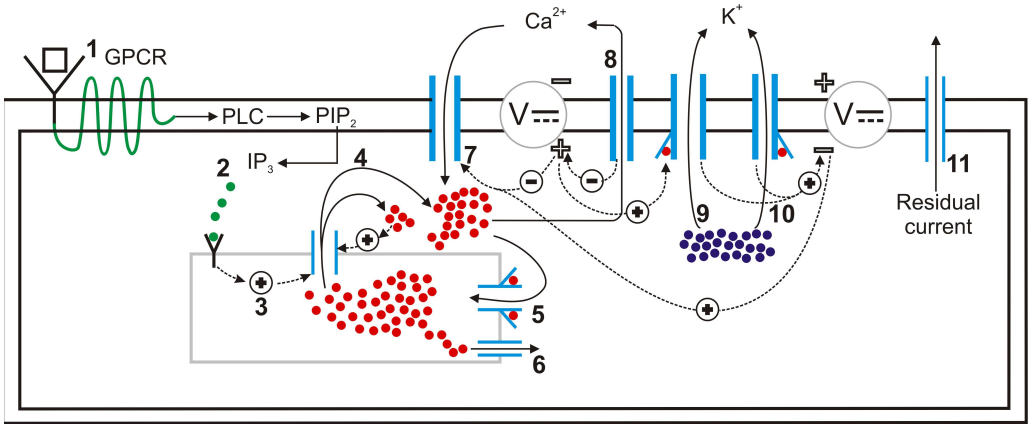

Figure 4.7: Schematic of an uncoupled EC showing cellular dynamical processes. (1)Agonist binds to the purinergic (P_2Y) receptors on the EC surface, activating the G protein coupled receptor (GPCR) which then activates membrane bound Phospholipase C (PLC). PLC activation allows phosphorylation of PIP_2, (2)PIP_2 gives rise to IP_3 that is then release in the intracellular space. This nascent IP_3 binds to IP_3 receptor (IP_3R) on the ER surface. (3)IP_3 bound IP_3R induce release of Ca^{2+} ions from the ER into the cytosol. (4) The Ca^{2+} release from intracellular store sensitizes the IP_3R further which releases more Ca^{2+} thus making a Ca^{2+} rich domain in the cytosol in both EC and SMC. The excess of intracellular Ca^{2+} depolarizes the membrane potential. (5) ER has low affinity binding sites on the cytosolic side of a channel which constitutes a pump called the SERCA pump. Cytosolic Ca^{2+} encourages the replenishment of the intracellular stores via this pathway. (6) Ca^{2+} leaks from ER consistently under concentration gradient between cytosolic and ER luminal Ca^{2+} and keeps the Ca^{2+} in equilibrium during non stimulated state of the cell. (7) The increase in cytosolic Ca^{2+} favours the influx of extracellular Ca^{2+} from nonselective cation channels. (8) CaATPase pumps out cytosolic Ca^{2+} to extracellular space. (9 and 10) In ECs activation of K_{Ca}, upon binding to Ca^{2+} ions intracellularly at $B_{K_{Ca}}$ and $S_{K_{Ca}}$, let K^+ move out of the cytosol. This hyperpolarizes the membrane potential. (11) Although K^+ efflux is the main repolarizing current, residual current (mainly consisting of monovalent ions) also contribute to membrane potential repolarization.

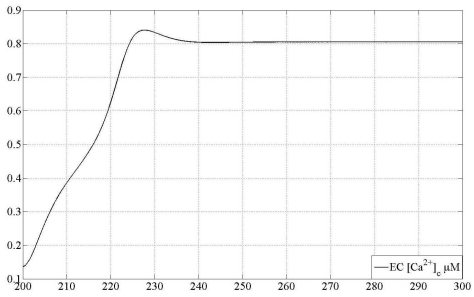

(a) Cytosolic Ca^{2+}

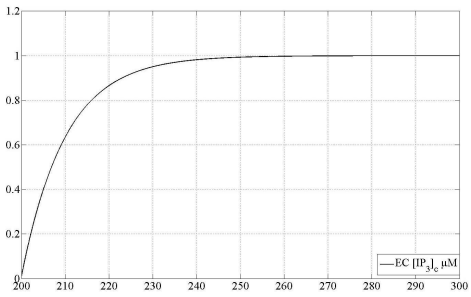

(b) Cytosolic IP_3

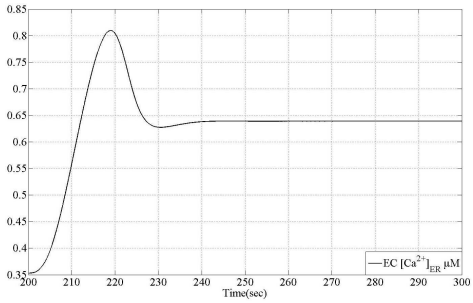

(c) ER Ca^{2+}

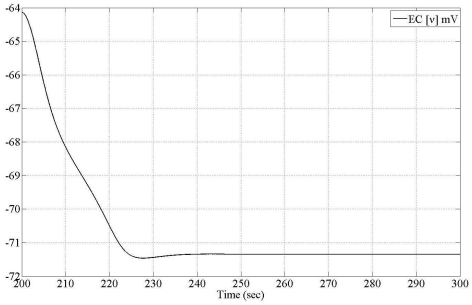

(d) Plasma membrane potential

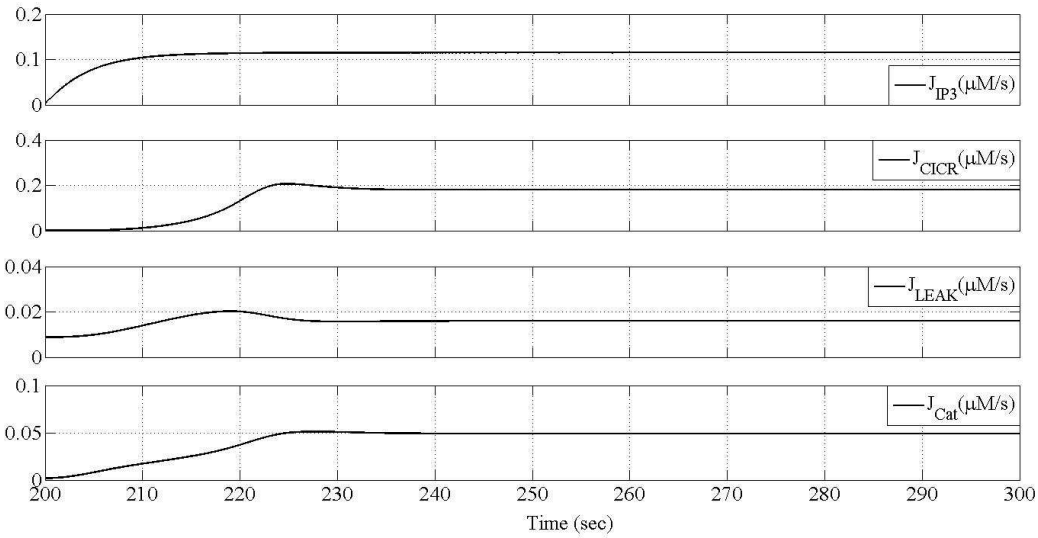

(e) Currents adding to cytosolic Ca^{2+}

Figure 4.8

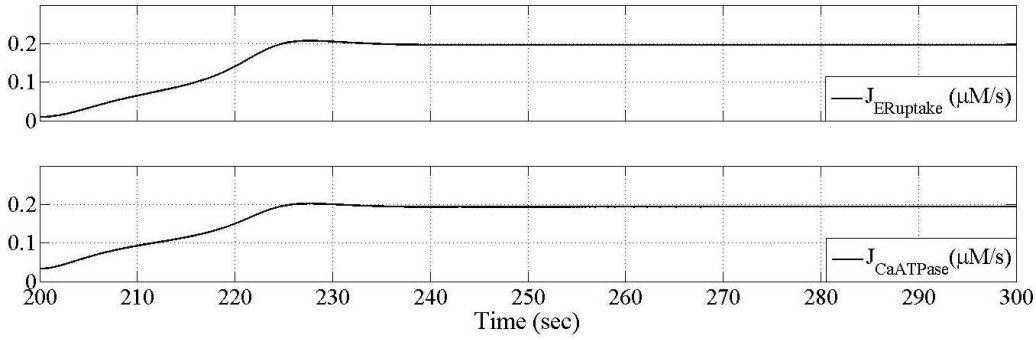

(f) Currents removing cytosolic Ca^{2+}

Figure 4.8: Time course of the state variables of an EC model, following the consistent stimulation of $\widetilde{J}_{PLC_{agonist}}$=0.1$\mu$M/s. Cytosolic Ca^{2+}increases on the expense of ER Ca^{2+}. Increase in cytosolic Ca^{2+} concentration coincides with hyperpolarization in membrane potential. Ionic currents responsible for increase in cytosolic Ca^{2+} are shown in (e) where as those removing it from the cytosol are in (f).

4.4 Agonist Effects on EC Cellular Dynamics

In Section 4.2 it was shown that the agonist stimulation produced an oscillatory Ca^{2+} response in a SMC in which amplitude and frequency of the oscillation were inversely related. In a single EC, the Ca^{2+} concentration does not oscillate at any agonist level. At any $\widetilde{J}_{PLC_{agonist}}$value, a Ca^{2+} transient is followed by a steady state equilibrium value, as shown in the Figure 4.9a. Both, the peak of the Ca^{2+} transient and the steady state equilibrium Ca^{2+} concentration initially increases with increase in $\widetilde{J}_{PLC_{agonist}}$. At relatively higher $\widetilde{J}_{PLC_{agonist}}$ (approximately at $\widetilde{J}_{PLC_{agonist}}$=0.160 μM/s onwards), this trend changes and the peak of Ca^{2+} transient and the steady state equilibrium concentration of the cytosolic Ca^{2+} starts to decrease. Figure 4.9b depicts these trends. With the increasing $\widetilde{J}_{PLC_{agonist}}$ values, the period of the transient, highlighted by the arrowheads in Figure 4.9a, decreases. This is because of the dependence of Ca^{2+} concentration on Ca^{2+} influx through nonselective cation channels, denoted as $\widetilde{J}_{cation}$ in the model.

The membrane potential hyperpolarization can be attributed to the involvement of the $B_{K_{Ca}}$ and $S_{K_{Ca}}$ channels. As equation 3.50 suggests, K^+ efflux through $B_{K_{Ca}}$ depends on both the cytosolic Ca^{2+} concentration and the membrane potential. Both, membrane depolarization and high cytosolic Ca^{2+} concentration favour

the K^+ efflux through the $B_{K_{Ca}}$ channels. The outward K^+ current through $B_{K_{Ca}}$ channels is more sensitive to membrane potential than the cytosolic Ca^{2+}. Two Ca^{2+} ions are required to bind the Ca^{2+} specific sites on the $B_{K_{Ca}}$ channel located on the intracellular face. Following the agonist stimulation and sudden increase in the cytosolic Ca^{2+}, this channel opens and repolarizes the membrane via K^+ efflux. Simultaneously, the Ca^{2+} removal takes place consistently via plasma membrane Ca^{2+} ATPase and refilling of SR. The progressive repolarization of membrane potential results in closure of the $B_{K_{Ca}}$ channels. Thus, although the conduction of these channels is large, the open time is not prolonged.

$S_{K_{Ca}}$ channels, which are sensitive to Ca^{2+} concentration such that higher Ca^{2+} concentration increases the K^+ efflux from these channels. This channel is kept open and $K^+$is pushed out constantly, so long as there are enough Ca^{2+} ions in the cytosol to activate its gates, irrespective of the state of the membrane potential. $S_{K_{Ca}}$ channels are, therefore, the source of hyperpolarization of membrane potential. The impact of the residual current, as expressed in the equation 3.49, is trivial on the total K^+ efflux.

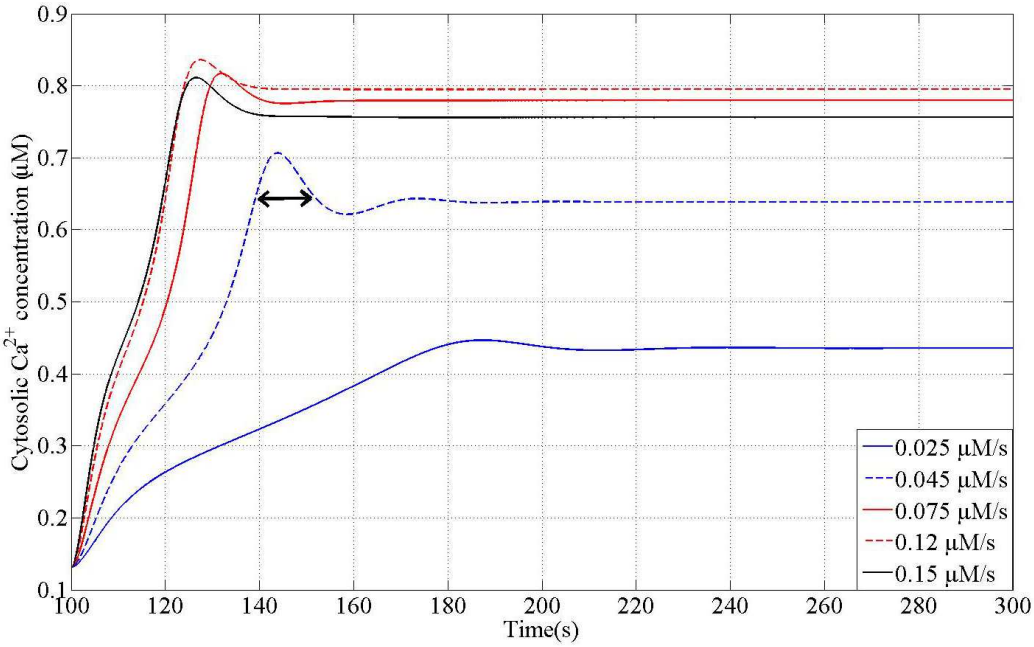

(a) Time course of cytosolic Ca^{2+} concentration at various $\widetilde{J}_{PLC_{agonist}}$.As the stimulation level increases, the peak transient Ca^{2+} first increases and then decreases. The period of the transient, highlighted by the arrowheads, decreases with increase in $\widetilde{J}_{PLC_{agonist}}$ value.

Figure 4.9

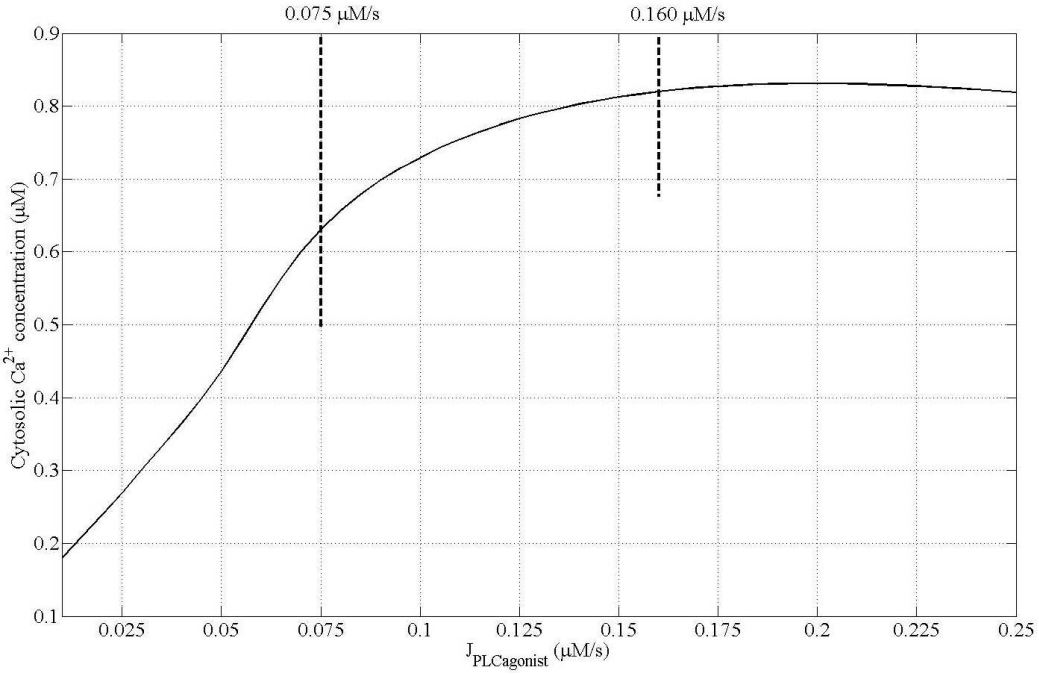

(b) Following the first Ca^{2+} transient, the cytosolic Ca^{2+} concentration attains an equilibrium state. The steady state equilibrium values are plotted against the $\widetilde{J}_{PLC_{agonist}}$ values. The dashed lines demarcate the $\widetilde{J}_{PLC_{agonist}}$ that corresponds to $J_{PLC_{agonist}}$ values in domain 2 of Figure 4.2a.

Figure 4.9: Eeffects of increasing $\widetilde{J}_{PLC_{agonist}}$ on the cytosolic Ca^{2+} response of an uncoupled EC.

Chapter 5

Computational Method and Ca^{2+} Dynamics of Coupled EC/SMC Model

Previously, the single cell models of a SMC and an EC, and their cellular dynamics were discussed. Anatomically, an EC and SMC which serve as structural building blocks of the vascular tissue are structurally interconnected through intercellular gap junctional. Cell cell contact is necessary for the formation of the gap junctional plaques. Specific proteins called connexins form the structural unit of a gap junction, a hemichannel or connexon, which traverses from the intracellular domain (golgi complex) into the plasma membrane domain of each apposing cell. When the two hemichannels come in contact, a process called 'docking', conformation changes occur in the constituent connexin protein and functional gap junction is formed. This gap junction allows passage of ions as well as neutral molecules of limited molecular weight (<1000 Da), including but not limited to Ca^{2+},Na^{+},K^{+},IP_3 etc. Three connexins (Cx37,Cx40 and Cx43) are commonly expressed in the human vasculature. The single channel gap junctional conductance varies with the constituent connexins and in most instances is voltage independent (Fall et al., 2002; Johnstone et al., 2009), although many new models are considering voltage dependent gating properties in modelling some heteromeric (having multiple connexin stoichiometry) gap junctions.

When modelling the gap junctions on a cell level, the net conductance can be represented by a constant which is equal to

mean number of open channels $\times$ *the single channel conductance.*

Two cytosolic oscillators of cells connected via intercellular gap junctions can synchronize by including a gap junctional current. Let us, for example, consider two cells idealized as isopotential(having uniform potential across the whole cell) compartments. For cell 1, the gap junctional current from cell 1 to cell 2 can be written as

$$I_{1,2} = -g_c(V_1 - V_2) \tag{5.1}$$

and for cell 2 it will be

$$I_{2,1} = -g_c(V_2 - V_1) \tag{5.2}$$

where g_c is the net conductance from all existing gap junction between the two cells and V_1 and V_2 are their membrane potentials, respectively. This current is added to the current balance equation for both the cells such that

$$C_m \frac{dV_1}{dt} = -I_{ion,1} + I_{1,2} \tag{5.3}$$

for cell 1 and

$$C_m \frac{dV_2}{dt} = -I_{ion,2} + I_{2,1} \tag{5.4}$$

for cell 2, where $I_{ion,1}$ is the sum of all transmembrane ionic currents in the i^{th} cell, and C_m is the cell membrane capacitance. As the direction of gap junctional transfer is from cell 1 to cell 2, the added term, $I_{1,2}$ will work as a sink in equation 5.3 and $I_{2,1}$ as source term in equation 5.4. Hence cell 1 and cell 2 are said to be *electrically coupled* (electrical being the medium of coupling as the quantity, the difference of which establishes the drive for the gap junctional current, is membrane potential V in this case). Subtracting equation 5.3 from 5.4 yields

$$\tau \frac{d(V_1 - V_2}{dt} \approx -(V_1 - V_2) \tag{5.5}$$

where $\tau = C_m/g_c$ is a time constant such that if cell 1 was perturbed (e.g. by

an exogenous current influx), the two oscillators will re-establish uniformity or synchronize with an effective time constant of τ. If after the perturbation, the two cells are such that $V_1 = V_2$, then the cells are said to be tightly or strongly coupled. For this to happen, g_c should be large. It g_c is small, i.e cells are weakly coupled then the response by the cellular oscillator, at best, can be antiphase, but not in phase (i.e $V_1 \neq V_2$ even after τ seconds).

5.1 Incorporation of intercellular coupling in single cell mathematical models

(Koenigsberger et al., 2005) models intercellular gap junctional coupling in the similar to the equation 5.1or 5.2. The media of coupling, however, are not limited to electrical coupling but Ca^{2+} and IP_3 coupling are also established between cells. This is because of the existence of Cx37, Cx40 and Cx43 gap junctions between the populations of ECs and SMCs and coupled EC SMC populations. There are two possible topologies of coupling between the two cells, homocellular and heterocellular coupling, as shown in Figure 5.1.

Cells are said to have homocellular coupling if the adjoining cell is of the same type i.e an EC coupled to another EC, or a SMC to another SMC. If an EC is coupled to a SMC or vice versa, it is termed as heterocellular coupling.

For n number of SMCs or ECs, each i^{th} cell is homocellularly coupled to a nearest neighbour k^{th} cell electrically by an expression modelled as

$$V^{\mathrm{SMC}\leftrightarrow\mathrm{SMC}} = -g\sum_{k}(v - v_k) \tag{5.6}$$

where $V^{\mathrm{SMC}\leftrightarrow\mathrm{SMC}}$ is the electrical coupling between an i^{th} and k^{th} SMC. g is the electrical coupling coefficient (equivalent to $1/\tau$) and is related to the net electrical coupling conductance G as $g = G/C_m$ with unit (s^{-1}), where C_m is the cell membrane capacitance of the coupled SMCs. v and v_k are the membrane potentials of the i^{th} and k^{th} neighbour SMC respectively. Similarly for an EC, the electrical

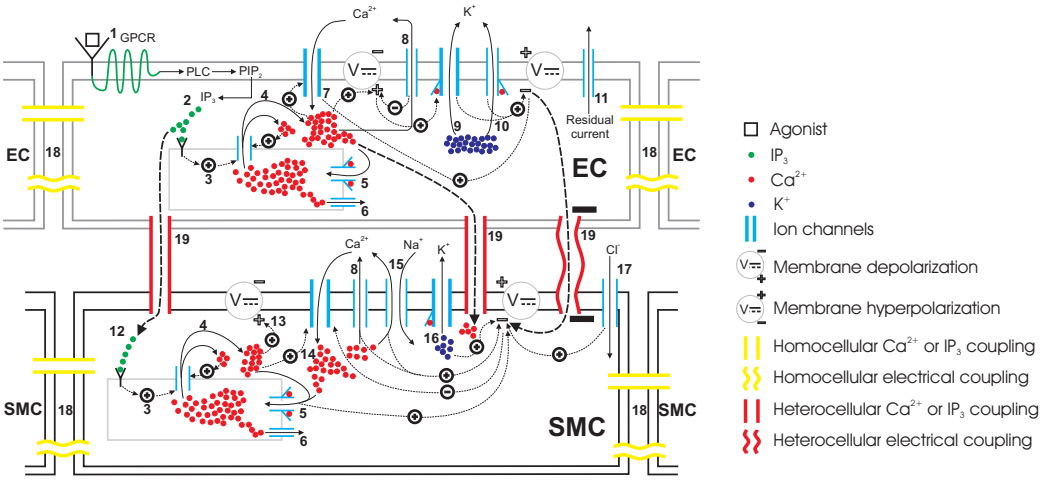

Figure 5.1: Schematic of a coupled EC and SMC showing Ca^{2+}, IP_3 and membrane potential dynamics. (1)Agonist binds to the purinergic (P2Y) receptors on the EC surface, activating the G protein coupled receptor (GPCR) which then activates membrane bound Phospholipase C (PLC). PLC activation allows phosphorylation of PIP2, (2)PIP2 gives rise to IP_3 that is then release in the intracellular space. This nascent IP_3 binds to IP_3 receptor (IP_3 R) on the ER/SR surface. (3)IP_3 bound IP_3 R induce release of Ca^{2+} ions from the ER/SR into the cytosol. (4) The Ca^{2+} release from intracellular store sensitizes the IP3R further which releases more Ca^{2+} thus making a Ca^{2+} rich domain in the cytosol in both EC and SMC. The excess of intracellular Ca^{2+} depolarizes the membrane potential. (5) ER/SR has low affinity binding sites on the cytosolic side of a channel which constitutes a pump called the SERCA pump. Cytosolic Ca^{2+} encourages the replenishment of the intracellular stores via this pathway. (6) Ca^{2+} leaks from ER/SR consistently under concentration gradient between cytosolic and SR/ER luminal Ca^{2+} and keeps the Ca^{2+} in equilibrium during non stimulated state of the cell. (7) In an EC, the cytosolic Ca^{2+} favours the influx of extracellular Ca^{2+} from nonselective cation channels. (8) CaATPase pushes out cytosolic Ca^{2+} to extracellular space. (9 and 10) In ECs activation of K_{Ca}, upon binding to Ca^{2+}ions intracellularly at BK_{Ca} and SK_{Ca}, let K^+ move out of the cytosol. This hyperpolarizes the membrane potential. (11) Although K^+ efflux is the main repolarizing current, residual current (mainly consisting of monovalent ions) also contribute to membrane potential repolarization. (12) The IP_3 concentration increases in SMC cytosol via transmission of IP_3 from coupled EC. This IP_3 attached to IP_3 R to activated downstream IP_3 induced Ca^{2+} release. (13) The IP_3 induced and CICR Ca^{2+} depolarizes the membrane potential. (14) The membrane depolarization result in the influx of Ca^{2+} from VOCCs which will close upon repolarization in the following steps. (15) Ca^{2+}, in addition to other pathways, is pushed out via Na/Ca exchanger. (16) Binding of Ca^{2+} ions to K_{Ca}opens BK_{Ca} channels in SMC causing K^+ efflux and membrane repolarization. (17) Influx of Cl^- ions add to the repolarization. (18) Medium for intercellular communication via homocellular gap junctions can either be Ca^{2+}, IP_3 or membrane potential coupling. (19)Heterocellular gap junctions can couple an EC and SMC via Ca^{2+}, IP_3 or membrane potential coupling. Hyperpolarized EC membrane potential can hyperpolarized SMC plasma membrane and consequently close VOCCs.

coupling to the ℓ^{th} EC neighbour is modelled by

$$V^{\mathrm{EC}\leftrightarrow\mathrm{EC}} = -\widetilde{g}\sum_{\ell}(\widetilde{v}-\widetilde{v}_{\ell}) \tag{5.7}$$

The values of C_m and $\widetilde{C}_m$ are taken as constant and are listed in Tables A.1 and A.2.

In addition to the electrical coupling, second messenger species such as Ca^{2+} (40 Da) and IP_3 ($\approx$ 220 Da) can also pass through the gap junctional pores.Homotypic (i.e whose hemichannels are made up of one connexin isoform) Cx40 gap junctions prefer the passage of Ca^{2+}, a divalent cation (Heyman et al., 2009) where as homotypic Cx43 gap junctions have large pores and are least charge selective of the three vascular connexins constituted gap junctions so they allow passage of IP_3 molecules, a bigger and charge neutral molecule(Harris, 2007). Although Cx43 gap junctions have low single channel conductance ($\approx$90pS) compared to the homotypic gap junctions formed of either Cx37 or Cx40 but the range of species that can pass through these pores is extended compared to the Cx37 and Cx43 gap junction, including Ca^{2+} ions and other monovalent molecules(Rackauskas et al., 2007b). Ca^{2+} and IP_3 coupling, driven by the concentration gradient between an i^{th} SMCs and a neighbouring coupled k^{th} SMC, is established by

$$J_{\mathrm{Ca}}^{\mathrm{SMC}\leftrightarrow\mathrm{SMC}} = -p_{\mathrm{Ca}}\sum_{k}(c-c_k) \tag{5.8}$$

$$J_{\mathrm{IP_3}}^{\mathrm{SMC}\leftrightarrow\mathrm{SMC}} = -p_{\mathrm{IP_3}}\sum_{k}(I-I_k) \tag{5.9}$$

where p_{Ca} and $p_{\mathrm{IP_3}}$ respectively are the Ca^{2+} and IP_3 coupling coefficients between SMCs. The c and c_k are the cytosolic Ca^{2+} concentrations and $I$and I_k are the cytosolic IP_3 concentrations in the i^{th} and the neighnouring k^{th} SMC. Similarly, intercellular Ca^{2+} and IP_3 fluxes between coupled i^{th} and the neighnouring ℓ^{th} ECs can be written as

$$J_{\mathrm{Ca}}^{\mathrm{EC}\leftrightarrow\mathrm{EC}} = -\widetilde{p}_{\mathrm{Ca}}\sum_{\ell}(\widetilde{c}-\widetilde{c}_{\ell}) \tag{5.10}$$

$$J_{\mathrm{IP_3}}^{\mathrm{EC}\leftrightarrow\mathrm{EC}} = -\widetilde{p}_{\mathrm{IP_3}}\sum_{\ell}(\widetilde{I}-\widetilde{I}_{\ell}) \tag{5.11}$$

To establish heterocellular coupling between an EC and SMC and vice versa, electrical, Ca^{2+} and IP_3 coupling are taken into account. From the physiological aspect, myoendothelial junctions exist in the intimal layer of the arterial tissue. Projections of EC plasma membrane protrude from the perforations present in the internal elastic lamina and come in close contact with te plasma membrane of the underlying SMCs (Sandow and Hill, 2000). Homotypic gap junctions consisting of Cx37, Cx40 and Cx43 hemichannels have been demonstrated in various vascular beds of a number of mammalian and human arterial tissues (Isakson and Duling, 2005; Lamboley et al., 2005) which lets second messengers (Ca^{2+} and IP_3) pass bidirectionally (i.e SMC to EC and vice versa). Therefore, heterocellular electrical, Ca^{2+} and IP_3 coupling from an i^{th} SMC to an n^{th} nearest neighbouring EC can be mathematically expressed respectively, as

$$J_{\mathrm{Ca}}^{\mathrm{SMC}\leftrightarrow\mathrm{EC}} = -P_{\mathrm{Ca}} \sum_{n} (c - \widetilde{c}_n) \tag{5.12}$$

$$V^{\mathrm{SMC}\leftrightarrow\mathrm{EC}} = -G \sum_{n} (v - \widetilde{v}_n) \tag{5.13}$$

$$J_{\mathrm{IP_3}}^{\mathrm{SMC}\leftrightarrow\mathrm{EC}} = -P_{\mathrm{IP_3}} \sum_{n} (I - \widetilde{I}_n) \tag{5.14}$$

Heterocellular coupling between an EC and nearest neighbouring m^{th} SMC can be written as

$$J_{\mathrm{Ca}}^{\mathrm{EC}\leftrightarrow\mathrm{SMC}} = -\widetilde{P}_{\mathrm{Ca}} \sum_{m} (\widetilde{c} - c_m) \tag{5.15}$$

$$V^{\mathrm{EC}\leftrightarrow\mathrm{SMC}} = -\widetilde{G} \sum_{m} (\widetilde{v} - v_m) \tag{5.16}$$

$$J_{\mathrm{IP_3}}^{\mathrm{EC}\leftrightarrow\mathrm{SMC}} = -\widetilde{P}_{\mathrm{IP_3}} \sum_{m} (\widetilde{I} - I_m) \tag{5.17}$$

5.2 Values for intercellular coupling coefficients

There is not much information available in the literature regarding the whole cell conductance or the mean number of formed channels on the surface of coupled cells compared to single channel conductance of homotypic gap junctions which is rather well documented. The reason behind this is the limitation of methodologies to do such experimentation. Furthermore, the expression of connexins differs *in vitro* in a dual voltage clamp experiments or even *in situ* methods when using arterial segment than *in vivo*. There is no suitable live cell or dynamic measurement technique available yet which can quantitate the number of formed gap junctions in a cell appropriately, either in ECs or SMCs, in a physiological environment. In the case of electrical coupling the macroscopic mean conductance G has been estimated by Van Rijen et al. (1997) to be 30nS whereas Lidington et al. (2000) estimated the macroscopic homocellular electrical resistance in ECs to be 3MΩ (or G=1/3MΩ = 333nS). For structural characterization or localization of the gap junction, Van Rijen et al. (1997) used staining (immunofluorescence) of human umbilical cord vein and artery endothelial cells, in situ and in vitro (cultured). For functional characterization, dye coupling using Lucifer Yellow was used. Double voltage patch clamp technique was used to measure the single gap junction conductance. Lidington et al. (2000) grew a monolayer of microvascular endothelial cells in vitro and mRNA and the connexins expressions were tested for presence. This was validated by the immunocytochemistry for the gap junctions. For evaluating functional cell coupling, hyperpolarization current was injected in a cell on one side of the monolayer and recorded on the other extremity. Bessel function was used to predict the spread of electronic signal and intercellular resistance was computed using the recording of the propagated currents.

As $g = G/C_m$, Van Rijen et al. (1997) results yield a g, one order of magnitude less than achieved by using Lidington et al. (2000) evaluation of G. Therefore in the interest of coherent use of the parameters G=30nS is used here, also chosen by (Koenigsberger et al., 2005). The membrane capacitance value between ECs is ≈ 30pF (Schuster et al., 2003) and for SMCs it is 10pF (Parthimos et al., 1999). Thus, for homocellular electrical coupling between SMCs, (Yamamoto et al., 2001) calculated the macroscopic gap junctional resistance of 90MΩ (or

G=1/90MΩ = 11nS). Therefore the value of homocellular electrical coupling coefficients g and $\widetilde{g}$, for SMC and EC respectively, is $1000s^{-1}$.

Although there has been some information on the single channel conductance of Cx40 and Cx43 formed gap junctions, to the best of our knowledge the information on a cell's macroscopic or net conductance of intercellular Ca^{2+} and IP_3 transfer is not available. (Koenigsberger et al., 2006) treat these values as free parameters and set the coefficients such that homocellular Ca^{2+} coupling between SMCs is able to synchronize the Ca^{2+} oscillations of five coupled SMCs in conjunction with the electrical coupling. SMCs are essentially, weakly coupled, p_{Ca} set to 0.05. EC homocellular Ca^{2+} coupling coefficient, $\widetilde{p}_{Ca}$ has also been set to 0.05.

For heterocellular coupling, ECs and SMCs are coupled via the same three media. Macroscopic intercellular resistance across myoendothelial junction has been estimated by (Yamamoto et al., 2001) to 900MΩ, with the net capacitance between the two cells being ≈20pF, therefore making the heterocellular electrical coupling coefficient $50s^{-1}$. For Ca^{2+} and IP_3 transport across myoendothelial junction, information on permeability is scarce and (Koenigsberger et al., 2005) set coupling coefficient to $0.05s^{-1}$ for Ca^{2+} and IP_3 . (Kapela et al., 2009) reduce the heterocellular IP_3 coupling coefficient by dividing it with the number of heterocellular nearest neighbours coupled to an EC or SMC. This argument is plausible and same logic may apply to heterocellular Ca^{2+} coupling. In the latter chapters, we test the effects of weakening the heterocellular coupling strength between ECs and SMCs according to the number of nearest neighbours coupled to each cell of each type. Other studies such as (Jacobsen et al., 2007) modelled the gap junction current as a function of the effective contact surface area, the ion specific permeability (distinguished by its valency) and the membrane potential difference between the two cell. This study confines to having static gap junction coupling coefficients as the first step towards understanding the dynamics of the response of the coupled cell however the dynamic aspects introduced by (Jacobsen et al., 2007) can be incorporated in the future work.

5.3 Coupling topology

The layout of the cells in the anatomical layer, tunica intima, of an artery dictates the intercellular coupling topology of each cell, i.e the number of homocellular and heterocellular nearest neighbours and their locations. In the present study, SMCs or ECs are homocellularly coupled in Van Neumann's nearest neighbour topology with a range 1. Therefore, each cell, EC or SMC, is coupled homocellularly with 4 other nearest neighbours cells of the same type, as shown in Figure 5.2.

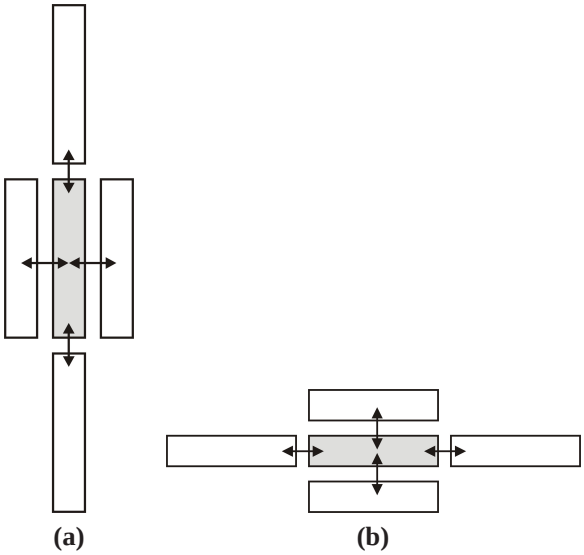

Figure 5.2: Topology for computationally interconnecting SMC-SMC in (a) and EC-EC in (b) via homocellular coupling.

Anatomically, an endothelial cell, while stretched under flow conditions, lies longitudinally or parallel to the axis of the artery. A SMC, on the other hand, lies circumferentially, wrapping the artery around its longitudinal axis. An endothelial cells is $\approx$ 50-141μm long and 5-10μm wide (Haas and Duling, 1997; Sandow and Hill, 2000; Sandow et al., 2003). A SMC is $\approx$ 50-100μm long (based on the state of their contractililty, either contracted or relaxed) and 2-8μm wide (Haas and Duling, 1997; Sandow and Hill, 2000). In the present case the the aspect ratio of the two cells is set such that an EC is approximately 1.3 times as long and twice as wide as a SMC. The cells are approximated as a rectangle and with the

aspect ratio set above, 13 SMC are coupled to one EC longitudinally and 5 ECs are coupled to one SMC circumferentially via heterocellular coupling. Figure 5.3 depicts a single block of coupled ECs and SMCs which is creates a unit segment which can be extended longitudinally as well as circumferentially for a longer or thicker arterial segment. Cells on the circumferential boundaries are periodically coupled to simulate a closed arterial loop circumferentially. This enables the computation algorithm to implement spatial gradients of agonist stimulus not only in the longitudinal direction but also in circumferential direction.

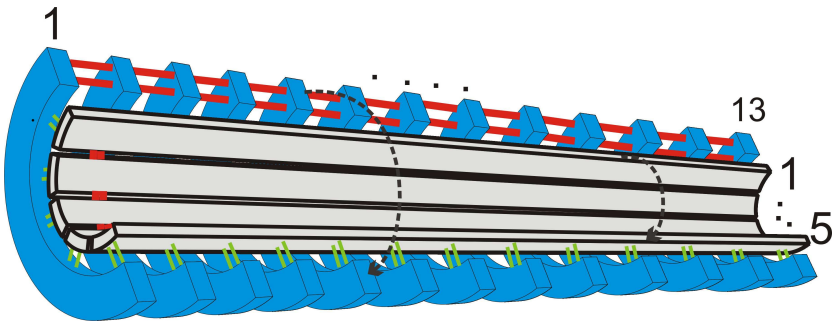

Figure 5.3: 1 EC long coupled block of cells with 13 SMCs longitudinally coupled to an EC and 5 ECs circumferentially coupled to 1 SMC. The arrow (with dashed black line) depicts the homocellular periodic coupling of SMCs or ECs situated on boundary. C shaped arcs in blue are SMCs wrapping around, the rectangular slab like structures in grey, the ECs. The red interconnections represent homocellular couple and the green ones represent the heterocellular coupling. For simulating a wider diameter, the number of cells will increase circumferentially, however, the nearest neighbour number of each cell type will remain conserved (i.e. 1 EC coupled to 13 SMCs longitudinally and 1 SMC coupled to 5 ECs circumferentially).

5.4 Numerical Algorithm

A structured C program uses the basic computational infrastructure, described in Section 3.4, to numerically integrate the intercellular dynamics of each constituent cell of a coupled population of ECs and SMCs. Based on the user defined length and diameter of the desired arterial segment, the algorithm generates two Cartesian grids, one for ECs and SMCs each. Each element of the grid is a cell.

Each cell is defined as a structure with members including the information of the row and column, the boundary tag, the place holders for the state variables and transmembrane ionic and gap junctional currents, and in the case of EC, the local values of the stimulus, i.e. $J_{PLC_{agonist}}$. the boundary tag is an identifier for each cell encoding the information about where the cell resides in the Cartesian grid. Figure 5.4 shows the possible boundary tags and the locations of the cells identified by them. The boundary tags help identify how many nearest neighbours a cell will have. Corner cells will couple to only two nearest neighbours. Cells in color coded in red and blue will have 3 nearest neighbours. The cells color coded with green and yellow have four nearest neighbours such. Each cell at j^{th} column of the green row couples to the cell at j^{th} column of the yellow row. This creates the periodic boundary condition and the vessel is a closed loop, circumferentially. All the cells in grey, in Figure 5.4 are coupled in the same way as in Figure 5.2.

5.4.1 Non-reflective boundary conditions

At $J_{PLC_{agonist}}$ values in domain 2 of Figure 4.2a, the cytosolic Ca^{2+} concentration of a SMC oscillates. The frequency of these oscillations depends on the value of the $J_{PLC_{agonist}}$ stimulating the SMC. For a population of homocellularly coupled SMCs in a longitudinal setting, the oscillation may be reflected back into the computational domain. This reflection can be caused by the cells at the boundaries, (tagged 1,2,3 and 4,5,6 of Figure 5.4) as they have no adjacent cell to couple to (see cation of Figure 5.4 for description of boundary tags). A boundary condition is therefore required which can safely lets the oscillations exit the computational domain. To this end, these boundary cells have been made sinks such that the flux from them to a preceding cell in the longitudinal direction is zero. Thus, if I_{couple} is the gap junctional flux form a $cell_{(i,j)}$ with boundary tag 3, to the $cell_{(i,j-1)}$ with boundary tag 9 then

$$\frac{dI_{couple}}{dt} = 0 \tag{5.18}$$

Thus, $cell_{(i,j-1)}$ will always be a source for the coupling boundary cell and this is shown by the unidirectional black arrows in Figure 5.4. Same rule applies to the EC Cartesian grid in the longitudinal/axial direction. At the compilation stage of the results, these boundary cells with tags 1 to 6 are discarded and only the cells

with boundary tag 9 is written into the files containing the results.

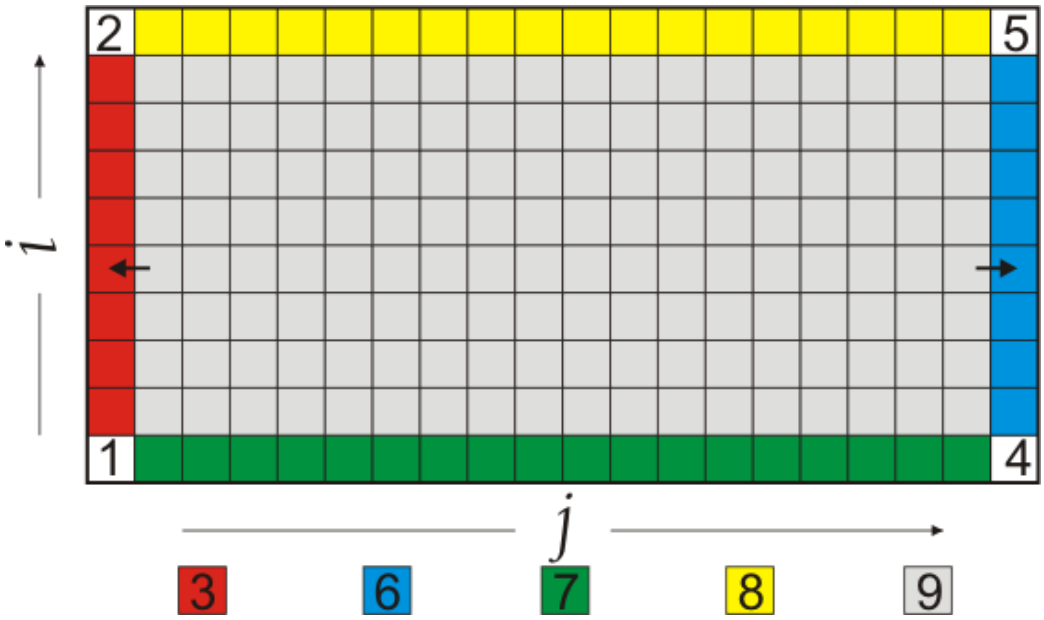

Figure 5.4: Homogeneous populations of either ECs or SMCs are set in a Cartesian grid. Each element of the grid is a structure containing relevant information for that cell regarding its location, the state variables, arrays for transmembrane ionic and coupling currents, the boundary tag, and the local stimulus value in the case of an EC. The cells at the boundaries are tagged with boundaries identifiers. 1,2,4 and 5 means that a cell (i,j) is a at one of the four corners of the Cartesian grid. Tags for other color codes are shown at the bottom of the grid. Red and blue cells are tagged as 3 and 6 respectively whereas green and yellow color code the cells with boundary tags 7 and 8 respectively. The cells belonging to the interior of the grid, colored grey, are all tagged as 9. Notice that the corners cells communicate with only two nearest neighbours, whereas either 3 or 6 communicate with a maximum of three nearest neighbours. Cells with tags 7 and 8 are coupled to four nearest neighbours such that a cell with tag 7 has its forth nearest neighbouring cell with tag 8 and vice versa. This creates the periodic boundary condition.

5.4.2 Solving Coupled Cells Model with RKSUITE

After demarcating the boundaries of the computational domain, RKSUITE is called to solve the system of coupled ODEs. The basic procedure of this call has been discussed previously in Section 3.4 for a single cell model and Figure 5.5 is

a schematic representation of the implementation of the algorithm for the system of coupled ODEs. The solution vector used by the RKSUITE is a 1D array of type *double* and it can hold as large a number of elements as the memory of the computing platform can accommodate. The vector length is the total number of equations *neq*, or **total number of state variables of SMC population + total number of state variables of EC population.** The relative and absolute tolerances are set to $1e^{-4}$ for enhancing the accuracy for the case of simulating coupled cells. The compute time for solving the computational domain depends on the size of the domain (i.e the cell load) and the spatial profile of the agonist concentration. Excessively high tolerance values may also result in longer compute time due to unnecessary addition of compute cycles, without any notable change in accuracy. Figure 5.6 relates the increase in compute time with the increasing computational load (i.e total number of cells).

Noteworthy is the asymptotic increase in the compute time as the payload or number of cells in the computational domain, increase. In the case of serial execution on one processor of *p5 575* is able to simulate a computational domain consisting of 1000 cells (ECs+SMCs) acceptably quickly. A computational domain of 1000 cells will have 18500 ODE to solve. Thus cell load is a bottle neck when executing the application on a serial platform. Other means such as multithreading will can be employed to reduce the compute time but the results may still be insufficiently satisfying when the goal is to simulate very large populations of coupled cells. The is due to the inherent dependencies of the functions evident in the Figure 5.5 where the core body of the program computing the single cell and coupling fluxes at each time step, are not mutually exclusive. This implies that no threads can be initiated to solve these two functions simultaneously. The significance of these two functions in terms of the contribution towards compute time has been highlighted in Figure 5.7, which shows that most of the compute time is spent in these two function while solving the computational domain for 100 real time seconds. Following the hierarchy, each function call made to *computeDerivatives* by the RKSUITE, is followed by a call to the function *single cell* and *coupling* successively. This can be confirm by comparing the number of calls in the Figure 5.7. Each call to *single cell* and a subsequent call to the function *coupling* results in the evaluation of ionic current for each cell, followed by the

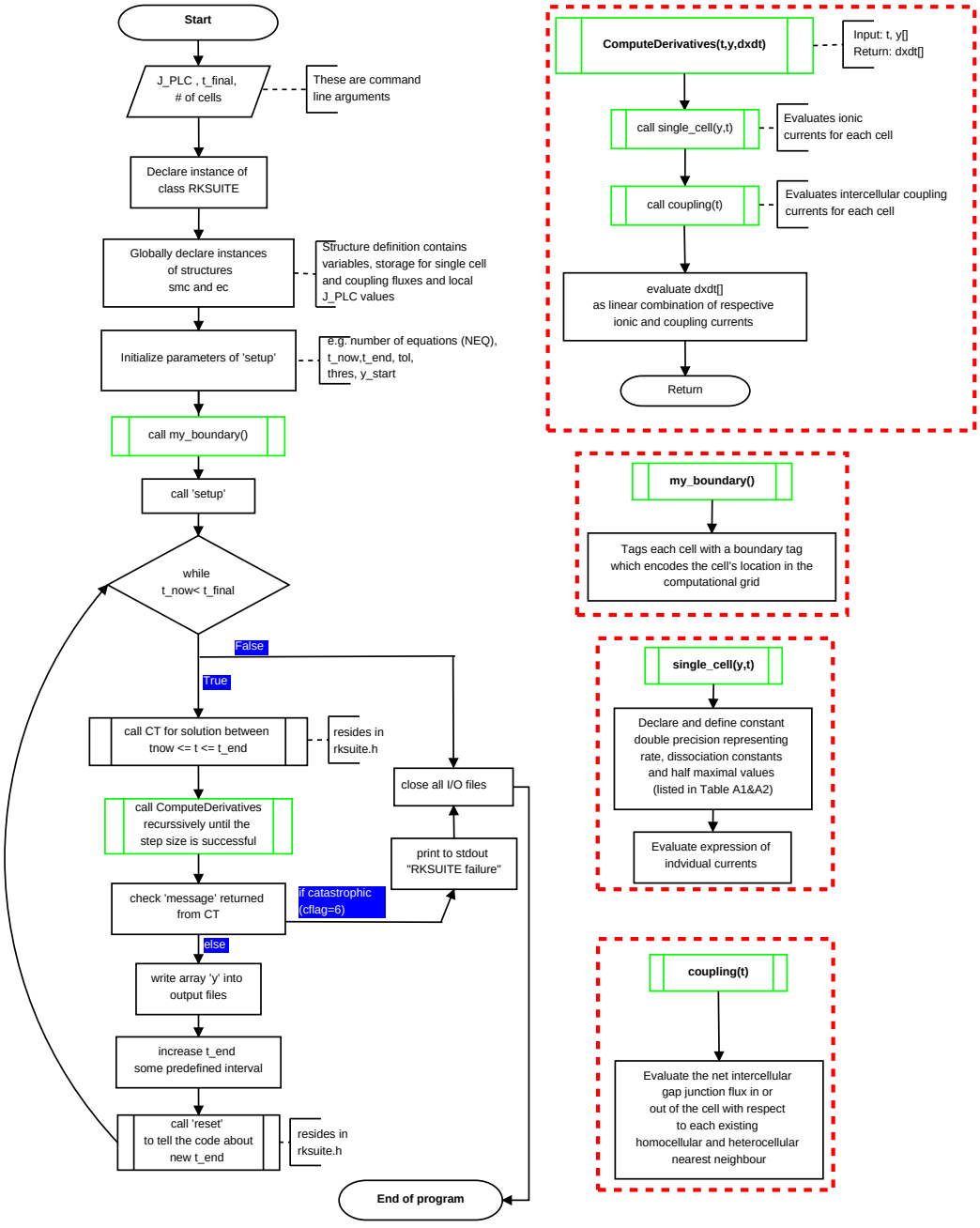

Figure 5.5: Execution of C code for solving coupled systems of ODEs for cells in populations of SMCs and ECs interconnected with intercellular specie and electrical coupling.

evaluation of the respective coupling currents, which makes these two functions computationally expensive.

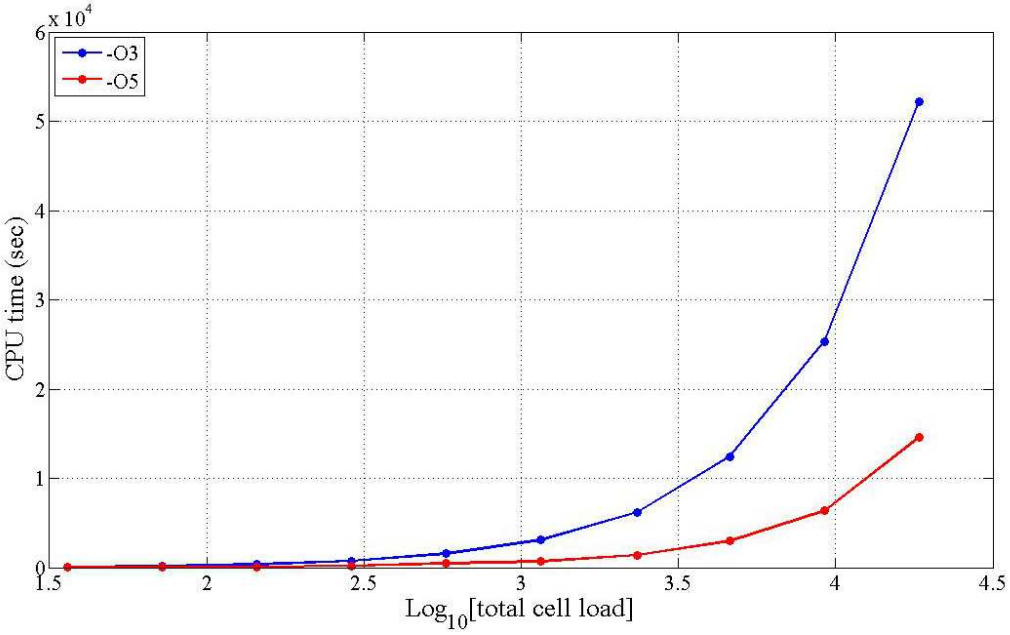

Figure 5.6: Figure shows CPU time versus the size of the computational domain in terms of cell load. The execution time increases after a cell load of $\approx$ 1000 cells is reached. A comparison between low level (-O3) and highest level (-O5) compiler optimization shows the reduction in the compute time. The simulations were executed on a single core (processor) of IBM *p5 575* system.

Another method of speeding up the execution is using a code optimization option that comes with most of the standard compilers. In the present case IBM's **XL C** , an C++ compiler for AIX or Linux operating systems, is used to compile the code. Depending on the level of the optimization chosen, the compiler can apply changes to memory management and consider architecture specific parameters (on which the program is being compiled) to maximize the use of resources, while compile the code. Figure 5.6 shows the effect of selecting increasing levels of code optimizations performed by the compiler.

ngranularity: Each sample hit covers 4 bytes. Time: 77.39 seconds

% time	cumulative seconds	self seconds	calls	self ms/call	total ms/call	name
21.4	16.57	16.57	1451156	0.01	0.01	.coupling [8]
18.5	30.90	14.33	224437	0.06	0.24	.step__7RKSUITEFPFdPdT2_vidPdN24T3RdN34T8bT3T4Rb [6]
12.9	54.02	10.02	1451156	0.01	0.01	.single_cell [9]
4.4	57.43	3.41	224437	0.02	0.02	.stepb__7RKSUITEFiPdT2dN32RdbT2 [11]
4.3	60.79	3.36	1451156	0.00	0.02	.computeDerivatives__FdPdT2 [7]
3.4	63.41	2.62				._log10 [12]
3.0	65.75	2.35	155094255	0.00	0.00	.max__FdT1 [13]
2.5	67.66	1.91				._exp [14]
2.3	69.47	1.81	72557800	0.00	0.00	.log10__Fd [16]
			. . .			
0.0	77.39	0.00	1	0.00	0.00	.tie__Q3_3std7_LFS_O.....XTw__ [445]

(a)

Figure 5.7

ngranularity: Each sample hit covers 4 bytes. Time: 6.81 seconds

% time	cumulative seconds	self seconds	calls	self ms/call	total ms/call	name
19.7	1.34	1.34	519068	0.00	0.00	.coupling [7]
18.5	2.60	1.26	77231	0.02	0.05	.step__7RKSUITEFPFdPdT2_vidPdN24T3RdN34T8bT3T4Rb [5]
16.2	3.70	1.10	519068	0.00	0.00	.single_cell [9]
16.2	4.80	1.10				.__vrec_GR_ [8]
8.1	5.35	0.55				.__vexp_GR [10]
6.0	5.76	0.41	519068	0.00	0.01	.@3@computeDerivatives__FdPdT2 [6]
4.6	6.07	0.31				___xl_tanh [13]
3.5	6.31	0.24				.log10 [14]
3.2	6.53	0.22	9896	0.02	0.04	.formi__7RKSUITEFPFdPdT2_viT2PdN44bN24 [12]
1.2	6.72	0.08	51596	0.00	0.08	.ct__7RKSUITEFPFdPdT2_vRdPdN23Ri [4]
			. . .			
0.0	6.81	0.00	1	0.00	0.00	.tie__Q3_3std7_LFS_...XTw__ [417]

(b)

Figure 5.7: Callgraphs showing the computationally expensive functions in the two cases of code optimization (-O3 and -O5) by the compiler. Functions highlighted in yellow are related to the main program, green called by the class instance RKSUITE, and those highlighted by light blue are math functions listed in math.h, called by other external functions iteratively. In both callgraphs, the function *coupling* and *single cell* are two of the three most expensive functions. Notice that the number of calls to the functions *computeDerivatives*, *single cell* and *coupling* are same in both cases, with or without optimization. The time, however, accounted for by the calling function (denoted by *self seconds*) shows that most of the total time is spent in either the function *coupling* or *single cell*, both of which are called by the function *computeDerivatives*.

Although the reduction in execution time is significant, it increases as a function of number of cells in the same manner. Other methods that may speedup the execution time of the code are, compiling with math.h and memory management libraries specifically designed for the machine architecture on which the code is to execute.

Also, the implementation of spatial non-uniformity in the agonist stimulation will result in the solver taking smaller steps because of the increased computational complexity. The reason for the increase in complexity is the contribution of gap junctional current from neighbouring cells which is updated and taken into account at each time step. A more innovative solution to this problem is discussed in the next chapter.

5.5 Cellular Dynamics in Coupled ECs/SMCs

In Chapters 3&4 the cellular dynamics of a single, uncoupled, SMC and EC were discussed. The aim was to understand how the dynamical state variables interacted with each other and result in a time course of intracellular Ca^{2+} dynamics that is agonist level dependent. In this section, the focus is upon the Ca^{2+} dynamics of cells when coupled to their nearest neighbours via homocellular and/or heterocellular coupling. Small homocellular populations of SMCs and ECs are coupled as a first step to investigate how homocellular coupling can affect the cellular dynamics in each cell type. Later, single SMC is coupled to an EC for studying the effects of heterocellular coupling.

5.5.1 Homocellular SMC coupling effects

Physiologically, intercellular gap junctional plaques can be found between vascular SMCs. To incorporate such homocellular coupling in the present computational environment, intercellular coupling is modelled by the equations 5.6, 5.8 and 5.9, for membrane potential, Ca^{2+} and IP_3 homocellular coupling. To understand how cellular dynamics evolve upon agonist stimulation, cells are coupled in the manner shown in Figure 5.8. SMC or EC, shaded in grey, is stimulated with $J_{PLC_{agonist}}$=0.1 μM/s, from 100-200 seconds of the total 300 second simulation,

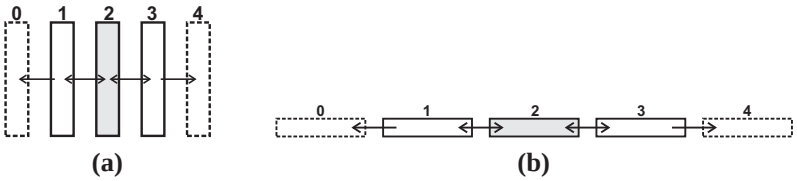

Figure 5.8: SMCs (a) and ECs (b) are connected via homocellular coupling. The cells on the extremities (drawn in dashed line) serve as permanent sinks to make the computational domain non-reflective and are not included in the results presented in later figures. Cells may exchange current information about membrane potential, Ca^{2+} and IP_3 .

whereas other adjoining cells are at $J_{PLC_{agonist}}$=0.01μM/s over the whole duration. Cells on either ends, in both the computational grids, are coupled to their nearest neighbours as sinks and are neglected while analysing the results. Figure 5.9 shows the time evolution of cytosolic Ca^{2+} concentration and the membrane potential of three SMCs demarcated by solid lines in Figure 5.8.

Four intercellular coupling cases are considered to see how enabling different coupling media affect the Ca^{2+} dynamics of these three cells. In the first case, Figure 5.9a, the intercellular coupling between the SMCs is completely disabled, i.e. the cells are uncoupled. Only in Cell 2 (in blue) the Ca^{2+} concentration oscillates upon stimulation (between 100 and 200 seconds) compared to the adjacent cells 1 and 3 in which the Ca^{2+} concentration takes a low steady state value. The corresponding membrane potentials depicts similar responses. For cell 2 the membrane potential oscillates while it is at steady state for the other two adjacent cells. In comparison, in the second case where the SMCs are coupled via the membrane potential only, oscillations in the Ca^{2+} concentration concentration occur in all cells, as shown in Figure 5.9b. On close inspection, the Ca^{2+} oscillations in the stimulated cell (cell2 in blue) and the two adjacent cells (cells 1 & 3 in red and green respectively) are antiphase. When compared to the no coupling case in Figure 5.9a, the frequency of oscillations has increased and the magnitude has decreased, except for the first transient which is larger than that in Figure 5.9a for cell 2. Unlike, the Ca^{2+} oscillations, the membrane potential oscillations of all three SMCs are synchronized and have identical magnitude. Also, unlike Figure 5.9a where cells were uncoupled, the peak to peak voltage of the oscillating

membrane potential of cell 2 is more positive. Therefore, by establishing the electrical coupling between SMCs, the membrane potential is *strongly* coupled, while the Ca^{2+} concentration is *weakly* coupled.

Upon enabling the Ca^{2+} coupling in Figure 5.9c, along with the electrical coupling, the oscillating Ca^{2+} concentration in the three SMCs attain similar peak to peak magnitude while the DC component of the cell 2 remains approximately at higher offset, similar to the Ca^{2+} concentration in Figure 5.9b. The membrane potential, in the present case, remains synchronous with a peak to peak voltage which is relatively smaller the previous case in Figure 5.9b,. Thus the addition of Ca^{2+} coupling strengthens the overall synchrony of the cells. In Figure 5.9d, SMCs are coupled via IP_3 in addition to electrical and Ca^{2+} coupling which does not produce any significant difference in the response than that seen in Figure 5.9c.

In Figure 5.9b, in the case of membrane potential coupling alone, the steady state oscillations are attained at $t=125$ seconds and the frequency of oscillations becomes more stable. Inclusion of Ca^{2+} and IP_3 coupling Figures 5.9c & d results in attaining the steady state response with a delay as opposed to the membrane potential coupling alone. In Figures 5.9c & d, the transient response ends at approximately $t=150$ seconds and steady state oscillations are observed beyond this time point. This is due to the selection of low Ca^{2+} and IP_3 coupling coefficients (listed in Tables A.1 & A.2)which establish weak species coupling environments.

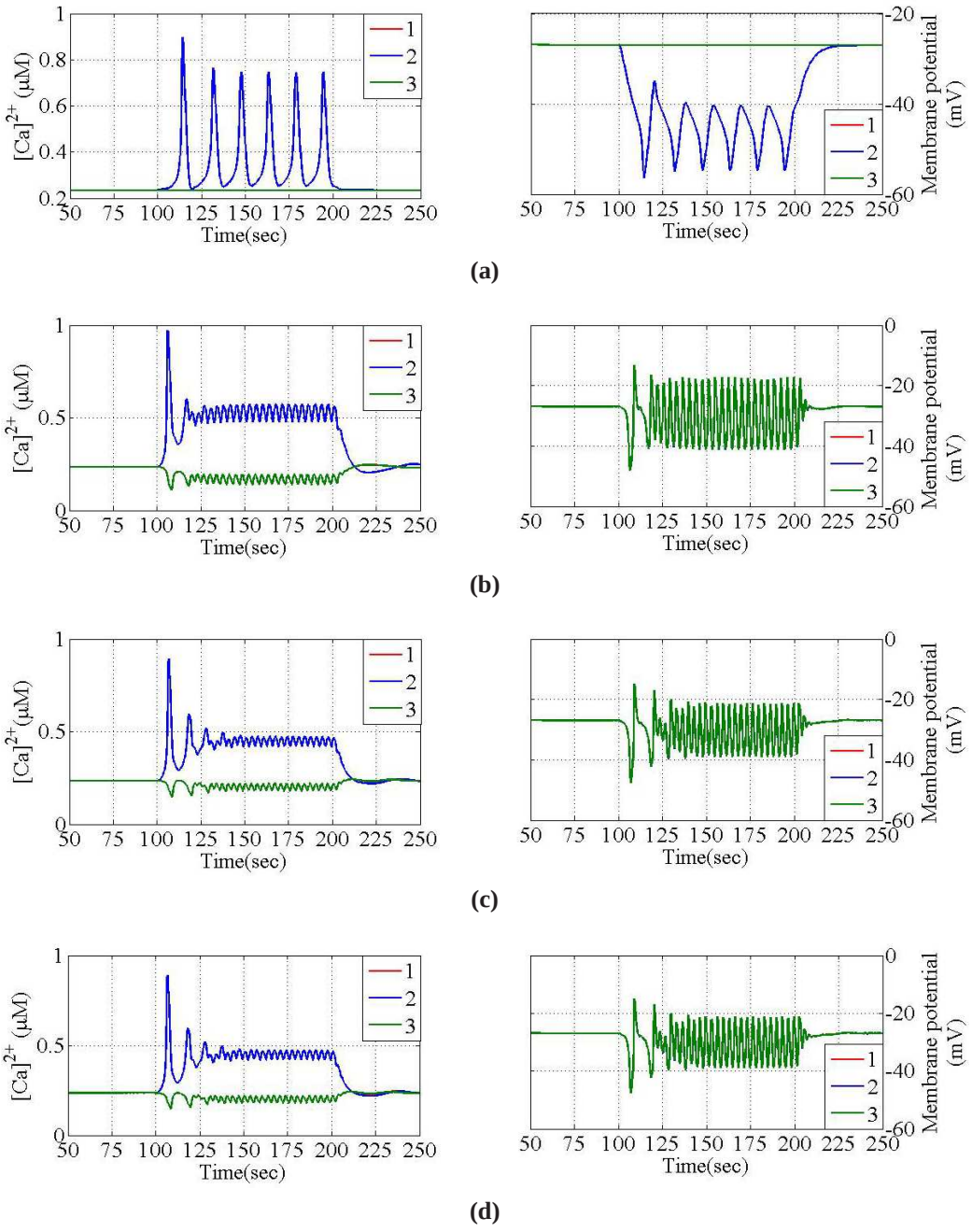

Figure 5.9: An array of homocellular coupled 5 SMCs , as shown in Figure 5.8a (cells on the flanks not shown in the results) was simulated for 300 real time seconds, stimulated with $J_{PLC_{agonist}}$=0.01μM/s over this time span. Cell 2 (shaded in gray in Figure 5.8a) was stimulated with $J_{PLC_{agonist}}$=0.1 μM/s from 100 to 200 seconds. Four modes of intercellular coupling were implemented, (a) no coupling, (b) electrical coupling, (c) electrical and Ca^{2+} coupling, and (d) electrical, Ca^{2+} and IP_3 coupling.

5.5.2 Homocellular EC coupling effects

Similar to the homocellular coupled SMCs, a population of 5 ECs, as shown in Figure 5.8b, is simulated for 300 seconds, with $\widetilde{J}_{PLC_{agonist}}$=0.01$\mu$M/s. Again, cell 2 of Figure 5.8b is stimulated with $\widetilde{J}_{PLC_{agonist}}$=0.1 μM/s from 100 to 200 seconds. To incorporate the homocellular coupling between ECs, the equations 5.7, 5.10 and 5.11, modelling membrane potential, Ca^{2+} and IP_3 homocellular exchange. In the Figure 5.10a, with no intercellular coupling, the cytosolic Ca^{2+} concentration in the stimulated EC rises to a higher value in response to the step increase in $\widetilde{J}_{PLC_{agonist}}$ from 0.01 μM/s to 0.1 μM/s. The membrane potential hyperpolarizes with increasing cytosolic Ca^{2+} concentration, while the adjacent cells 1 & 3 continue to retain a steady state value of more positive membrane potential and low Ca^{2+} concentration. Enabling electrical coupling between ECs, the membrane potential of the cells tends to synchronizes, as shown in Figure 5.10b. Because of the coupling, the more positive membrane potential of the adjacent cells 1 & 3, influence the hyperpolarized membrane potential of cell 2 and makes it slightly positive. The Ca^{2+} concentration, however, remains unaffected by the homocellular electrical coupling.

With Ca^{2+} coupling switched on, the Ca^{2+} concentration of the coupled ECs also tends to synchronize, as shown in Figure 5.10c. Upon stimulation of cell 2 with increased $\widetilde{J}_{PLC_{agonist}}$ at the 100 second mark, the Ca^{2+} concentration increases in the three ECs with a transient increaser in the Ca^{2+} concentration at first, and then assuming a steady state. The magnitudes however of the Ca^{2+} concentration in the EC, directly stimulated is higher then the and the adjacent ECs 1 & 3. No significant change between membrane potentials, in the presence or absence of Ca^{2+} coupling, is evident, except for the hyperpolarizing transients around the 100 second mark, which correspond to the transient increase in Ca^{2+} concentration around that time stamp. Intercellular exchange of Ca^{2+} enables the CICR and the successive refilling of ER stores, which makes up this Ca^{2+} transient in each EC.

In addition to the electrical and Ca^{2+} couplings, IP_3 coupling is also enabled and results shown in Figure 5.10d. Contribution of IP_3 from EC 2 to ECs 1 & 3 aids in increasing the cytosolic Ca^{2+} concentration by adding Ca^{2+} the IP_3 induced Ca^{2+} release from the ER or $\widetilde{J}_{IP_3}$, to the cytosol. The membrane potential also

follows the same pattern and becomes relative more negative because of the added cytosolic Ca^{2+}, as compared to either Figure 5.10b or c.

Conclusively, in the case of ECs, the intercellular electrical coupling is not as strong as in SMCs but can still be categorized as *strong* coupling as the membrane potential of acceptor cells follow the membrane potential of the donor cells closely. Ca^{2+} coupling, on the other hand, can still be characterized as *weak* coupling, however, enabling all there coupling modes improves the extent of synchronization of Ca^{2+} concentration of the coupled ECs.

5.5.3 Effects of heterocellular coupling on an EC/SMC unit

Now that there is some awareness on how homocellular coupling affects the Ca^{2+} and membrane potential of SMCs or ECs in a homocellular population, let us turn our attention to the influence of heterocellular coupling between SMCs and ECs. For this, a single unit consisting of an EC, heterocellularly coupled to a SMC, is considered. To implement heterocellular coupling, the heterocellular electrical, Ca^{2+} and IP_3 currents, from a SMC to and EC, modelled by equations 5.12,5.13,5.14, and from an EC to a SMC, modelled by equations 5.15,5.16,5.17, are added to the respective ODEs modelling the membrane potential, cytosolic Ca^{2+} concentration and cytosolic IP_3 concentration of each cell type, described in detail in sections 3.2.1 and 3.2.2.

Section 4.1 established that in an uncoupled SMC, a range of $J_{PLC_{agonist}}$ (0.08-0.19 μM/s) produces oscillations in the cytosolic Ca^{2+} concentration and the membrane potential, with respect to time. It is important to understand how the heterocellular coupling with an EC influence this oscillatory behaviour. Since the eventual interest lies in the study of spatially varying agonist concentration on the luminal side or the EC surface of an arterial segment, only the EC of this SMC/EC unit is stimulated, as shown in Figure 5.1. Figure 5.11 shows the effect of increasing $\widetilde{J}_{PLC_{agonist}}$ on the cytosolic Ca^{2+} concentration of the SMC from the coupled SMC/EC single unit. Unlike an uncoupled SMC, the Hopf bifurcation starts at $\widetilde{J}_{PLC_{agonist}} \approx 0.365\mu$M/s and ends at $\approx 0.95\mu$M/s. Thus, compared to the response of an uncoupled SMC shown in Figure 5.11a, the oscillatory effect in Figure 5.11b for a SMC of single unit has shifted significantly to the right on x axis. Since SMC

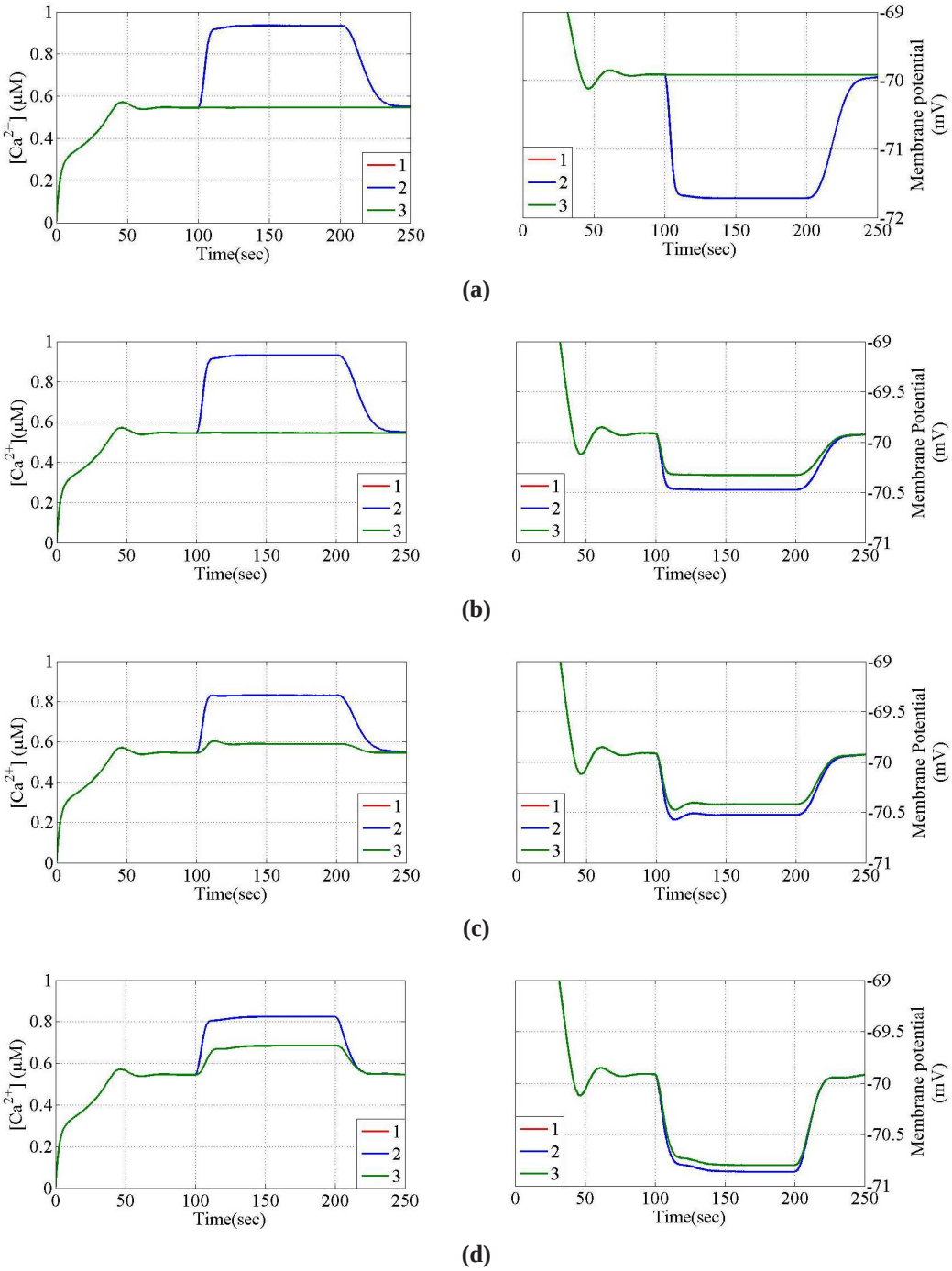

Figure 5.10: An array of homocellular coupled 5 ECs , as shown in Figure 5.8b (cells on the flanks not shown in the results) was simulated for 300 real time seconds, stimulated with $\widetilde{J}_{PLC_{agonist}}$=0.01$\mu$M/s over the whole time span. Cell 2 (shaded in grey in Figure 5.8b) was stimulated with $\widetilde{J}_{PLC_{agonist}}$=0.1 μM/s from 100 to 200 seconds. Four modes of intercellular coupling were implemented, (a) no coupling, (b) electrical coupling, (c) electrical and Ca^{2+} coupling, and (d) electrical, Ca^{2+} and IP_3 coupling.

is not being stimulated directly, it solely depends on the IP_3 transport from the coupled EC. Another reason is the closure of VOCCs in SMCs due to the hyperpolarization of the plasma membrane. VOCCs contributes to the commencement of Ca^{2+} oscillations in an uncoupled SMC by adding the extracellular $Ca^{2+}$to its cytosol, thereby aiding the Ca^{2+} induced Ca^{2+} release. Closure of VOCCs under hyperpolarization disables this pathway of Ca^{2+} entry thus increasing the dependence of Ca^{2+} oscillations on the cytosolic availability of IP_3 . Another important difference between the two cases is the span of the oscillatory behaviour that has extended significantly in Figure 5.11b. This feature is dictated by the strength of heterocellular IP_3 coupling (the value of coupling coefficient). Another distinction between the two response is the maximum Ca^{2+} concentration which is lower in the case of uncoupled SMC in Figure 5.11a than in b.

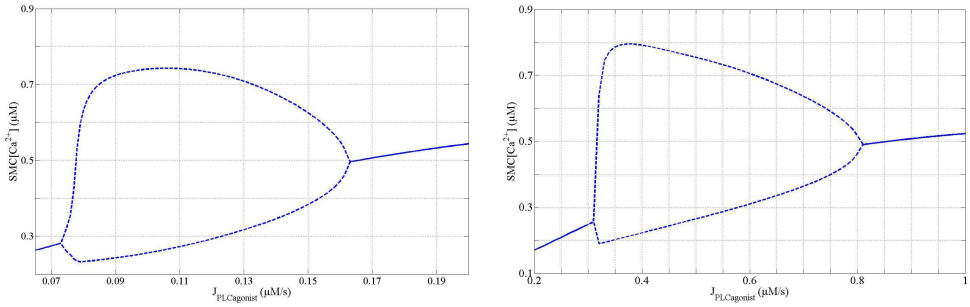

(a) **(b)**

Figure 5.11: A comparison of the cytosolic Ca^{2+} concentration of (a) an uncoupled SMC and (b) a SMC from a single EC/SMC coupled unit. In (b), EC and SMC are heterocellular coupling via electrical and IP_3 coupling and the agonist stimulation takes place only at the EC surface. The Hopf bifurcation has shift to the right on x axis in (b) compared to (a).

Figure 5.12 shows the influence of different media of heterocellular coupling affect the Ca^{2+} dynamics in a SMC, in (a) and (b) and an EC in (c) and (d). $\widetilde{J}_{PLC_{agonist}}$ is increased from 0.01 μM/s to 0.4 μM/s at 100 second mark. In the case electrical coupling only (dynamics shown in red), it alone fails to elicit an increase in the SMC Ca^{2+} concentration (Figure 5.12a). There is a prominent increase in the Ca^{2+} concentration of the EC in Figure 5.12c which apparent is biomodal, first peak around 100 seconds and the second one is beyond 200 seconds. The second peak is by virtue of decreasing IP_3 in the cytosol of the EC

due to removal of the stimulus, $\widetilde{J}_{PLC_{agonist}}$, at 200 seconds. The membrane potential, however, is hyperpolarized in both cells. SMC membrane potential, although relatively less negative than that of EC's, follows the pattern of EC's membrane potential faithfully, suggesting *strong* electrical coupling.

Enabling two way Ca^{2+} coupling between the EC and SMC allows flow of cytosolic Ca^{2+} of EC, into the cytosol of SMC, under concentration gradient. Thus a corresponding slight increase in the SMC Ca^{2+} concentration can been see in Figure 5.12a (dynamics shown in blue). Even though Ca^{2+} via coupling enters the SMC cytosol, it is unable to produce a marked increase in the cytosolic Ca^{2+} concentration, primarily because of the inavailability of cytosolic IP_3 . The membrane potential is hyperpolarized but relatively less negative than in the case of electrical coupling only. This is due to increased Ca^{2+} concentration in the SMC, which tends to depolarize the SMC's membrane potential while the EC membrane potential tends to make it more negative. The resultant membrane potential, therefore, is less negative than the previous case of electrical coupling alone.

In the third case (dynamics shown in green), enabling the passage of IP_3 between the two cells has a significant impact on the SMC Ca^{2+} concentration. Influx of IP_3 from the EC cytosol to SMC encourages the IP_3 induced Ca^{2+} release from the SR. Combined with the Ca^{2+} influx from the coupled EC, the cytosolic Ca^{2+} concentration is enough to put the cytosolic oscillator into an oscillatory state. Thus, the presence of IP_3 is an enabling factor to induce Ca^{2+} oscillations in the coupled SMC. Before examining the EC Ca^{2+} concentration, let us first probe the status of membrane potential in the two cells. In SMC, in Figures reffig:EC/SMCdynamicsa & b, the membrane potential oscillations are in phase with the Ca^{2+} oscillations and also with EC's membrane potential in Figures reffig:EC/SMCdynamicsd. Note that in Section 4.1, it was shown in the Figure 4.3 that the oscillations in the Ca^{2+} concentration and membrane potential of an uncoupled SMC are anti-phase. The cytosolic Ca^{2+} concentration of the EC also oscillates, which is a significant feature since the cytosolic Ca^{2+} concentration of an uncoupled EC can not oscillate at any stimulation level, as shown in Figure 4.9a & b. This behaviour in the EC can be attributed to both, the oscillating membrane potential of the EC and also the Ca^{2+} coupling with the neighbouring SMC, whose oscillating Ca^{2+} concentration, at times surpasses the maxi-

mum Ca^{2+} concentration of the EC, thus reversing the direction of gap junctional Ca^{2+} flux, i.e. Ca^{2+} flowing from SMC to EC on those instances. The downstream consequence of the oscillations in EC's Ca^{2+} concentration of and membrane potential have not been addressed in detailed in this thesis but it is probable that this behaviour can contribute to fluctuating activation of a downstream process, such as activation of eNOS, and elicit responses which are unlike those seen in an uncoupled or homogeneously coupled populations of ECs.

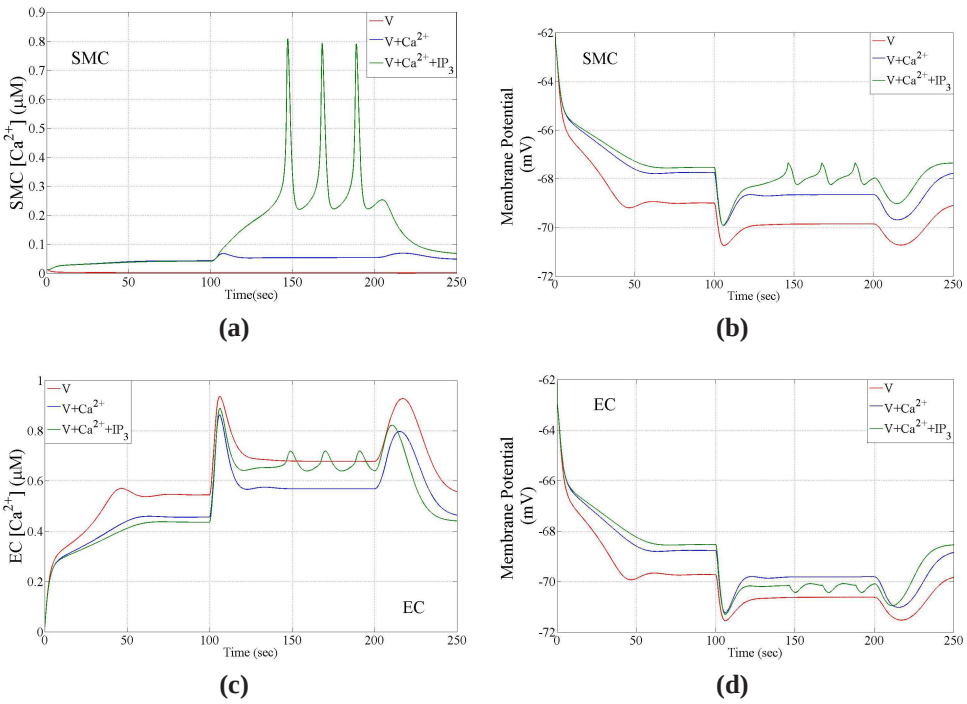

Figure 5.12: A single unit consisting of an EC and a SMC coupled via electrical (red), electrical and Ca^{2+} (blue), and electrical, Ca^{2+} and IP_3 coupling (green). (a) and (c) shows the cytosolic Ca^{2+} concentrations of a SMC and EC respectively. (b) and (d) show the time course of membrane potential for a SMC and EC respectively. Only the EC is stimulated with $\widetilde{J}_{PLC_{agonist}}$=0.4 μM/s between $100.0 < t \leq 200.0$, and $\widetilde{J}_{PLC_{agonist}}$=0.01 μM/s elsewhere. Only in the case of adding IP_3 coupling between the two cells, the SMC Ca^{2+} concentration and membrane potential oscillates. These oscillation also induce a similar and in phase response in the cytosolic Ca^{2+} concentration and membrane potential of the neighbouring EC.

Chapter 6

Parallelization for Large Scale Computational Domain

The length of an atherosclerotic lesion in muscular arteries such as internal carotid or coronary arteries, ranges from an order of millimetres to a few centimetres (Ryan et al., 1988). A high incidence of these plaques occur near the bifurcation areas in of the arteries. These regions experience complex blood flow profiles, termed as disturbed flow, with consequent substantial spatial gradients in the wall shear stress. Accompanying the spatially varying wall shear stress boundary layer, is the spatial variation in the concentration boundary layer of the blood borne species (e.g. ATP), which are agonist to specific receptors expressed on the endothelial surface of the arterial wall. Thus the areas with disturbed flow and accompanying impaired mass transport, where atherosclerosis occurs (Cheng et al., 2006), form the computational domain of interest for the present study.

6.1 Motivation for Parallel Computation

In order to make the computational domain of interest physiologically relevant, it is important to match the scale over which the physiology and pathophysiology takes place. Considering the morphology of the cells (i.e. the cell length, width and volume) and the orientation in which these cells sit in a small section of an arterial tissue, suggests that a mere centimetre (1 cm) contains the number of cells

ranging from hundreds of thousands, to millions of cells. The basis of this notion is the length scale of a single EC or SMC, which is of the order of a few tens of micrometers (μM) and each cell contains 4 to 7 and some times 8 nearest neighbours. From the computational point of view, each single cell model expressed as 4 ODEs in the case of an EC and 5 ODEs for a SMC. Considering the characteristic lengths of single EC or SMC and coupling topology as described in the Section 5.3, an arterial segment of length 1 cm and a diameter of 4 mm (of the order of a coronary artery diameter) can have 220320 cell (159120 SMCs and 61200 ECs). This gives rise to a computational domain with over 2.362 million degrees of freedom or ODEs to evaluate the solution at each time step. Solving this computational domain clearly needs extensive computational resources and a very fast CPU speed to compute practically long time scales which can demonstrate the evolution of slow cellular processes locally and globally across the axial and circumferential planes.

Figure 6.1 highlights the increase in the computational expense with increasing cell load (i.e. number of cells in the computational domain), in terms of the compute time. The exponential increase in the compute time with increasing number of cells can not promise acquiring the solution for a computational domain of the sort described above, for a time scale of at least hundreds of seconds. For the same computational ensemble, the computational expense is expected to exacerbate when the agonist stimulation or $J_{PLC_{agonist}}$ in non-uniform, across the axial of circumferential plane. Spatial nonuniformity in stimulus in circumferential direction has not been included in this thesis and it is only confined to variation in the axial dimension. Thus on a serial platform executing a structured program, compute time becomes a bottleneck to simulate large, physiologically relevant length of an arterial segment.

Another important parameter to consider is the virtual memory allocated to the program by the operating system (OS). Upon compiling (and linking) of a procedural or structured C program, an Executable and Linking File (ELF) generates which is in binary format. Soon as this ELF is executed, some memory space is allocated to it by the OS in the global memory space. This space is segmented into four virtually contiguous segment or frames viz, text, data, heap and stack, as shown in Figure 6.2. *Text* contains all the instructions (in binary for) written

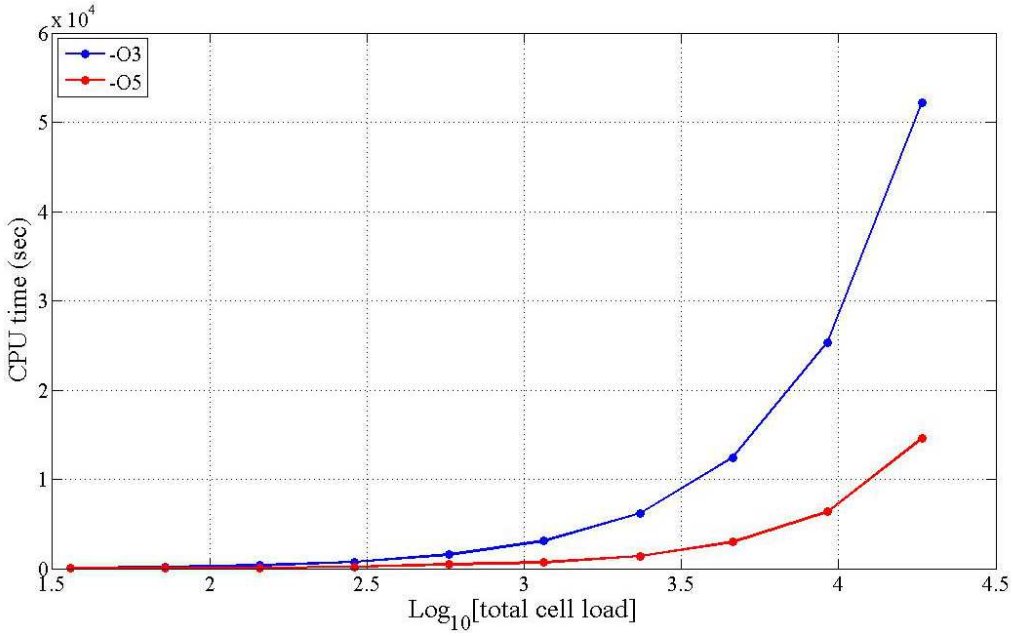

Figure 6.1: (A repeatation of Figure 5.6) Figure shows CPU time versus the size of the computational domain in terms of cell load. The execution time increases after a cell load of ≈ 1000 cells is reached. A comparison between low level (-O3) and highest level (-O5) compiler optimization shows the reduction in the compute time. The simulations were executed on a single core (processor) of IBM *p5 575* system.

in the source code. The access permission to this segment is *read and execute* only. Stacked upon this is another segment called *Data*, which actually is divided into two segments, *data and BSS*(BSS = Block Started from Symbol, this name is now depreciated), which contain initialized variable and constant declared in the global scope and uninitialized variables, respectively. The access of this segment is read and write.

Soon as the execution of the program starts, the memory allocated to the program is *text+data* and some overhead. The program memory, however, can expand if calls to function for dynamic memory allocation, such as **malloc()**, are there in binary of the source code . This dynamic memory allocation is located above the data segment and is called *heap*. Heap and expand or contract with the allocation and deallocation of the dynamic memory.

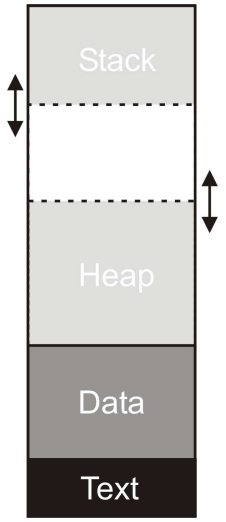

Figure 6.2: Memory map of a structure C program's virtual memory. Solid lines represent that the segment size cannot vary where as the dashed line represent that the segment can expand or contract according to the dynamic allocation or deallocation or pushing new temporary variables belonging to functions called subsequent to the *main()* function. Note that this contiguous map is of virtual memory allocated to the program, which is related to the physical or real memory space (may or may not be contiguous) by a lookup table, called *page table*, maintained by the operating system.

Structured C programs have a local hierarchy of function calls. Each calling function passes arguments to the function called. The called function may also

have some temporary variables, initialized or uninitialized, that are declared in the local scope of that function. These are stored at the top of the virtual memory in the segment called *call stack* or just *stack*. Stack can also expand but the direction of its expansion is from top to bottom and data is access by LIFO or last in first out basis.

In the program flowchart shown in Figure 5.5 each cell, either an EC or SMC, is a C structure with members including all state variables, ionic and coupling currents and other local information such as location in the matrix and local hemodynamic variables e.g. $J_{PLC_{agonist}}$ or WSS. Multiple instances of these structures form the populations of EC or SMC by dynamically allocating the memory using **malloc()**. Also, the solver RKSUITE requires multiple arrays of the same length as the number of equations (remembering that each SMC is 5 ODEs and an EC is 4 ODEs). While setting up the solver to solve with *method 2* or Runge Kutta(4,5), it requires allocation of memory as big as $32 \times neq$ (where *neq* is the total number of ODEs), for its own use. Thus increasing the cell load (number of cells) will increase the number of instances of these structures and the overheads that come with the solver, and stored in the heap segment. While dealing with very large populations of cells, the memory resource thus can be a serious limitation.

In order to avoid these bottleneck when dealing with physiologically relevant cell population size, related to memory resource or impractically long compute time to simulate the system for a physiologically relevant time scale, alternative computing options must be sought. Parallel computing can provide an answer to these limitations. Pooling of computational resources to solve a single problem or run the same C program over a multiprocessor machine is a promising prospect for solve large scale computational problems. The next section discusses some platforms and the pros and cons of their use. Later sections elaborate the development and implementation of the parallel code on the computing platform of choice.

6.2 Architecture for High Performance Computing

Flynn's Taxonomy, presented by Micheal J Flynn in 1966 (Flynn, 1972), classify the multi-processor computer architectures along two independent dimensions, instruction and data and each of these two dimensions can have either of the two

states, single or multiple. Computers can either be:

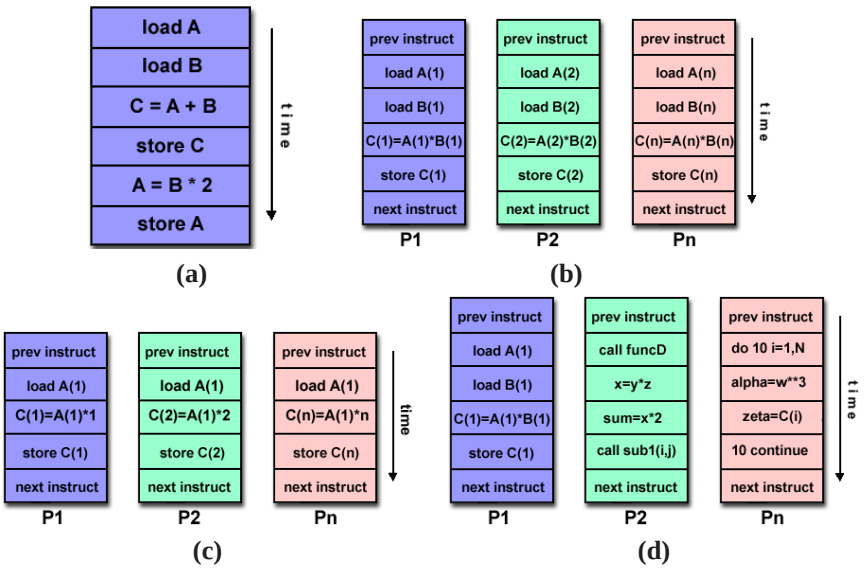

Figure 6.3: Theoretical single processor and multiprocessor architectures described by Flynn's Taxonomy. (a) Programs execute sequentially on an SISD machine irrespective of the dependencies. (b) Multiple data streams can be worked upon at a time on a SIMD machine. This can be a multiprocessor or multithreaded approach. (c) Real world realization of a MISD machine, where multiple instructions can be executed on the same data stream, has not been possible. (d) The most common multiprocessor architecture used today is MIMD, where multiple instruction streams can work simultaneously on multiple data segment.

- **Single Instruction, Single Data (SISD)**:As shown in Figure 6.3a, this is a serial computer with one instructions stream is executed by the CPU at a time, acting upon a single data stream. The execution of such architecture is deterministic i.e. predictable. Right from the olden day to this date, this architecture is used even in most of the modern day PCs.

- **Single Instruction Multiple Datat (SIMD)**: A type of parallel computer, as shown in Figure 6.3b, where all processors in a multicore or multiprocessor machine execute the same instruction on different chunks of data. This type of computing architecture is an appropriate choice for problems where data is highly regular/structure (i.e. arranged in a matrix) and the data elements

are coupled. This also gives rise to the requirement of synchronization in communication thus making the execution deterministic.

- **Multiple Instruction Single Data (MISD)**:Theoretically these machines should be able to execute multiple instructions on a single data stream. To-date, no such architecture has been realized. For this to happen, each processor should be able to access the same data location at a time and since every processor is executing different sets of instructions, they should all be able to manipulate the same data location at a time. This, in practicality, not possible.

- **Multiple Instructions Multiple Data (MIMD)**: Several instruction sets can be executed on different data sets, at a time by several processors on a multiprocessor machine. As shown in Figure 6.3d, this architecture is best suited for the problems were the data is mutually exclusive and has no dependencies. Thus making subtask executing on segments of mutually exclusive data can shorten the time of computation significantly. MIMD system cannot be adequately classified by Flynn Taxonomy alone. This is because both small (few processors) and large (thousands of processors) clusters of processors capable of such multitasking fall into the MIMD category and they behave differently. Another dimension to add in classifying the MIMD systems efficient is the memory where the data is kept.

  Shared Memory Systems: With multiple CPUs, these systems share the same memory address space. Thus the user need not be aware of the location of data when accessing it by any of the member processors of the cluster. Shared memory systems can be both SIMD or MIMD. A vector processor (a single CPU capable of executing single instruction set on an array of data simultaneously) is an example of shared memory SIMD class or (SM-SIMD). Shared memory MIMD subclass is implemented by *Symmetric Multiprocessing* (SMP) where identical CPUs or processors share the main memory address space. Interestingly, a SMP machine can be made to work as a SM-SIMD by using specialised vector operation libraries designed to implement simultaneous operations on large arrays and eliminated the need for excess use of loops, but the vice versa is not possible. This can

be achieved by using software protocols such as *OpenMP*. The programs written using OpenMP are compiled by specialized compiler. Multithreading is another way to exploit the capabilities of such architectures. Figure 6.4a elaborated the SM-MIMD architecture.

Ideally, the memory access to all CPUs should be direct and uniformly quick, which can be best achieved if all processors are on chip. Unfortunately, the progress in adding multiple cores or processors on a single chip and high performance memory hardware has not been as fast as the increasing speed of a single core/processor. Large shared memory clusters are made of connecting two or more SMP machines through fast interconnect buses. Although a processor from one SMP unit may access the memory of another SMP unit, the access is not as fast as the local memory access.

Distributed Memory Systems: Figure 6.4 shows the layout of a distributed memory machine. Each CPU in this case has its own associated memory space and other CPUs in the cluster cannot have direct memory access to its memory address space. The user, therefore, must be aware of the location of the data before accessing it and this access is explicit, unlike the SM-MIMD case where CPUs can access memory address space directly. A distributed machine can either be of SIMD or MIMD architecture i.e. DM-SIMD or DM-MIMD. DM-SIMD machines are also known as *processor array* machines because they operate in a lock step where all CPUs execute the same instruction set on different data elements, at the same time and interprocessor synchronization is required. A master processor issues the instruction sequence to the processor array. This processing layout is best suited for applications with no data exchange between the processors, therefore no interprocessor synchronization will be required. In case where applications require data exchange between processors, it has to be sent, upon request, explicitly from the local memory via external network routers. This can be done using message passing protocols such as *Message Passing Interface* or MPI, a standard library for interprocessor communication in distributed memory architectures. This can significantly limit the performance of the machine. This makes a DM-SIMD machine not a fea-

sible choice for applications were interprocessor exchange is required. A DM-MIMD machine provides the option of implementing multiple instruction streams by several processors on multiple data streams in their local memory address space, at a time. For applications with no requirement of data exchange, several tasks can be performed autonomously on different individual processors or sets of processors, on different data segments. This gives significantly enhancement in performance.

Formally put, the *memory bandwidth* (the rate at which data can be read from or stored into the memory by a processor) should increase linearly with the number of processors. The major advantage of having distributed memory or shared memory is that the memory bandwidth scales up with the number of processors. The major disadvantage in the case of distributed memory is that the latency (formally defined as the delay in sending 0 bytes of data from one processors to another) increases, as compared to a shared memory architecture. Implementation of high bandwidth and low latency communication links for interconnection of processors has bridged this gap and put DM-MIMD machines as front runners. For transfer of data from one processor to another, MPI protocol is implemented in software, and is a *de facto* message passing standard. Despite the obvious advantages of simpler programming on SMP clusters and faster memory access compared to the a distributed memory architecture, the lack of memory and CPU scalability makes them an inferior choice for problems that are large scale and require substantial amount of interprocessors data exchange. On the expense of relatively slower interprocessor communication, distributed architectures, especially DM-MIMD machines provide scalable bandwidth over very large number of processors. Although the programming is tougher than for shared memory architectures, the gain is worth the effort since the local memory access is fast, and the isolation of local memory from the memory of other processors eliminates the need for maintaining cache coherency (the need for updating the data brought to L3 cache from the main memory by a processor, while another remote processor does a write operation on it), which is important in a SMP machine.

Hybrid architectures where shared memory and distributed memory are simultaneously implemented, have made computation possible on petascale and show

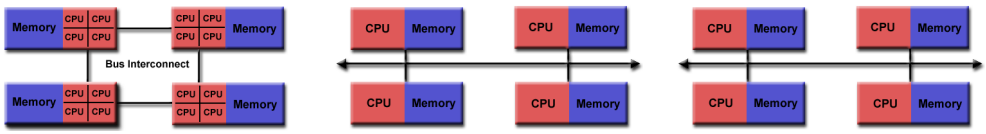

Figure 6.4: MIMD machines can be classified into to categories based on the hard-wired permission of client to the memory address of the host. a Processors in a Symmetric Multiprocessing (SMP) machine can shared common memory address space, making the data location transparent to the user. Multiple SMP units can be connected via high performance buses allowing direct access to memory space of each other. The communication between two SMP units is slower than when processors of the same SMP communicate. (b) In case of distributed memory, each processors (either single core or multicore) have their own associated memory to which direct access by another processor is not allowed. Processors are networked through high performance (high bandwidth, low latency) interconnect and the processors communicated via exclusive calls made in the program using message passing protocols such as the Message Passing Interface or MPI. (c) A hybrid shared-distributed memory machine physically widens the extends the memory address scape of a processor by increasing the number of cores per processor. Each core can aces the associated memory space while other remote processors have to make an exclusively call/request to access data in the memory address space residing in its memory using MPI.

promise in to achieve exascale performance. Figure 6.4c shows the memory address arrangement in hybrid distributed-shared memory architecture.

Bluefern®, UC's supercomputing facility formally known as University of Canterbury Supercomputer (UCSC), houses two supercomputers. One is a symmetric multiprocessing machine **IBM p5 575** and the other is a massively parallel DM-MIMD machine **IBM Blue Gene L**. Salient features of these two parallel computers are discussed in the following sections.

6.2.1 IBM p5 575

An example of a distributed shared memory MIMD machine, IBM System p5™ 575 is a member of IBM's *p* Series and uses IBM Power5+™ microprocessor as its core building block. Eight Power5 processors, operating at 1.9GHz clock frequency and sharing a total of 32 GB of memory (4GB associated with each processor), make a *symmetric multiprocessing node* or SMP node, shown in Figure 6.5. Power5+ is a dual core processor and both cores share a L3 (or level 3) cache of 36MB and L2 cache of 1.9MB and each has its local L1 instruction (64KB) and data (32KB) cache. A 16 core version is also available where both cores of the dual core Power5+ processor are active. Each processor can read from the L2 or L3 cache of another processor but can only store or write on its local L2 or L3 cache. At Bluefern®, the p5-575 serve consists of 10 such nodes.

A mix of interconnect networks (e.g. Gigabit Ethernet and dual channel Infiniband, which is, theoretically, 10 times faster than Gigabit Ethernet) connect these nodes to provide a sustained bandwidth of 105.5 Gigabytes/sec. This is considered a high bandwidth and provides the backbone of internode communication. Hence, each p5 575 node can aces a total of 15.2MB of L2 cache, 288MB of L3 cache and 32GB or main memory (expandable to 256GBs as the node card provides 64 slots for DDR2 memory DIMMs i.e. 4GB$\times$64=256GBs). Each of the available nodes in the UCSC's p5-575 system are logically partitioned (virtually made as a separate computer) into LPARs or Logical Partitions. Each LPAR runs its own Operating System Instance (OSI). Some of the LPARs run AIX 5.3, IBM's UNIX based operating system, while others run SUSE Linux Enterprise Server 9 (SLES9). Depending on the requirement of memory resources, the user can

choose to use a development node which serves a standalone 8 processor shared memory or SMP machine with 32GB memory. It is worth noting here that despite the high bandwidth and low latency of the network interconnect, Infiniband, the *intranode* communication is much superior in efficiency and speed. Thus one could expect a drop in performance when doing internode communication than executing an application on a single node.

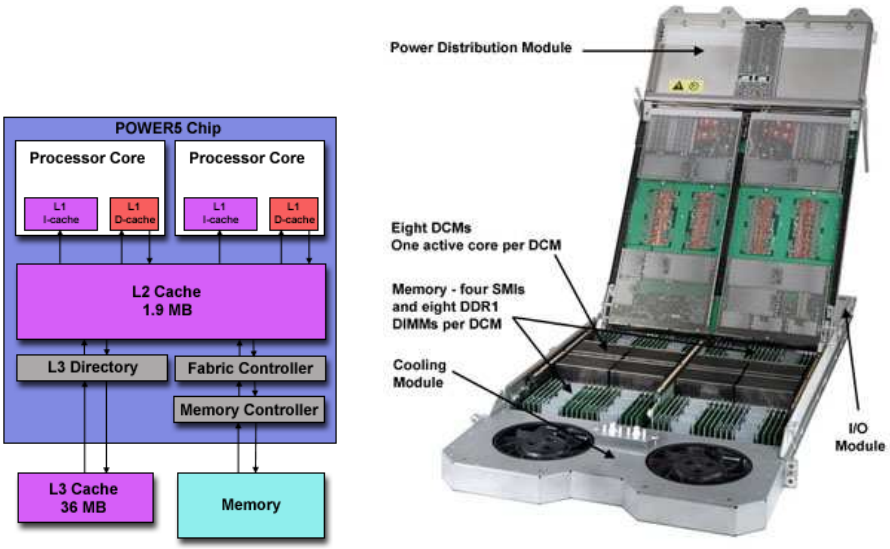

(a) **(b)**

Figure 6.5: (a) Schematic of a Power5+™ chip. (b) An open node case of p5-575 showing the memory, the dual chip module (DCM) and the fans.

6.2.2 IBM Blue Gene/L

Blue Gene/L (BG/L), is an example of distributed memory MIMD architecture, is the first of IBM's Blue Gene series. The goal of the Blue Gene design was to make ecofriendly, a power miser, yet extremely fast supercomputers to enable computation of the complex problems that are limited by the availability of computing power. A node, in the case of BG/L, constitutes a 700 MHz dual core Power PC 440 (PPC440) processor (Gara et al., 2005). A compromise on the processor speed comes with a gain on lower power consumption. Depending of the preferential use of the two cores, either in *coprocessor mode*, where the computation and commu-

nication are handled by two separate cores, or in *virtual node mode*, where each core handles both its computation and communication independently, thus virtually presenting itself as an independent processors or another node. Figure 6.6a shows the PPC440 schematic of internal resources. It is based on system-on-chip design where each of the two cores has separate L1 instruction and data caches (32KB), a separate L2 cache (2KB) for each core and a shared high bandwidth, low latency embedded DRAM serving as a 4MB L3 cache which provides fast compensation to the L1 caches in the case of a cache miss. This makes each core a high performance core on its own. The second core, in the *coprocessor mode* serves as an I/O processors to handle communication whereas the other core does the computation simultaneously. Unlike the standard PowerPC440 processors, the ones used in BG/L are modified to have an on-chip *floating point unit* or FPU, code named *double hummer*. It has two FPU functional units that are capable of performing 64 bit arithmetic operations such as multiply-adds, divisions and square-roots thus provided high performance precision arithmetic facility that is on-chip and avoids limitations caused by bandwidth issues. In the *coprocessor mode* the node has an exclusive access to 512MB main memory whereas in virtual node mode each core or *virtual node* can access 256MB. Again, the gain of have a system on chip comes with a trade-off of how much can be put on a chip.

The dual core compute chip is used to horizontally scale and make a many core system. Here it is important to realize that the system on chip design means that no other processor has direct access to the memory of a processors and the only way to exchange interprocessor information is through external routing, as per nature of a distributed memory architecture. In order to exploit the computational acceleration provided by the on-chip resources of a node/compute chip, the network should also be of high performance. Nodes are connected via a high bandwidth, low latency network, 4X InfiniBand. It is a point to point, bi-directional serial link (sending one bit at a time) between nodes and is designed to be scalable. The 4X stands for the signalling rate or data rate which is 4 times as fast as the signalling rate of the standard serial connection via InfiniBand. 4X Infiniband has become a standard implementation today and is popular in internode communication within distributed machine or connecting nodes with high performance peripherals such as file systems or high speed disk drives.

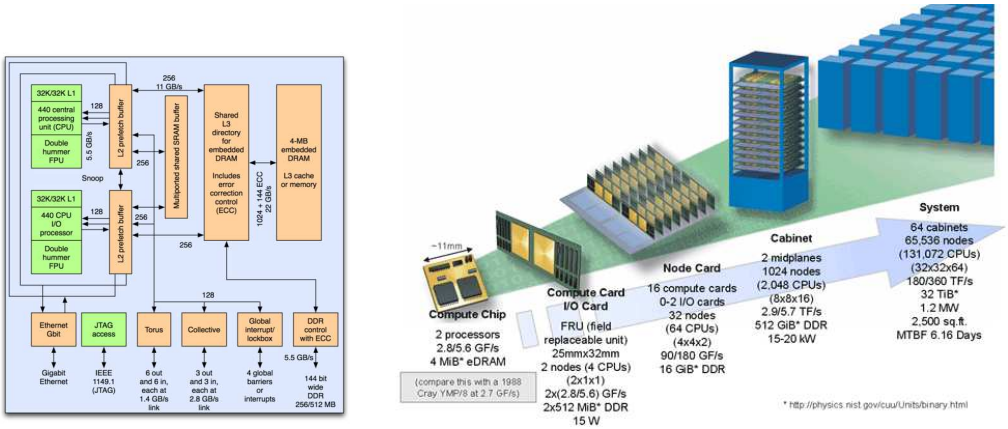

(a) **(b)**

Figure 6.6: (a) The dual core Power PC 440 processor is the computational unit of BG/L. Schematic shows the internal resources of the PPC 440 processor. (b) Schematic shows how the system is scale out (horizontally scaled) to make a *rack or cabinet* of BG/L consisting of 1024 processors (i.e 1024 dual core PPC440 modules) or 2048 cores. BG/L at the Bluefern® is a two rack system with a total of 2048 compute nodes or 4096 cores.

Internode communication may involve the transit of the message through many other nodes in the system. BG/L nodes are connected in such a way so as to reduce the displacement of the message from one node to another. Each node is connected in six different directions for nearest neighbour communication in *3D torus* configuration. Nodes not located on the boundaries form a 3D mesh with their six nearest neighbours. Nodes on the edges are looped back, as shown in the Figure 6.7, thus ensuring that each not has identical number of nearest neighbours. In 3D torus connection, each node support an aggregate bandwidth of 2.1 Gigabytes/s and a latency od 100 nanoseconds. In addition to this, two other network configurations are implemented; *collective network* and the *barrier network or global interrupt*. The collective network handles the interprocessor communications of *one to all, all to one* or *all to all* nature. These broadcast communications are used in parallelizing, via software, the global arithmetic operations such as *max, min, global sum or mere updates* for interprocessor synchronizations. The barrier network implements a global boolean operation “OR” on all the nodes. This is very useful while implementing barrier synchronization of processors in

the software. The physical network ensures the parallelization such operation so as to match the performance with other networks when they are used in combination.

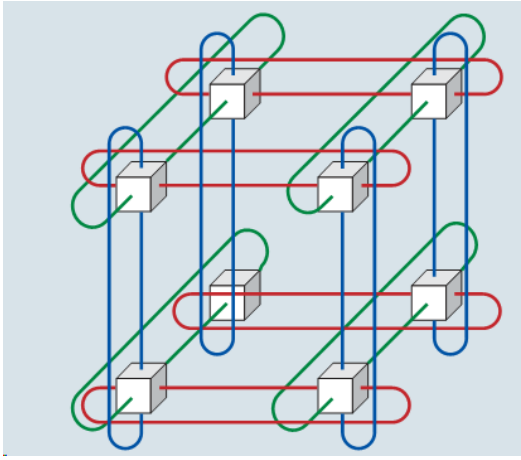

Figure 6.7: 3D torus network is the backbone of the BG/L interprocessor communication. Each node is connected six way to its nearest neighbours. Figure shows how the nodes on the edges are wrapped to avoid edge effect which mapping a problem. Red, blue and green lines are the physical links by 4X InfiniBand interconnect.

6.3 Parallel Algorithm

Granularity is an qualitative measure of the ratio of computational versus interprocessor communication in a multicore environment. A *coarse grain parallelism* suggests that in a period where one unit of work is completed the computation dominates and interprocessor communication is less in comparison, whereas *fine grain parallelism* indicates a higher communication to computation ratio. In the present scenario, the intent is to solve a problem containing very large number of arterial coupled cells exchanging information in a point to point manner rather than globally. Although the information exchange is between the nearest neighbours in this case, the very nature of intercellular coupling call for the completion of information exchange over the whole problem set before heading forward in the next time step set by the solver's (RKSUITE's) adaptive step size controller. Thus

there exists an implicit barrier synchronization of all the cells, in time. Shared memory architecture such as IBM p5 575 can hold large sets of data because of the processors can access vast memory address space. *Automatic parallelization* is a method of testing the potential of parallelism in an application on a symmetric multiprocessor. When compiling with IBM's XL C/C++ compiler, optimized for AIX operating system that runs on IBM pSeries machine, an option **-qsmp** is used for generating a binary/executable file that is optimized to run on a SMP machine. Compiling the serial C program, whose flowchart has been shown in the Figure 5.5, gives no performance enhancement when executed on the UCSC's p5-575. Table 6.1 shows the CPU times for a simulation of 10 seconds of a coupled cell population constituting a straight arterial segment, 1.6 cm in axial length, 100 μm in diameter, and contains 7680 ECs and 19968 SMCs. The CPU time remains more or less unaffected with either mapping the problem on to one node or multiple nodes. Also, increasing the number of processors has no effect on the CPU time. It should be noted that in a shared memory system, more than one processors cannot access a data location in the memory. While one processor reads this data location, others will have to wait. Members of the structures holding local information of a cell is required to be accessed by more than one processors. This situation occurs more frequently in the case of *coupling* function, where an i^{th} cell may have its nearest neighbours mapped on different processors or nodes and each these processors attempts to read the contents of the i^{th} cell.

Worth mentioning is that the compile time automatic parallelization tends to find the iterative loops, e.g. *for or while loops* which are not dependent on one another. Once sighted, the **-qsmp** option directs the compiler to make these loops thread safe (i.e make the loops capable of running simultaneously without effecting the integrity of the code). Loops which are mutually exclusive but address the same data locations are not suitable for parallelization by the **-qsmp** option. This is applicable to the present case where loops in multiple functions in Figure 5.5, such as *single cell* or *coupling*, address the same data location and thus cannot be parallelized.

Parallel programming model based on *OpenMP* exploits the shared memory architecture to its fullest but in the instances such as the present case where many processors may access a data location at a time, blocking or semaphore technique

Total no. of processors	No. of nodes	No. of processors per node	CPU Time
1	1	1	2024.00
8	1	8	2064.00
8	4	2	2031.00
8	8	1	2018.00
32	8	4	2044.00
64	8	8	2066.00

Table 6.1: Compute times of different scenarios of mapping the problem on nodes of IBM p5-575 machine compiled with automatic parallelization.

is used where the data location is made accessible to one processor at a time. Performance may increase substantially in the case where the data is seldom accessed in an iteration by the processors. In the present case however, the memory locations holding the state variables of each cell are accessed frequently especially while the function *coupling* is called, this may limit the performance yield. Restructuring from functional or data flow aspect of the algorithm may make it conducive for multithreaded program. This can make a significant improvement when targeting hybrid computing architectures (i.e. shared and distributed memory working together) is employed.

Close inspection of the pattern of information exchange between the cells reveals resemblance with the architecture of the Blue Gene/L. As has been discussed in the previous section, a 3D torus connection in BG/L enables connecting a process to six nearest neighbours in x, y and z directions. The management of interprocessor communication adheres to a standard message passing protocol implemented by Message Passing Interface (MPI), a library of C functions the calls to which are embedded in the program. This parallel programming model is thus called the *message passing model*. Although not being the only one, MPI has become the *de facto* industry standard for message passing. Although suits most to distributed memory systems, the use of a message passing model is not limited to these architectures. Data exchange between two processors is cooperative, unlike shared memory. A *send* operation by more processor must be complemented by a *receive* operation or call by the receiving processor. The interprocessor can be in either of the three mode:

- one to one
- one to many, and
- many to one
- all to all

All except the first are characterized as collective communication, where as the first one is a *point to point* communication operation.

A problem can be decomposed on the basis of two aspect, computational domain or function. *Domain decomposition* implies dividing the complete computational domain into small chunks and mapping them onto various processors. On the other hand, if a program application is segmented such that smaller chunks of tasks/instructions are mapped onto multiple processors, this is termed as *functional decomposition*. When one program is executed on all processors containing a domain decomposed data set, this is called a SPMD or *single program multiple data* approach to parallel programming. Domain decomposition and SPMD are employed here, in the case of coupled cells, the details of which are covered in the following sections.

6.3.1 Problem Decomposition

Coupled matrices of cells with different aspect ratios is to be mapped on a number of processors. In the program executing on a serial platform, the numerical solver, RKSUITE, takes a solution vector of length *neq*, which is the total number of ODEs in the computational domain, to solve the computational domain at each time step taken. Moreover, the time step selection is adaptive to the steepness or *stiffness* of the solution, i.e. more *stiff* the solution, smaller the next step, until the *global error* is within a user defined range. This summarizes the salient feature that are to be dealt with when mapping the problem onto many processors of BG/L.

The strategy for parallelizing the arterial segment is by domain decomposing the computational domain in axially direction and mapping each chunk onto one BG/L node. This is shown in the Figure 6.8. Each BG/L node then calls an instance of the C++ object numerical solver, RKSUITE, which then solves for the ODEs in time, corresponding to the cells mapped locally. The cells on the edges

of subdomains on each node communicate there coupling information the their immediate neighbours (adjacent nodes in this case) and this internode communication is handelled by point to point MPI communication at each time step. The parallel C code executing on each BG/L node is discussed in detail in Section6.3.2. A straight arterial segment of length and diameters that were impractical to solve with a serial C code, discussed in Sections 5.4.2, can be mapped onto several processors. How well the algorithm scales on BG/L is discussed in Section 6.4.

6.3.2 Implementation of SPMD

Figure 6.9 depicts the algorithm that each BG/L node executes on the subdomain allocated to from the *global* computational grid. The subdomaining is managed by a *master node*, node 0 in this case, which calculates the total size of the computational domain from the information received from the user, such as axial length and the required diameter of the arterial segment. The algorithm executed by the master node corrects the actual axial length and circumference of the arterial based on the hardcoded information on the morphology of each cell (i.e the length and the width of an EC or SMC). Based on this information, an integer number of the ECs accommodatable in the new axial length, the number of ECs axially per node and therefore the subdomain size is decided. This information is then communicated to each processor in the global scope of existence, called communicator, namely MPI_COMM_WORLD. From here on, all further instructions are executed by each node in MPI COMM WORLD. upon receiving the subdomain information, each node creates instances of each cell of the computational subdomain as a C structure whose members include state variables, information on location on the grid and local stimuli values e.g $J_{PLC_{agonist}}$. Each node also allocates memory of Send and Receive buffers where the coupling information is stored or received at each time step.

Once the memory allocation is complete, each node initiates a local instance of C++ object of the solver, RKSUITE, which will have to deal with a computational domain of size $\frac{\text{Global computaional domain}}{\text{number of nodes in the communicator MPI COMM WORLD}}$. Unlike the serial program explained in Section 5.4.2 where RKSUITE was used in “CT” mode, it is setup in “UT” or *Usual Task* mode in the present case. In the UT mode, RK-

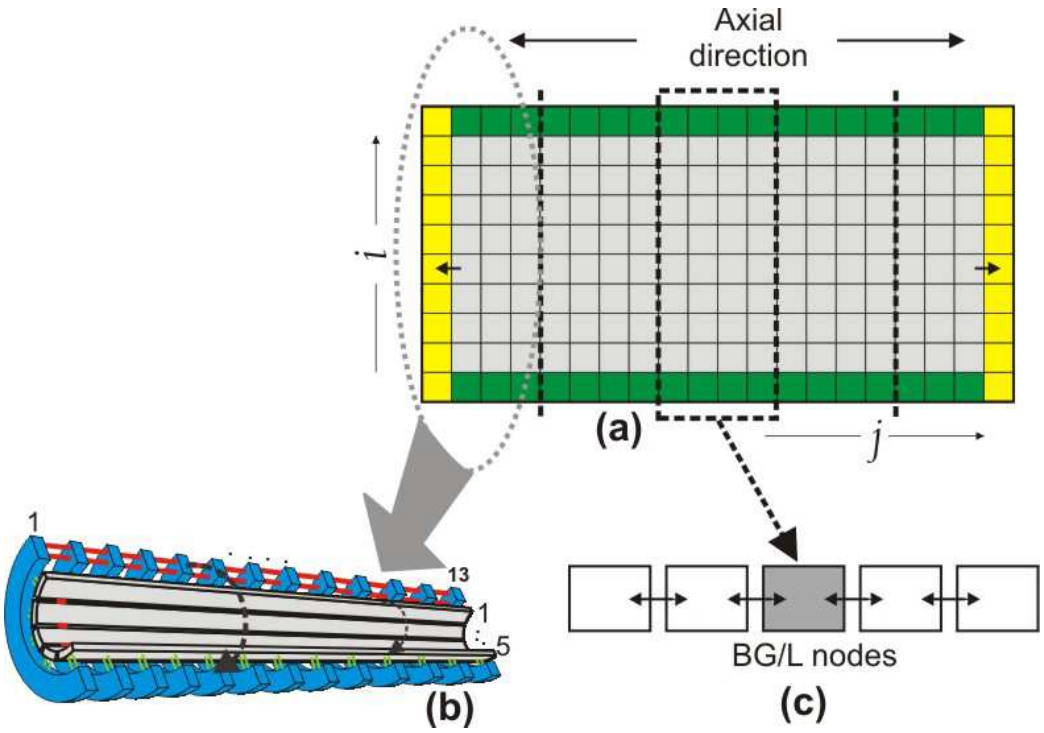

Figure 6.8: Schematic shows the domain decomposition strategy to map the complete computational domain on several Blue Gene/L nodes. The grid in (a) represents the computational domain simulating a straight arterial segment, decomposed in the axial direction (demarcated by the black dashed line). The cells in green at the bottom are coupled to the cells in in green on top, implementing the periodic coupling (closing the circumferential loop). The cells in yellow are sinks to the effective computational domain (comprised by cells in grey and green) making the boundaries non reflective. Each chunk, such as the one encircled by dashed grey line an magnified in (b) consists of blocks of cells populations, ECs and SMCs homocellularly and heterocellularly coupled where, the minimum segementable axial distance is equivalent to the length of 1 EC or 13 SMCs. The number of SMCs or ECs circumferentially depends on the diameter of the simulated arterial section, which is user defined. Each such periodically coupled segment is then mapped to on BG/L node. The bidirectional arrows in (c) represent the exchange of coupling information between the cells on the edge of each segment, using MPI calls by each processor.

SUITE is given short time intervals between which it attempts to integrate the solution for ODEs using its adaptive step size selection. Using UT in a loop allows incrementing the solution by a defined interval. This aides in synchronizing the internode communication which sends and receives the coupling information necessary for integrating the solution at each time step. After completion of every successful step, statistics report of RKSUITE is called by calling an RKSUITE function STAT, which, amongst other things, reports the next step size. Each node then communicates its locally estimated new step size to all nodes, where the minimum step size is selected as new step size to proceed the solution in time. This way all the node *march* forward in time, in synchrony. MPI_Alltoall is one of the functions of the MPI library which can do a *many to many* or broadcast communication and is an example of collective communication. Thus at the end of each time step,the intercellular coupling data is exchange between two neighbouring nodes via *point to point* MPI calls and the each BG/L node subsequently broadcasts the next step size suggested by its local instance of the RKSUITE, to all the processors of MPI_COMM_WORLD. Once all the nodes have received the step size of all other nodes, every node then evaluates the minimum step size and sets it as the next step size for the RKSUITE.

Point to point MPI communication between two nodes can be implemented in either *synchronous* or *asynchronous* mode. In synchronous mode, each MPI_Send must have a matching MPI_Recv posted on the destination node. If there is a mismatch, the code will be stuck waiting for the appropriate action to be taken by the other node. This is called a “deadlock”. The computational domain decomposition, as shown in the Figure 6.8, each node, except for the first and the last node, has to communicate with two adjacent nodes, one on each side. In the case of synchronous point to point messaging, at the end of each time step, each node will posts an MPI_Send to two nodes it is communicating to and then posts a MPI_Recv, expecting a message from each adjacent node. This is bound to produce a deadlock because each processor is going to expect a *message received* acknowledgement from the destination nodes it has sent its message to. One way around this is implementing one sided communication where each preceding node posts a MPI_Send and the following node post a corresponding MPI_Recv. Once it is completed in one direction, i.e. from node *1* to *n*, the same should be imple-

mented in the reverse direction, i.e. from *n* to *1*, thus node *n* sends first and *n-1* posts a corresponding receive.

Load balancing is a term used to refer to extent of evenness of the work (computation) distribution to each node in the MPI_COMM_WORLD. In the present case, load imbalance can occur in two scenarios; either a node is mapped with more number of cells compared to other nodes, or a node has to compute more than other node. The later can occur when simulating the spatial gradient in agonist concentration, where RKSUITE on one node may decide to take smaller steps than other nodes in MPI_COMM_WORLD. If the internode communication is one sided communication in synchronous mode, a load imbalance may result in slower execution of the code and the speed will be dictated by the slowest node amongst the group.

In *nonblocking or asynchronous* mode communication between nodes allows a node to post a MPI_Isend for the destination node or MPI_Irecv for the source node (I being the prototype for calling MPI send and receive asynchronously) and continue the computation without waiting for *receive* acknowledgement by the destination node or arrival of the message from the source node . In the case of uneven subdomain mapping or excessive computation by a node of the MPI_COMM_WORLD, asynchronous communication helps in preserving the performance of the code by avoiding the wait time while communication is carried out. The parallel algorithms presented in this thesis employed asynchronous point to point MPI communication.

In the case of implementation of spatial gradient in the agonist concentration, there is a possibility that the solution on a node **N** may be more stiff than others. In this case, the adaptive step size selection of node **N** may result in dictating unnecessarily small step size to all the nodes in MPI_COMM_WORLD. Another issue that the above presented algorithm may present is the increase in communication overhead due to the repeated calls to collective communications while using MPI_Alltoall for broadcasting of the local step size. The flowchart in Figure6.10 shows a modification in the algorithm to avoid this from happening. Instead of selecting the minimum step size broadcast by all the nodes to all the node, the internode communication for transmitting the intercellular coupling information is done at every $1e^{-2}$ or 100^{th} of a second. During this interval, RKSUITE on each

node adaptively selects the step size depending on the stiffness of the solution locally. This comes with no significant compromise on the validity of the computational results, as shown in Figure 8.1, and will be discussed in the 8 where the results of different intercellular coupling scenario are considered. The performance gain by using the improved version of the algorithm was non-existent in the case where intercellular coupling was trivial and had no major influence on the computation of the destination node, but it did matter non-trivial intercellular coupling environment was implemented. The improvement in the performance has been discussed in Section 8.1.

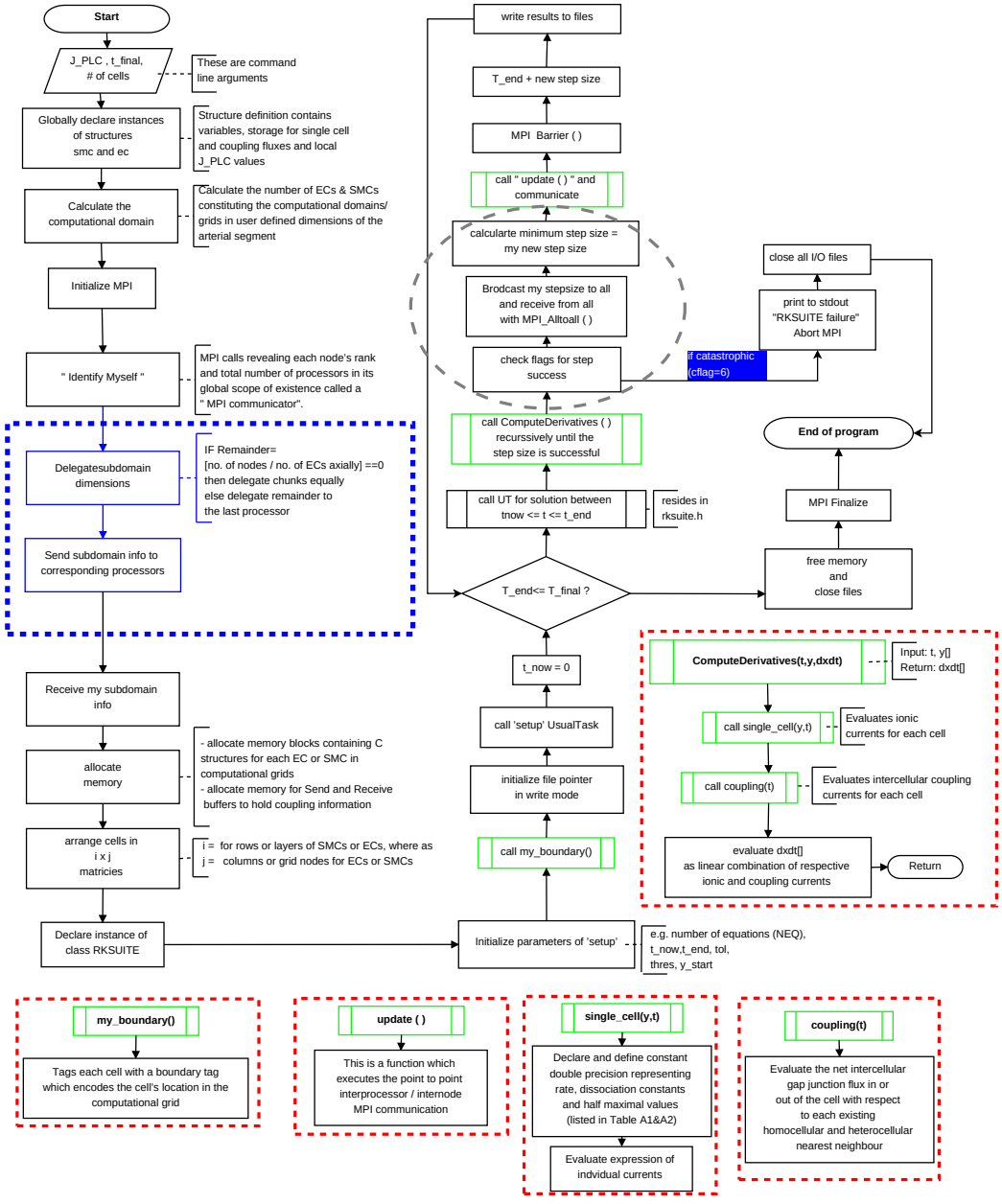

Figure 6.9: Flowchart shows the C code for every BG/L node. All work in boxes bounded by black solid lines is executed by all the processors, where as work in blue box (dashed line) is to be carried out by the *master node* exclusively. The boxes in green are function that are further highlighted in red boxes bounded by dashed lines. The grey circle specifies the time synchronizations of the nodes existing in the global instance of the communicator "MPI_COMM_WORLD". After receiving the subdomain information, each node creates its own sets of unitary structures encoding either an EC or SMC. Each node than initiates a local C++ object instance of RKSUITE to solve its computational subdomain. Upon successful completion of the step, every nodes communicates to all the nodes, the step size for the next step reported by its local RKSUITE instance. The minimum step size of all the nodes is then taken as the new step size by all the nodes.
Magnified version of this flowchart can be found on page 211.

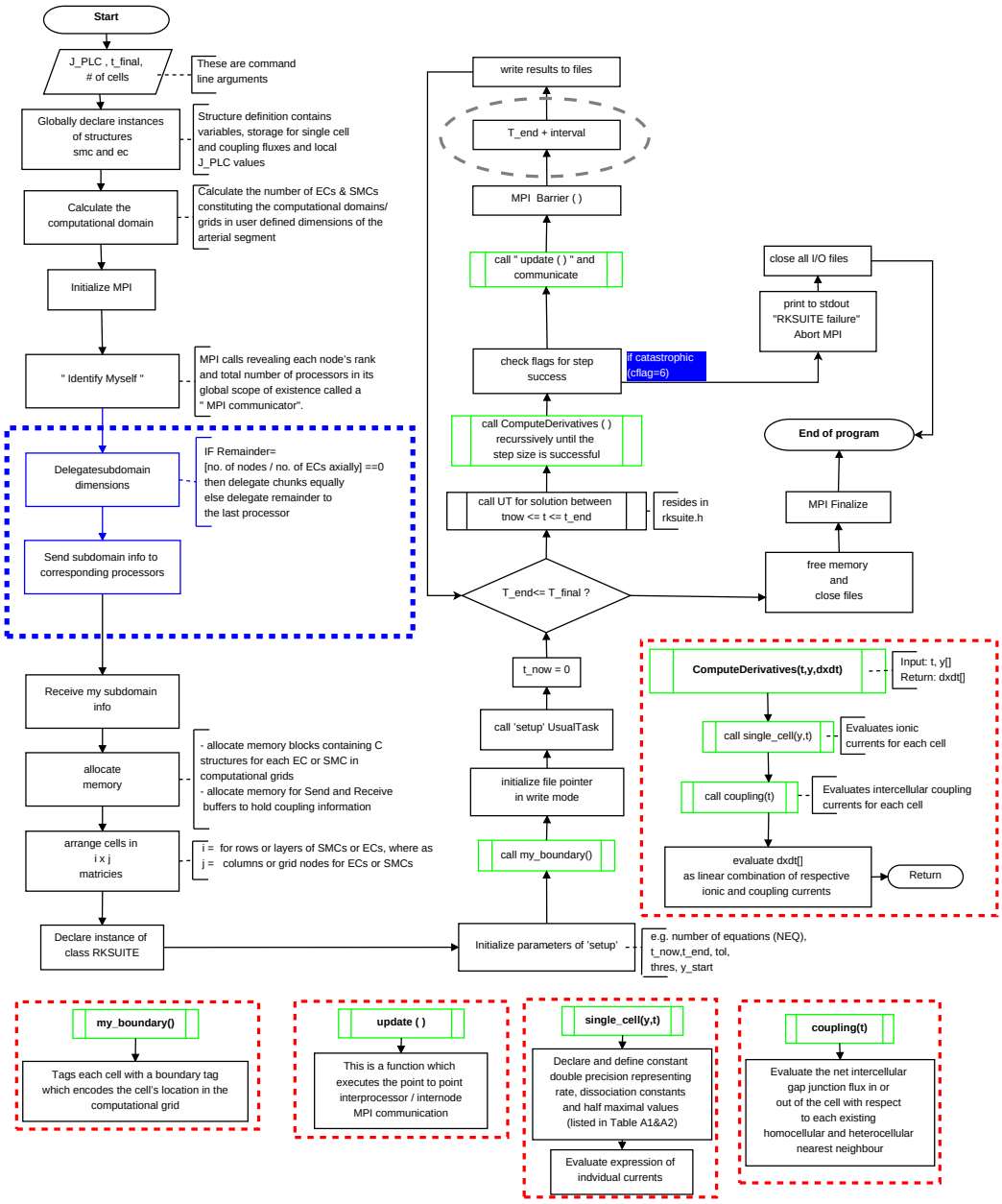

Figure 6.10: Comparing with the flowchart in Figure 6.10, the box encircled in grey is the ammendment where INTERVAL= $1e^{-2}$ is a constant increment made to the T_end, during which RKSUITE on each node can select the next step size adaptively within this interval.
Magnified version of this flowchart can be found on page 212.

6.4 Distributed memory SPMD implementation performance

Scalability is a property of a system, or a software application (algorithm) in the present case, that relates the performance of the algorithm with the expansion of the hardware resources or the workload (problem size). A code is said to *scale* if it performs linearly when resources (compute nodes or memory) are added to the system executing it. Scalability is a measure of the performance of an algorithm, especially when mapping it on multicore computers. A scalable code is always desired as adding more computing resources improves the performance of such a code. In the light of this fact, it is useful to analyse how the two parallel programs discussed in Section 6.3.2 scale.

Two notions of scalability are of interest which determining the performance of a code, especially the one built on message passing model. Defining hardware resource as nodes on BG/L, *Strong scaling* is how the solution time varies with increasing number of nodes for a fixed problem size. Strong scaling tells us how fast can an application run as number of nodes increase. In this context, *speedup* is ratio of the compute time of a computational domain of size N on 1 node and compute time of running the same computational domain on p number of nodes.

$$Speedup = \frac{T_1}{T_p} \tag{6.1}$$

where T_1 and T_p are compute times for running the application/code on 1 and p nodes.

Weak scaling is how the solution time scales with increasing problem size, for a fixed amount of work per node. Weak scaling is tested by keeping the problem size per node constant and increasing the number of nodes. While the strong scaling is a qualitative indication of how the parallel overhead varies with number of nodes n, weak scaling shows how fast or slow these overheads vary with the growing amount of work per node. Figure 6.11 shows the performance of the two codes. As a fixed problem size for strong scaling, an artery of axial length 13.312cm (2048 ECs axially) and of 50 μm radius, comprising a total of 61440 ECs and 159744 SMCs were simulated. The arterial segment was stimulated with

$\widetilde{J}_{PLC_{agonist}}$=0.4 μM/s on ECs, a rate of PLC known to cause oscillations in the underlying SMCs, as was shown in Section 5.5.3. The intercellular coupling was switched off when simulating the artery in the case of both code. This was done to avoid the possible bias caused by the smaller time step taken by the numerical solver because of Ca^{2+} oscillation in SMCs, especially in the improved version of the code, where the internode communication is allowed at every 100^{th} of a second, which effectively means that the adaptive step size control of the numerical solver, RKSUITE, has been switched off.

Figures 6.11a & b show the strong scaling of the two codes, original and improved versions, respectively. The intercellular coupling data is exchanged between the nodes using the point to point MPI implementation in asynchronous mode, as described in Section 6.3.2. The coupling coefficients of the intercellular coupling environments (i.e. membrane potential, Ca^{2+} and IP_3) have been set to zero thus making the influence of intercellular coupling trivial. This makes the computation, independent of the intercellular coupling and each node can now do same amount of computation. This is important to do to assess the increase in communication cost as the size of the system (i.e. number of nodes in MPI_COMM_WORLD) increases.

In the case of strong scaling in Figure 6.11a & b, both codes scale strongly on BG/L nodes. The linear scaling in the case of trivial intercellular coupling highlights that the communication cost does not increases severely with increase in the system size. This means that the mapping of larger data sets on bigger number of nodes is plausible and comes with negligible communication cost and any additional cost will be arising from the computational aspect of the problem. Thus both codes are scalable.

Weak scaling results, shown in Figures 6.11 c & d for original and improved versions of the MPI code respectively, suggest that the change in the cost of communication with increase in number of nodes is trivial. This is essentially the because of the nature of the MPI communication implemented in the algorithms, i.e. the *point to point communication*. Because of the *3D torus* interconnect of the BG/L nodes and because of the dimension in which the computational domain is decomposed (i.e. axially), each node can physically talk to the two adjacent nodes. The collective communication in the original code dose not add significantly to the

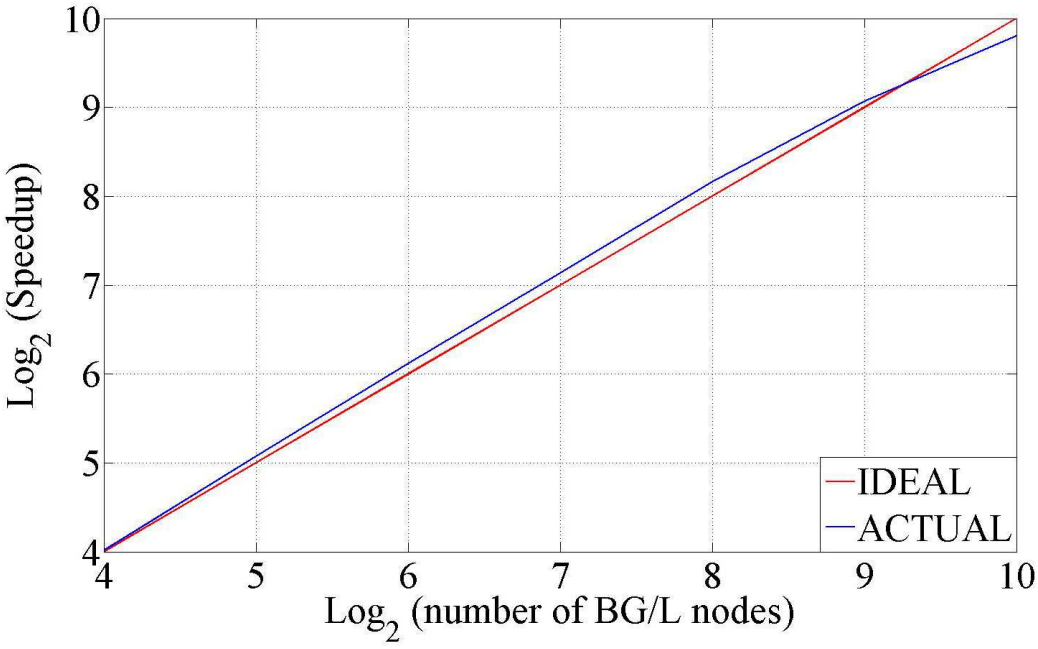

(a) Strong scaling of original code

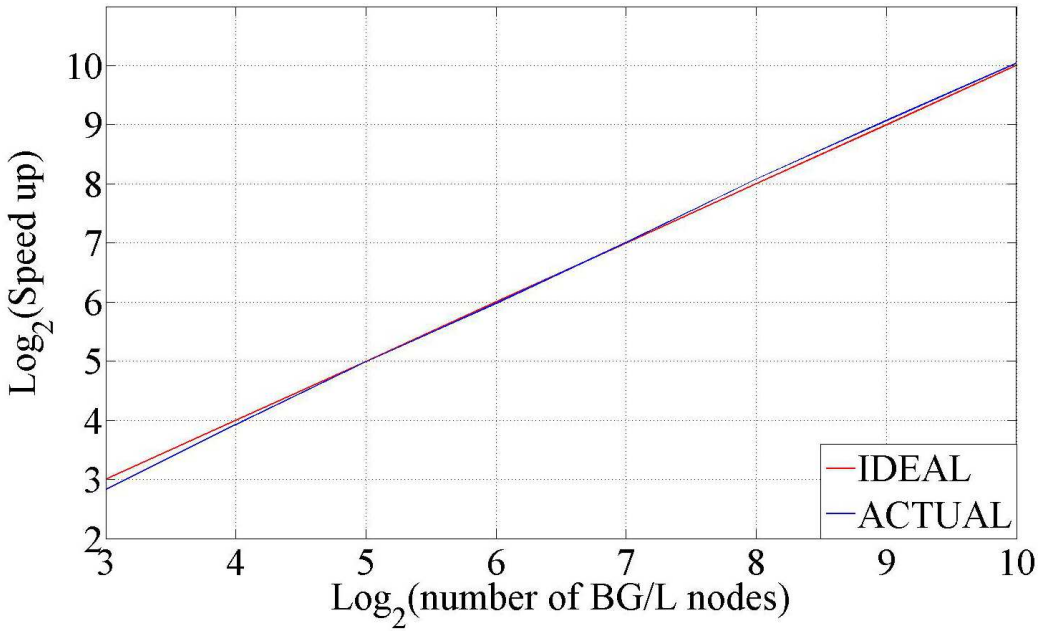

(b) Strong scaling of improved code

Figure 6.11

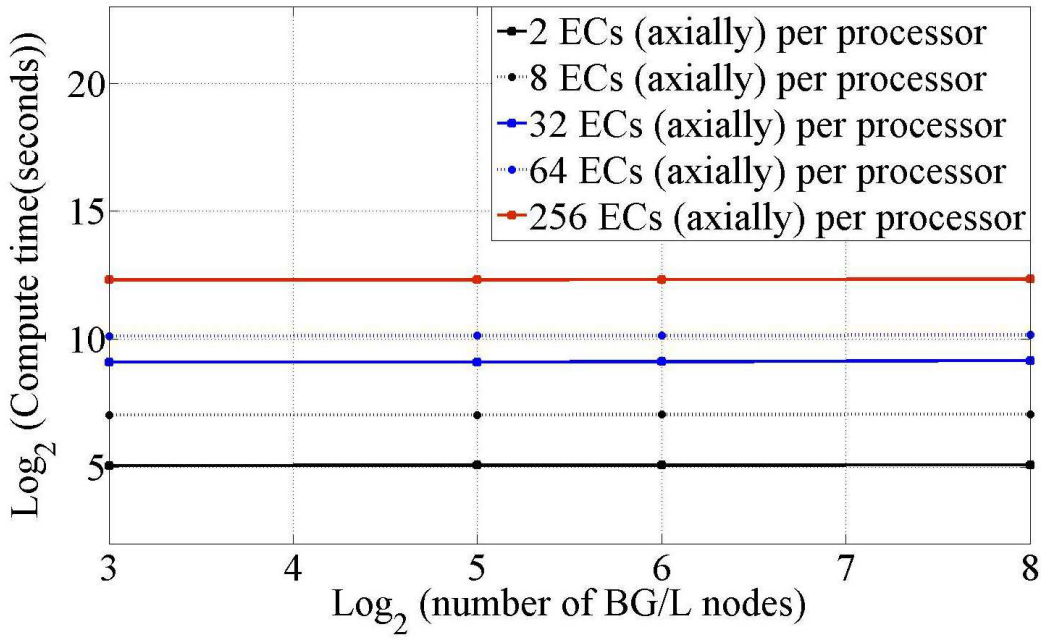

(c) Weak scaling of original code

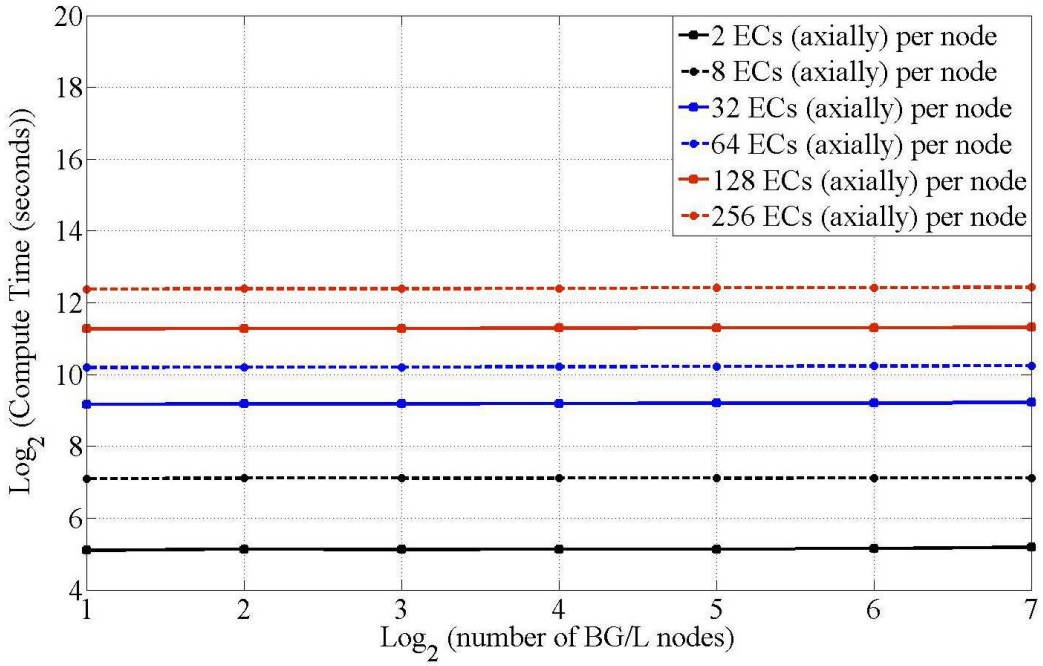

(d) Weak scaling of improved code

Figure 6.11: Figure shows scaling results of mapping the problem on the Blue Gene/L nodes. Figures a & b show strong scaling of the two codes, the original and the improved versions respectively. Both are comparably fast and scale linearly. Figures c & d, in the same order, depict the weak scaling of the two codes. Both codes scale well on many nodes with little communication cost.

communication cost, as suggested by the constant plot lines in Figure 6.11c.

The scaling results presented in this chapter indicate the possibility of simulating large systems of coupled nonlinear equations by mapping them on many nodes of BG/L. The speedups demonstrated in the figures provides with an expectation that physiologically relevant time scales can be simulated with in practical compute times. The infrastructure developed in this chapter, therefore, is put to test in Chapter 7.

Chapter 7

Spatial Effect of Coupled Arterial Cells

The knowledge of the mechanics of networks of cells is becoming increasingly important to further the understanding of how, and mainly why, systems work they way they do. This need is not limited to human physiology but extends to more diverse domains such a plant biology, zoology and insect biology, with applications of varying significance. Simulating coupled units, which are often small scale systems in themselves, need computational power that was not available to man before this day and age. In many problems where the units being coupled have nonlinear dynamics, it is sometimes difficult to extrapolate the expected behaviour of a large scale (physiologically relevant) system on the basis of simulation results of smaller spatial or temporal scale model. Large scale simulations become necessary to gain insight into the mechanistic understanding of the physiological observations.

In the last chapter parallel algorithms were presented to simulate coupled populations of ECs and SMCs on multiple Blue Gene/L nodes. The scaling results promised the viability of mapping large populations of cells over a large number of compute nodes. This provides pertinent grounds to investigate physiological hypotheses which require the analysis of behaviours of large scale systems and an attempt to understand the mechanistic reasoning of pathophysiologies or *pathogenesis*, thus contributing to the therapeutic enhancement of the diseases caused

by these pathophysiologies. One such attempt is made in this chapter.

We begin by implementing an arterial segment comprising of large populations of coupled ECs/SMCs, represented by systems of nonlinear coupled ODEs and stimulate them with spatially uniform agonist concentration. The Ca^{2+} dynamics of ECs and SMCs will be presented and analysed. In order to understand the system's response stimulated by spatially non-uniform biochemical signal, we simulate a *point stimulation* scenario, where a finite part of arterial segment is stimulated by a high agonist concentration axisymmetrically. This is a nonphysiological scenario, commonly conducted in *in vitro* studies of conducted vasomotion, to observe the system's response in terms of it "connectedness", or its ability to propagate information. Lastly, a physiologically relevant scenario is considered where the agonist concentration profile is an approximation of the spatial varying time averaged ATP concentration at the arterial wall. Here, the variation of intercellular coupling is also considered to represent the states of the arterial segment ranging from normal to early atherosclerosis and finishing with coupling in mature atherosclerotic plaque. Again, Ca^{2+} dynamics of ECs and SMCs is observed in these cases to argue the mechanics of the responses reported.

7.1 Coupled ECs/SMCs Ca^{2+} Dynamics Under Spatially Uniform Agonist Concentration

A straight arterial segment as shown in Figure 7.1a, coupling via heterocellular and homocellular coupling, is simulated to investigate the response of coupled cells under a spatially uniform agonist concentration. Between time interval $100 \leq t \leq 200$, $\widetilde{J}_{PLC_{agonist}}$ increases from 0.2μM/s to 0.4μM/s. The agonist stimulates the artery axisymmetrically from the luminal side, i.e. only ECs are stimulated by the agonist which models the binding of ATP in peripheral blood to the purioreceptors P2Y4, which activates the G protein coupled receptor cascade thus generating IP_3 in the EC cytosol. The details of downstream intracellular processes and the mathematical expression modelling them have been presented in Chapters 3 and 5. The schematic representation of the cells are coupled has been shown in the Figure 5.1.

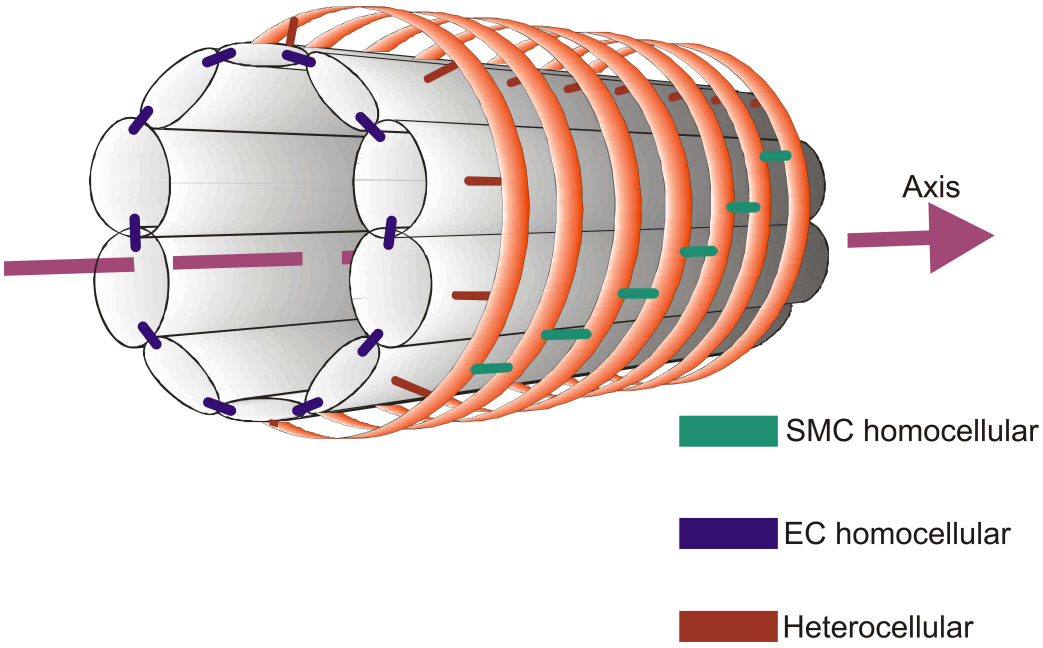

Figure 7.1: A straight arterial segment consisting of longitudinally stretched endothelial cells, circumferentially wrapped around by contractile smooth muscle cells. Cells are coupled with one another either homocellularly or heterocellularly, as suggested by the colour code.

	Heterocellular						Homocellular					
	EC			**SMC**			**EC**			**SMC**		
	V	Ca^{2+}	IP_3	V	Ca^{2+}	IP_3	V	Ca^{2+}	IP_3	V	Ca^{2+}	IP_3
1							✓	✓	✓	✓	✓	✓
2	✓			✓			✓	✓	✓	✓	✓	✓
3	✓	✓		✓	✓		✓	✓	✓	✓	✓	✓
4	✓	✓	✓	✓	✓	✓	✓	✓	✓	✓	✓	✓

Table 7.1: By setting up various intercellular coupling configurations the effects of spatially uniform agonist concentration on the Ca^{2+} dynamics of the two cells is considered. The homocellular coupling was altered in Sections 5.5.1 and 5.5.2. Here heterocellular coupling is enabled or disabled to see how the *many cells scenario* is different than the response of *single unit* or *homocellular coupled isolated populations* to spatially and temporally uniform agonist concentration.

The simulated arterial segment is 0.416 cm long, 50 μm in radius, and comprise of 4992 SMCs and 1920 ECs. Although the dimensions are approximately of the order of 1st order arteriole, it is shown later in the chapter that the diameter dose not matter in the case when the agonist stimulates the arterial in an axisymmetrical manner. Four cases of altered intercellular couplings are investigated here, tabulated in Table 7.1.

In the first case, heterocellular coupling between ECs and SMCs is disable completely. Figure 7.2a shows the Ca^{2+} concentration in SMCs and ECs laid out parallel to the longitudinal axis. The Ca^{2+} concentrations are taken at t=100 sec, when the systems of equations have evolved to their steady states. The ECs in the case of disabled heterocellular coupling assume a high steady cytosolic Ca^{2+} concentration, uniform axially. The SMCs on the other hand, attain a steady state Ca^{2+} concentration which is low, similar to what they will attain when stimulated by low or no agonist (i.e. IP_3 generation=0). In Figure 7.2b, only heterocellular membrane potential coupling is enabled. The hyperpolarized EC membrane potential has now an influence on the membrane potential of SMCs, making it more negative. The effect is increase in the activity of the membrane bound Na^+/Ca^{2+}exchanger which is responsible for efflux of Ca^{2+} from cytosol to the extracellular space and brings in the Na^+ ions in a ratio of 1 : 3, hence the color of SMC Ca^{2+} concentration is mapped as dark blue compared to the former case in

Figure 7.2a.

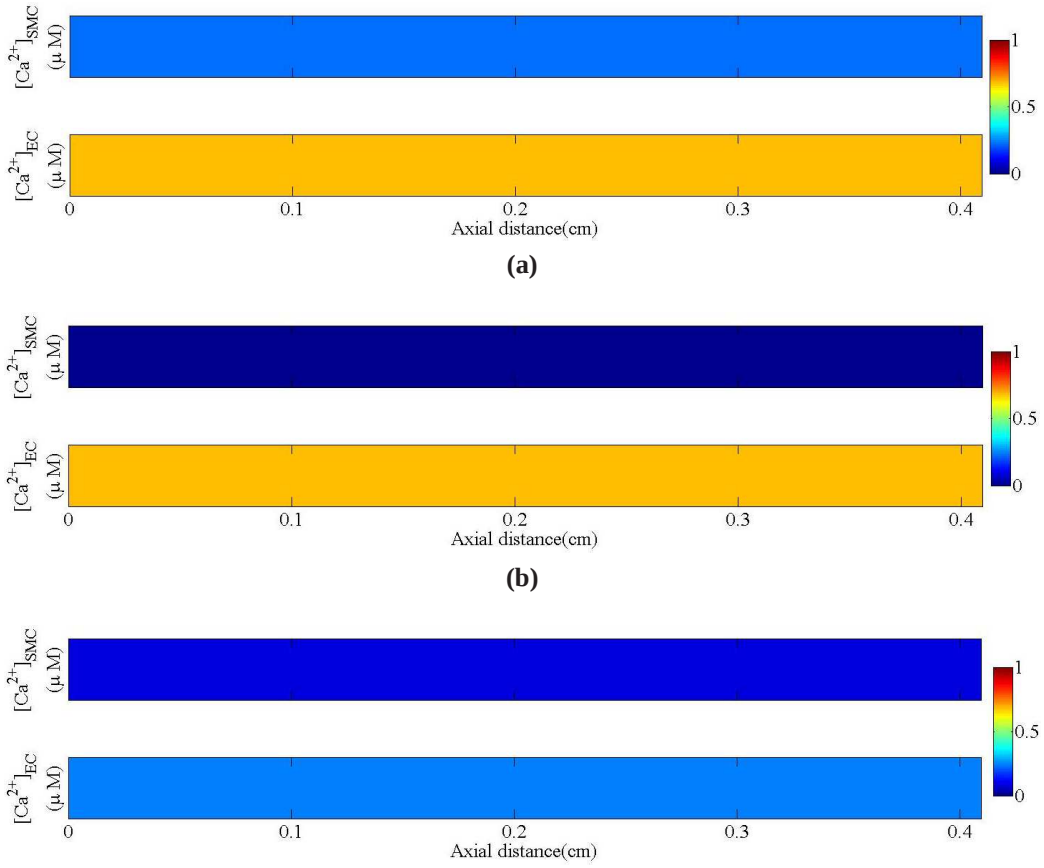

Figure 7.2

Figure 7.2c presents the case where heterocellular membrane potential and Ca^{2+} coupling are enabled between the ECs and SMCs whereas the two cell types are coupled homocellularly via Ca^{2+}, IP_3 and membrane potential. Stimulating with the same $\widetilde{J}_{PLC_{agonist}}$ value of 0.4μM/s, the Ca^{2+} concentration in the cytosols of the ECs is low compared what was observed in Figures 7.2a & b. The SMC Ca^{2+} concentration has risen in comparison to that seen in Figure 7.2b where only membrane potential coupling existed. Ca^{2+} diffuses from high concentration pool in ECs to the low concentration pool in SMCs in this case. The effect of the intercellular Ca^{2+} transport is controlled, between the two cells because of the coexistence of hyperpolarized membrane potential coupling. The hyperpolar-

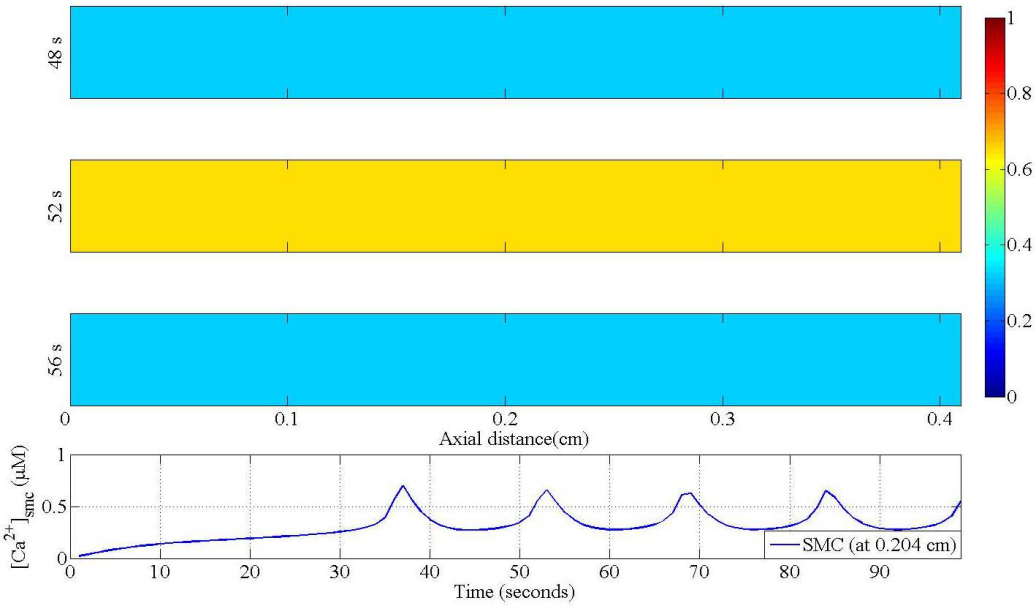
48 s
52 s
56 s
0
0.1
0.2
0.3
0.4
Axial distance(cm)
1
0.8
0.6
0.4
0.2
0
[Ca2+]smc (μM)
1
0.5
0
0
10
20
30
40
50
60
70
80
90
Time (seconds)
SMC (at 0.204 cm)

(d)

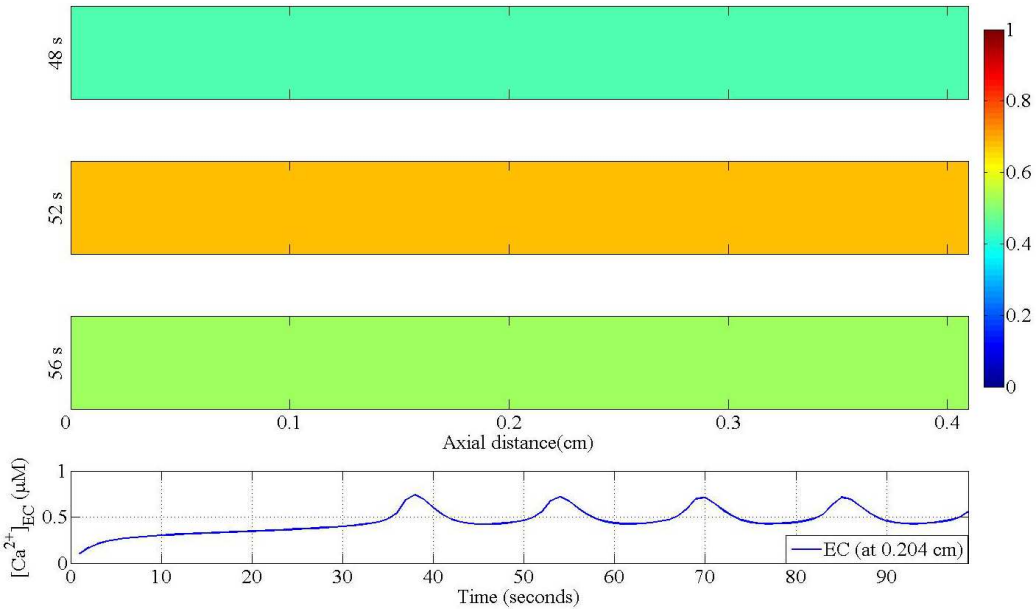
48 s
52 s
56 s
0
0.1
0.2
0.3
0.4
Axial distance(cm)
1
0.8
0.6
0.4
0.2
0
[Ca2+]EC (μM)
1
0.5
0
0
10
20
30
40
50
60
70
80
90
Time (seconds)
EC (at 0.204 cm)

(e)

Figure 7.2

Figure 7.2: Results show Ca^{2+} dynamics of ECs and SMCs of a straight arterial segment stimulated by $\widetilde{J}_{PLC_{agonist}}$=0.4$\mu$M/s. The step increase in $\widetilde{J}_{PLC_{agonist}}$ takes place between $100 < t < 200$ seconds. (a) Heterocellular coupling is disabled as the first case of simulation. (b) As a second case, heterocellular membrane potential is enabled. (c) Heterocellular Ca^{2+} coupling in also enabled in this case, in conjunction with the membrane potential coupling. (d) shows the time evolution of cytosol Ca^{2+} concentration on the axial scale at time stamps 48,52 and 56 seconds. The color map at the three time steps suggests the rise and fall of the Ca^{2+} concentration in all the cells synchronously. The last bar is a Ca^{2+} concentration plot versus time of a SMC located at 0.204 cm on the longitudinal axis of the artery, which shows the Ca^{2+} oscillations clearly. (e) shows a similar behaviour in ECs which do not oscillate as isolated cells or in homocellular population. The Ca^{2+} oscillations are demonstrated by the varying color in the top three bars, suggesting a rise and fall of the Ca^{2+} concentration (the peak to peak difference is smaller than what was witnessed in SMCs in (d)). The following plot at the bottom shows the time evolution of an EC located at 0.204cm axially. The Ca^{2+} oscillations are in phase with the SMC Ca^{2+} oscillations.

ized SMC membrane potential promotes the efflux of Ca^{2+} through Na^{+}/Ca^{2+} exchanger while the Ca^{2+} contributed by ECs tends to increase cytosolic Ca^{2+} in the neighbourhood SMCs. The net Ca^{2+} concentration in the SMC cytosol is thus relatively higher than seen in Figure 7.2b.

Enabling heterocellular IP_3 coupling, bidirectionally (i.e. from EC to SMC and vice versa), produces Ca^{2+} oscillations in SMCs, as shown in the Figure 7.2d. Similar oscillations are also observed in the cytosol Ca^{2+} concentration of the ECs in Figure 7.2e. IP_3 generated in the ECs, in response to the agonist stimulation at $\widetilde{J}_{PLC_{agonist}}$=0.4$\mu$M/s diffuses through heterocellular junctions, modelling the anatomical occurrence of myoendothelial junctions between ECs and the SMCs. The resultant IP_3 increase in SMC cytosol enables SR Ca^{2+} release and downstream processes. The oscillations in the EC Ca^{2+} concentration (as shown for a single cell located at 0.204cm on the axis, are not indigenous but an effect of the coupled membrane potential. The membrane potential of the SMC also oscillates with the Ca^{2+} oscillation, thus producing oscillation in the EC membrane potential too. Such effect was also observed in the case of single unit in Section 5.5.3 and shown in the Figure 5.12. Thus in the case of stimulation with spatially uniform

agonist concentration, the ECs and SMCs behave in synchrony over the complete axial length. The significance of heterocellular IP_3 coupling has been highlighted by the results. In the absence of heterocellular IP_3 coupling, the SMC Ca^{2+} concentration does not evolve to an oscillatory state. Heterocellular membrane potential coupling is shown to play an important role in hyperpolarizing the SMC membrane potential and closing the *voltage operated* Ca^{2+} *channels*. Hyperpolarized membrane potential also inhibits the sustained increase in the Ca^{2+} concentration by promoting the efflux of cytosolic Ca^{2+} into extracellular space via Na^{+}/Ca^{2+} exchanger.

7.2 Effects of point stimulation on arterial coupled cells

As the first step towards simulating the spatially non uniform agonist profiles, point stimulation is considered here to investigate how coupled cells react to such stimulus pattern. For this, a straight arterial section, 3.328 cm long and of 50μm radius, is mapped with a uniform basal $\widetilde{J}_{PLC_{agonist}}$=$0.2\mu$M/s. A local step change is induced where $\widetilde{J}_{PLC_{agonist}}$ value increases to a higher value between time interval $100 > t > 200$ seconds on ECs located at axial distance between $1.475 < x < 1.846$cm. Two cases are simulated with two different values of step increase in $\widetilde{J}_{PLC_{agonist}}$, 0.4μM/s and 0.7μM/s. The choice the value of step increase is dictated by the fact that in coupled ECs/SMCs, $\widetilde{J}_{PLC_{agonist}}$=$0.4\mu$M/s stimulation of ECs is capable of inducing low frequency high magnitude whereas $\widetilde{J}_{PLC_{agonist}}$=$0.7\mu$M/s stimulation induces high frequency and low magnitude cytosolic Ca^{2+} oscillation in underlying SMCs. This has been shown previously in Section 5.5.3. The stimulus is removed at time=200 seconds and the $\widetilde{J}_{PLC_{agonist}}$ value resumes to the basal level in both cases. Figure 7.3 shows the SMC Ca^{2+} dynamics at different times and also the time course of cytosolic Ca^{2+} in three cells, in each case, chosen from upstream , downstream and from the middle of the location where stimulus is applied.The status of the intercellular coupling is such that all homocellular and heterocellular couplings are enabled.

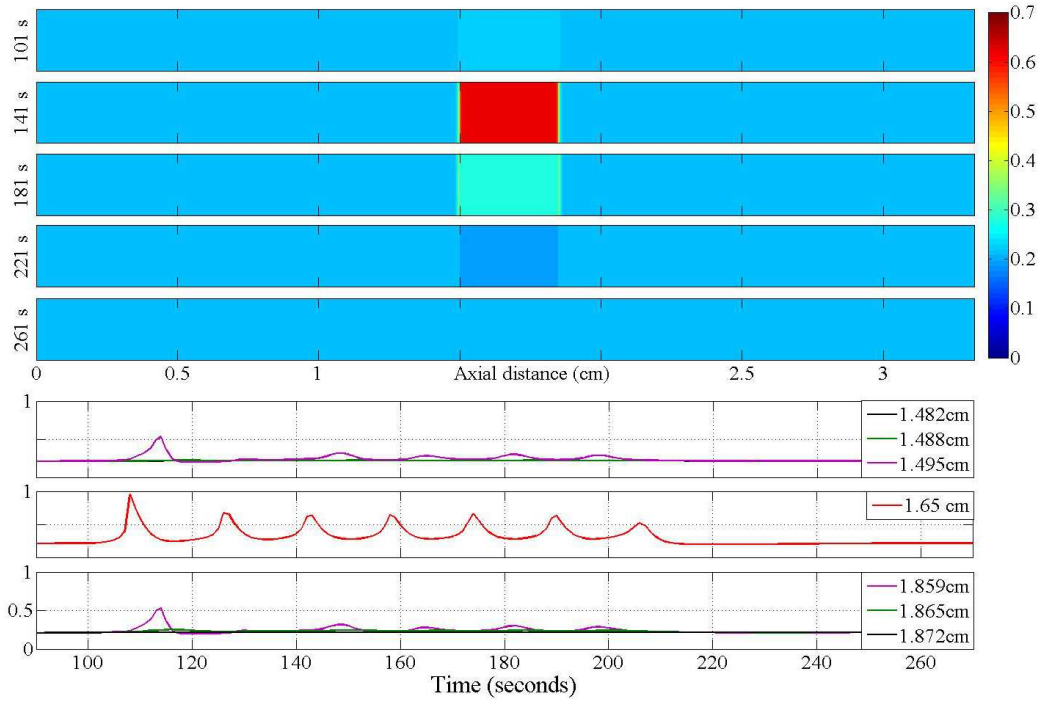

(a) $\widetilde{J}_{PLC_{agonist}}$=0.4$\mu$M/s

Figure 7.3

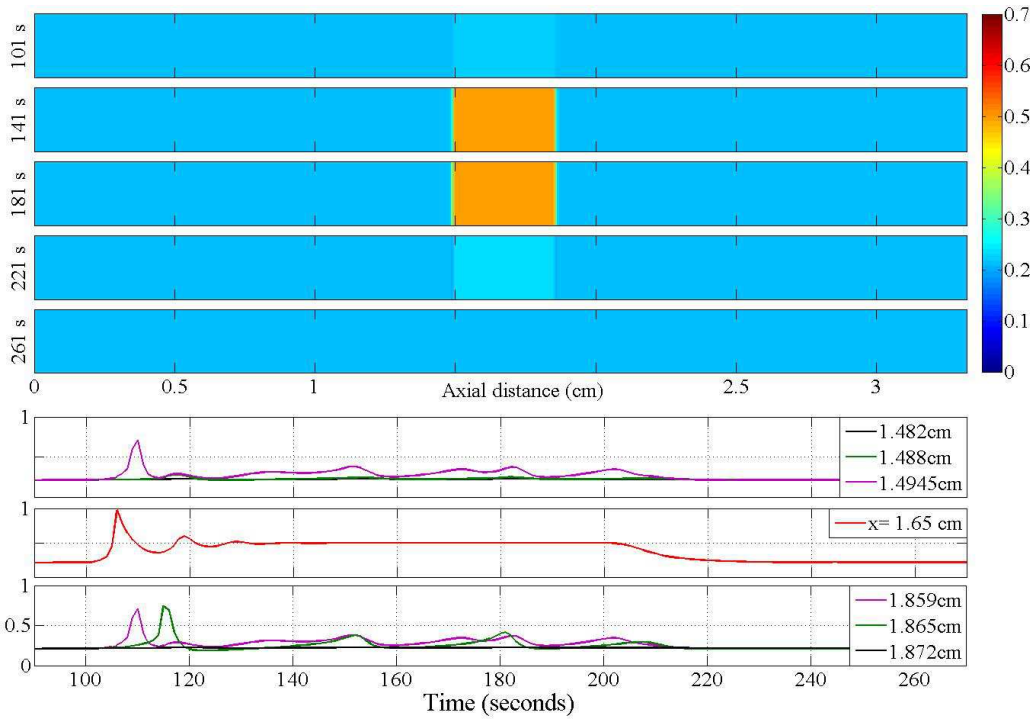

(b) $\widetilde{J}_{PLC_{agonist}}$=0.7$\mu$M/s

Figure 7.3: Figure shows the Ca^{2+} dynamics of the SMCs in axial direction, at different time steps. For *Time < 100.0 seconds* the ECs of the arterial segment are stimulated by $\widetilde{J}_{PLC_{agonist}}$=0.2$\mu$M/s. The ECs between axial distance 1.475 < x < 1.846cm experience a step increase in $\widetilde{J}_{PLC_{agonist}}$ value (a) $\widetilde{J}_{PLC_{agonist}}$=0.4$\mu$M/s and (b)$\widetilde{J}_{PLC_{agonist}}$=0.7$\mu$M/s, at *Time = 100.0 seconds)* simulating point stimulation for a time interval. SMCs underlying the stimulated ECs attain either steady state oscillations or a equilibrium Ca^{2+} concentration, as is the case in (a) and (b) respectively. This change in response cannot propagate to the upstream and downstream cells. SMCs coupled to the ECs stimulated with high $\widetilde{J}_{PLC_{agonist}}$ oscillate. The immediate neighbours coupled to the first and the last cell of this block of oscillating SMCs tend to synchronize their Ca^{2+} concentration. The bottom plots in (a) and (b) show time course of Ca^{2+} concentration in SMCs at locations, stated in the legends of the plot. The Ca^{2+} concentration of the immediate neighbours, color coded in purple, oscillates prominently whereas in those farthest, color coded in black, Ca^{2+} concentration assumes a low steady state value.

In both cases point stimulation fails to elicit an altered response in the neighbouring cells, both upstream and downstream. Soon after the 100 seconds mark, where $\widetilde{J}_{PLC_{agonist}}$ assumes a high value in cells between axial distance $1.475 < x <$ 1.846cm (where x denotes axial distance), a boundary layer builds at the edge on either sides of the block of cells collocated and coupled with stimulated ECs. This boundary layer also contains SMCs which are coupled to the ECs spatially experiencing the basal $\widetilde{J}_{PLC_{agonist}}$ value of 0.2μM/s. These SMCs fail to attain a higher Ca^{2+} concentration. The Ca^{2+} concentration, however, oscillates, producing nearly the same number of Ca^{2+} oscillation in the 100 seconds interval (between $100 > t > 200$ seconds). This process is observed in both cases in Figure 7.3a&b. $\widetilde{J}_{PLC_{agonist}}$=$0.7\mu$M/s is a value of stimulus which produced sustained Ca^{2+} oscillations in SMC of the single EC/SMC unit (see Figure 5.11). The SMCs underlying the ECs directly experiencing the step change in $\widetilde{J}_{PLC_{agonist}}$ from 0.2μM/s to 0.7μM/s, attains a steady state Ca^{2+} concentration, well before the stimulus is removed. This is because both, the heterocellular Ca^{2+} and IP_3 couplings, are enabled simultaneously. In addition to the contribution of IP_3 from ECs, the addition Ca^{2+} entering the cytosol of underlying SMC elevates the Ca^{2+} such that it switches off the cytosolic oscillator. On disabling the heterocellular Ca^{2+} coupling, an oscillatory state, similar to that seen in the Figure 7.3a, was observed but with higher frequency oscillations and diminished magnitude.

Raising the basal level of agonist activity to $\widetilde{J}_{PLC_{agonist}}$=$0.25\mu$M/s prolongs the oscillatory behaviour, even after the step increase in $\widetilde{J}_{PLC_{agonist}}$ is removed. As shown in the Figure 7.4, the oscillatory behaviour in the SMCs stimulated with step increase in $\widetilde{J}_{PLC_{agonist}}$ and in the neighbourhood cells at the constant basal $\widetilde{J}_{PLC_{agonist}}$ is sustained for longer time compared to the cells at the same locations with basal $\widetilde{J}_{PLC_{agonist}}$=$0.2\mu$M/s.

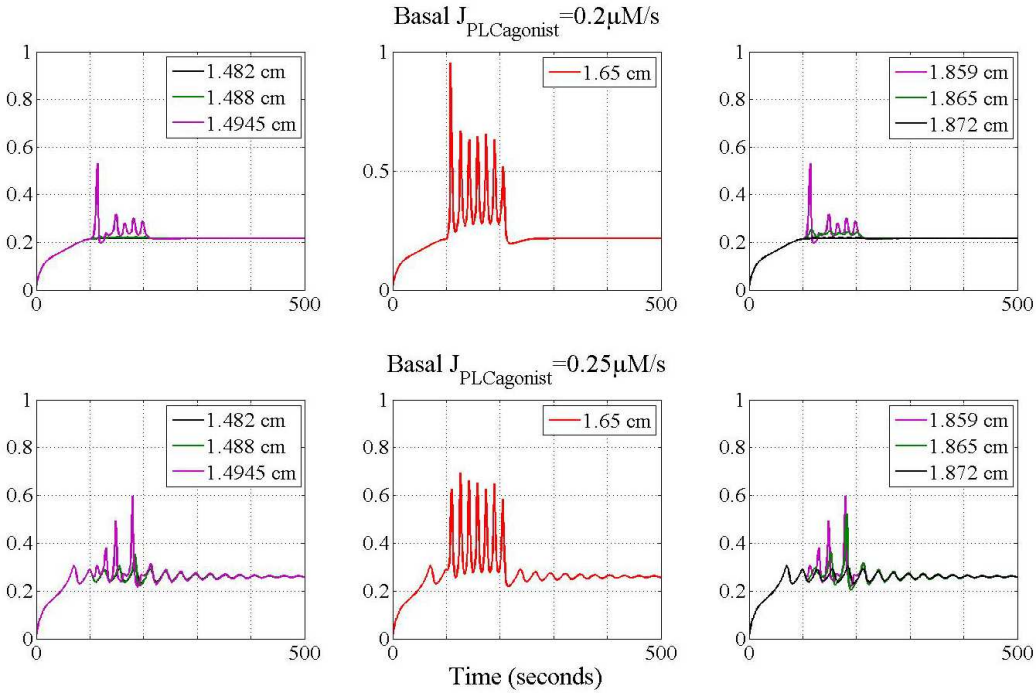

Figure 7.4: Figure shows the effect of raising the basal $\widetilde{J}_{PLC_{agonist}}$ from 0.2μM/s to 0.25μM/s. The top three plots show time course of Ca^{2+} concentration in SMCs located at axial distances stated in the legends of the plots. The bottom three plots are showing the Ca^{2+} dynamics at the same axial locations but with raised basal $\widetilde{J}_{PLC_{agonist}}$. Note that the SMCs color coded in red are the ones coupled to their respective EC neighbours experiencing step increase in $\widetilde{J}_{PLC_{agonist}}$=$0.4\mu$M/s, in both the cases of basal $\widetilde{J}_{PLC_{agonist}}$. The Ca^{2+} oscillations in non stimulated neighbours are sustained for longer at higher basal $\widetilde{J}_{PLC_{agonist}}$(in bottom plots).

7.3 Spatially Varying Agonist and Macroscale Phenomena in Arterial Coupled Cells

Lastly, a straight arterial segment computational layout is considered for mapping a physiologically relevant agonist profile that has been shown to occur at the arterial bifurcations of muscular arteries (e.g. carotid artery or anterior descending coronary arteries). These regions are known to have a strong correlation of altered hemodynamics (low wall shear stress), altered connexin expression and formation of early atherosclerotic lesion which develop into plaques as the pathology progresses over a long time period, subject to the environmental influences such as hypertension, genetic predisposition, hypercholestrimia, smoking, obesity, diabetes etc (Cheng et al., 2006). The arterial wall is reactive to local hemodynamics in normality. This reactivity is partly via the Ca^{2+} pathway, described in Section 2.6, which play a significant role in the regulation of blood flow and maintains the perfusion of the downstream vital organs. In altered hemodynamic patterns, usually observed at the arterial bifurcations in the vasculature, the state of Ca^{2+} dynamics is a relatively unknown territory for experimental scientists because of limitations in *in vitro* techniques. Computational studies such as the present one provides an opportunity to include physiologically valid mathematical models and map them with physiological relevant hemodynamics to acquire mechanistic understanding of the pathobiology that underlies atherosclerosis. An attractive prospect in this practice is the ability to visualize the effects of global change on local Ca^{2+} dynamics (as local as in single cell) and the alteration in the global response of the system because of the additive changes caused by the single cells.

Results in this section have been published in Shaikh et al. (2011). To simulate areas within the arterial segment where flow separation and variation of agonists (ie atheroprone areas and lesion growth) occur, a spatial gradient of agonist concentration (whose scale length is much larger than a single cell) in the axial direction was simulated by altering the $\widetilde{J}_{PLC_{agonist}}$ in a sigmoidal fashion (Figure 7.5) on EC layer. The choice of this particular function reflected two important facts. Firstly work by Comerford and David (2008) has shown that even in a time-dependent solution the ATP concentration can be well represented by a time-averaged profile in areas known to be prone to atherosclerosis, as described in

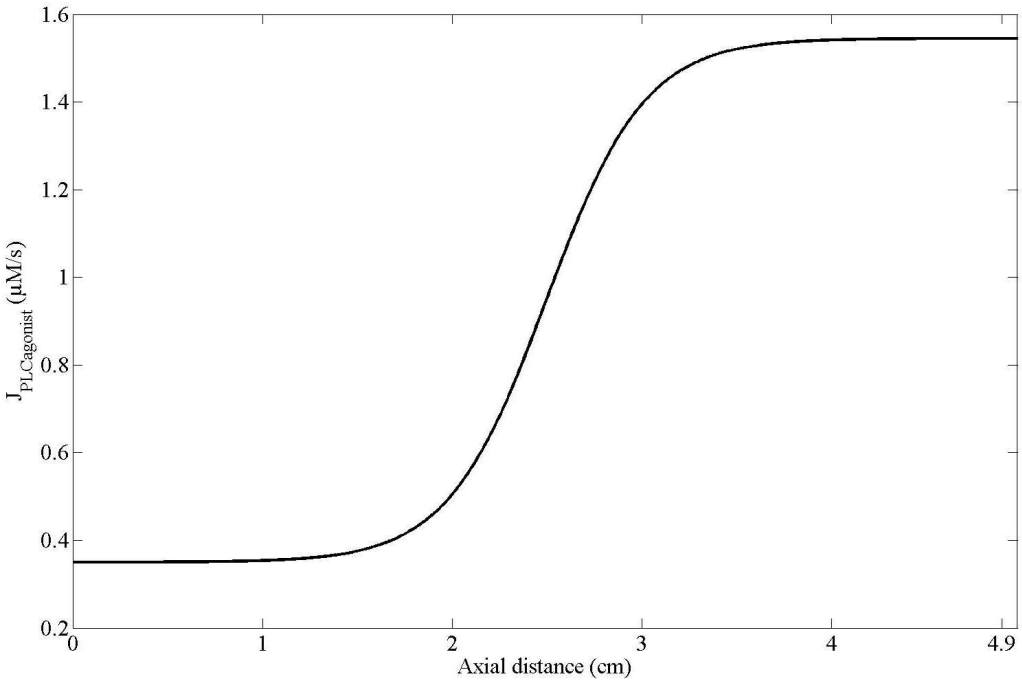

Figure 7.5: Axial profile of the $\widetilde{J}_{PLC_{agonist}}$ flux on the EC layer. From 1.25cm to 3.75cm, ECs experience a steep change in the $\widetilde{J}_{PLC_{agonist}}$ where as at the extremities it is almost uniform.

Section 2.4 and shown in the Figure 2.13. Secondly that we wished to investigate areas of the arterial segment where there existed both constant and "linearly varying" ATP concentrations . Our reasoning behind this is that careful examination of the neighbourhood of fluid stagnation points (where lesions have been shown to exist as noted previously) shows a wall shear stress of linear form followed downstream by a constant shear stress profile as shown in the work of Plank et al. (2006a) and Comerford and David (2008) in the Figure 2.12. Indeed the areas of constant ATP flux also helped in developing a pair of non-reflecting boundaries which allowed waves of Ca^{2+} concentration to properly exit the computational domain. Although in atheroprone regions cells experience low WSS and the mass transfer characteristics are complex it can be shown that the concentration boundary layer of mass transfer thickens in these areas and does not change much with pulsatile flow due to the high Peclet number (Comerford et al., 2008) therefore the simplification of a sigmoid agonist profile seems plausible.

Figure 5.11 in Section 5.5.3 showed the cytosolic Ca^{2+} concentration for a single coupled unit of an EC and an SMC as a function of the agonist flux $\widetilde{J}_{PLC_{agonist}}$. There existed three different areas as noted by Koenigsberger et al. (2005). These correspond to areas of constant Ca^{2+} concentration separated by a range where the Ca^{2+} undergoes oscillatory behaviour and whose amplitude is also a function of the $\widetilde{J}_{PLC_{agonist}}$ value (essentially a monotonic decreasing function). It will be shown below that for large macro-scale coupled simulations this relatively simple 3 domain state does not occur and a far more complex dynamic scenario is present along the arterial segment both in time and space.

Firstly, two prospective scenarios (Case 1 and 2) of intercellular communication corresponding to a healthy arterial segment within a region of disturbed flow and attempt to investigate the Ca^{2+} dynamics in the underlying SMCs.

To avoid confusion it should be noted that there exist two oscillatory phenomena occurring during any one time. Firstly that of the SMC itself (in the time domain) and secondly that of a spatial wave, where at some specified time a concentration gradient exists between adjoining cells due to a phase lag in oscillation of the adjoining cells thus forming a wave in space. For case 1, Figure 7.6 shows the cytosolic Ca^{2+} concentration in SMCs laid out in the axial direction (left is upstream) for eight (8) different times (a - h) in an arteriole of radius 50 μm. For the

case of a spatially uniform agonist concentration (results shown in Section 7.1), cells give a well coordinated Ca^{2+} response, oscillatory or non oscillatory, depending on the value of the agonist concentration or $\widetilde{J}_{PLC_{agonist}}$ value experienced by the ECs as expected when comparing with Figure 5.11. In Figure 7.6 however, in the presence of homocellular Ca^{2+},IP_3 and membrane potential coupling between SMCs, Ca^{2+} and membrane potential coupling between ECs and heterocellular IP_3 and membrane potential coupling across the MEJ, cells show spatially differential intracellular Ca^{2+} responses as a function of axial distance. Bands of varying Ca^{2+} concentration (a Ca^{2+} wave) are visible in the middle of the arterial segment in Figure 7.6a & b where steep gradient exists in the agonist concentration. Units of cells on either sides of this steep gradient region respond in a non-oscillatory behaviour with different steady state intracellular Ca^{2+} concentrations. The Ca^{2+} waves however decrease their wavelength as time increases. Figure 7.6c,d & e show the thinning of these oscillatory bands and by definition an increase in their wave number. In Figure 7.6f, we see this Ca^{2+} wave effect moving towards cells which were originally at low agonist concentration and in a non-oscillatory state. Noteworthy is the fact that an SMC from a single isolated EC SMC pair would not normally oscillate at these concentrations as would be the case from comparing with Figure 5.11. Moreover, thinning of the bands is a requisite to this propagatory response and is a consequence of the cells undergoing oscillatory desynchronisation where cells show a phase lag between neighbours. Hence at any time there exists a concentration gradient capable of transferring Ca^{2+} ions across gap junctions.

To test the relationship between the radius of the artery and the phenomenon noted above a simulation was completed for an artery with 2000 μm radius which allowed 3.5 million cells coupled together and mapped on to 384 Blue Gene/L nodes. Figure 7.7 shows Ca^{2+} concentrations for the 2000 μm radius artery. Direct comparisons can be made to Figure 7.6 for the first 60 minutes. It is clear that there exists no difference in the concentration distribution. This is to be expected given the problem definition since we assume an axisymmetric condition.

Figure 7.8 shows the time evolution of intracellular Ca^{2+} concentration in 12 selected SMCs co-located in groups of 4 at three upstream and downstream space domains (I, II & III), each at three different time durations (each 50 seconds long).

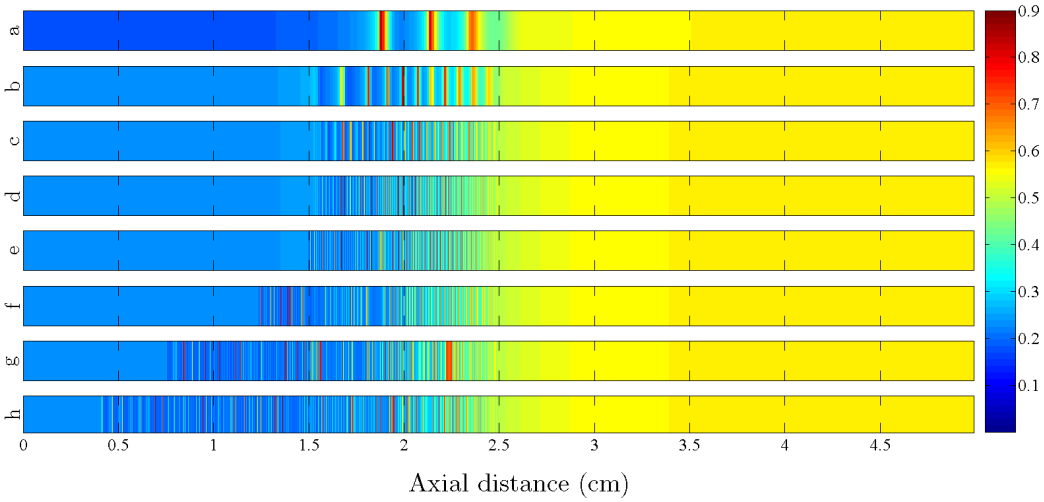

Figure 7.6: (a) to (h) show cytosolic Ca^{2+} concentration in SMCs at time steps 2.5, 4,10,20,30,60,120 minutes and 2.75 hours for an artery of radius 50 μm. The colour in each graph corresponds to the amplitude of cytosolic calcium concentration in each SMC ranging from red (high Ca^{2+} concentration) to dark blue (low concentration), as depicted by the colorbar. Oscillations propagate to upstream cells in (h) where they were absent in (a) to (e).

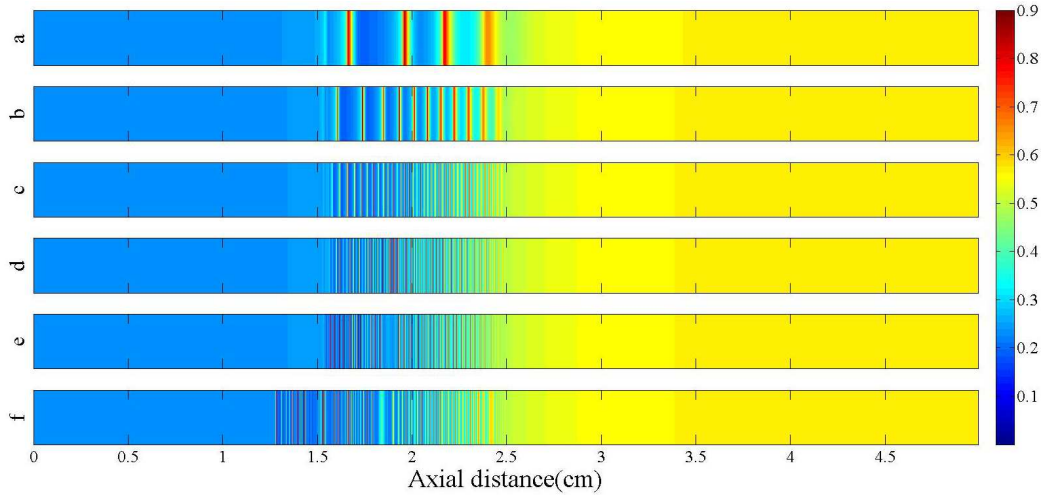

Figure 7.7: (a) to (f) show cytosolic Ca^{2+} concentration in SMCs at time steps 2.5, 4,10,20,30 and 60 minutes for an artery of radius 2000 μm. The colour in each graph corresponds to the amplitude of cytosolic calcium concentration in each SMC ranging from red (high Ca^{2+} concentration) to dark blue (low concentration), as depicted by the colorbar. Oscillations propagate to upstream cells in (h) where they were absent in (a) to (e)

SMCs located in space domain I do not oscillate until the oscillations in the downstream SMCs desynchronize and Ca^{2+} is therefore transported differentially via gap junctions due to the concentration gradient existing at any specific time. Also notable was the observation that absence of homocellular Ca^{2+} coupling between SMCs caused a cessation of the Ca^{2+} propagation to upstream cells. The proposed mechanism driving this behaviour is touched upon further in the Discussion section.

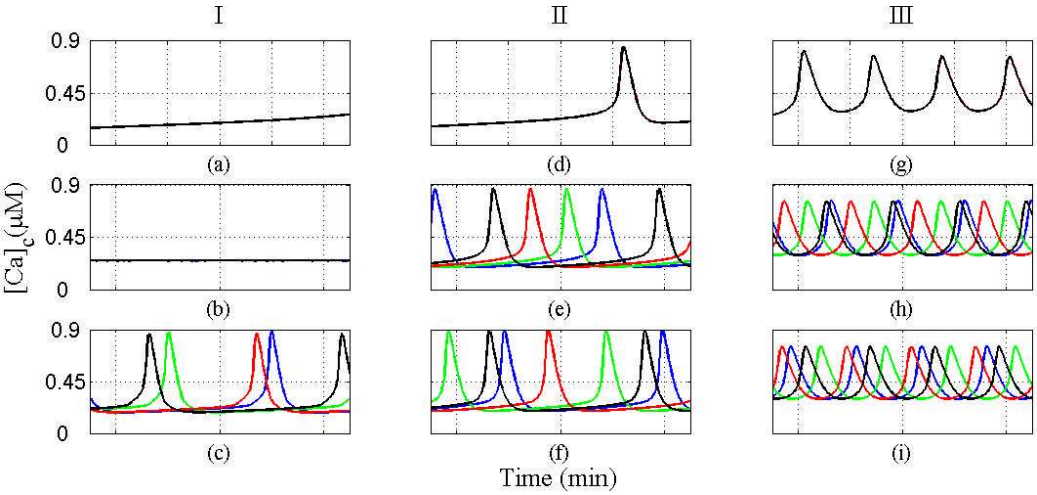

Figure 7.8: Time evolution of intracellular Ca^{2+} concentration in adjoining SMCs at selected axial distances from three space domains, I,II&III, of the arterial segment in oscillatory state. Domain I extends from 1.225cm to 1.234cm, II from 1.472cm to 1.478cm and III from 2.226cm to 2.232cm, axially. Four SMCs from each domain are color coded as black(solid line), grey(solid line), black(dashed line) and grey(dashed line)(cell with Ca^{2+} concentration in black (solid line) being most upstream in each domain) . Ca^{2+} concentration in these SMCs is compared at three 50 seconds long time intervals, 2.08 to 2.92 minutes in a,d and g; 19.6 to 20.416 minutes in b,e and h and 34.6 to 35.42 minutes in c,f and i. These time intervals correspond to the state of the vessel segment shown in Fig 7.6(a,d&e). In the first time interval cells either assume a steady state or oscillate in phase locked loop, as shown in a,d and g. In the latter time intervals the Ca^{2+} oscillations in individual cells from domains II and III desynchronize, prior to the appearance of Ca^{2+} oscillations in SMCs located in domain I.

In the second case of intercellular communication in a healthy vessel, heterocellular Ca^{2+} coupling was enabled in addition to the previously described configuration of intercellular coupling whilst stimulated with the same agonist profile as

before. Figure 7.9 shows the cytosolic Ca^{2+} concentration in the SMCs along the arterial segment at three (3) different times (a - c). Compared with the Ca^{2+} dynamical response in case 1 where heterocellular Ca^{2+} coupling was disabled, the propagation of Ca^{2+} wave to the upstream SMCs is rapid in case 2. Similar to case 1, SMCs at axial locations corresponding to the steep spatial gradient in agonist concentration show bands of varying Ca^{2+} concentration. These bands in Figure 7.9a and b, precedes an increase of Ca^{2+} concentration in upstream cells in Figure 7.9c. However, the extent of the thinning of the oscillatory bands (ie the degree of oscillatory desynchronisation in adjoining cells) is not as severe as in case 1. Also, a comparison of Figure 7.6(f-h) with Figure 7.9c shows that the spatial wave in upstream cells is synchronized in case 2 as compared to case 1 despite the fact that the Ca^{2+} concentration is oscillating temporally in the SMCs of an upstream region in both the cases. More SMCs attain a steady state Ca^{2+} concentration on the downstream side than in case 1. Thus the Ca^{2+} response in SMCs in the intercellular coupling configuration of case 2 is more definitive and rapid, compared to the case 1 where heterocellular Ca^{2+} coupling was disabled.

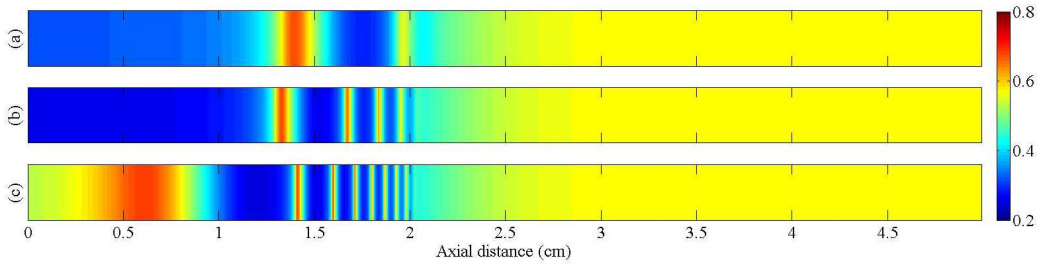

Figure 7.9: (a) to (c) show cytosolic Ca^{2+} concentration in SMCs at time steps 2.5, 4 and 6 minutes for an artery of radius 50 μm with heterocellular coupling enabled (case 2). The colour in each graph corresponds to the amplitude of cytosolic Ca^{2+} concentration in each SMC ranging from red (high Ca^{2+} concentration) to dark blue (low concentration), as depicted by the colorbar. Oscillations propagate to upstream cells in (c) where they were absent in (a) to (b).

Inclusion of homocellular IP_3 coupling between ECs, which simulates the first of the two pathological cases (case3 in Table A.3) did not change the Ca^{2+} dynamical response in the SMCs and was not substantially different from the second healthy case as given in Figure 7.9. Thus upregulation of Cx43 in the presence of unaffected heterocellular Ca^{2+} coupling does not alter the spread of homogeneity

in amongst the SMCs axially.

Implementation of case4 of Table A.3 however had a different outcome compared to other cases. Figure 7.10 shows the Ca^{2+} concentration in SMCs in the axial direction at time intervals of 2.5, 10 and 30 minutes in the simulation. SMCs along the axial distance show moderately high Ca^{2+} concentration, either steady state in cells located at distance $>$2.25cm or oscillating with time in the rest of the vessel segment (upstream). Figure 7.10a when compared to Figure 7.6a is notably different. Case1 at time step 2.5 minutes (Figure 7.6a) was piecewise homogeneous compared to what is seen in Figure 7.10a. We see Ca^{2+} concentration waves from the start of the simulation which leads to a global spatially oscillatory state in Figure 7.10a & b, except for the part of the arterial segment where there exists coupling to ECs experiencing a relatively higher agonist concentration and thus attaining a steady state Ca^{2+} concentration early in simulation. The homocellular coupling between ECs is limited to IP_3 coupling only in this case and the heterocellular coupling is also restricted to IP_3 transfer through MEJs (refer to case4 in Table A.3). SMCs however remain homocellularly coupled via all three media. This simulates intercellular coupling in an advanced atheroma especially at the shoulder of the atheroma where expressions of Cx37 and Cx40 are severely downregulated and Cx43 is upregulated in ECs (Brisset et al., 2009; Burnier et al., 2009). Thus we see the propagation of a Ca^{2+} wave from SMCs provided with a relatively higher amount of agonist flux to those at positions where overlying ECs experience low agonist concentration. This propagation however was much faster when compared with case1; notably Figure7.6f corresponds to 2.75 hrs. We discuss the mechanism behind this accelerated response in the Chapter 8.

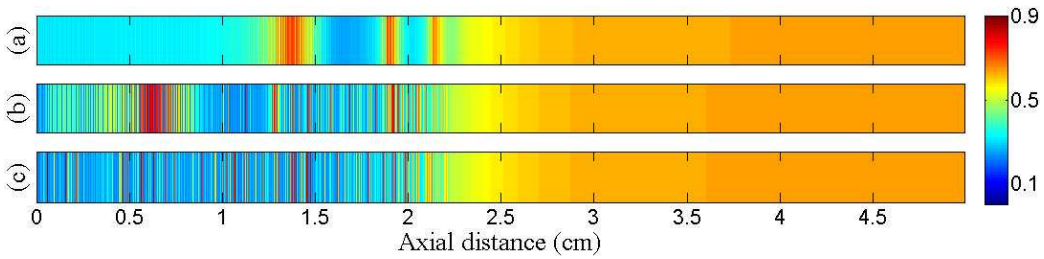

Figure 7.10: (a) to (c) show cytosolic Ca^{2+} concentration in SMCs at time steps 2.5, 10 & 30 minutes for case 4. The color in each graph corresponds to the amplitude of cytosolic calcium concentration in each SMC ranging from red (high Ca^{2+} concentration) to dark blue (low concentration), as depicted by the colorbar.

Chapter 8

Discussion

There are two basic aspects on which the aims and objectives of this thesis are based, one is physiological and the other is the computational aspect. In this chapter, the attempt will be to analyse these aspects separately and join them together in Chapter 9, Conclusion.

8.1 Comparison of Parallel Algorithms

In Chapter 6 two *Single Program Multiple Data* (SPMD) implementations were presented. Noteworthy were the almost perfectly linear speedups observed in the strong scaling in Figure 6.11, for the original and the improved versions of the codes. These results highlight the economic use of the MPI communication implemented in both codes. Thus increasing the problem size and mapping it to a larger number of nodes will not severely hamper the efficiency of the code because of the added communication overheads. Thus it is safe to say that the performance of the code will become a function of computational expense only and mapping of the same problem over larger number of processors will increase the performance the two algorithms.

When mapping bigger segments of the computational domain on a node, gig data portions would reside in the main memory and in the case of a cache miss (when data addressed by L1 cache is not present in L2 or L3 cache and is to be fetched from main memory) a delay will be produced. This is a perpetual issue

when the data portion allocated to a node is big and these delays, per iteration, pile up and result in added resultant compute time. With increasing number of nodes, the data size is per node becomes smaller. Ultimately the whole data size can fit into L3 cache and the no cache miss takes place. Thus one way of reducing the computational cost could be to make the problem size per node small enough to let it fit in L3 cache. Based on the scaling results, this can be achieved with the two algorithms.

Physiologically relevant problems, such as addressed in Chapter 7, seldom present spatially uniform agonist conditions. In the case of non trivial coupling coefficients with spatially varying $\widetilde{J}_{PLC_{agonist}}$, the computational expense increases dramatically because of the increased computational complexity. In such a case, adaptive step size selection in RKSUITE ends up selecting unnecessarily small step sizes, thus increasing the compute time to reach the T_{end} of the solution. Since the techniques used for selection of the next time step are different in the two implementations, original and the improved versions of the code (for details see Section 6.3.2) it is important to test the validity of the results and performance gains obtained from the two codes. For this purpose, intercellular coupling of Case 1, simulating a healthy vessels was considered. The coupling coefficient of this intercellular coupling case are tabulated in Table A.3. Sigmoidal $\widetilde{J}_{PLC_{agonist}}$ profile was imposed on an arterial section, 5 cm long with a 50 μm radius. Figure 8.1 compares the SMC Ca^{2+} dynamics at different time steps, (a) solved by the original code and (b) by the improved version. Notice that there is no significant difference between the two results but the time taken by the original version of algorithm is twice as much as the compute time of the improved version of the code. Figure 8.2 benchmarks the two versions of the algorithm to demonstrate the superior performance of improved version of the algorithm while simulating the spatially nonuniform case of stimulation.

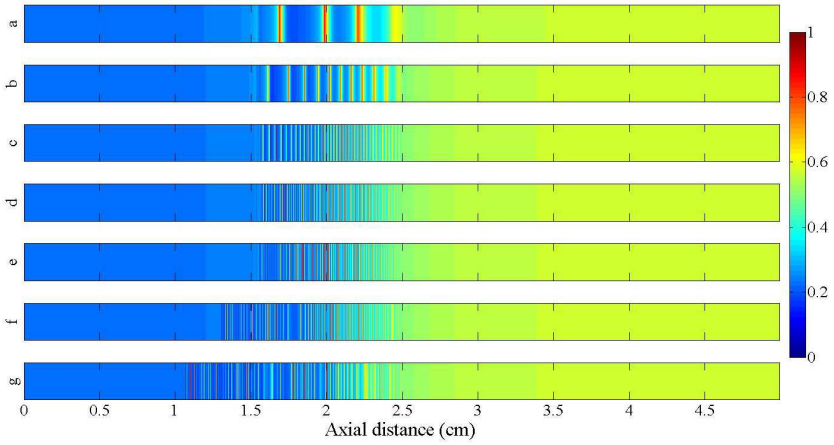

(a) Case 1 solved with original version of parallel algorithm

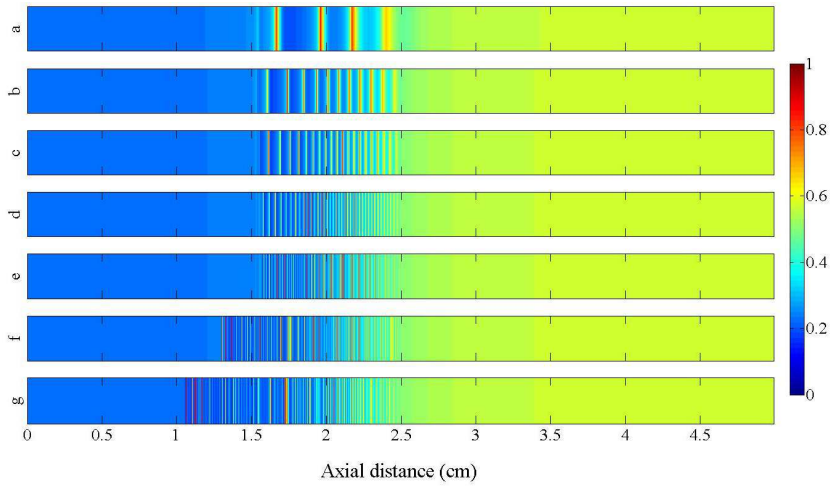

(b) Case 1 solved with improved version of parallel algorithm

Figure 8.1: Figure compares the SMC Ca^{2+} dynamics simulated using the original and improved versions of the algorithm in the case of intercellular coupling corresponding to Case 1 in Table A.3, at time steps, 2.5, 4, 10, 20, 30 and 90 minutes. The qualitative comparison reveals no anomaly in the results from the two codes. The compute time of the improved version, however, was half of that taken by the original algorithm, while the problem size, number of nodes (384 nodes) and the dimensions of the arterial segment were the same.

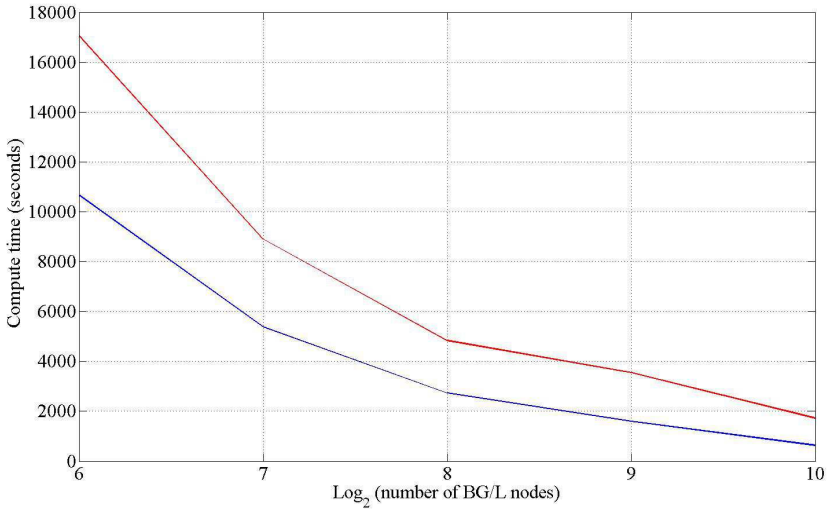

Figure 8.2: Figure depicts the compute time taken by the two codes, plot in red is for original and the in blue is for the improved version of the algorithm. In the case of spatially varying agonist conditions, keeping the problem size constant, the improved version is approximately twice as fast.

8.2 Point Stimulation and Its Spatial Effects

From the physiological aspect, the goal was to employ coupled populations of ECs and SMCs, arranged in a computational layout representing a straight arterial segment, and simulate mass transport characteristics, specifically the near wall ATP concentration, prevalent in the areas of arterial bifurcation. By nature, this concentration profile is of spatially varying nature, as has been established in literature review in Chapter 2 and in Chapter 7, where the choice the profile for $\widetilde{J}_{PLC_{agonist}}$ has been explained.

As the first step towards understanding how Ca^{2+} dynamics differ in spatially non-uniform conditions, simulations of point stimulations with localized high $\widetilde{J}_{PLC_{agonist}}$ was implemented. Point stimulation simulations gave an idea of how the cells respond to spatially non-uniform agonist stimulation. Stimulating a small number of ECs with a step increase in the stimulation level for a finite time interval, could elicit a response locally as the Ca^{2+} concentration of underlying SMCs oscillated. With a stronger stimulation (step increase of $\widetilde{J}_{PLC_{agonist}}$=0.7$\mu$M/s), the heterocellular Ca^{2+} coupling between the cells shifted the behaviour from oscillating to non-oscillating SMCs. Disabling heterocellular Ca^{2+} coupling reverted the non-oscillating response to an oscillating Ca^{2+} concentration in SMCs. An additional concentration of Ca^{2+} entering the SMC cytosol via heterocellular transfer from ECs saturates the cytosolic oscillator and puts the intracellular Ca^{2+} stores into replenishment mode, thus ceasing the Ca^{2+} induced Ca^{2+} release (CICR).

The effects of increasing the basal $\widetilde{J}_{PLC_{agonist}}$ and implementing the point stimulation on top of it indicated that a threshold exists above which the oscillatory response in one SMC can propagate to a non stimulated SMC in coupled cells. Raising the basal $\widetilde{J}_{PLC_{agonist}}$ produced longer oscillatory behaviour in coupled SMCs, thus prolonging the decay process. Because of higher indigenous IP_3 generated by higher local $\widetilde{J}_{PLC_{agonist}}$ stimulation (basal $\widetilde{J}_{PLC_{agonist}}$=0.25$\mu$M/s), less IP_3 is required from the adjacent SMC (coupled to an EC stimulated by a step increase in $\widetilde{J}_{PLC_{agonist}}$) to get into the oscillatory mode. Thus the rate of diffusion of IP_3 will be slower in this case and the system will take more time to damp to the level where all cells stop oscillating. This may also increase the reach of the oscillatory signal to the cells further upstream and downstream from the stimulated SMC in

Figure 7.4, compared to the response of the SMCs at the same location when the stimulation occurs lower basal $\widetilde{J}_{PLC_{agonist}}$=0.2$\mu$M/s. This observation also strengthens the idea of the existence of a threshold level over which an SMC, adjacent to another oscillating SMCs, with low local $\widetilde{J}_{PLC_{agonist}}$ may adapt to an oscillatory response.

8.3 Macroscale Phenomena in Arterial Coupled Cells

In Section 7.3 four cases of intercellular communication were investigated with the endothelial cell layer experiencing an axial variation in ATP concentration simulated by a parameter $\widetilde{J}_{PLC_{agonist}}$, modelling a proportional change in the production of PLC serves as a precursor to IP_3 dependent increase in intracellular Ca^{2+} in ECs. In Case 1 (coupling configuration tabulated in Table A.3), downstream Ca^{2+} dynamics played a vital role in eliciting a response in upstream SMCs in a time dependent manner.

The Ca^{2+} waves (see Figure 7.6a) observed in the first few seconds after the application of an agonist gradient(Figure 7.5) in areas of steep spatial variation of stimulus was found to be solely gradient dependent.

Homocellular Ca^{2+} coupling between SMCs had a fundamental role in the increase of the wave number (the number of oscillatory bands seen in Figure 7.6) of these Ca^{2+} waves and the eventual propagation to upstream SMCs. These SMCs were coupled to ECs that were in an environment of low agonist concentration (i.e would not necessarily oscillate if uncoupled). Low wave number of the Ca^{2+} oscillations in Figure 7.6 are representative of synchronized Ca^{2+} oscillations in "bunches" of SMCs experiencing a relatively uniform heterocellular IP_3 transmission from ECs that are coupled to them. Thinning of these bands (higher wave numbers) at later time steps suggests the desynchronisation of these Ca^{2+} oscillations in neighbouring cells . In these SMCs it is found that desynchronisation is a requisite to the propagatory behaviour shown in Figure 7.6.

We suggest that the mechanism behind such propagation behaviour involves, due to the desynchronisation of Ca^{2+} oscillations, at a specific moment in time, a difference in concentration between adjoining cells and thus a flux of extracellular Ca^{2+} through gap junctions. This is followed by the stimulation of the CICR de-

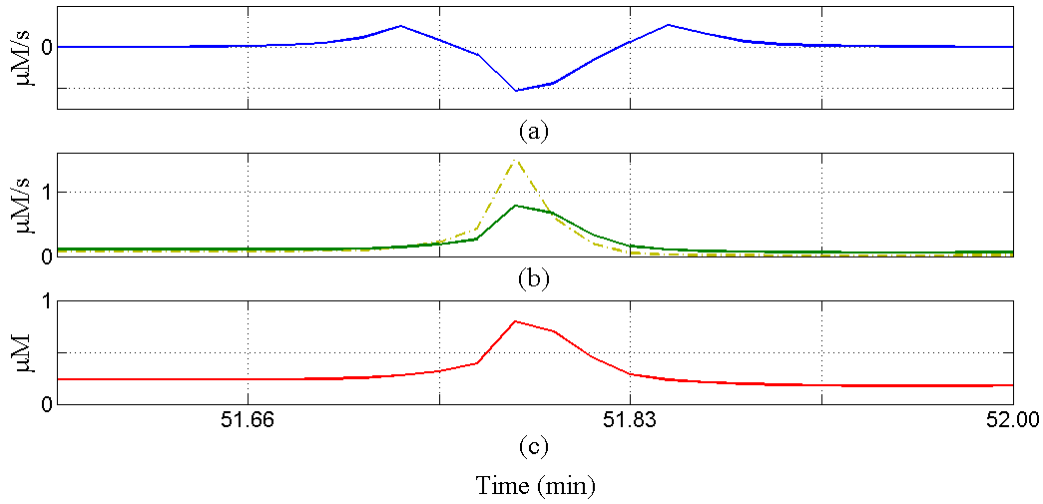

Figure 8.3: Time evolution of component fluxes in a SMC situated at 1.303cm axial distance. (a) shows the Ca^{2+} flux through gap junction, positive being influx of Ca^{2+} from adjacent SMC and negative represents efflux to an apposing SMC. (b)Curve plotted with dashed line shows rate of CICR production and solid line represents rate of Ca^{2+} pumped into SR via SERCA pump. (c) cytosolic Ca^{2+} concentration in SMC.

pendent cytosolic Ca^{2+} increase in SMCs. Figure 8.3 shows the temporal relationship between components of this process for one SMC located at an axial distance of 1.303cm downstream. Note that the Ca^{2+} flux through the gap junction precedes all other fluxes in time. The flux of CICR and SERCA activity continuously changes in time and correspondingly affects the cytosolic Ca^{2+} concentration in Figure 8.3c. The influx of Ca^{2+} from an adjacent SMC enters the intracellular domain and is pumped back into the SR via a SERCA pump immediately. With an increase in the rate of change of Ca^{2+} via the SERCA pump, an increase in the rate of change of CICR and subsequent elevation of cytosolic Ca^{2+} can also be observed. Furthermore, disabling the CICR function caused a cessation of desynchronisation and thus the propagatory effect. SMC VOCCs are not involved in this process because of the continual closure due to membrane hyperpolarization induced by neighbouring hyperpolarized ECs. Membrane coupling alone could not elicit the desynchronisation process and thus no propagation was seen for this case. Homocellular IP_3 coupling between SMCs caused the thinning of bands (increase in the Ca^{2+} wavenumber) but was unable to produce a propagatory effect

since it could not activate the CICR mechanism in cells that were in a low agonist environment. The thinning was not via the CICR dependent process stated above, but mainly due to redistribution of IP_3 from enabled homocellular IP_3 coupling in this case.

In Case 2 of Table A.3, enabling the heterocellular Ca^{2+} coupling had a rapid effect on intracellular Ca^{2+} concentration in SMCs. The response showed trends similar to those seen in case 1 but the propagation of the Ca^{2+} wave needed less oscillatory desynchronization amongst adjoining cells. This is shown in Figure 7.9. This is a much more definitive vasoconstrictor response. Elevated intracellular Ca^{2+} in upstream SMCs, although oscillatory, increases actomyosin activity proportionally and hence mediates SMC contraction with a resultant reduction in arterial radius. Addition of Ca^{2+} from ECs via heterocellular Ca^{2+} coupling sensitizes the underlying SMCs to any further injection of Ca^{2+} from an adjoining SMC. This process was observed in the point stimulation simulation where the step increase in $\widetilde{J}_{PLC_{agonist}}$=0.7$\mu$M/s stimulated a block of ECs. This extra Ca^{2+} aids the spatial wave originating in the cells under the steep agonist gradient to reach the upstream cells relatively quickly. Each upstream SMC now needs only a small homocellular Ca^{2+} influx from an adjoining SMC to induce Ca^{2+} oscillations in it (via the CICR pathway shown in Figure 8.3) thus producing a spatially synchronized Ca^{2+} response. The heterocellular Ca^{2+} coupling, therefore, abates the temporal desynchronisation of intracellular Ca^{2+} oscillations in the SMCs whilst achieving the propagation of a high agonist concentration signal to upstream cells. We thus suspect that heterocellular Ca^{2+} coupling could be an integral part of the vascular apparatus eliciting a rapid global response to alterations in the local agonist concentration. This should help in preserving the structural integrity of the intima by reducing the effect of hemodynamically induced gradients acting on the endothelial surface by homogenizing the contractile activity of SMCs axially. It is yet to be investigated how circumferential gradients cause arterial responses in such cases.

Case 3 simulates a pathological scenario where the inclusion of homocellular IP_3 coupling between ECs simulates the upregulation of connexin Cx43 in atheroprone areas Burnier et al. (2009); DePaola et al. (1999). No difference was seen in the response of the intercellular Ca^{2+} for case 3 compared to the response in case

2. The presence of heterocellular Ca^{2+} coupling in both cases inhibits the gradient effects and resulting in a diffused spatial Ca^{2+} wave and synchronized temporal oscillations of intracellular Ca^{2+} concentrations in SMCs located upstream. This highlights the importance of heterocellular Ca^{2+} coupling between SMCs and ECs in arterial segments.

Case 4, where EC homocellular coupling and EC/SMC heterocellular coupling was severely restricted, provided a different response to any of the above three cases. In cases 1 to 3 the presence of heterocellular membrane potential coupling suppressed the entry of Ca^{2+} into the SMCs via their VOCCs due to EC mediated hyperpolarization of the SMC membrane potential. In this case, due to the inhibition of heterocellular membrane potential and the consequential disabled hyperpolarization it allows the Ca^{2+} influx via VOCCs into the SMCs following adequate IP_3 stimulation. This offsets the Ca^{2+} concentration globally in the whole population of SMCs in the axial direction. Further exchange of Ca^{2+} via homocellular gap junctions in SMCs, as we go forward in time, elicits the same response as seen in case 1. However for an SMC the time to reach an oscillatory behaviour in case 4 is much less than that observed in case 1. This observation points out the role and extent of coupling between two populations of cells. In case 4, where both cell types had weak heterocellular coupling and ECs were also weakly coupled homocellularly, the response resembles a condition where the EC layer was non existent and SMCs were experiencing the agonist directly onto their cell membrane. Relatively lower agonist concentrations stimulating ECs in this case would also produce a similar response suggesting that, unlike cases 1 to 3, the arterial segment with such intercellular coupling becomes hypersensitive and would contract even at low agonist concentrations.

In the coupling configuration cases representing a healthy arterial segment the presence of homocellular Ca^{2+} coupling between SMCs ensures the propagation of a high agonist concentration signal to upstream cells at low agonist concentration. This is achieved rather slowly in the absence of heterocellular Ca^{2+} coupling, as in case 1 (Figure 7.6) compared to case 2 (Figure 7.9), where heterocellular Ca^{2+} coupling between ECs and SMCs ensures a rapid and spatially definitive response. In both the cases the intracellular Ca^{2+} concentration in each SMC (situated axially at $<$2.5cm) oscillates in a temporally desynchronized fashion, the

degree of which is much greater in case 1 than in case 2. This desynchronisation is the main source of the propagation of the Ca^{2+} wave in both the cases in the upstream direction and is CICR mediated between SMCs, as suggested by the results above. This behaviour ceases in the absence of homocellular Ca^{2+} coupling between SMCs.

When considering the cases of a pathological nature of intercellular coupling in the presence of an agonist gradient, case 3 was not different from case 2. Case 4 however highlights the inhibitory effect of hyperpolarized EC membrane potentials on SMC Ca^{2+} dynamics. In the absence of such a leash, the intracellular Ca^{2+} concentration oscillated in each SMC (situated at $<$2.5cm) in similar fashion as observed in case 1 but the response was much more rapid. We suggest that because the cells become sensitive, even to the presence of low agonist concentrations, the vessel segment will be in a contracted state more frequently than in other cases. Thus the presence of heterocellular membrane potential coupling seems to be essential for imposing a range of agonist concentration where vasoconstrictor effects are seen.

Of all the intercellular coupling cases, Case1 was computationally most expensive as it took longest time to compute a problem size. As Figure 7.6 showed the propagation of the oscillatory process, the problem becomes increasingly stiff and the numerical solver is bound to take small steps. Cases 2 and 3 were relatively less intensive computationally. For the sake of comparing the computational cost of simulating an arterial segment of 2mm radius implementing an intercellular coupling of Case 1 for 100 seconds, took 36294.89 CPU seconds to complete. An arterial segment of same length but of 24μm radius, implementing Case 1 intercellular coupling, took 394.12 CPU seconds. 384 BG/L nodes were used in Coprocessor mode to compute each simulation. Therefore, with an axisymmetric agonist concentration profile, the narrow radius artery (simulating an arteriole) was computed 80 times faster than a arterial section with larger radius.

Chapter 9

Conclusion

The main objective of the project was to build a computer model capable of investigating the effects of physiologically relevant cases of hemodynamics (specifically ATP concentration), within an arterial segment, on the cellular dynamics of coupled populations of arterial ECs and SMCs. This chapter summarizes the current findings from the physiological and computational aspects.

Ca^{2+} wave propagation has been demonstrated previously in hepatocytes (Dupont et al., 2000; Tordjmann et al., 1997) and pencreatic acinar cells (Sneyd and Tsaneva-Atanasova, 2003; Straub et al., 2000). The mechanism suggested in these coupled cells is either Ca^{2+} induced Ca^{2+} release mediated (in the pancreatic acinar cells) or intercellular IP_3 diffusion dependent (in hepatocytes). In the present study, in the case of spatial variation of agonist on the intercellular coupling cases simulating healthy vessel, the desynchronization in the Ca^{2+} oscillations of SMCs is the main source of the propagation of Ca^{2+} wave in the upstream direction. This phenomenon of regenerative Ca^{2+} wave is mediated by the CICR mechanism discussed in Chapter 8. Case 4 highlighted that in the absence of the hyperpolarization induced by the ECs, the underlying SMCs become sensitized and respond in an oscillatory behaviour to low local agonist concentrations of agonist. Thus hyperpolarization has a vital role in thresholding the oscillatory response to a range of local agonist concentration.

Thus heterocellular Ca^{2+} and membrane potential coupling could, on the basis of our results, have an **atheroprotective effect** in an arterial segment stimulated

by a time averaged agonist gradient in coupled EC/SMC populations. Homocellular Ca^{2+} coupling between SMCs also has a **compensatory effect** and helps in homogenizing the response on a global scale in response to such gradients, the rapidness of which is heavily influenced by the presence or absence of appropriate heterocellular coupling.

Through the use of massively parallel simulations our results have shown that there exist **macro-scale phenomena** which indicate the propagation of Ca^{2+} dynamics upstream within arterial segments. **It is believed that this is one of a number of possible explanations of how lesions may grow upstream in opposition to convective transport effects.**

From the above conclusions, the reasoning for the use of large scale multicellular coupled models is highlighted for computationally investigating coupled **micro-scale** events which elicit a **macro-scale** response. This is the first time that a computational infrastructure has been introduced which is capable of accommodating a computational domain, as long as 5 cm in axial length, and can cover arterial radii, from 16μM/s (of the order of a 1^{st} or 2^{nd} order arteriole), up to 2mm, the order of a left main coronary artery, right and left descending and circumflex arteries. Because of the choice of an axisymmetric profile of the agonist effect, the observed marco-scale phenomena were found insensitive to the radius of the arterial segment, however, selection of more complex agonist profiles, with spatial variations in more than one direction are expected to produce different results in arterial segments of different radii. The use of computational architectures such as Blue Gene in this project have demonstrated the ability to simulate highly complex cellular effects on a scale large enough to be seen with the naked eye.

It can be safely deduced from the scaling results on Blue Gene/L that more computationally intensive problems comprising a larger number of cells and more dynamical variables then simulated at present, by horizontally scaling the computational resources (i.e. adding more BG/L nodes). The limitations can only be revealed by conducting larger strong and weak scaling tests.

From the simulated results it is evident that the perpetual influx of Ca^{2+} through gap junctions contributed by the adjacent cells is capable of raising stiffness of the solution of set ODEs of a cell, SMC or EC, from a coupled population of cells under spatially varying agonist. This potentially motivates the attempt to use a stiff

solver such as *backward differentiation formula* or BDF instead of using an adaptive step size nonstiff solver such as RKSUITE, hence is one of the future goals.

In the light of current findings, the need for implementing cell models including arterial compliance has been highlighted. The EC and SMC models can also include physiological realistic models of *Nitric Oxide* production and diffusion pathways to test the hypotheses that exist regarding the modulatory role of "Endothelium Derived Relaxing Factor" (EDRF). This may also help quantitate the importance of EDRF versus "Endothelium Derived Hyperpolarizing Factor" (EDHF), included in the present models as Ca^{2+} activated potassium channels.

Using the existing parallel algorithm, and with the inclusion of arterial compliance, the effects of various coupling environments on the myogenic response can be demonstrated in muscular arteries under pressure gradient. The compute time for simulating arteries of large radius (millimetre radius) approximately hundred times longer than for simulating an artery of a radius on micrometer scale. Since the domain decomposition is applied only in the axial dimension, there is a need to decompose the problem in the circumferential direction. This modification in the existing algorithm is expected to enhance its performance.

Ca^{2+}, in its ionic state, is a reactive specie and it binds to various intracellular proteins with different affinities. The binding of free cytosolic Ca^{2+} with these substrates is termed as Ca^{2+} buffering. One of the known Ca^{2+} buffering reactions is Ca-CaM or Ca^{2+} Calmodulin complex. Calmodulin (CaM) is a cytosolic protein which has four Ca^{2+} binding sites. In SMCs, this Ca^{2+} binding activates an enzyme call *myosin light chain kinase* or MLCK which then phosphorylates mysoin light chain and allow crossbrige formation and alters the cytoskeleton so the SMC contracts. Ca^{2+} buffering, is a rapid process (Hofer et al., 2001) and most of the Ca^{2+} arriving in the cytosolic domain is buffered quickly. In the single cell models used in the present study, this effect has been modelled implicitly. More to this, a possibility has been demonstrated that large molecules like Ca-CaM complex (molecular weight= $\approx$17 kDa) can pass through gap junction in invertebrates (Richard, 2005), and recently it has been validated in some vertebrate species *in vitro* (Curran and Woodruff, 2007). In such case, the intercellular transport of Ca^{2+} in nonreactive state (i.e. as Ca-CaM complex) may not contribute significantly to the intracellular Ca^{2+} concentration, but may have a considerable

influence on the membrane potential. This is due to the fact that Ca^{2+}, even in Ca-CaM complex form, will bare a charge (as valency of Ca^{2+} is 2+). This effect has not been included in the present intercellular coupling model. Future work will include addition of the buffered Ca^{2+} transport in the intercellular coupling model and testing for the hypothesis considered in the present investigation. More to that, by altering coupling coefficient, strengthening or weakening those intercellular couplings which are proposed as driving mechanisms of the propagatory behaviour seen in SMCs, the validity of the current results can be partially tested. Future work will include considering such coupling scenarios.

Portability of an algorithm is desired so as to be able to enhance its performance on vertical scaled computing architectures (i.e. more computing resources added on one node) such as IBM Blue Gene/P. Modifications in the existing algorithm will be required to fully exploit the computing power of a hybrid (shared distributed) memory system such as BG/P.

Furthermore, the existing computational layout has the potential to add the geometric enhancement to build a computation model for complete arterial bifurcation. This can be used to demonstrate the effects of complex tangential wall shear stresses acting on the cytoskeleton of the cell and concentration patterns associated with arterial bifurcations. Combining the numerical solution of fluid component (blood phase) with the solution of coupled cell models may aid in implementing physiologically relevant circumferential gradients in wall shear stress and agonist concentrations. These are expected to be computationally intense problems, with high complexity due to involvement of spatial effects in a substantial than one direction (i.e. longitudinal and circumferential).

Bibliography

Aalkjaer, C. and Nilsson, H. (2005). Vasomotion: cellular background for the oscillator and for the synchronization of smooth muscle cells. *Br J Pharmacol*, 144(5):605–16. 41, 42

Aboyans, V., Lacroix, P., and Criqui, M. H. (2007). Large and small vessels atherosclerosis: Similarities and differences. *Progress in Cardiovascular Diseases*, 50(2):112–125. 9, 11

Arensbak, B., Mikkelsen, H. B., Gustafsson, F., Christensen, T., and Holstein-Rathlou, N. H. (2001). Expression of connexin 37, 40, and 43 mrna and protein in renal preglomerular arterioles. *Histochemistry and Cell Biology*, 115(6):479–487. 33

Asakura, T. and Karino, T. (1990). Flow patterns and spatial distribution of atherosclerotic lesions in human coronary arteries. *Circ Res*, 66(4):1045–1066. 13

Augst, A. D., Ariff, B., McG. Thom, S. A. G., Xu, X. Y., and Hughes, A. D. (2007). Analysis of complex flow and the relationship between blood pressure, wall shear stress, and intima-media thickness in the human carotid artery. *American Journal of Physiology - Heart and Circulatory Physiology*, 293(2):H1031–H1037. 17

Barakat, A. I. (2001). A model for shear stress-induced deformation of a flow sensor on the surface of vascular endothelial cells. *Journal of Theoretical Biology*, 210(2):221–36. 25, 26

Bennett, M. R., Farnell, L., and Gibson, W. G. (2005). A quantitative description of the contraction of blood vessels following the release of noradrenaline from sympathetic varicosities. *Journal of Theoretical Biology*, 234(1):107–122. 44

Beny, J. L. (1999). Information networks in the arterial wall. *News Physiol Sci*, 14:68–73. 31

Berridge, M. J. (2007). Inositol trisphosphate and calcium oscillations. *Biochemical Society symposium*, (74):1–7. 41

Blatter, L. A. and Wier, W. G. (1992). Agonist-induced [ca2+]i waves and ca(2+)-induced ca2+ release in mammalian vascular smooth muscle cells. *American Journal of Physiology - Heart and Circulatory Physiology*, 263(2):H576–H586. 41

Bogacki, P. and Shampine, L. F. (1996). An efficient runge-kutta (4,5) pair. *Computers & Mathematics with Applications*, 32(6):15–28. 70

Boittin, F.-X., Macrez, N., Halet, G., and Mironneau, J. (1999). Norepinephrine-induced ca2+waves depend on insp3 and ryanodine receptor activation in vascular myocytes. *American Journal of Physiology - Cell Physiology*, 277(1):C139–C151. 41

Brankin, R., Gladwell, I., and Shampine, L. (1991). Rksuite release 1.0. Technical report. 71, 72

Brisset, A. C., Isakson, B. E., and Kwak, B. R. (2009). Connexins in vascular physiology and pathology. *Antioxid Redox Signal*, 11(2):267–82. 176

Burnier, L., Fontana, P., Angelillo-Scherrer, A., and Kwak, B. R. (2009). Intercellular communication in atherosclerosis. *Physiology (Bethesda)*, 24:36–44. 176, 186

Burt, J. M., Fletcher, A. M., Steele, T. D., Wu, Y., Cottrell, G. T., and Kurjiaka, D. T. (2001). Alteration of cx43:cx40 expression ratio in a7r5 cells. *American Journal of Physiology - Cell Physiology*, 280(3):C500–C508. 33

Caro, C. G., Fitz-Gerald, J. M., and Schroter, R. C. (1969). Arterial wall shear and distribution of early atheroma in man. *Nature*, 223(5211):1159–1161. 10.1038/2231159a0. 4, 12, 23

Caro, C. G., Fitz-Gerald, J. M., and Schroter, R. C. (1971). Atheroma and arterial wall shear observation, correlation and proposal of a shear dependent mass transfer mechanism for atherogenesis. *Proceedings of the Royal Society of London. Series B. Biological Sciences*, 177(1046):109–133. 23

Cheng, C., Tempel, D., van Damme, L., van Haperen, R., Krams, R., and de Crom, R. (2006). Patterns of fluid shear stress determine atherosclerotic lesion size and vulnerability. *Vascular Pharmacology*, 45(3):e51–e51. 4, 127, 169

Chien, S. (2007). Mechanotransduction and endothelial cell homeostasis: the wisdom of the cell. *American Journal of Physiology - Heart and Circulatory Physiology*, 292(3):H1209–H1224. 13, 14

Chiu, J. J., Wang, D. L., Chien, S., Skalak, R., and Usami, S. (1998). Effects of disturbed flow on endothelial cells. *J Biomech Eng*, 120(1):2–8. 17

Colgan, O. C., Ferguson, G., Collins, N. T., Murphy, R. P., Meade, G., Cahill, P. A., and Cummins, P. M. (2007). Regulation of bovine brain microvascular endothelial tight junction assembly and barrier function by laminar shear stress. *American Journal of Physiology - Heart and Circulatory Physiology*, 292(6):H3190–H3197. 17, 18

Comerford, A. and David, T. (2008). Computer model of nucleotide transport in a realistic porcine aortic trifurcation. *Annals of Biomedical Engineering*, 36(7):1175–1187. 13, 25, 26, 28, 29, 169, 171

Comerford, A., David, T., and Plank, M. (2006). Effects of arterial bifurcation geometry on nucleotide concentration at the endothelium. *Ann Biomed Eng*, 34(4):605–17. 25

Comerford, A., Plank, M. J., and David, T. (2008). Endothelial nitric oxide synthase and calcium production in arterial geometries: An integrated fluid me-

chanics/cell model. *Journal of Biomechanical Engineering*, 130(1):011010–13. 25, 26, 27, 171

Cooke, J. P. (2003). Flow, no, and atherogenesis. *Proceedings of the National Academy of Sciences*, 100(3):768–770. 21

Curran, J. E. and Woodruff, R. I. (2007). Passage of 17kda calmodulin through gap junctions of three vertebrate species. *Tissue and Cell*, 39(5):303–309. doi: 10.1016/j.tice.2007.06.002. 191

Dai, G., Kaazempur-Mofrad, M. R., Natarajan, S., Zhang, Y., Vaughn, S., Blackman, B. R., Kamm, R. D., Garcia-Cardena, G., and Gimbrone, M. A. (2004). Distinct endothelial phenotypes evoked by arterial waveforms derived from atherosclerosis-susceptible and -resistant regions of human vasculature. *Proceedings of the National Academy of Sciences of the United States of America*, 101(41):14871–14876. 33

David, T. (2003). Wall shear stress modulation of atp/adp concentration at the endothelium. 25

Davies, P. F. (2000). Spatial hemodynamics, the endothelium, and focal atherogenesis : A cell cycle link? *Circ Res*, 86(2):114–116. 21

DePaola, N., Davies, P. F., Pritchard, W. F., J., Florez, L., Harbeck, N., and Polacek, D. C. (1999). Spatial and temporal regulation of gap junction connexin43 in vascular endothelial cells exposed to controlled disturbed flows in vitro. *Proc Natl Acad Sci U S A*, 96(6):3154–9. 17, 33, 37, 39, 186

Diep, H. K., Vigmond, E. J., Segal, S. S., and Welsh, D. G. (2005). Defining electrical communication in skeletal muscle resistance arteries: a computational approach. *The Journal of Physiology*, 568:267–281. vi, 45, 46, 47

Dupont, G., Tordjmann, T., Clair, C., Swillens, S., Claret, M., and Combettes, L. (2000). Mechanism of receptor-oriented intercellular calcium wave propagation in hepatocytes. *The FASEB Journal*, 14(2):279–89. Journal Article Research Support, Non-U.S. Gov't United states official publication of the Federation of American Societies for Experimental Biology. 189

Ebong, E. E., Kim, S., and DePaola, N. (2006). Flow regulates intercellular communication in haec by assembling functional cx40 and cx37 gap junctional channels. *Am J Physiol Heart Circ Physiol*, 290(5):H2015–23. 31, 33, 39

Ethier, C. R. (2002). Computational modeling of mass transfer and links to atherosclerosis. *Annals of Biomedical Engineering*, 30(4):461–471. 13

Fall, C., Marland, E., Wagner, J., and Tyson, J. (2002). *Computational Cell Biology*. Interdisciplinary Applied Mathematics. Springer-Verlag New York. 52, 55, 56, 59, 99

Figueroa, X. F. and Duling, B. R. (2008). Dissection of two cx37-independent conducted vasodilator mechanisms by deletion of cx40: electrotonic versus regenerative conduction. *Am J Physiol Heart Circ Physiol*, 295(5):H2001–2007. 31

Figueroa, X. F. and Duling, B. R. (2009). Gap junctions in the control of vascular function. *Antioxid Redox Signal*, 11(2):251–66. 30

Flynn, M. J. (1972). Some computer organizations and their effectiveness. *Computers, IEEE Transactions on*, C-21(9):948–960. 131

Frieden, M., Sollini, M., and Beny, J. (1999). Substance p and bradykinin activate different types of kca currents to hyperpolarize cultured porcine coronary artery endothelial cells. *The Journal of Physiology*, 519 Pt 2:361–71. Journal Article Research Support, Non-U.S. Gov't England. 57

Gabriels, J. E. and Paul, D. L. (1998). Connexin43 is highly localized to sites of disturbed flow in rat aortic endothelium but connexin37 and connexin40 are more uniformly distributed. *Circ Res*, 83(6):636–643. 37, 38, 40

Gara, A., Blumrich, M. A., Chen, D., Chiu, G. L. T., Coteus, P., Giampapa, M. E., Haring, R. A., Heidelberger, P., Hoenicke, D., Kopcsay, G. V., Liebsch, T. A., Ohmacht, M., Steinmacher-Burow, B. D., Takken, T., and Vranas, P. (2005). Overview of the blue gene/l system architecture. *IBM Journal of Research and Development*, 49(2-3):195–195–212. 2008-10-01 Hoenicke, D 0018-8646 Computer & Information Systems (CI) Blumrich, M A Haring, R A Liebsch, T

A 290124686 OB-OH-0001221778 Chen, D Steinmacher-Burow, B D 200705-90-053400 (CI) Giampapa, M E English Gara, A Ohmacht, M Chiu, G L-T Coteus, P Heidelberger, P Takken, T 195-212 Vranas, P Kopcsay, G V. 138

Glagov, S., Zarins, C., Giddens, D. P., and Ku, D. N. (1988). Hemodynamics and atherosclerosis. insights and perspectives gained from studies of human arteries. *Arch Pathol Lab Med*, 112(10):1018–1031. 16

Goldbeter, A., Dupont, G., and Berridge, M. J. (1990). Minimal model for signal-induced ca2+ oscillations and for their frequency encoding through protein phosphorylation. *Proceedings of the National Academy of Sciences of the United States of America*, 87(4):1461–5. Journal Article Research Support, Non-U.S. Gov't United states. 57

Gustafsson, F., Mikkelsen, H. B., Arensbak, B., Thuneberg, L., Neve, S., Jensen, L. J., and Holstein-Rathlou, N. H. (2003). Expression of connexin 37, 40 and 43 in rat mesenteric arterioles and resistance arteries. *Histochem Cell Biol*, 119(2):139–48. 33

Haas, T. L. and Duling, B. R. (1997). Morphology favors an endothelial cell pathway for longitudinal conduction within arterioles. *Microvascular Research*, 53(2):113–120. 107

Haddock, R. E. and Hill, C. E. (2005). Rhythmicity in arterial smooth muscle. *J Physiol*, 566(Pt 3):645–56. Haddock, Rebecca E Hill, Caryl E Review England The Journal of physiology J Physiol. 2005 Aug 1;566(Pt 3):645-56. Epub 2005 May 19. 42

Haefliger, J. A., Nicod, P., and Meda, P. (2004). Contribution of connexins to the function of the vascular wall. *Cardiovasc Res*, 62(2):345–56. 30, 33

Hai, C. M. and Murphy, R. A. (1988). Cross-bridge phosphorylation and regulation of latch state in smooth muscle. *The American journal of physiology*, 254(1):106. 48

Harris, A. L. (2007). Connexin channel permeability to cytoplasmic molecules. *Prog Biophys Mol Biol*, 94(1-2):120–43. Harris, Andrew L R01 GM036044-

14/GM/NIGMS NIH HHS/United States R21 DC007470-02/DC/NIDCD NIH HHS/United States Review England Progress in biophysics and molecular biology Prog Biophys Mol Biol. 2007 May-Jun;94(1-2):120-43. Epub 2007 Mar 19. 103

Heyman, N. S., Kurjiaka, D. T., Ek Vitorin, J. F., and Burt, J. M. (2009). Regulation of gap junctional charge selectivity in cells coexpressing connexin 40 and connexin 43. *American Journal of Physiology - Heart and Circulatory Physiology*, 297(1):H450–H459. 103

Hill, C. E., Phillips, J. K., and Sandow, S. L. (2001). Heterogeneous control of blood flow amongst different vascular beds. *Medicinal Research Reviews*, 21(1):1–60. 33

Hofer, T., Politi, A., and Heinrich, R. (2001). Intercellular ca2+ wave propagation through gap-junctional ca2+ diffusion: A theoretical study. *Biophysical journal*, 80(1):75–87. 191

Iino, M., Kasai, H., and Yamazawa, T. (1994). Visualization of neural control of intracellular ca2+ concentration in single vascular smooth muscle cells in situ. *EMBO J*, 13(21):5026–31. 41

Isakson, B. E., Damon, D. N., Day, K. H., Liao, Y., and Duling, B. R. (2006). Connexin40 and connexin43 in mouse aortic endothelium: evidence for coordinated regulation. *Am J Physiol Heart Circ Physiol*, 290(3):H1199–205. 33

Isakson, B. E. and Duling, B. R. (2005). Heterocellular contact at the myoendothelial junction influences gap junction organization. *Circ Res*, 97(1):44–51. 33, 34, 35, 40, 104

Jacobsen, J. C. B., Aalkjaer, C., Nilsson, H., Matchkov, V. V., Freiberg, J., and Holstein-Rathlou, N.-H. (2007). A model of smooth muscle cell synchronization in the arterial wall. *Am J Physiol Heart Circ Physiol*, 293(1):H229–237. v, 43, 45, 106

Jeng-Jiann, C., Li-Jing, C., Cheng-Nan, C., Pei-Ling, L., and Chih, I. L. (2004). A model for studying the effect of shear stress on interactions between vascular

endothelial cells and smooth muscle cells. *Journal of biomechanics*, 37(4):531–539. 17

Johnstone, S., Isakson, B., and Locke, D. (2009). Biological and biophysical properties of vascular connexin channels. *Int Rev Cell Mol Biol*, 278:69–118. 30, 33, 99

Kaazempur Mofrad, M. R., Wada, S., Myers, J. G., and Ethier, C. R. (2005). Mass transport and fluid flow in stenotic arteries: Axisymmetric and asymmetric models. *International Journal of Heat and Mass Transfer*, 48(21-22):4510–4517. 25

Kapela, A., Bezerianos, A., and Tsoukias, N. M. (2008). A mathematical model of ca2+ dynamics in rat mesenteric smooth muscle cell: Agonist and no stimulation. *Journal of Theoretical Biology*, 253(2):238–260. 324TM Times Cited:3 Cited References Count:113. 82

Kapela, A., Bezerianos, A., and Tsoukias, N. M. (2009). A mathematical model of vasoreactivity in rat mesenteric arterioles: I. myoendothelial communication. *Microcirculation*, 16(8):694–713. 106

Kapela, A., Nagaraja, S., and Tsoukias, N. M. (2010). A mathematical model of vasoreactivity in rat mesenteric arterioles. ii. conducted vasoreactivity. *Am J Physiol Heart Circ Physiol*, 298(1):H52–65. 46

Kjaernes, M., Svindland, A. U. D., Walloe, L., and Wille, S. (1981). Localization of early atherosclerotic lesions in an arterial bifurcation in humans. *Acta Pathologica Microbiologica Scandinavica Section A Pathology*, 89A(1-6):35–40. 13, 24

Koenigsberger, M., Sauser, R., Beny, J. L., and Meister, J. J. (2005). Role of the endothelium on arterial vasomotion. *Biophysical journal*, 88(6):3845–3854. 931RO Times Cited:15 Cited References Count:45. ix, 46, 48, 57, 62, 63, 64, 67, 80, 101, 105, 106, 171, 209, 210

Koenigsberger, M., Sauser, R., Beny, J. L., and Meister, J. J. (2006). Effects of arterial wall stress on vasomotion. *Biophysical journal*, 91(5):1663–1674. 074CP Times Cited:5 Cited References Count:47. vi, 48, 49, 106

Ku, D., Giddens, D., Zarins, C., and Glagov, S. (1985). Pulsatile flow and atherosclerosis in the human carotid bifurcation. positive correlation between plaque location and low oscillating shear stress. *Arterioscler Thromb Vasc Biol*, 5(3):293–302. 13

Kwak, B. R., Mulhaupt, F., Veillard, N., Gros, D. B., and Mach, F. (2002). Altered pattern of vascular connexin expression in atherosclerotic plaques. *Arterioscler Thromb Vasc Biol*, 22(2):225–30. 33, 36, 37

Lamboley, M., Pittet, P., Koenigsberger, M., Sauser, R., Beny, J. L., and Meister, J. J. (2005). Evidence for signaling via gap junctions from smooth muscle to endothelial cells in rat mesenteric arteries: possible implication of a second messenger. *Cell calcium*, 37(4):311–20. Journal Article Research Support, Non-U.S. Gov't Scotland. 104

Lamboley, M., Schuster, A., Beny, J. L., and Meister, J. J. (2003). Recruitment of smooth muscle cells and arterial vasomotion. *Am J Physiol Heart Circ Physiol*, 285(2):H562–9. Lamboley, Mathieu Schuster, Alexander Beny, Jean-Louis Meister, Jean-Jacques Research Support, Non-U.S. Gov't United States American journal of physiology. Heart and circulatory physiology Am J Physiol Heart Circ Physiol. 2003 Aug;285(2):H562-9. Epub 2003 Feb 6. 57, 80

Ledoux, J., Werner, M. E., Brayden, J. E., and Nelson, M. T. (2006). Calcium-activated potassium channels and the regulation of vascular tone. *Physiology (Bethesda)*, 21:69–78. Ledoux, Jonathan Werner, Matthias E Brayden, Joseph E Nelson, Mark T Review United States Physiology (Bethesda, Md.) Physiology (Bethesda). 2006 Feb;21:69-78. 91

Lee, C. H., Poburko, D., Sahota, P., Sandhu, J., Ruehlmann, D. O., and van Breemen, C. (2001). The mechanism of phenylephrine-mediated [ca(2+)](i) oscillations underlying tonic contraction in the rabbit inferior vena cava. *J Physiol*, 534(Pt 3):641–50. 41

Lidington, D., Ouellette, Y., and Tyml, K. (2000). Endotoxin increases intercellular resistance in microvascular endothelial cells by a tyrosine kinase pathway. *Journal of Cellular Physiology*, 185(1):117–125. 105

Little, T. L., Beyer, E. C., and Duling, B. R. (1995). Connexin 43 and connexin 40 gap junctional proteins are present in arteriolar smooth muscle and endothelium in vivo. *American Journal of Physiology - Heart and Circulatory Physiology*, 268(2):H729–H739. 33

Ma, P., Li, X., and Ku, D. N. (1997). Convective mass transfer at the carotid bifurcation. *J Biomech*, 30(6):565–71. 13, 14, 24, 25, 26

Mahinpey, N., Leask, R., Ojha, M., Johnston, K. W., and Trass, O. (2004). Experimental study on local mass transfer in a simplified bifurcation model: Potential role in atherosclerosis. *Annals of Biomedical Engineering*, 32(11):1504–1518. 13, 25

Malek, A. M., Alper, S. L., and Izumo, S. (1999). Hemodynamic shear stress and its role in atherosclerosis. *JAMA: The Journal of the American Medical Association*, 282(21):2035–2042. 17

Matturri, L., Ottaviani, G., Corti, G., and Lavezzi, A. M. A. M. (2004). Pathogenesis of early atherosclerotic lesions in infants. *Pathology - Research and Practice*, 200(5):403–410. 12

Mese, G., Richard, G., and White, T. W. (2007). Gap junctions: Basic structure and function. *J Invest Dermatol*, 127(11):2516–2524. 32

Meyer, T. and Stryer, L. (1988). Molecular model for receptor-stimulated calcium spiking. *Proc Natl Acad Sci U S A*, 85(14):5051–5. Meyer, T Stryer, L Research Support, Non-U.S. Gov't Research Support, U.S. Gov't, P.H.S. United states Proceedings of the National Academy of Sciences of the United States of America Proc Natl Acad Sci U S A. 1988 Jul;85(14):5051-5. 78, 82

Milei, J., Ottaviani, G., Lavezzi, A. M., Grana, D. R., Stella, I., and Matturri, L. (2008). Perinatal and infant early atherosclerotic coronary lesions. *Can J Cardiol*, 24(2):137–41. 12

Mukherjee, S. (2009). Adult onset atherosclerosis may have its origin in the foetal state in utero. *Current Opinion in Lipidology*, 20(2):155–156 10.1097/MOL.0b013e3283295713. 12

Nelson, M. T., Patlak, J. B., Worley, J. F., and Standen, N. B. (1990). Calcium channels, potassium channels, and voltage dependence of arterial smooth muscle tone. *American Journal of Physiology - Cell Physiology*, 259(1):C3–C18. 42

Nerem, R. M. (1992). Vascular fluid mechanics, the arterial wall, and atherosclerosis. *Journal of Biomechanical Engineering*, 114(3):274–282. 14

Nilius, B. and Droogmans, G. (2001). Ion channels and their functional role in vascular endothelium. *Physiol Rev*, 81(4):1415–59. Nilius, B Droogmans, G Research Support, Non-U.S. Gov't Review United States Physiological reviews Physiol Rev. 2001 Oct;81(4):1415-59. 90, 91

Nollert, M. U. and McIntire, L. V. (1992). Convective mass transfer effects on the intracellular calcium response of endothelial cells. *J Biomech Eng*, 114(3):321–6. 13

Parthimos, D., Edwards, D. H., and Griffith, T. M. (1999). Minimal model of arterial chaos generated by coupled intracellular and membrane ca2+oscillators. *American Journal of Physiology - Heart and Circulatory Physiology*, 277(3):H1119–H1144. 105

Plank, M. J., Comerford, A., David, T., and Wall, D. J. N. (2006a). Concentration of blood-borne agonists at the endothelium. *Proceedings: Mathematical, Physical and Engineering Sciences*, 462(2066):671–688. 25, 171

Plank, M. J., Wall, D. J., and David, T. (2006b). Atherosclerosis and calcium signalling in endothelial cells. *Prog Biophys Mol Biol*, 91(3):287–313. 25, 26, 27

Pohl, U., Wagner, K., and De Wit, C. (1993). Endothelium-derived nitric oxide in the control of tissue perfusion and oxygen supply: physiological and pathophys-

iological implications. *European Heart Journal, Suppl I, 93-98*, 14(Supplement 1):93–98. 30

Press, W. H., Teukolsky, S. A., Vetterling, W. T., and Flannery, B. P. (1992). Adaptive stepsize control for runge-kutta. In *Numerical Recipies in C*. 2nd edition. 69

Rackauskas, M., Kreuzberg, M. M., Pranevicius, M., Willecke, K., Verselis, V. K., and Bukauskas, F. F. (2007a). Gating properties of heterotypic gap junction channels formed of connexins 40, 43, and 45. *Biophysical journal*, 92(6):1952–1965. 30

Rackauskas, M., Verselis, V. K., and Bukauskas, F. F. (2007b). Permeability of homotypic and heterotypic gap junction channels formed of cardiac connexins mcx30.2, cx40, cx43, and cx45. *Am J Physiol Heart Circ Physiol*, 293(3):H1729–1736. 103

Richard, I, W. (2005). Calmodulin transit via gap junctions is reduced in the absence of an electric field. *Journal of Insect Physiology*, 51(8):843–852. doi: 10.1016/j.jinsphys.2005.03.013. 191

Rummery, N. M., McKenzie, K. U. S., Whitworth, J. A., and Hill, C. E. (2002). Decreased endothelial size and connexin expression in rat caudal arteries during hypertension. *Journal of Hypertension*, 20(2):247–253. 35

Ryan, T. J., Faxon, D. P., Gunnar, R. M., Kennedy, J. W., King, S. B., Loop, F. D., Peterson, K. L., Reeves, T. J., Williams, D. O., and Winters, W. L. (1988). Guidelines for percutaneous transluminal coronary angioplasty. a report of the american college of cardiology/american heart association task force on assessment of diagnostic and therapeutic cardiovascular procedures (subcommittee on percutaneous transluminal coronary angioplasty). *Circulation*, 78(2):486–502. 127

Sakamoto, N., Saito, N., Han, X., Ohashi, T., and Sato, M. (2010). Effect of spatial gradient in fluid shear stress on morphological changes in endothelial cells in response to flow. *Biochemical and Biophysical Research Communications*, 395(2):264–269. 17

Sandow, S. L. and Hill, C. E. (2000). Incidence of myoendothelial gap junctions in the proximal and distal mesenteric arteries of the rat is suggestive of a role in endothelium-derived hyperpolarizing factor-mediated responses. *Circ Res*, 86(3):341–346. 34, 49, 104, 107

Sandow, S. L., Looft-Wilson, R., Doran, B., Grayson, T. H., Segal, S. S., and Hill, C. E. (2003). Expression of homocellular and heterocellular gap junctions in hamster arterioles and feed arteries. *Cardiovasc Res*, 60(3):643–53. Sandow, Shaun L Looft-Wilson, Robin Doran, Beth Grayson, T Hilton Segal, Steven S Hill, Caryl E F32 HL67626/HL/NHLBI NIH HHS/United States R01 HL41026/HL/NHLBI NIH HHS/United States Comparative Study Research Support, Non-U.S. Gov't Research Support, U.S. Gov't, P.H.S. Netherlands Cardiovascular research Cardiovasc Res. 2003 Dec 1;60(3):643-53. 107

Schuster, A., Beny, J.-L., and Meister, J.-J. (2003). Modelling the electrophysiological endothelial cell response to bradykinin. *European Biophysics Journal*, 32(4):370–380. 57, 63, 64, 65, 105

Seeley, R. R., Stephens, T. D., and Philip, T. (2006). *Anatomy and Physiology, 7/e*. McGraw-Hill Higher Education. 8

Segal, S. S. and Beny, J. L. (1992). Intracellular recording and dye transfer in arterioles during blood flow control. *The American journal of physiology*, 263(1 Pt 2):H1–7. Segal, S S Beny, J L R29-HL-41026/HL/NHLBI NIH HHS/United States Research Support, Non-U.S. Gov't Research Support, U.S. Gov't, Non-P.H.S. Research Support, U.S. Gov't, P.H.S. United states The American journal of physiology Am J Physiol. 1992 Jul;263(1 Pt 2):H1-7. 31

Shaikh, M. A., Wall, D. J. N., and David, T. (2011). Macro-scale phenomena of arterial coupled cells: a massively parallel simulation. *Journal of The Royal Society Interface*. 169

Simon, A. M. and McWhorter, A. R. (2003). Decreased intercellular dye-transfer and downregulation of non-ablated connexins in aortic endothelium deficient in connexin37 or connexin40. *J Cell Sci*, 116(11):2223–2236. 33

Sneyd, J. and Tsaneva-Atanasova, K. (2003). Modeling calcium waves understanding calcium dynamics. volume 623 of *Lecture Notes in Physics*, pages 179–199. Springer Berlin / Heidelberg. 189

Straub, S. V., Giovannucci, D. R., and Yule, D. I. (2000). Calcium wave propagation in pancreatic acinar cells: functional interaction of inositol 1,4,5-trisphosphate receptors, ryanodine receptors, and mitochondria. *The Journal of General Physiology*, 116(4):547–60. DK54568/DK/NIDDK NIH HHS/United States Journal Article Research Support, U.S. Gov't, P.H.S. United states. 189

Szymanski, M. P., Metaxa, E., Meng, H., and Kolega, J. (2008). Endothelial cell layer subjected to impinging flow mimicking the apex of an arterial bifurcation. *Ann Biomed Eng*, 36(10):1681–9. 20

Tada, S. and Tarbell, J. (2006). Oxygen mass transport in a compliant carotid bifurcation model. *Annals of Biomedical Engineering*, 34(9):1389–1399. 13

Toma, I., Bansal, E., Meer, E. J., Kang, J. J., Vargas, S. L., and Peti-Peterdi, J. (2008). Connexin 40 and atp-dependent intercellular calcium wave in renal glomerular endothelial cells. *American Journal of Physiology - Regulatory, Integrative and Comparative Physiology*, 294(6):R1769–R1776. 33

Tordjmann, T., Berthon, B., Claret, M., and Combettes, L. (1997). Coordinated intercellular calcium waves induced by noradrenaline in rat hepatocytes: dual control by gap junction permeability and agonist. *EMBO J*, 16(17):5398–5407. 10.1093/emboj/16.17.5398. 189

Tran, C. H. and Welsh, D. G. (2009). Current perspective on differential communication in small resistance arteries. *Can J Physiol Pharmacol*, 87(1):21–8. Tran, Cam Ha T Welsh, Donald G Research Support, Non-U.S. Gov't Canada Canadian journal of physiology and pharmacology Can J Physiol Pharmacol. 2009 Jan;87(1):21-8. 46

Truskey, G. A., Yuan, F., and Katz, D. F. (2009). *Transport phenomena in biological systems*. Prentice Hall, 2nd edition. 13

Tseng, Y.-C., Chang, S.-F., Zhou, J., Chiu, J.-J., and Chien, T.-Y. (2010). Mechanotransduction in vascular endothelium in response to fluid shear stress. *Clinical Molecular Medicine*, 2(1):4–15. 21

Tzima, E. (2006). Role of small gtpases in endothelial cytoskeletal dynamics and the shear stress response. *Circ Res*, 98(2):176–85. Tzima, Eleni Research Support, Non-U.S. Gov't Review United States Circulation research Circ Res. 2006 Feb 3;98(2):176-85. 18, 19

van Kempen, M. J. A. and Jongsma, H. J. (1999). Distribution of connexin37, connexin40 and connexin43 in the aorta and coronary artery of several mammals. *Histochemistry and Cell Biology*, 112(6):479–486. 33

Van Rijen, H., van Kempen, M. J., Analbers, L. J., Rook, M. B., van Ginneken, A. C., Gros, D., and Jongsma, H. J. (1997). Gap junctions in human umbilical cord endothelial cells contain multiple connexins. *American Journal of Physiology - Cell Physiology*, 272(1):C117–C130. 105

VanderLaan, P. A., Reardon, C. A., and Getz, G. S. (2004). Site specificity of atherosclerosis: Site-selective responses to atherosclerotic modulators. *Arterioscler Thromb Vasc Biol*, 24(1):12–22. 11

White, C. R. and Frangos, J. A. (2007). The shear stress of it all: the cell membrane and mechanochemical transduction. *Philosophical Transactions of the Royal Society B: Biological Sciences*, 362(1484):1459–1467. 15

Wit, C. and Wolfle, S. E. (2009). Connexins in the vasculature. In Harris, A. L. and Locke, D., editors, *Connexins*, pages 457–468. Humana Press. 30

Yamamoto, Y., Klemm, M. F., Edwards, F. R., and Suzuki, H. (2001). Intercellular electrical communication among smooth muscle and endothelial cells in guinea-pig mesenteric arterioles. *The Journal of Physiology*, 535(1):181–195. 105, 106

Yang, J., Clark, J. W., Bryan, R. M., and Robertson, C. S. (2005). Mathematical modeling of the nitric oxide/cgmp pathway in the vascular smooth muscle cell. *American Journal of Physiology-Heart and Circulatory Physiology*, 289(2):H886–H897. 944VO Times Cited:11 Cited References Count:47. 23

Yeh, H.-I., Lu, C.-S., Wu, Y.-J., Chen, C.-C., Hong, R.-C., Ko, Y.-S., Shiao, M.-S., Severs, N. J., and Tsai, C.-H. (2003). Reduced expression of endothelial connexin37 and connexin40 in hyperlipidemic mice: Recovery of connexin37 after 7-day simvastatin treatment. *Arterioscler Thromb Vasc Biol*, 23(8):1391–1397. 33, 36

Zhang, J. and Hill, C. E. (2005). Differential connexin expression in preglomerular and postglomerular vasculature: Accentuation during diabetes. *Kidney Int*, 68(3):1171–1185. 33

Appendix A

Table A.1: Table lists parameters used in describing single cell SMC model by Koenigsberger et al. (2005)

F	Maximal rate of activation-dependent calcium influx	0.23μM/s
K_r	Half saturation constant for agonist dependent calcium entry	1μM
G_{Ca}	Whole cell conductance for VOCCs	0.00129μM/mV/s
v_{Ca1}	Reversal potential for VOCCs	100.0mV
v_{Ca2}	Half point of the VOCC activation sigmoidal	-24.0mV
R_{Ca}	Maximum slope of the VOCC activation sigmoidal	8.5mV
$G_{Na/Ca}$	Whole cell conductance for Na^+/Ca^{2+} exchange	0.00316μM/mV/s
$c_{Na/Ca}$	Half point for activation of Na^+/Ca^{2+} exchange by Ca^{2+}	0.5μM
$v_{Na/Ca}$	Reversal potential for the Na^+/Ca^{2+} exchanger	-30.0mV
B	SR uptake rate constant	2.025μM/s
c_b	Half point of the SERCA activation sigmoidal	1.0μM
C	CICR rate constant	55μM/s
s_c	Half point of the CICR Ca^{2+} efflux sigmoidal	2.0μM
c_c	Half point of the CICR activation sigmoidal	0.9μM
D	Rate constant for Ca^{2+} extrusion by the ATPase pump	0.24 s^{-1}
v_d	Intercept of voltage dependence of extrusion ATPase	-100.0mV
R_d	Slope of voltage dependence of extrusion ATPase	250.0mV
L	Leak from SR rate constant	0.025s^{-1}
γ	Scaling factor relating net movement of ion fluxes to the membrane potential(inversely related to cell capacitance)	1970mV/μM
$F_{Na/K}$	Net whole cell flux via the Na^+-K^+-ATPase	0.0432μM/s
G_{Cl}	Whole cell conductance for Cl^- current	0.00134μM/mV/s
v_{Cl}	Reversal potential for Cl_- channels	-25.0mV
G_K	Whole cell conductance for K^+ efflux	0.00446μM/mV/s
v_K	Reversal potential for K^+	-94.0mV
l	Rate constant for net K_{Ca} channel opening	45.0
c_w	Translation factor for Ca^{2+} dependence of K_{Ca} channel activation sigmoidal	0μM
b	Translation factor for membrane potential dependence of K_{Ca} channel activation sigmoidal	0.13μM^2
v_{Ca3}	Half point for the K_{Ca} channel activation sigmoidal	-27.0mV
R_K	Maximum slope of the K_{Ca} activation sigmoidal	12.0mV
k	Rate constant of IP_3 degradation	0.1s^{-1}

Table A.2: Table lists parameters used in describing single cell EC model by Koenigsberger et al. (2005)

$\widetilde{F}$	Maximal rate of activation-dependent calcium influx	0.23μM/s
$\widetilde{K}_r$	Half saturation constant for agonist dependent calcium entry	1μM
$\widetilde{B}$	SR uptake rate constant	2.025μM/s
$\widetilde{c}_b$	Half point of the SERCA activation sigmoidal	1.0μM
$\widetilde{C}$	CICR rate constant	55μM/s
$\widetilde{s}_c$	Half point of the CICR Ca^{2+} efflux sigmoidal	2.0μM
$\widetilde{c}_c$	Half point of the CICR activation sigmoidal	0.9μM
$\widetilde{D}$	Rate constant for Ca^{2+} extrusion by the ATPase pump	0.24 s^{-1}
$\widetilde{L}$	Leak from SR rate constant	0.025s^{-1}
$\widetilde{k}$	Rate constant of IP_3 degradation	0.1s^{-1}
$\widetilde{G}_{cat}$	Whole cell cation channel conductivity	0.66μM/mV/s
$\widetilde{E}_{Ca}$	Ca^{2+} equilibrium potential	50 mV
$\widetilde{m}_{3_{cat}}$		-0.18μM
$\widetilde{m}_{4_{cat}}$		0.37μM
$\widetilde{J}_0$	Constant calcium influx	0.029μM/s
$\widetilde{C}_m$	Membrane capacitance	25.8pF
$\widetilde{G}_{tot}$	Total potassium channel conductivity	6927pS
$\widetilde{v}_K$	K^+ equilibrium potential	-80mV
x		53.3μMmV
y		-80.8mV
z		-0.4μM
$\widetilde{m}_{3b}$		$1.32\times10^{-3}\mu$M/mV
$\widetilde{m}_{4b}$		0.30μM/mV
$\widetilde{m}_{3s}$		-0.28μM
$\widetilde{m}_{4s}$		0.389μM
$\widetilde{G}_R$	Residual current conductivity	955pS
$\widetilde{v}_{rest}$	Membrane resting potential	-31.1mV

Table A.3: Table lists coupling coefficients in different intercellular communication configurations considered here; cases 1 & 2 simulate healthy whereas 3 & 4 simulate pathological states, early and progressive atherosclerotic lesion, respectively. Tilde represents parameters for ECs.

		Case 1	Case 2	Case 3	Case 4
Homocellular	g	1000.00	1000.00	1000.00	1000.00
	$\tilde{g}$	1000.00	1000.00	1000.00	0.00
	p_{Ca}	0.05	0.05	0.05	0.05
	$\tilde{p}_{\mathrm{Ca}}$	0.05	0.05	0.05	0.00
	p_{IP_3}	0.05	0.05	0.05	0.05
	$\tilde{p}_{\mathrm{IP}_3}$	0.00	0.00	0.05	0.05
Heterocellular	G	50.00	50.00	50.00	0.00
	$\tilde{G}$	50.00	50.00	50.00	0.00
	P_{Ca}	0.00	0.05	0.05	0.00
	$\tilde{P}_{\mathrm{Ca}}$	0.00	0.05	0.05	0.00
	P_{IP_3}	0.05	0.05	0.05	0.05
	$\tilde{P}_{\mathrm{IP}_3}$	0.05	0.05	0.05	0.05